Innovative solutions to improve the formability of Aluminium alloys

Politecnico di Bari

Department of Mechanics, Mathematics and Management

MECHANICAL AND MANAGEMENT ENGINEERING

Ph.D. Program

SSD: ING-IND/16–MANUFACTURING TECHNOLOGY AND SYSTEMS

Final Dissertation

Innovative solutions to improve the formability of Aluminium alloys

---

by

Piccininni Antonio:

Supervisors:

Prof Gianfranco. Palumbo

Eng. Andrea Lo Franco

Coordinator of Ph.D. Program:

Prof. Giuseppe Demelio

Course n°32, 01/11/2016-31/10/2019

Politecnico di Bari

Department of Mechanics, Mathematics and Management

MECHANICAL AND MANAGEMENT ENGINEERING

Ph.D. Program

SSD: ING-IND/16–MANUFACTURING TECHNOLOGY AND SYSTEMS

Final Dissertation

Innovative solutions to improve the formability of Aluminium alloys

---

by

Piccininni Antonio:

Referees:

Prof. Beatriz Silva

Prof. Paolo Renna

Supervisors:

Prof. Gianfranco Palumbo

Eng. Andrea Lo Franco

Coordinator of Ph.D. Program:

Prof. Giuseppe Demelio

Course n°32, 01/11/2016-31/10/2019

Believe in something

Even if it means sacrificing everything

(Colin Kaepernick)

Politecnico di Bari
DEPARTMENT OF MECHANICS, MATHEMATICS AND MANAGEMENT ENGINEERING

Study about MATerials & Innovative technologies – S.MAT.I. group

Declaration of originality

This is to certify that, to the best of my knowledge, the content of this thesis is my own work. This thesis has not been submitted for any degree or other purposes. I certify that the intellectual content of this thesis is the product of my own work and that all the assistance received in preparing this thesis and sources have been acknowledged.

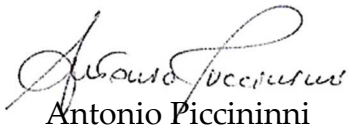

Antonio Piccininni

Acknowledgments

It has been a long journey and during these last three years I've been filling my "luggage" with lots of personal experiences, failures and achievements, wins and losses. And, fortunately, lots of supporting people surrounded me during this incredible experience.

Foremost, I am more than extremely grateful to my advisor, Prof. Gianfranco Palumbo, for being a reference point and a model to emulate, always being by my side in all the steps I took; thanks for being more than my advisor, thanks for being more than a guide, thanks for being more than a friend. I'm very proud to be a part of your team.

At the same time, this work would not have been in this present form without the huge support of my industrial advisor, Eng. Andrea Lo Franco, a wonderful person before being a top-level engineer who taught me how to live and love the O.Me.R. company, to whom I owe so much for funding my PhD grant. A huge thank especially goes to Eng. Giuseppe Russello, an insightful person whose point of view has always been hugely inspiring for me.

Beside my advisors, I owe a huge contribution to Prof. Yannis Korkolis for his amazing hospitality during the period I spent at the Ohio State University: it has been a great honor to work under your supervision and thanks for being an inspiring figure and a precious advisor. The period at the OSU will always have a special place in my mind also because I met there two special women, Beatriz and Jinjin, to whom I owe so much: thanks for your advices, thanks for being trusty colleagues, thanks for having shared lots of things with me.

A big thank goes also to my room/lab/office mate, Lino: we started together, we're working together, and hopefully we'll keep this team joined for many years.

At last, but not least, none of my achievements would have been possible without my family, a solid and constant presence throughout these years. Thanks mom, dad, sis, grandma and grandpa (I'm sure you're still taking care of me from there) and, above all, my irreplaceable and unique other half without whose support everything would have been much more difficult; thanks for unconditionally being by my side. I'm blessed to be surrounded by unique people like you.

Contents

List of figures

List of tables

Introduction

The environmental impact of human activities is becoming one of the key aspects to be regulated by the current standards in terms of reduction of harmful emissions. Among those activities, emissions related to the mass transportation sector are constantly increasing over the last years especially because of the continuous growing of the big cities and, consequently, of the transport line and infrastructure. For this reason, the big brand manufacturers are acting in the direction of updating the design criteria for the vehicle of the near future. Recent statistics from the International Council on Clean Transportation report that the adoption of "greener" propulsion configurations (as in the case of the hybrid systems) are constantly spreading for automotive applications as being considered an immediate solution to tackle the problem of the harmful emissions. Nevertheless, it is strongly believed that one of the promising alternative is based on the reduction of the vehicles mass by extensively adopting light alloys for the structural components: Aluminium alloys are then considered a serious candidate being able to provide superior mechanical properties combined with a low density (one third of a steel grade for stamping applications); in addition, with a particular focus on the railway transportation field, they are ranked as the most performing material in terms of safety since not producing any toxic smoke in case of fire (which is considered a primary aspect especially for all the underground applications). On the other hand, the poor formability at room temperature still remains the main drawback hindering the definitive implementation as the primary structural material for ground transportation. It becomes clear the reason why the scientific research, over the last two decades, has put lots of efforts in finding valuable solutions to overcome such a big limitation: higher formability means the production of more complex components, which can then be accomplished in fewer manufacturing steps thus sensibly reducing the cycle time.

Within this scenario, the cooperation between the Politecnico di Bari and the O.Me.R. S.p.A. company (located in Carini, province of Palermo, Sicily), leading the sector of interior design and components production for railway transport (www.omerspa.com), has started with the full funding of the PhD grant whose activities, described in details in the present final dissertation, has to be intended as the company serious intention to develop and optimize innovative technological solutions to be definitely implemented within its production schemes with the final aim of remarking its leading presence in the railway interiors trade market.

The present dissertation starts with the current scenario in the railway transportation sector reporting recent statistics about the constant growth of the passenger activities especially on the high speed and metro lines; accurate predictive models – as in the case of the High Rail Scenario – suggest that, only by means of huge investments in the infrastructures and in the vehicle design, a significant portion of user can be shifted from less efficient transport modes (cars, truck and aviation) to make the railway transportation become the main, or at least one of the most used, mean and then

achieve a significant reduction of emissions. The need for more performing vehicles to support such a growth has to be matched with the capabilities of the current sheet metal forming processes, focussing the discussion on two approaches currently used to improve the formability of Aluminium alloys: (i) the Heating During Forming (HDF) based on the increase of the working temperature during the forming operation (the alloy formability increases in warm conditions) and (ii) the Heating Before Forming (HBF) based on a preliminary modifications of the material properties by local heating to carry out the subsequent forming operation at room temperature.
Regardless of the specific approach, the definition of the operative window, due to the large number of variables involved in the process, is not trivial and the adoption of the process simulation is considered an effective way for a proper process design. The creation of an accurate numerical model, described in detail in the present dissertation, passes through a prior knowledge of the material behaviour: the importance of the conventional characterization route (i.e. based on uniaxial tensile tests or formability tests) as well as the research for faster and comprehensive innovative approaches (for example those based on the physical simulation) is strongly underlined since providing the necessary data to the process simulation to improve the accurateness of the numerical prediction.
The Finite Element (FE) based process design is described in detail in the second part of the dissertation when applied for the stamping of industrial case studies according to the base principles of the two abovementioned methodologies. In the case of the HBF, starting from the extensive characterization of the alloy under investigation (the strain hardenable AA5754 alloy purchased in the annealed state), the warm stamping of a large-scale window panel has been designed according to an uncoupled thermo-mechanical approach, starting from a preliminary optimization of the temperature distribution over the blank to be transferred in the forming simulation to optimize the variables of the stamping process. The accurateness of the numerical prediction has been then validated by means of experimental trials leading to the successful manufacturing of the designed component.
The strongly innovative connotation of the HDF approach and the intent to further develop and optimize the current state of the technology, has led the Politecnico di Bari and the O.Me.R. company to jointly submit a 4 years research proposal within the framework of the National Operative Programme (PON) 2014-2020: the For.Tra.In. project – Italian acronym for **For**matura di componenti per il settore ferroviario con **Tra**ttamento termico localizzato **In**tegrato –has been funded by the Italian Ministry of Economic Development (MiSE) and officially started in April 2017. The effectiveness of the HDF approach is then discussed at first when applied to a simple geometry, as in the case of cylindrical cups obtained by the deep drawing process. The optimization of the heating strategy to obtain a favourable distribution of the material properties (the alloy under investigation belongs to the age hardenable AA6082 alloy) has been numerically designed and the extent of the treated region to maximize the Limit Drawing Ratio was determined by an optimization procedure managed by a genetic algorithm. Deep drawing tests, carried out for validation purposes, have shown a

remarkable increase of the material formability if compared to as-received conditions. The adoption of the HDF approach is then also described when applied to the design of the stamping of an industrial component, belonging to the category of the window panel, whose stamping at room temperature has been demonstrated to be too critic: in this particular case, the definition of the proper heating strategy has been carried out by means of a double round optimization procedure based on the creation of accurate metamodels fitting the results from a designed set of numerical simulations. Pareto designs picked from both the optimization rounds have been then numerically validated once again demonstrating that a proper distribution of material properties is able to overcome the stamping limit of the alloy at room temperature.

1. The lightweighting challenge

The demanding reduction of harmful emissions from mass transportation mean as well as ground vehicles in general has pushed the big brand manufacturers to accept the challenge of implementing new criteria for the vehicle design: the downsizing of the installed power, sometimes combined with hybrid propulsion scheme, is one of the feasible solutions to reduce the pollutant emission without excessively affect the vehicle performance. As reported by the International Council on Clean Transportation [1], the hybrid technology, even though it is far from being considered a mature technology, is currently providing vehicles able to achieve a reduction in the fuel consumption by 25 to 30 percent with a remarkable reduction of the harmful emissions. In addition to the improvement in the propulsion system performance, the reduction of the sprung masses has been indicated as the big goal to definitely tackle the abovementioned problem: reducing the vehicle masses means to massively rely on light alloys: Aluminium (Al) alloys, for example, as widely mentioned in several scientific researches as a serious candidate to satisfy the demanding requirements of the environmental standards since characterized by good mechanical properties, exceptional strength-to-weight ratio and, above all, the low density (one third of the steel grades). On the other hand, the main limitation hindering the definitive implementation of Al alloys as the main structural material for ground vehicles components is the poor formability at room temperature. For this reason, the scientific research has put and is currently spending lots of efforts in the development of effective methodologies to overcome such a limitation, proposing innovative technological solution to be definitely implemented in the industrial environment. After a preliminary overview focussed on the current performance of mass transportation means – with a particular attention to the rail transport – the current state of the art regarding the innovative technology to improve the Al alloys formability are discussed in detail in the following sections.

1.1 The current scenario and future trends of the railway sector

The normative framework in the environmental field has imposed, from September 2015 on, the maximum oxide emissions of both petrol and diesel engine to be drastically reduced. In order to respect those limitations, ground vehicle manufacturers are moving toward substantial modifications of the design criteria as in the case of (i) engine downsizing, i.e. relying on turbocharged systems with fewer cylinders, (ii) "greener" propulsion systems (electric engines, fuel cells, hybrid configurations) or (iii) more performing power transmission architectures (CVT) making the engine work near the economy operative conditions (as in the case of the continuously variable transmissions [2]). Even though new design criteria are on their way to be implemented, the problem of the harmful emissions – above all CO_2 and NO_x – remains still unsolved: carbon dioxide is a greenhouse gas (GHG) produced by natural processes and everyday human activities, especially the burning of fossil fuels. The evolution CO_2 concentration is monitored by means of regular measurements

from the Hawaii's Mauna Loa laboratory since 1958 (it is the longest-running measurement in the world) [3]: the "history" of the CO_2 emissions over the years is graphically plotted by the Keeling curve, considered one of the most important results of the Scripps CO_2 research program initiated in 1956 by Charles David Keeling

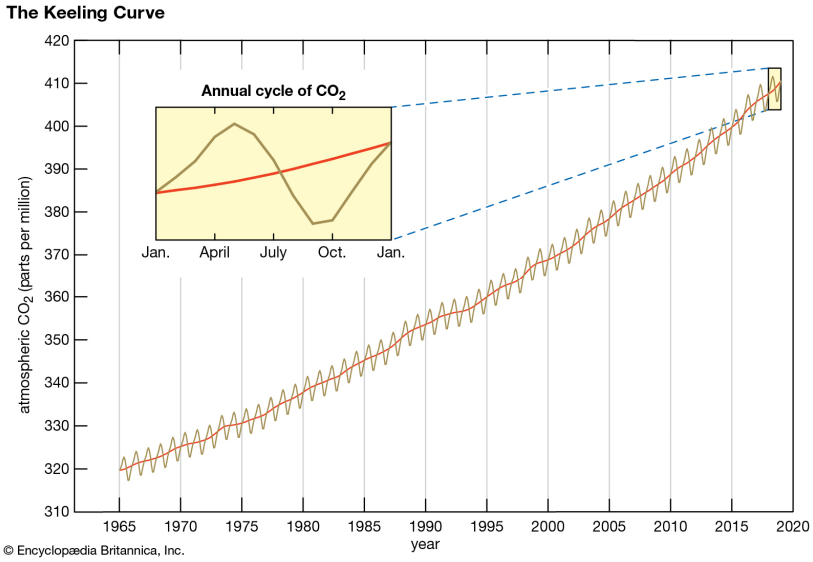

Figure 1 CO2 emissions (Mauna Loa Observatory): evolution over the last 50 years [4]

The situation depicted in Figure 1 clearly suggests that the continuous increase in carbon dioxide concentration may have tremendous implication in increasing the Earth's average temperature combined with unbalancing in the climate patterns. Nevertheless, it has to be underlined that pollutant emissions are not strictly related to the industrial or human activities: in fact, the activities related to the mass transportation mean "provide" their non-negligible contribution. If focussing the attention on the global transportation sector, as shown in the pie chart of Figure 2, recent statistics report that the railway sector was globally responsible for 1.9% of transport final energy demand, and for 4.2% of CO_2 emissions from the transport sector in 2015.

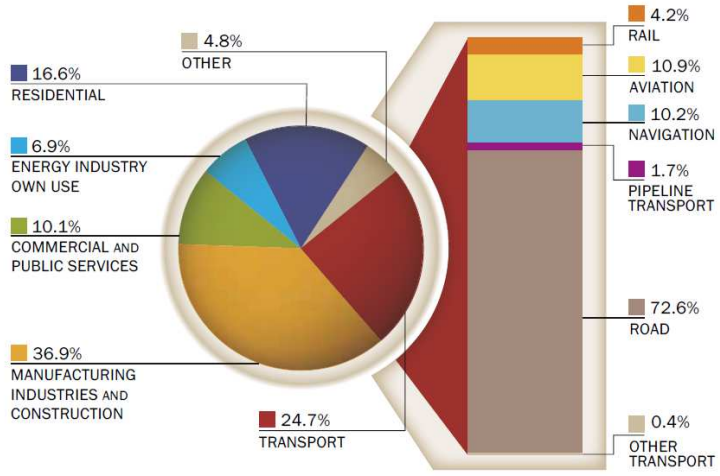

Figure 2 Share of CO_2 emissions from fuel combustion by sector (2015) [5]

In the same year, rail has accounted for 6.3% of global passenger transport activity (in passenger-km) and for 6.9% of global freight transport activity (in tonne-km) demonstrating the continuously growing accessibility to trains as a mass transportation mean. In fact, among the several rail transports, passenger rail transport (including urban rail services) accounted for 9% of global passenger activity (passenger-km): such a phenomenon, still growing, is strictly connected to the increased rail urban activities and the most evident example is provided by the Chinese big cities where high-capacity/high frequency rail activity within Chinese cities has grown by 150% between 2005 and 2015. The downside to the increased railway activities is the consequential increased in the polluting emissions: the pie chart in Figure 3 categorized the railway emissions by geographic area.

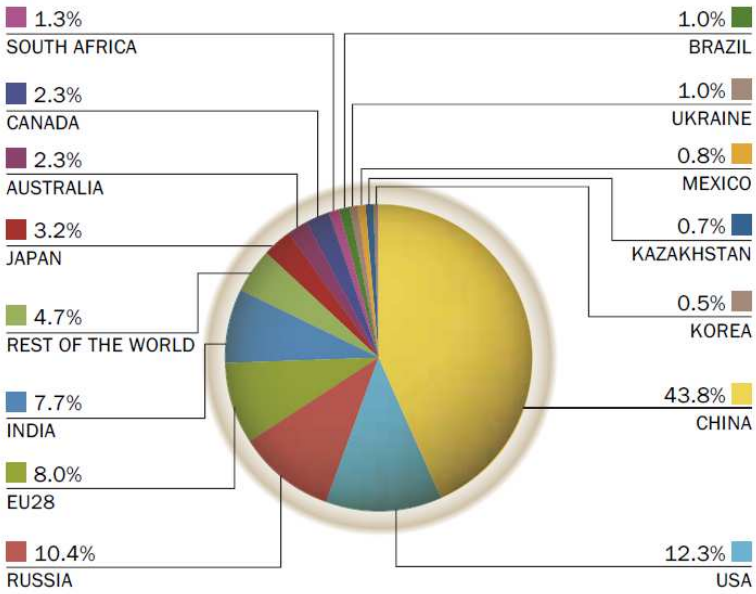

Figure 3 Railway CO_2 emissions categorized by geographic (2015) [5]

The increase in the railway activities can be analysed in term of different factors, among which one of the most representative is the evolution of the total length of a country railway track, considered to be an accurate indicator of the priority given to investment in rail transportation. If considering the railway as composed of conventional (passenger and freight trains), high-speed and urban (consisting of metro and light rail systems) tracks, despite conventional rail covers almost 94% of all rail track-kilometres, their length has grown very little in recent years (see the cyan lines in Figure 4).

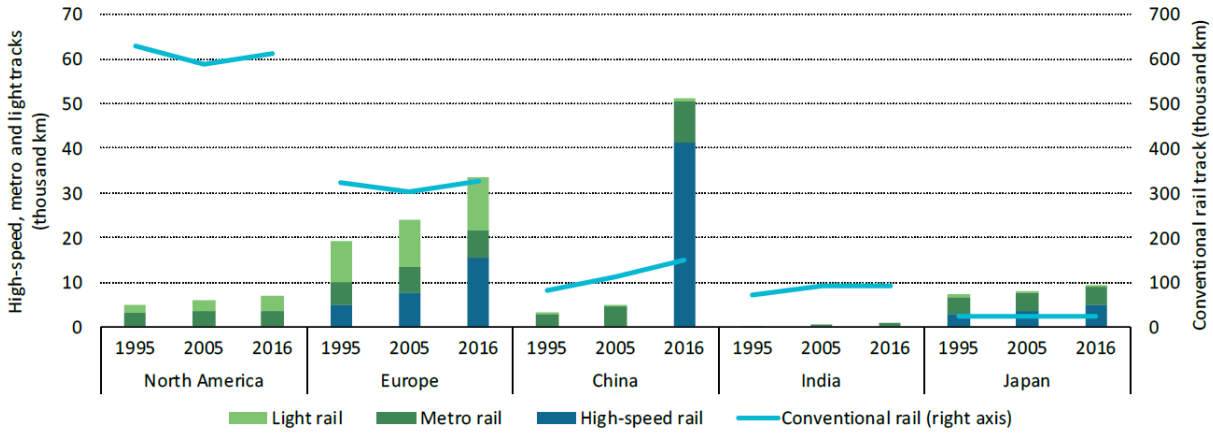

Figure 4 Track length by region and network type (from 1995 to 2016) [6]

On the other hand, urban and high-speed rail networks have grown significantly, especially in the Asian continent (as previously mentioned), still considered the epicentre of most recent and ongoing developments. Today, nearly two-thirds of the world's high-speed rail lines are in China and this percentage is even more outstanding if considering that no high-speed network existed before 2008 and the current length of China's high-speed rail network has overtaken that of all other countries in the world combined. If looking at the bar chart in the Figure 5a, passenger rail transport activity (comprising urban and non-urban movements) has increased significantly over the past twenty years but is concentrated in a few regions.

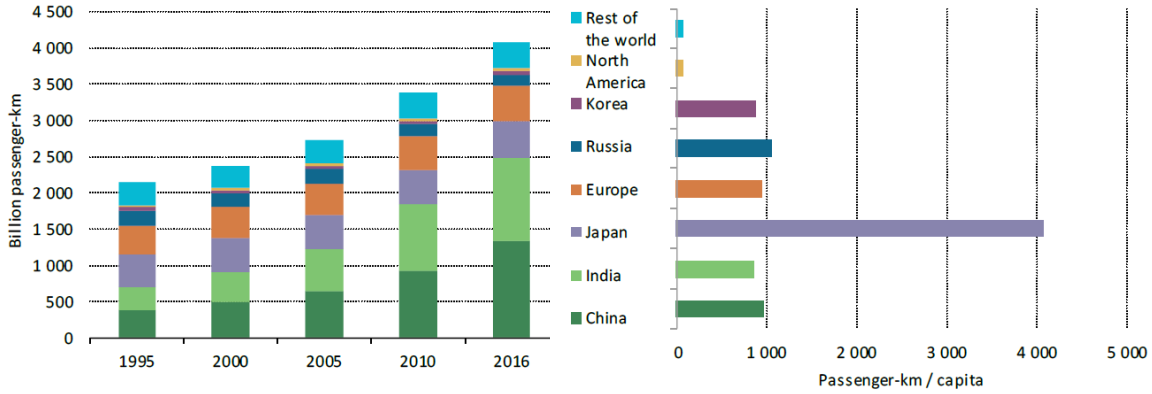

a) b)

Figure 5 Passenger rail activity arranged a) by geographic area (1995-2016) and b) by passenger-kilometres per capita in 2016 [6]

Even though the highest activity in terms of passenger-kilometres per capita in 2016 belongs to Japan (see Figure 5b), the most impressive growth over the last 20 years have been observed in China as an immediate reflection of the bigger investments in high-speed rail lines and urban rail networks. Within the European borders – historically the first region to build an international rail network – urban and non-urban rail activity has risen slowly (see the stacked orange bars in Figure 5a) but steadily in recent decades mainly due to the shifting of passenger activity from conventional to highspeed rail.

Despite the above described scenario delivers the idea railway vehicles gaining importance and accessibility as the preferred mass transportation mean, the continuous challenge against the other ground and air vehicles is still open. In fact, in the case of the passenger transport, rail has to face the increasing demand for individual and flexible mobility, immediately available at any time of day and for any possible destination. For this reason, rail transportation has to continuously challenge the performance offered by personal cars (especially after the advent of electric and hybrid cars [1]) and also air travel, capable of connecting people faster and with more flexibility to their destination. For this reason, new trends in railway infrastructure and vehicles are predicted by accurate models, as in the case of the Base Scenario (BS) models describing how rail transport may handle competitive pressures based on existing policies of other energy sectors, including power, industry and buildings. The BS model predicts that the global rail network (urban, conventional and high-speed rail) is going to expand from 1.6 to 2.1 million track-kilometres: in the same period (see Figure 6a) the number of passenger-kilometres on the global rail network will almost double. As reported in the pie chart in Figure 6b, by 2050, North America will remain the region with the most extensive conventional rail network followed by Europe, India, China and Russia.

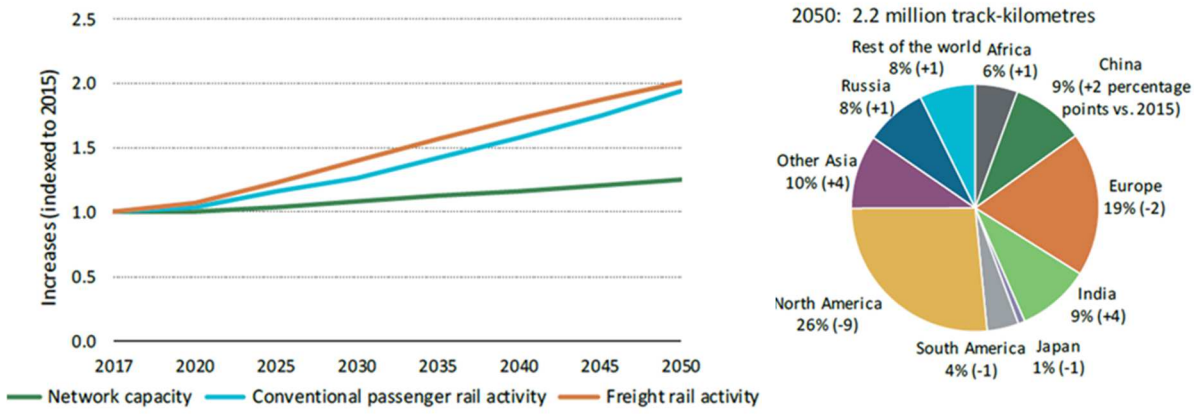

a) b)

Figure 6 BS prediction for the period 2017-2050: a) global conventional rail activity and b) regional distribution of conventional rail extension by 2050 [6]

The prediction in the bar chart of Figure 7 regarding the metro and high-speed rail reflects the current situation, announcing an even more faster growth of about 140% for metro and 65% for high-speed rail by 2050. As the data clearly report, China maintains its recently attained standing as the country with the world's largest metro network: by 2050, the length of its metro network tracks increases more than threefold to over 30 000 kilometres, making up 40% of the world's metro track length. Europe, North America, India and other Asian countries also expand their metro and light rail systems.

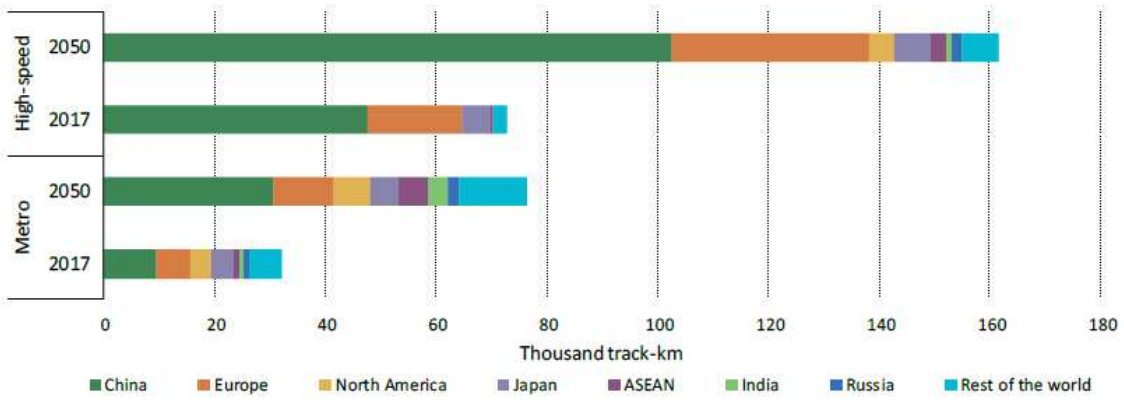

Figure 7 BS prediction for the global metro and high-speed rail by track-kilometres categorized by geographic area (2017-2050) [6]

Based on the presented prediction of the BS model, a remarkable increase of the CO_2 emissions by 2050 is expected; on the other hand, it has to be underlined that the carbon intensity of GHG emission is not only dependent by the type of traction used by the rail vehicle (mainly diesel or electric), but also on the energy intensity of the rail service. Thus, electric trains can effectively reduce emissions, compared with diesel-powered trains, but only if the power generation mix is not largely dependent on primary fuels with high carbon content, such as coal. For this reason, new rail project aimed at reducing the GHG emissions should account for not only the influence of the specific vehicle, but also the contribution coming from the construction of the railway network, the manufacturing of the rolling stock as well as its maintenance and final disposal. Based on these considerations, an alternative scenario – i.e. the High Rail Scenario (HRS) - exploring the extent to which rail can replace less efficient transport modes as cars, two-three wheelers, aviation and trucks. If compared with the prediction of continuously growing CO_2 concentration from the BS, the HRS (see the bar chart in Figure 8) predicts a peak of emissions between 2035 and 2040, after which a decline is achieved by 2050. Such a reduction becomes possible only if shifting 11.2 trillion passenger-kilometres from road transport and aviation, which will result in a reduction of roughly 1 Gt CO_2-eq GHG emissions.

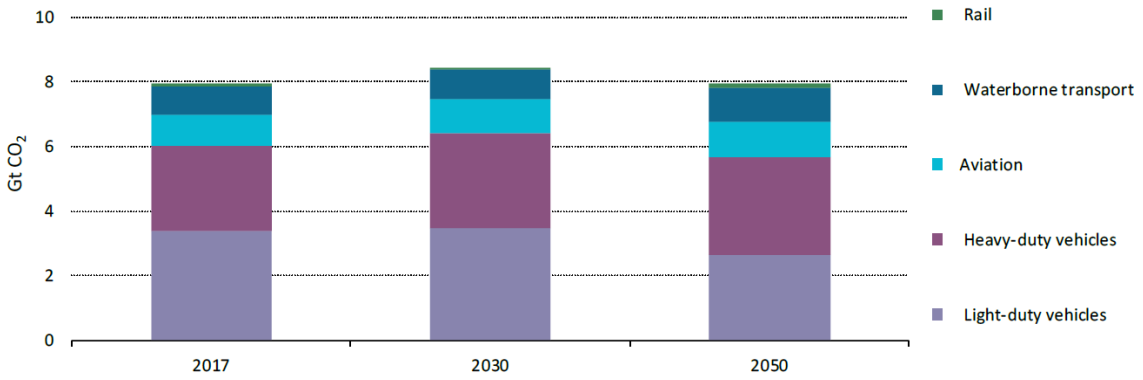

Figure 8 Direct CO2 emissions from fuel combustion in the High Rail Scenario, 2017-50 [6]

The described scenario delivers a clear "big picture" of the current situation of the railway transportation and draws quite clearly the new trends for the reduction of polluting emissions. The HRS, in fact, demonstrates the energy and environmental benefits that can be achieved through stronger action to enhance the role of rail, which most probably will not eliminate entirely the problem of the environmental impact of transport but offers a well promising solution. For this reason, the pillars on which the development of "greener" railway projects have to be founded on are: (i) the improvement of the infrastructure characteristics (minimizing the need for large amounts of steel, iron and concrete per kilometre), (ii) a re-design of the vehicle performance, in terms of optimized propulsion system and reduction of the sprung masses (vehicle lightweighting) and (iii) the shifting away from transport modes with high carbon intensities (aviation and cars for passenger rail, trucks for freight rail).

1.2 Light alloys for vehicles lightweighting

The big scenario described in the previous section suggests the need of huge investments to make the rail transportation as the main, or at least one of the most used, solution for passenger activities. The improvements in the infrastructure runs parallel with the growth in the vehicles performance, which can be achieved by: (i) upgrading the propulsion and transmission sub-systems and (ii) improving the aerodynamic behaviour adopting more complex shapes and lighter structural components. Matching all those requirements is not trivial, and the research for the optimal combination between the most suitable structural alloy and the most performing manufacturing process is still ongoing. To dramatically reduce the sprung masses of a vehicle (regardless of its specific application), the adoption of light alloys, as in the case of Aluminium (Al) [7] or Magnesium (Mg) alloys [8], is widely recognized as the most promising solution without excessively decreasing the performance and ensuring, at the same time, a high level of passengers' safeness [8,9]. In the case of automotive applications [10], thanks to the high strength-to-weight ratio, an Al body-in-white car chassis is about 40% lighter with a consequent weight saving of more than 400 kg [11]. In the case of railway transportation, the vehicle lightweighting must not penalise the safety aspect that is considered a key indicator of the overall performance. The reference standard, EN 45545 [12], contains the countermeasures and requirements intended to protect passengers and staff in railway vehicles in the event of a fire on board. In particular, the normative states that the design of rolling stock – where the terms "rolling stock" refer to railway vehicles in general, including both powered and unpowered – and the products have to limit the fire development in the case of the occurrence of an ignition event so that an acceptable level of safety can be ensured. In such a way, in the event of a fire, passengers and staff will be able to escape from the fire and be able to reach a place of safety. The standard categorizes the hazard levels – from level 1 (HL1) to level 3 (HL3)

- of all the material installed on a vehicle according to the operation categories and the design categories as listed in Table 1.

Table 1 Hazard level classification [12]

Operation category	Design category			
	N*	A**	D***	S****
1	HL1	HL1	HL1	HL2
2	HL2	HL2	HL2	HL2
3	HL2	HL2	HL2	HL3
4	HL3	HL3	HL3	HL3

* Standard vehicles

** Vehicles forming part of an automatic train having no emergency trained staff on board

*** Double decked vehicle

****Sleeping and couchette vehicles

The operation categories are divided as follows:

- Operation Category 1: vehicles not designed or equipped to run on underground sections, tunnels and/or elevated structures and which may be stopped with minimum delay, after which immediate side evacuation to a place of ultimate safety is possible.
- Operation category 2: vehicles designed or equipped to run on underground sections, tunnels and/or elevated structures, with side evacuation available and where there are stations or emergency stations that offer a place of ultimate safety to passengers, reachable within a short running time.
- Operation category 3: vehicles designed or equipped to run on underground sections, tunnels and/or elevated structures, with side evacuation available and where there are stations or emergency stations that offer a place of ultimate safety to passengers, reachable within a long running time.
- Operation category 4: vehicles designed or equipped to run on underground sections, tunnels and/or elevated structures, without side evacuation available and where there are stations or emergency stations that offer a place of ultimate safety to passengers, reachable within a short running time.

It becomes then clear that, especially for the operation category 4, materials for the structural components have to be carefully selected not only to ensure the sufficient mechanical resistance for a prolonged time in case of fire but also to avoid any production of toxic smoke to help the passenger evacuate the train. For this reason, the standard ranks the Al alloys in terms of safety, being the only material that doesn't produce smoke (in contrast to resin based structural components). Even though the low density, the good mechanical properties and the safety performance make the Al alloys a serious candidate, the final choice for the best material is not so straightforward: as widely documented in literature [13], the huge advantages coming from the Al alloys are counterbalanced by the poor formability at room temperature

as it can be seen when comparing the Forming Limit Curve (FLC) of a low carbon steel with the one of an Al alloy (Figure 9).

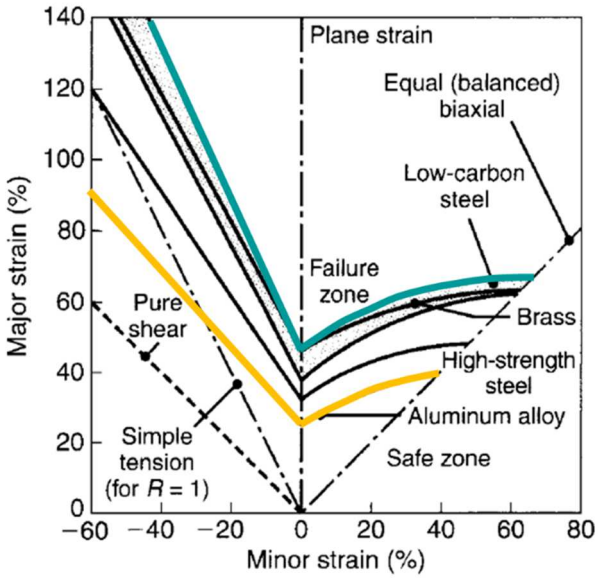

Figure 9 Comparison between the Forming Limit Curves (FLC) of a low carbon steel and an aluminium alloy [14]

In the case of a low formable alloy, due to the limited capability to be deformed according to a specific geometry without the occurrence of rupture, the geometrical complexity that can be achieved in one step process is inevitably reduced, thus forcing to re-design the stamping operations in a multi-step process or to manufacture separate sub-parts to be subsequently joined (with an increase in the manufacturing time cycle).

The scientific research, over the last twenty years, has put lots of effort to find effective solutions to overcome the limitation of the poor formability at room temperature. The technological solutions can be grouped in two main categories based on: (i) the Heating During Forming (HDF) approach according to which the blank heating is maintained during the forming operations and (ii) the Heating Before Forming (HBF) approach according to which the blank is preliminary subjected to local heat treatment to obtain an optimal distribution of properties and subsequently formed at room temperature. Both of the two approaches, whose effectiveness is widely documented in literature, are discussed more in the details in the following sections.

1.3 Limitations and possible solutions

The increased of the working temperature has been extensively documented as one of the most promising solutions that have been proposed over the last year to overcome the limitation of the poor formability of several alloys at room temperature [15]. As reported by Li and Ghosh [16], uniaxial tensile tests carried out on both 5xxx and 6xxx series specimens demonstrated that the total elongation increased as the temperature

increased and decreased with the increasing strain rate. Moreover, it was reported that for a given strain rate level and with the increasing temperature, the strain hardening rate tended to decrease whereas the strain rate sensitivity increased, thus playing a dominant role in enhancing the material ductility. The reported results were in good accordance with the research proposed by Ozturk et al. [17] and Panicker and Panda [18] confirming the key role played by the strain rate sensitivity index in enhancing the material formability. The increased elongation at failure in warm conditions – usually below the recrystallization temperature [19] – opened the way to the development and optimization of new technological solutions for the sheet metal forming processes [20,21]: the influence of the increased temperature on the material properties (reduction of the yield point and increase in its formability) had a huge impact on the performance of the manufacturing processes, since the production of more complex components in one step processes became much easier to be achieved. One of the first application of the warm process conditions was on the deep drawing process that, besides being one of the most conventional sheet forming processes, was frequently used as a benchmark test to evaluate the formability of metallic materials: as shown in Figure 10a, a circular blank is forced by the action of a cylindrical punch to fill the cavity of a cylindrical die.

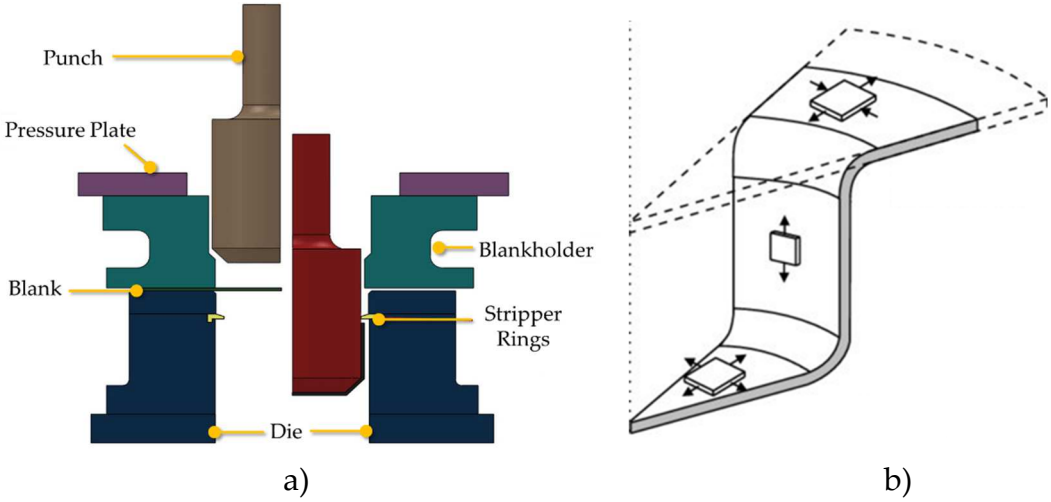

Figure 10 Deep drawing process: a) main components [14] and b) stress conditions over the formed blank [22]

As it can be noted in Figure 10b, each section of the drawn cup is characterized by a specific stress conditions [23]: in particular, the flange is generally the portion that withstands the highest plastic strain levels. In particular, a small element from the flange is subjected to a tensile stress due to the material drawing, accompanied by the rise of a compressive hoop stress state that tends to form wrinkles on the flange. For this reason, the load applied by the blankholder is a fundamental parameter not only to regulate the relative sliding between the blank and the tools (thus having an influence of the blank drawing inside the die cavity) but also to avoid the occurrence of wrinkling phenomena. Along the wall region, as it can be seen, the strain in the hoop direction is mainly blocked and the material is subjected to a state of tensile stress along the axial direction due to the action of the punch; from a strain point of

view, the blank portion in contact with the punch bottom radius is indicated as the most critic one. For the deep drawing process, the Limit Drawing Ratio (LDR) – defined as the ratio between the maximum drawn diameter without the occurrence of rupture and the punch diameter – is considered an accurate indicator of the material formability: the higher the LDR, the more formable is the alloy. Preliminary studies [24] have demonstrated that Al alloys are characterized by a value of the LDR around 2 (in the case of Al alloys belonging to the age hardenable 6xxx series, the LDR can be even lower if the material is in the T6 state). According to the description of the deformative conditions shown in Figure 10b, if improving the material drawing from the flange region, the risk of rupture can be dramatically reduced: at the same time, the blank portion in contact with the punch radius must retain his initial strength. For this reason, most of the published researches regarding the Warm Deep Drawing (WDD) report the adoption of an experimental equipment as the one reported by Palumbo and Tricarico [25] and shown in Figure 11.

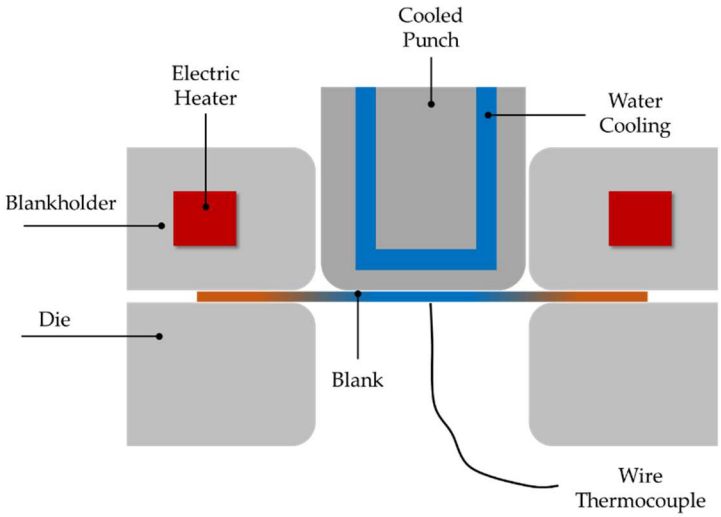

Figure 11 Scheme of the equipment for the Warm Deep Drawing (WDD)

The heating of the sole flange portion (thanks to the adoption of an electric heater in the blankholder) combined with the action of the cooled punch on the central portion of the sample created a gradient of material properties able to counterbalance the stress state during the drawing operation. Due to the increased sensibility of the material behaviour to the strain rate, it was demonstrated that, the optimization of both the heating temperature and the punch speed (that has an immediate reflection in the applied strain rate), it was possible to reach an improvement of the LDR of more than 40% up to the value of 2.85. It is worthy of notice that, despite the deep drawing is considered a conventional sheet metal forming process, the number of variables involved in the process increases sensibly when switching to the warm conditions and a more refined methodology to accurately design the process becomes necessary. The adoption of the numerical approach, based on the creation of a reliable Finite Element model, has been widely documented as a powerful solution to effectively design the process without an excessive waste of time and material. On the other hand, the

reliability and accurateness of the FE model needs the accomplishment of previous intermediate steps, as in the case of an extensive material characterization campaign for the prior knowledge of its behaviour: currently, tensile and formability tests represent the rule of thumb to comprehensively gather information about the mechanical (flow curve) and deformative behaviour (Forming Limit Curves) of several metallic materials. In the case of the material testing for the design of sheet metal forming process, the two abovementioned tests may not be sufficient and specifically designed testing procedures [26,27] has to be considered. For example, in the case of a blank sheet, the previous rolling operation induces in the material a predefined texture characterized by elongated grains in the rolling direction which reflects in an anisotropic behaviour under loading conditions. The investigation of the anisotropic behaviour by means of specifically designed characterization tests [28–30] becomes of first importance to properly calibrate advanced anisotropic yield criteria – as those proposed by Barlat and Banabic [31–35] – able to better reproduce the material plastic behaviour: thus, the choice and calibration of a proper hardening law and a suitable yield function represents another intermediate step to construct a reliable FE model. As an example, Abedrabbo et al. [36] calibrated the anisotropic coefficient of the Barlat's YLD2000-2d anisotropic yield function [32] for the warm forming simulation of two strain hardenable Al alloys, namely AA5182-O and AA5754-O. Coefficients of the yield criterion were calibrated as a function of the working temperature and then implemented into the commercial FE code LS-Dyna via a user material subroutine (UMAT). The temperature- dependent material model was used to simulate the coupled thermo-mechanical finite element analysis of the stamping using a hemispherical punch under the pure stretch boundary condition (no material drawing was allowed): it was demonstrated that a combination of a thermo-mechanical FE analysis with an accurate anisotropic temperature- dependent material model could accurately predict the outcome of the experimental tests. The adoption of an accurate numerical model resulted to be a powerful tool also for the design of more innovative stamping process using flexible media as in the case of the warm hydroforming, in which the action of the punch is replaced by a pressurized fluid [37]. As reported by Palumbo and Piccininni [38], the correct choice of the working temperature and oil pressure profile could be numerically determined for the correct stamping of a complex component as the bipolar plate of a proton exchange fuel cell. As demonstrated in the case of the deep drawing process, the strain rate applied to the material has an enormous effect on the post forming properties of hydroformed components: as reported by Palumbo et al. [39], in accordance with other data available in literature [40,41]., when increasing the oil pressure rate in the forming of a benchmark component (AA5754-H111), a sensible reduction in the die cavity filling was registered. The scenario described in the present section underlines once more how the combination of a proper material characterization in warm conditions and the choice of the more suitable material model (hardening law, yield criterion) has a remarkable influence on the reliability of the FE model and, consequently, on the accurateness of the numerical prediction. On the other hand, it has to be pointed out

that such advantages are partially counterbalanced by the need of a more complex equipment: even in the case of a simple equipment as the one described in Figure 11, active heating elements had to be installed into the blankholder, thermocouples were necessary to monitor both the blank and the tools temperature as well as a cooling circuit to keep the punch at low temperature; in addition, the preliminary step of the blank heating before the drawing step increases not only the time cycle but also the energy consumption of the process. For this reason, in the last years, a promising alternative to the forming operation in warm conditions has been proposed: the HBF approach literally splits the manufacturing process since it is based on a preliminary heat treatment of the blank to obtain a specific distribution of properties (according to the component to be manufactured) so that the subsequent forming step can be carried out at room temperature thus needing a press machine for cold forming (lower cost, prolonged tools life). Blanks subjected to the local heat treatments are usually indicated in literature as Tailored Heat Treated Blanks (THTB) [42]; the local modification of the material properties can be obtained adopting different heating technologies: for example, the high flexibility of the laser radiation becomes the best solution for the local treatment of prototype or small-batch series even though partially counterbalanced by the higher investment for the machine set up (see Figure 12).

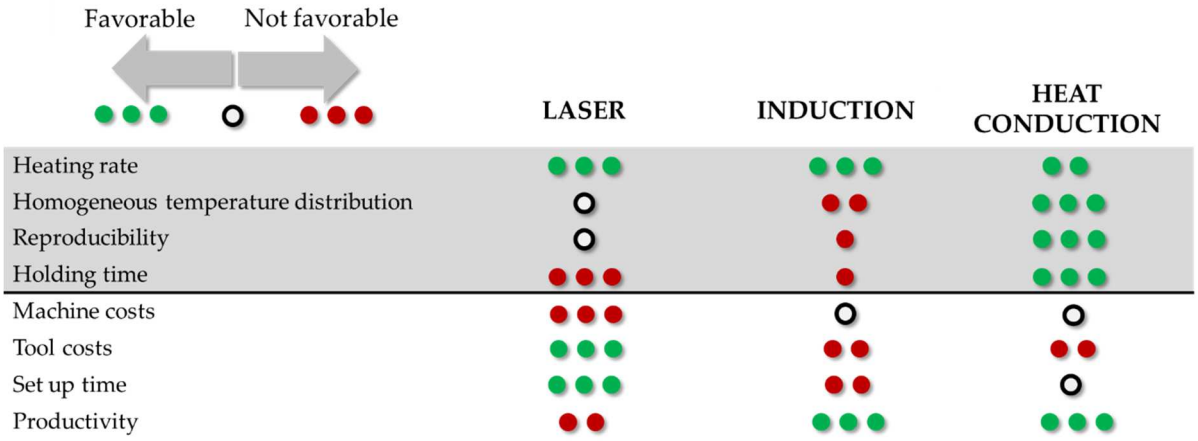

Figure 12 Performance indicator for the different heating technologies for the HDF approach

On the other hand, uniformity of the temperature distribution, the high replicability and the applicability to high volume production are the strong points of the heating by a conductive plate. The HDF approach is mainly based on two basic principle: (i) the application of the treatment to local soften the material is intended for the reduction of the force needed during the stamping operations (in the case of the deep drawing process, a softened flange creates the proper gradient of material properties necessary to achieve higher LDR); (ii) tailoring the distribution of the material properties to promote the material flow from softened areas to prevent excessive stretching of adjacent critical regions (Figure 13).

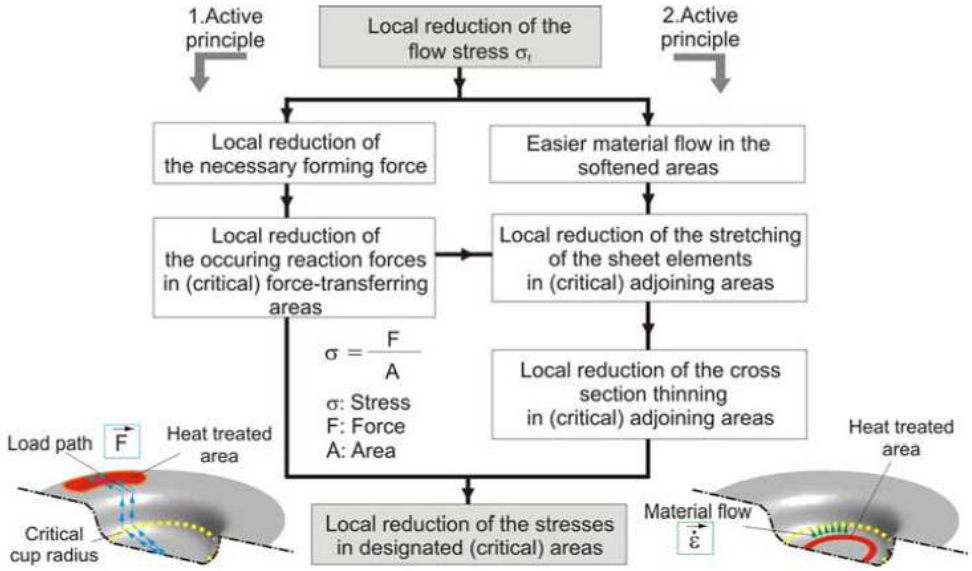

Figure 13 Basic principle of the local heat treatment of Al alloys [42]

The local modification of the material properties has been extensively in the case of age hardenable Al alloys (as those belonging to the 6xxx series) [43]: in fact, the heat treatment can be properly designed to dissolve precipitation at the grain boundaries (for example starting from a T6 or T4 state) to improve the material formability or start from a more formable conditions and use the local treatment to promote the precipitation of hardening secondary phases. Nevertheless, the HDF approach can be equally applied on strain hardenable Al alloys (as those belonging to the 5xxx series) [44,45]: since no modification can be induced by a local treatment, the material is usually purchased in a pre-strained condition characterized by an initial cold working (higher density of dislocation and higher yielding point). The subsequent heat treatment can be carried out: (i) below the recrystallization temperature to anneal lattice imperfection (the material can then reach higher elongation with almost the initial strength) or (ii) above the recrystallization temperature, so that the microstructure is totally reformed and the material is fully softened (i.e. characterized by an increased ductility).

As underlined in the previous section, the HDF approach, due to the high number of variables involved in both the preliminary local treatment and the subsequent stamping operations, needs accurate approach to properly define the operative windows. In particular, when heating Al alloys via laser radiation, the high thermal conductivity of the alloy represents the big challenge for an effective treatment: in fact, ensuring a sufficient quantity of energy to soften the material has to be balanced with the need to localize as possible the treated region an limiting the heat transition zone [46]. It is reported that the heating time, the holding time at the maximum temperature are considered the key factors to be designed for a proper local heating (see Figure 14a): as anticipated, if the treated area has to be localized as possible, the short term heating is the only possible solution so the maximum temperature (and any deviation from that value) plays a key role.

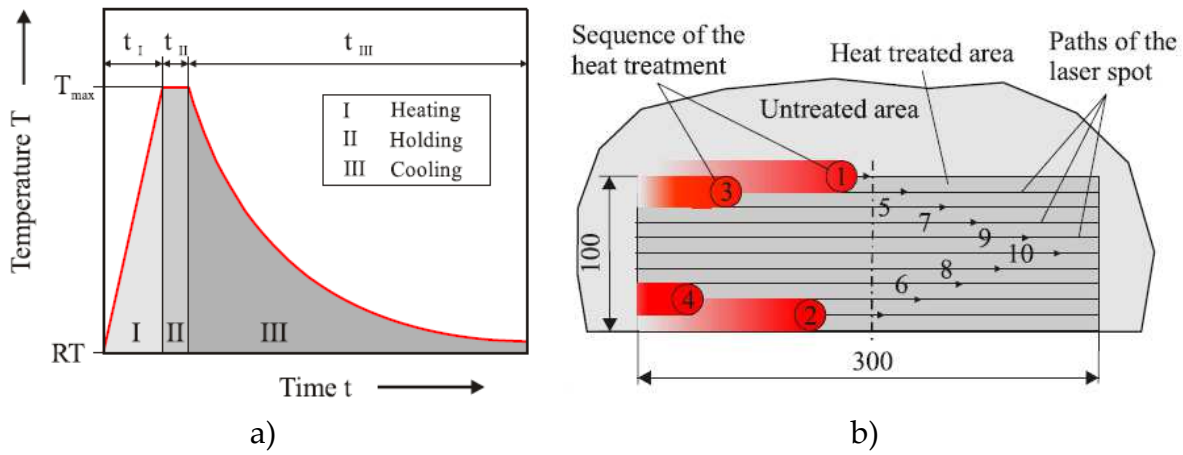

a) b)

Figure 14 Local heating by laser radiation: a) main parameters involved and b) optimization of the heating strategy

In addition, when a wider area has to be treated by laser technology, another key aspect is the optimization of the heating strategy: as shown in Figure 14b, the optimized sequence of laser tracks is essential for an effective modification of the material properties. It becomes then clear that the designing of the manufacturing process via the HBF approach is not trivial: the two sub-steps are strictly connected and the definition of the operative window of the local treatment has a tremendous implication on the successful outcome of the stamping at room temperature. The wide number of parameters involved in the process drives the attention toward the need of a design tool capable of correctly define the optimal value of the process parameter: as already discussed in the previous sections, the numerical simulation is one of the most promising solution to get the ambitious goal of correctly design the HBF methodology. It is even easier to understand that the design of the two steps cannot disregard the prior knowledge of the material [47,48]: characterization tests has to be properly designed in order to provide useful data especially regarding the material data in the post-treated condition. The creation of an extended database containing not only the information regarding the combination of time and temperature for the proper modification of the material properties but also all the information regarding the mechanical and strain behaviour in each of the investigated post-treatment conditions. In such a way, the correct formulation of the thermal problem will provide the exact distribution of temperature during the heating and, consequently, the final distribution of the material properties after the heat treatment [49]; if modelling the material behaviour in the stamping simulation implementing the experimental data according to the predicted post-treatment conditions, the quality and accurateness of the numerical simulation can be substantially increased thus providing a powerful tool for a proper process design by the HDF approach [50,51].

2. Materials & Methodologies

As discussed in the first chapter, the research activities described in this dissertation aimed at investigating the two main approaches documented in literature as effective in improving the formability of Al alloys, the Heating During Forming (HDF) and the Heating Before Forming (HBF) approaches. Research activities were carried out investigating both strain hardenable (AA5754) and age hardenable (AA6802) Al alloy. The distinctive characteristic of the research activities here described is their application to large scale components for railway applications, i.e. of industrial interest, whose geometries were provided by the O.Me.R. company. The design of the manufacturing processes according to the basic principles of the two abovementioned technological solutions, due to the large number of variables involved, was carried out by means of a FE-based approach capable of tackling the excessive time and material wasting, typical of the trial-and-error methodology. According to the specific process to be investigated, the prior knowledge of the material behaviour played a key role: alloy characterization activities were based on both conventional tests (as in the case of the tensile and formability tests to evaluate the material behaviour in warm conditions) and more innovative tests (as in the case of the physically simulating the action of a laser radiation on a strain hardenable Al alloy to evaluate the distribution of the material properties after the heat treatment. Material data coming from the experimental test were implemented within the FE models (created with the commercial code Abaqus 2017) and the results from the numerical simulations were finally validated by means of experimental trials.

2.1 The investigated alloys

The attention was focussed mainly on two alloys, one of them belonging to the category of the strain hardenable Al alloys, i.e. the AA5754. Material chemical composition is reported in Table 2.

Table 2 Chemical composition of the AA5754 under investigation

Al%	Cr%	Cu%	Fe%	Mg%	Mn%	Si%	Ti%	Zn%
Bal.	< 0.3	< 0.1	< 0.4	2.6 – 3.6	< 0.5	< 0.4	< 0.15	< 0.2

The investigation of the material behaviour was carried out on specimen both in the annealed condition (H111) and characterized by an initial cold working (H32). On the other hand, the AA6082 was other alloy under investigation belonging to the group of the age hardenable, initially purchased in its peak hardening conditions (T6) characterized by high resistance and very limited elongation. Chemical composition is reported in Table 3.

Table 3 Chemical composition of the AA5754 under investigation

Al%	Si%	Fe%	Cu%	Mn%	Mg%	Cr%	Zn%	Ti%	Si%
Bal	0.7 – 1.3	≤ 0.5	≤ 0.1	0.4 – 1	0.6 – 1.2	≤ 0.25	≤ 0.2	≤ 0.1	0.7 – 1.3

2.2 The Finite Element approach

It is universally recognized that adopting an FE approach is a valuable solution to design, and eventually optimize, the manufacturing process avoiding the unbearable costs of a "trial-and-error" approach. Most of the activities related to the design of the manufacturing process were based on the adoption of the numerical simulations: the FE commercial code Abaqus/CAE allows to choose two different schemes from the process solution (the implicit and the explicit formulation), whose main properties are discussed in the following. In the case of the implicit solver, or the implicit method, the starting point is the solution of the equilibrium condition [52], expressed by Equation 1.

$$\{F\}=[K]\{u\} \quad (1)$$

Where {F} and [K], respectively the vector of acting loads and the stiffness matrix, represent the known quantities, whereas the vector of displacements, {u}, is the unknown quantity. According to the implicit formulation, the solution of Equation 1 is based on the inversion of the stiffness matrix to calculate the vector of displacement, as expressed by Equation 2.

$$\{u\}=[K]^{-1}\{F\} \quad (2)$$

One of the main properties of the stiffness matrix is its symmetry along the diagonal and its positive determinant as a necessary condition for its invertibility. As shown in the previous equation, the implicit solver requires inversion of the stiffness matrix so that the displacement can be easily calculated. One drawback of the implicit scheme is the requirement of bigger storage capacity and core memory for the inversion of the stiffness matrix when the dimension of the simulated system increases. Moreover, if nonlinearities are present, the stiffness matrix becomes a function of the displacement: in this way, it has to be updated before its inversion making the proceeding to the subsequent time increment more computationally intensive [53]. On the other hand, especially for the numerical simulation of the sheet metal forming processes (where the model is usually dominated by the presence of multiple contacts) explicit formulation is preferred [54]. In this second case, Equation 3 provides the solution of the nodal equilibrium.

$$M\ddot{u}= P-I \quad (3)$$

Where *P* is the vector of the applied loads, *I* vector that accounts for the internal stresses, *M* is the lumped mass matrix and $\ddot{u}$ is the nodal acceleration. The explicit formulation, designed to be highly performing in the solution of impact problems, reveals its potentialities also for the solution of quasi static problems (where the nodal acceleration can be considered negligible within the increment). In addition, the improved capability of managing the contact formulation and their evolution makes the explicit solver particularly attractive for the numerical simulation of sheet metal forming problems where contact dominates the solution and local instabilities may form due to wrinkling of the sheet. The explicit solver adopts the central difference time integration rule to satisfy the dynamic equilibrium equation: the nodal accelerations calculated at the increment time *t* are used to calculate in advance the velocity solution at time $t+\Delta t/2$ and the displacement solutions at the time $t+\Delta t$. If considering the *i*-th increment in an explicit analysis step, the equations of the motion (nodal velocity and displacement) are integrated using the central difference integration rule as described in Equation 4.

$$\begin{aligned} \dot{u}^N_{\left(i+\frac{1}{2}\right)} &= \dot{u}^N_{\left(i-\frac{1}{2}\right)} + \frac{\Delta t_{(i+1)}+\Delta t_{(i)}}{2}\ddot{u}^N_{(i)} \\ u^N_{(i+1)} &= u^N_{(i)} + \Delta t_{(i+1)} u^N_{\left(i+\frac{1}{2}\right)} \end{aligned} \tag{4}$$

The superscript *N* refers to a generical degree of freedom (displacement or rotation component); the central difference integration operator is explicit since the kinematic state is advanced using known value of the nodal velocity and acceleration from the previous increment. The computational efficiency of the explicit procedure is ensured by the adoption of the lumped matrix *M* necessary to calculate the acceleration at the beginning of the increment from Equation 3. In addition, the adoption of a lumped matrix provides computational advantages since the vector multiplication of the mass inverse by the inertial forces requires a number of operation equal to the number of the model degrees of freedom (the explicit procedure does not need any iteration or the calculation of the tangent stiffness matrix). One of the main properties of the explicit solution is its conditional stability: it means that an accurate solution can be obtained only if the Δt is lower than the stable time increment Δt_{min} otherwise oscillations may occur in the system response (the out-of-balance forces are propagated as stress waves between neighbouring elements). The stable time increment can be considered as the minimum time needed to a dilatational (i.e. volume expansion and contraction) wave to move across any of the element in the model: a good estimation is provided by Equation 5, where L^c is the characteristic length of the mesh element while c_d is the dilatational wave speed that is a function of the material Young's modulus (E) and density (ρ).

$$\Delta t_{min} = \frac{L^c}{c_d} = \frac{L^c}{\sqrt{\frac{E}{\rho}}} \tag{5}$$

Results of the explicit dynamics simulations are not automatically checked, even though this may not represent a source of concern because the previously mentioned stability condition imposes a time increment small enough to prevent sensible changes of the solution within the increment itself. In general, if compared with the Implicit solver, explicit simulation may take a huge number of increments (even higher than 10^5) and the simulation time can be extremely dilated [55]: the "mass scaling approach" is commonly used to speed up the simulation and it is based on an artificial variation of the material density – if increased by k^2, the total number of increments is reduced by k. An alternative way to speed up the numerical simulations is to force toward a value of the stable time increment higher than the one that initially guess by the solver at the beginning of the simulation. It should be underlined that, despite the mass scaling approach is an effective solution to reduce the computational cost and considering the conditionally stability of the explicit solver, to preserve the accurateness of the numerical results, all the artificial energies (such as strain energy, mass scaling work, damping dissipation) has to be negligible if compared to the "real" energies (as the strain energy or the internal energy). In particular, when speeding up the numerical simulation for the solution of a quasi-static problem, the kinetic energy should represent a very small fraction (between 5% and 10%) of the total internal energy of the system.

2.3 The "Heat During Forming" approach: stamping of a window panel

The increase of the working temperature during the stamping operations is the basic principle of the HDF approach, whose capability to improve the achievable geometrical complexity is strictly related to the enhanced formability of the alloy in warm conditions. An HDF based approach was used to design the warm stamping of a large-scale industrial component for railway applications (a window panel). The alloy under investigations – the AA5754 initially purchased in the annealed conditions (H111) – was initially characterized so that material data could be implemented within the numerical model with which, thanks to an uncoupled thermo-mechanical approach, the optimal heating strategy and the proper value of the forming process variable were defined. The accurateness of the approach was then validated via experimental trials carried out on the warm press machine available at the industrial plant of the O.Me.R. company.

2.3.1 The case study

As a case study, a large-scale component for railway applications was considered: Figure 15a shows the 3D representation of the window panel under investigation, currently mounted on the Movia C30 train serving the Stockholm underground metro service (Figure 15b).

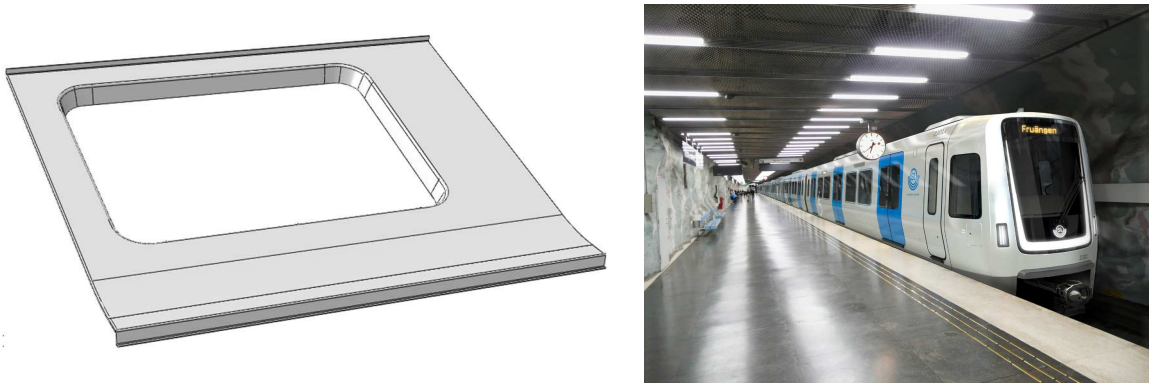

a) b)

Figure 15 Case study: a) 3D representation of the inner pane, b) the Movia C30 train

The Transportation Division of the Bombardier leader company (headquartered in Berlin, Germany) declared, at the beginning of 2017, to have won the order from the Stockholm Public Transport Authority (SL) to deliver the new generation of the C30 metro vehicles (the order was approximately valued at 590 million euro). The new Movia metro was designed on the same platform of former vehicles, already delivered by the company from New York to Singapore, and customized to meet the specific requirements of SL, being capable of travelling around 150,000 km per year and offering the capacity to transport up to 60,000 passengers per hour. The Movia C30 was designed to fulfil the strict environmental standards in terms of masses reduction, being equipped with an innovative bogie frame, the *Flexx Eco* bogie (shown in Figure 16a) able to reduce the weight up to 30% if compared to a conventional one, and the *Mitrac* propulsion system (shown in Figure 16b) [56,57].

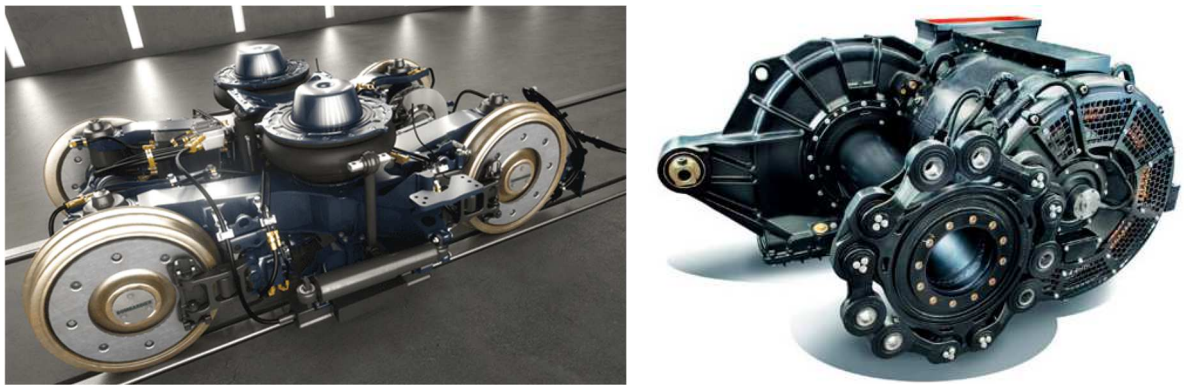

a) b)

Figure 16 Movia C30 lightweighting: a) Flexx Eco bogie and b) Mitrac propulsion system

The adoption of a light alloy, as in the case of the investigated AA5754, for the window panels (4 per each car, with a totality of 16 panels per vehicle) was considered an evident investment in the direction of the vehicle mass reduction.

2.3.2 Material Characterization in warm conditions

Uniaxial tensile tests were carried out on dog-bone specimens (initial thickness 1.5 mm) designed according to the International Standard [58,59] (the main quotes are

reported in Figure 17a) and extracted from an AA5754 blank purchased in the annealed condition (H111). After having tested the material at room temperature, the characterization of the mechanical behaviour was assessed in warm conditions using the Gleeble 3180 physical simulator shown in Figure 17b: tests were carried out at different temperatures (150, 200 and 250°C) and at three different strain rate levels (0.001, 0.01 and 0.1 s^{-1}). Each test was replicated three times. Additional tests were carried out at a strain rate level equal to 0.0001 s^{-1} to calculate the Young's modulus as prescribed by the ISO standard [59].

a) b)

Figure 17 Material characterization: a) dog-bone specimen main quotes, b) physical simulator Gleeble 3180

When dealing with sheet metal forming processes, the investigation of the alloy formability plays a key aspect in the process design. The formability can be defined as the attitude of the material to be deformed without the occurrence of blank tearing/ruptures. Material formability is graphically described by the *Forming Limit Diagram* (FLD) [60], developed for the first time by Keeler and Backofen [61,62] and completed by Goodwin later on [63], showing the limit principal strains in the blank plane the material can withstand before the onset of the localized necking in the thickness direction. The two principal strains – namely the *major strain* as the strain in the direction of the maximum strain and the *minor strain* defined as the strain perpendicular to the major strain – if fitted by an analytical relation, compose the *Forming Limit Curve* (FLC), considered to be the boundary between the safe and the failure region [64]. The major strain is always positive and plotted on the FLD vertical axis, while the minor strain is reported on the horizontal axis (it can be positive or negative).

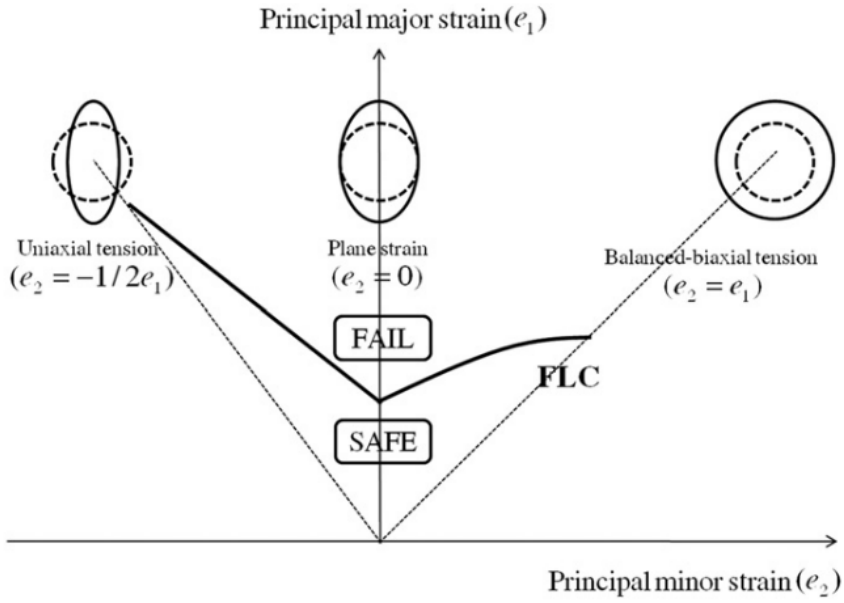

Figure 18 Graphical representation of the Forming Limit Curve (FLC) [65]

As it can be seen from Figure 18, the FLC represents the locus of the limit strains the material can undergo along different strain paths from the pure drawing (when the minor strain is negative and its absolute value is approximately equal to half of the major strain) to the stretching conditions (major and minor strains are both positive and equal) passing through the plane strain condition (the minor strain is zero or negligible), which is indicated as the deformation states the material reaches before the occurrence of rupture [66]. FLCs can be experimentally obtained according to two main alternative approaches that were independently developed, i.e. the Nakazima test [67] and the Marciniak test [68]. Both tests use several specimen geometries to investigate different strain paths, but the main difference is in the punch geometry: Nakazima test adopts a spherical punch (Figure 19a) while the Marciniak a flat one (Figure 19b).

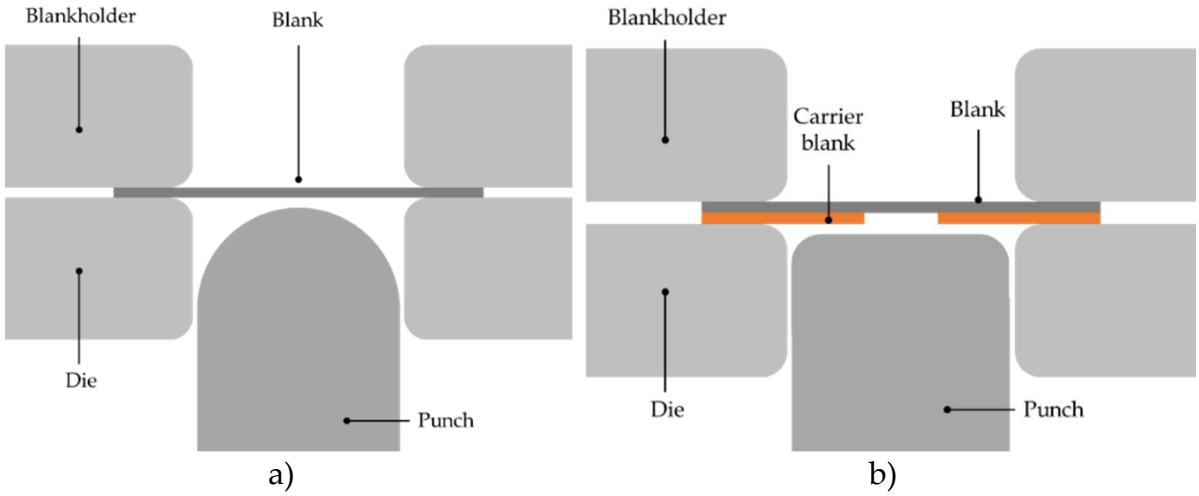

Figure 19 Formability test: a) Nakazima scheme (hemispherical punch), b) Marciniak scheme (flat punch)

In the case of the Marciniak formability test, one of the key differences lies in the adoption of carrier blank (positioned between the blank and the flat punch, highlighted in orange in the picture) with a central hole, necessary to ensure that the maximum plastic strain is achieved in the flat area of the specimen. Despite such a test can ensure linear paths, regardless of the specimen geometry, the adoption of an additional blank makes the whole process too material consuming. For this reason, the Nakazima test has been indicated as the reference test over the last decades: it should be also underlined that, despite its lower complexity, the evaluation of the limit strains can be affected (over- or underestimated) by the non-linear strain paths (NLSP) and the not negligible influence of the sheet curvature [69]. On the other hand, thanks to the adoption of more sophisticated measurement procedure (as in the case of the Digital Image Correlation systems [70]), new methods to compensate such a process-dependent effect in the evaluation of the necking limits have been proposed in literature [71]. Moreover, the experimental determination of the FLCs, regardless of the adopted scheme, can become too time consuming, especially in the case the formability at different temperature has to be assessed: for this reason, over the last years, both analytical and numerical methodologies have been developed to predict the FLC reaching a good correspondence with the experimental validation [68,72]. As it may seem reasonable, the accurateness of the FLCs is not only dependent on the identification of the exact moment when necking occurs, but also on the calculation of the limit strains. The first attempt to obtain a reasonably accurate determination of the limit strains was based on measuring the displacement between markers on the specimen surface before and after the deformation. The adoption of a grid (based on an ordered sequence of squares/circles as shown in Figure 20a) represented the first attempt to obtain a visual displace of both the magnitude and the direction of the final strain state [73], even though the measurements on the deformed grid were carried out manually and thus affected by the operator error; the introduction of an image processing device noticeably increased the accurateness of the measured strains [74].

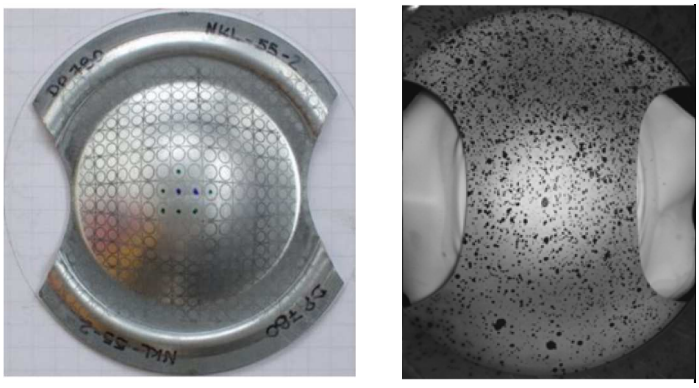

a) b)

Figure 20 Example of specimen marking: a) circle grid [75]**, b) speckle stochastic pattern** [76]

During the last decades, the grid-based strain measurement system has been progressively replaced by a more precise non-contact speckle based technique [77,78]. Thanks to a proper painting of the surface overlooking the stereo cameras – Figure

20b shows the appearance of a Nakazima specimen – the speckle based measurement technique, universally indicated as the Digital Image Correlation (DIC) technique, subdivides the reference image in multiple subsets matching each with the correspondent subset in the deformed image showing the highest similarity [79,80].
As regarding the characterization activities here described, the formability of the investigated AA5754, initially purchased in the annealed state (H111), was assessed by means of Nakazima tests carried out both at room temperature and in warm conditions. The adopted equipment, shown in Figure 21a, was specifically designed in order to (i) be easily interfaced with the Instron 4485 universal testing machine and (ii) be equipped with the two 2 Megapixels cameras belonging to the DIC system ARAMIS assisting the test. As previously mentioned, the specimens were previously painted to obtain a stochastic pattern of randomly distributed black dots on a white background (an example is shown in Figure 21b).

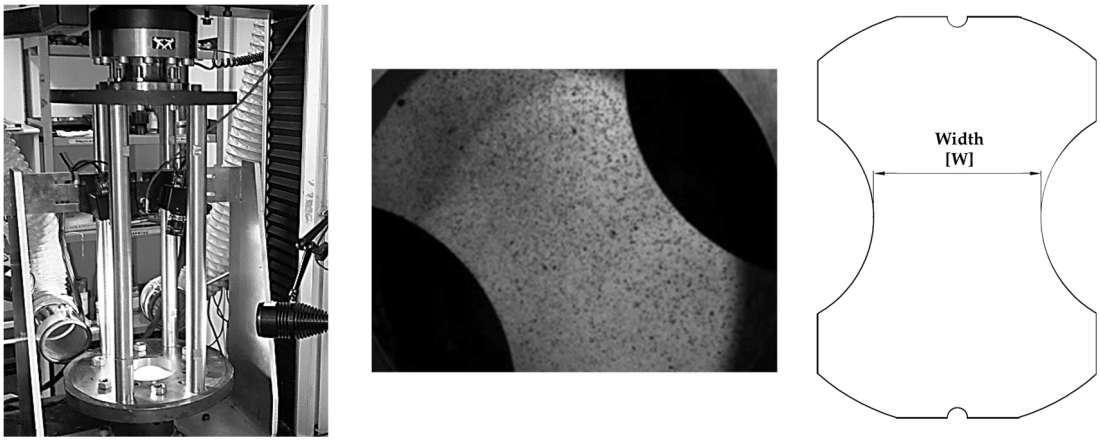

a) b) c)

Figure 21 Formability tests: a) the adopted equipment; b) stochastic pattern for the DIC analyses; c) drawing of the Nakazima specimen

Different specimen geometries were used, each characterized by a different value of the width (indicated with the letter W followed by the dimension in mm as shown in Figure 21c) to account for different strain paths from the drawing to the stretching.

2.3.3 FE simulation of the warm forming: the uncoupled approach

From a numerical point of view, the forming process in warm conditions implies the simultaneous solution of the thermal and the mechanical problem [25,36] which may result too time consuming and sometimes hindered by convergence issues of the implicit solver due to the presence of several contacts. An alternative approach, based on uncoupling the thermal solution from the mechanical problem, was proposed for the process under investigation: purely transient thermal simulation were initially run to evaluate the best heating strategy to obtain an optimal distribution of temperature over the blank that was subsequently transferred as an initial predefined field on the stamping simulation (Abaqus/Explicit) under the assumption that the imported distribution did not significantly changed during the forming step. As an initial

assumption, the window opening was initially modelled as located at the centre of the panel, so that only one quarter of the system could be modelled (thus remarkably reducing the computational time in both the uncoupled runs) as shown in see Figure 22a. All the component of the warm forming press machine (Figure 26a, section 2.3.6) were reproduced within the Abaqus CAE environment, modelled as 3D solid bodies and meshed with tetra and hexahedral elements (around 850000 elements with an average dimension of 10 mm).

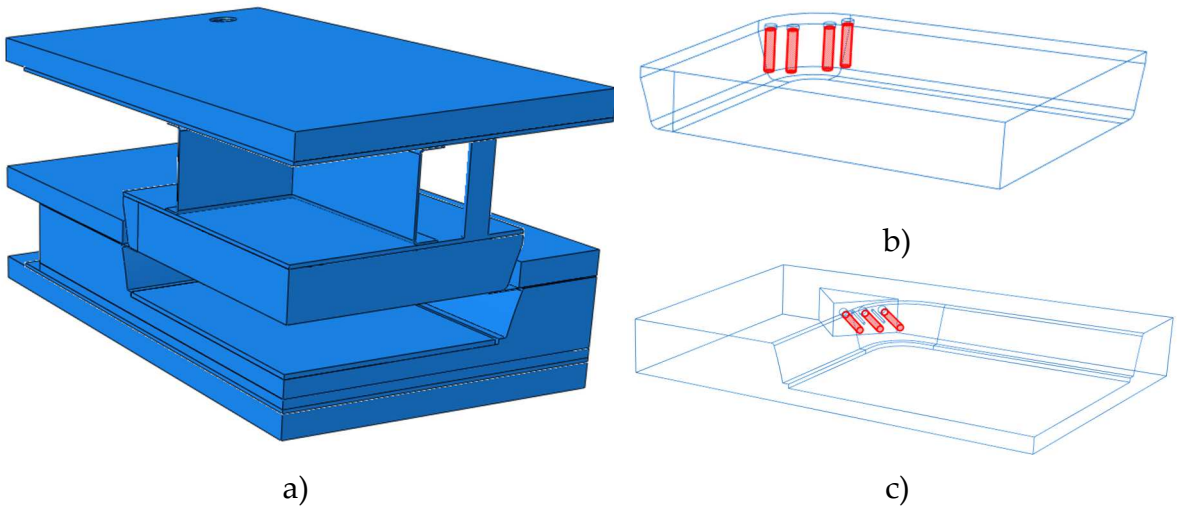

Figure 22 FE thermal model: a) assembly, b) cartridge housing on punch side and c) on die side

As shown by the wireframe detailed views of the punch (Figure 22b) and the die (Figure 22c), housings for the rod type heaters were located at the corner of the tools reproducing the positioning on the real press machine: two different types of cartridges were then selected (technical data are listed in Table 4).

Table 4 Technical specification of the rod type heating cartridges

Tool	Diameter [mm]	Length [mm]	Total Power [W]	Power Density [W/mm²]
Punch	19	76	750	0.24
Die	19	152	1500	0.22

In addition to the provided details, as specified by the supplier [81], if considering a radial clearance of 0.05 mm between the heater and its housing, the maximum working temperature of both types had to be lower than 650°C. As previously anticipated, the tools temperature is regulated by 4 thermocouples on the punch side and other 4 on the die side so that each angular zone of both tools can be monitored (and consequently regulated) independently from the other ones. In the FE model, thermal loads were specified in terms of power density while the amplitude was managed by a UAMP user subroutine necessary to numerically reproduce the thermocouple feedback control. In particular, the working temperature on the punch side was set at 300°C, while 120°C was specified on the die side being that value below the maximum working temperature of the gas springs. The thermal problem was

subdivided into two steps: during the first one (time period equal to 3600 s), only the tools were heated (no contact with the blank) to evaluate how the time needed to reach the tools target temperature was influenced by the specific heating strategy (number of active heating elements both on punch and die side). During the second step (time period equal to 600 s), the contact with the blank was activated and the final temperature distribution on the blank was analysed. As previously mentioned, two alternative blank initial geometries were proposed: the NG#1 geometry, indicated by the black profile in Figure 23a and compared with the one used for the preliminary simulation at room temperature (orange profile in Figure 23a), was characterized by a circular opening in the corner region to reduce the severity of the strain condition during the stamping. Moreover, the central stripe was conceived to improve the contact between the punch and the blank thus facilitating its drawing during the stamping. Alternatively, the NG#2 geometry (indicated by the blue profile in Figure 23b) aimed at evaluating the influence of the central stripe on the outcome of the stamping.

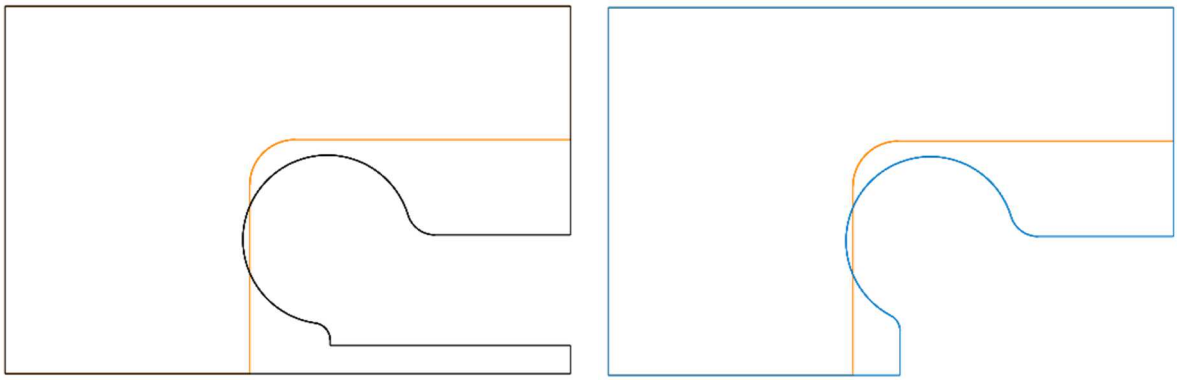

Figure 23 Blank initial geometry for the warm stamping simulation (the initial blank geometry is in orange): a) NG#1 and b) NG#2

Several combinations of active heating elements (on both punch and die side) were numerically simulated, each univocally identified by a code reporting the number of active heaters on the die side followed by the letter "D" and the number of active heaters on the punch side followed by the letter "P" (e.g. the 2D2P scheme refers to the thermal simulation when 2 active cartridges were modelled both on the die and the punch side). The aim of the thermal simulation was to determine the heating strategy, in terms of number of active heating elements on the both tools, to obtain an optimal temperature distribution on the blank. In such a way, the optimal temperature distribution could be then transferred on the simulation of the forming step as an initial predefined field: also in this case, the geometrical symmetry was exploited and one quarter of the system was modelled as shown in Figure 24a. Numerical simulation were run adopting the Explicit solver in combination with the mass scaling approach – setting the stable time increment to 10^{-4} –to speed up the numerical simulation.

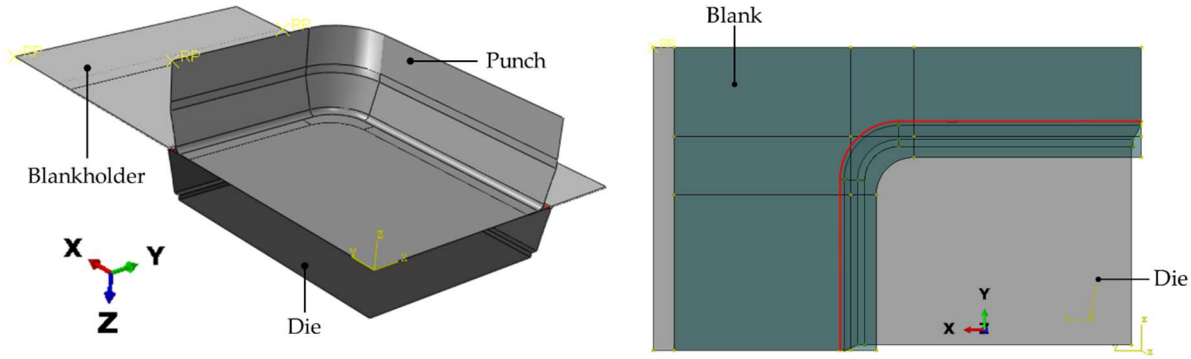

Figure 24 Numerical approach: a) modelled parts, b) initial blank geometry

The tools – i.e. the die, the blankholder and the punch – were modelled as discrete 3D rigid bodies while the blank as a 3D deformable shell (thickness equal to 2 mm): the initial blank geometry (see Figure 24b) was at first designed offsetting the edge of the die entry radius (highlighted in red in Figure 24b) by a quantity equal to the drawing depth of the final component (76 mm). Figure 25a provides a detailed view of the meshed surfaces: all the rigid bodies were meshed with a R3D3 and R3D4 (respectively 3 and 4 nodes rigid element available in the Abaqus element library with an average size of 30 mm), while the blank with S4R and S3R shell elements (approximately 26000 elements with an average dimension of 4 mm).

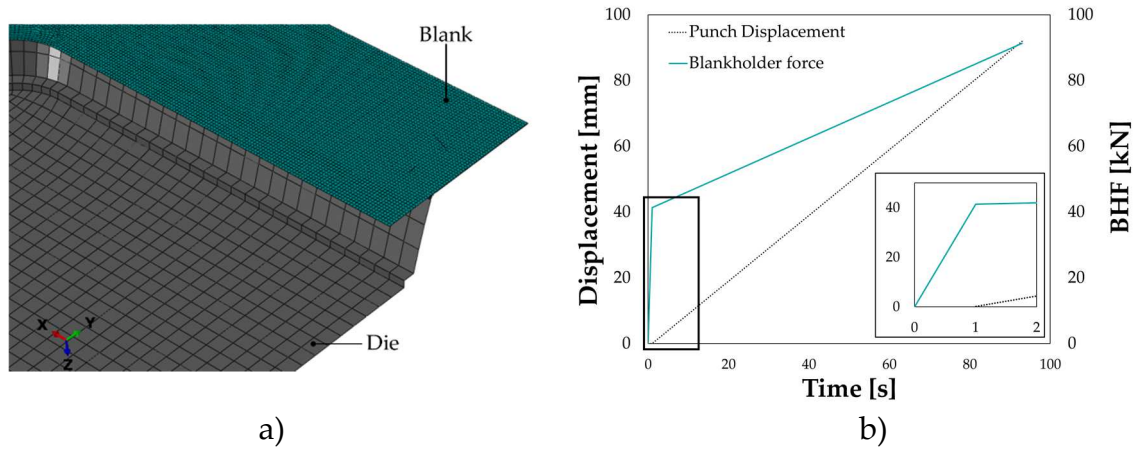

Figure 25 FE model: a) detail of the meshed parts; b) punch stroke and BHF profiles

The pair contact blank/tools was modelled with the surface-to-surface discretization method, adopting as enforcement method the hard contact on the normal direction whereas the penalty formulation in the tangential direction setting a value of the coefficient of friction equal to 0.1. Material behaviour once the yield occurred was modelled according to the Von Mises isotropic formulation. The press machine blankholder (a detailed description of the facility is provided in section 2.3.6) exerts its action on the blank thanks to the presence of 18 gas springs, each applying a load linearly increasing from an initial value of 9.2 kN to the maximum value of 20.3 kN (at the maximum spring displacement): due to the symmetry of the system, one quarter of the entire load was applied in the FE model on the blankholder reference

point and modelled according to the profile in Figure 25b (green straight line labelled as BHF, linearly increasing from 41.4 kN up to 91.4 kN). As it can be denoted in Figure 25b, the punch started its stroke only when the BHF reached its initial value. The total time period was set equal to 91 seconds (the first one for the BHF to reach its initial value and the other 90 to complete the forming operation). As previously mentioned, the implementation of the FLCs in the numerical model activated a damage criterion able to predict the occurrence of rupture simply monitoring the FLDCRT output variable, directly available in the Abaqus post processing environment [54].

2.3.4 Equipment for the validation of numerical results

The experimental stamping trials, as well as the final validation, were carried out on the 60 tons warm press machine shown Figure 26a.

a) b)

Figure 26 Experimental stamping trials: a) press machine, b) control panel of the heating system

The heating system is controlled by the PLC located on the side of the press machine: the working temperature on both tools, the heating time (once the blank is loaded between the tools) before the stamping and the total forming time can be set by the operator accessing the screen control panel (Figure 26b). The heating system of the press machine is composed of heating rod cartridges positioned on the corners, as it can see on the punch side in Figure 27a and on the die side in Figure 27b; in the proximity of the cartridges, rod thermocouples were positioned to regulate the tools temperature (the current acquisition of each thermocouple is also reported on the PLC control screen). Moreover, the detailed view of the punch in Figure 27a shows the gas spring adopted to apply the necessary load to the blankholder [82] during the forming operations.

a) b)

Figure 27 Heating strategy: cartridge positioning on a) the punch side and b) the die side

As a general approach, all the experimental stamping trials started with the tools heating according to the optimized strategy defined by the thermal transient FE simulations (and described in the section 2.3.3); once reached the target temperature both on die and punch side, the blank was positioned and clamped between the die and the blankholder (step 1 in Figure 28). After that, the dies moved upward to get in contact with the punch (step 2 in Figure 28) : as soon as the blank was in contact with the punch, the blank heating step started and at the end of the heating the die started moving to complete the forming operation (step 3 in Figure 28).

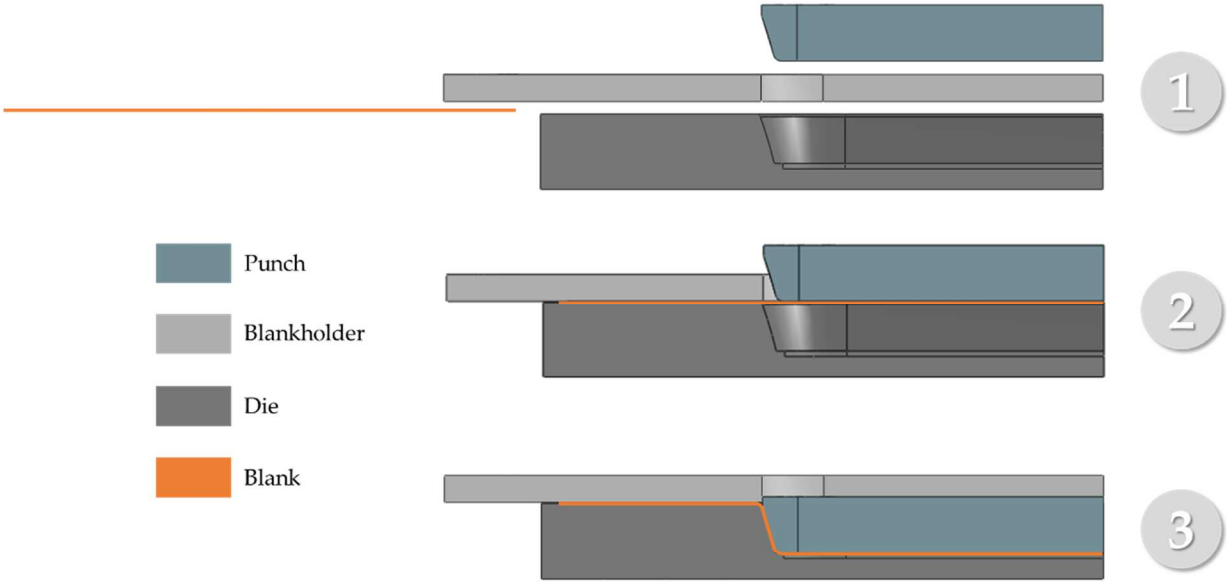

Figure 28 Schematic description of the warm forming process

2.3.5 Evaluation of the blank distortion after forming

As a further development of the designed process in warm conditions, the effect of the initial material conditions on the feasibility of the process and on the post-forming properties in terms of blank distortion was investigated. In the specific case of the

window panel here described, the forming in warm conditions was again designed but considering the blank with an initial pre-strain condition (AA5754-H32): the choice to adopt a blank with an initial cold working came from the consideration that, according to literature [83,84], the material yield point has a strong relation with the dent resistance, whose enhancement can lead to a prolonged exercise life of the component (especially being in continuous contact with millions of passengers and may be damaged by uncontrolled movements or hit and scratched by luggage). After having characterized the material in warm conditions as described in section 2.3.2, the forming process was designed by FE simulations (section 2.3.3) and validated with the facility shown in section 2.3.4. The effect of the material initial conditions on the post-forming properties was evaluated in terms of blank distortions by means of 3D scans adopting the HandyScan 3D provided by Creaform [85]. Before the 3D scanning, circular markers were uniformly applied on the surfaces to be acquired as shown in Figure 29 (a and b).

a)

b)

Figure 29 Evaluation of the post-forming properties of the formed panels by 3D laser scanning: initial blank in a) AA5754-H32, b)AA5754-H111

2.4 "Heat Before Forming" approach: the deep drawing process

The local modification of the material properties prior to the stamping operation has been widely indicated as a promising solution to enhance the poor formability of the Al alloys at room temperature. As already indicated in the chapter 1, the HDF approach disregards from the specific category of alloy, being applicable to both the age hardenable and the strain hardenable Al alloys. In addition, being the manufacturing process split into two sub-steps, the advantages coming from an FE-based process design can be even more remarkable. As regarding the activities here described, the HDF approach was applied on the conventional deep drawing process. The mechanical and strain behaviour of the alloy under investigation, the age hardenable AA6082 in the initial peak hardening (T6) condition, was preliminarily characterized; after that, the local treatment by laser heating was designed by means of FE simulations and then optimized – in terms of extent of the region to be treated – by means of an automatic procedure managed by a multi objective genetic algorithm (MOGA-II).

2.4.1 Material characterization

The age hardenable Al alloy AA6082 was initially investigated focussing the attention on two antithetical condition: (i) the purchasing one (T6) characterized by high mechanical resistance and limited formability and (ii) the fully solutioned condition characterized by a more pronounced formability. The heating cycle to get the latter condition at room temperature, i.e. the Solution Heat Treatment (from now on indicated with the acronym SHT) necessary to fully dissolve the existing precipitates at the grain boundaries, was precisely tuned by means of the physical simulation. Plenty of data available in literature report several combinations of the heating temperature and the holding time to effectively solution the initial T6 condition of a AA6082 alloy [86–93]: regardless of the specific values of the two parameters, the heating cycle is mainly based on a preliminary heating phase (adopting a heating rate in the range of tens of °C/s) up to the heating temperature, a soaking time (whose duration is proportional to the heating temperature) necessary to completely bring the material in the monophasic alpha region [94], and a quick temperature drop (drastic cooling) to freeze the Super Satured Solid Solution (SSSS) at room temperature. Such a material condition is energetically unstable (Si is characterized by a very limited solubility in the Al matrix at room temperature [94]) and tends toward a more stable energetic one promoting the precipitation of secondary phases, i.e. triggering the natural ageing phenomenon [93]. In order limit the number of experimental tests, the SHT was tuned using the Gleeble 3180 physical simulator: striped AA6082 specimens (120mm x 30mm, initial thickness 1.5 mm) in the T6 condition were heated by Joule effect due to the passage of a current flow modulated according to the temperature acquisition of the pilot thermocouple welded in the middle of the specimen (TC2 in Figure 30a); additional thermocouples were welded 15 mm (TC1) and 30 mm (TC3 and TC4) far from TC2 (on opposite sides) for temperature monitoring purposes.

Being the ends of the specimen clamped between cooled jaws, a parabolic distribution of temperature was obtained (clearly visible in Figure 30b) and maintained for the whole duration of the heating test).

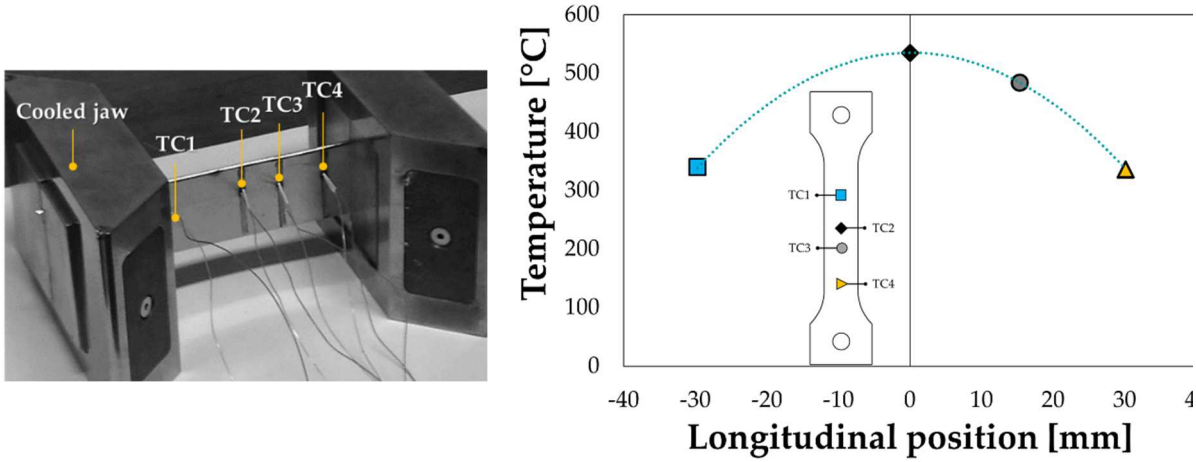

a) b)

Figure 30 SHT tests: a) thermocouple positioning; b) resulting parabolic temperature distribution

Once properly tuned the SHT condition via the physical simulation, uniaxial tensile tests were carried out on the Instron 4485 universal testing machine, available in the *Physical Simulation of Manufacturing processes* (Department of Mechanics, Mathematics and Management – Politecnico di Bari), assisted by the Digital Image Correlation (DIC) system ARAMIS (provided by GOM) to continuously acquire the strain distribution during the test: the experimental setup is reported in Figure 31a.

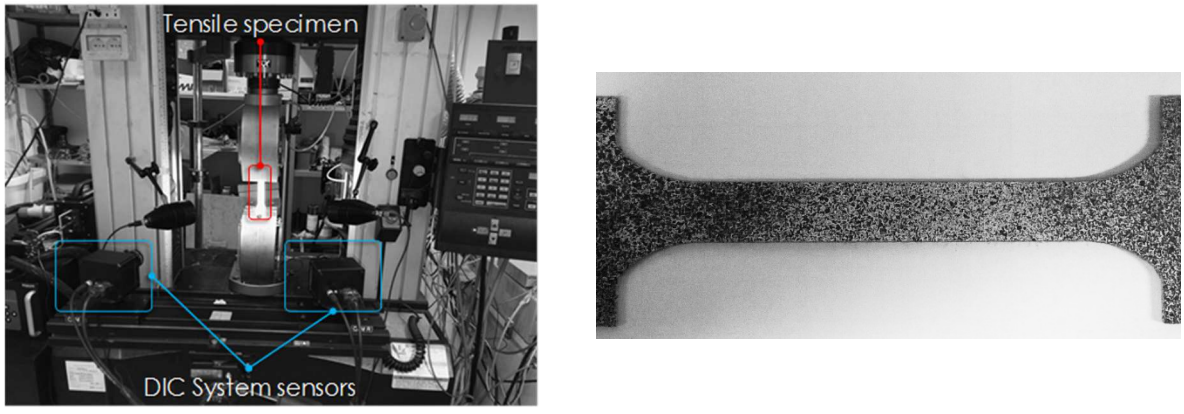

a) b)

Figure 31 Tensile test: a) experimental equipment, b) detail of the speckled specimen gauge length

Before the tensile test, AA6082 specimens were sprayed with a first white matte layer to avoid reflections and then superimposing a random distribution of black dots, so that the resulting pattern (speckle) could thus be recognized by the two cameras as a virtual grid (Figure 31b). Strain behaviour, carried out at room temperature on the same material condition (T6 and SHT) of the uniaxial tensile tests, was assessed by means of Nakazima formability tests adopting the same equipment shown in Figure 21a.

The characterization step was then completed by investigating the material properties at room temperature after being locally treated. Dog-bone specimens (the main quotes have been previously shown in Figure 17a) were locally heated via a Laser Heat Treatment (LHT) and, once cooled down at room temperature, subjected to the uniaxial tensile test adopting the same experimental equipment shown in Figure 31a. The specimen was laser heated using the 2.5 kW CO_2 Rofin DC025 source available in the *Advanced Forming & Manufacturing* laboratory (Department of Mechanics, Mathematics and Management – Politecnico di Bari): the laser beam, once conveyed through the scan optics, was focussed by a Diffractive Optical Element (DOE visible in Figure 32a immediately above the copper plate) lenses carrier to obtain a top-hat energy distribution over a square spot (three different dimensions could be obtained). In the case of the activities here described, a 20 mm square spot was adopted to laser heat the central portion of the tensile specimen as shown in Figure 32b: the focus distance was kept constant as specified by the technical data (it is a function of the set spot dimension) while the specimen was positioned on an annular cooler so that an excessive heat conduction to the ends could be prevented. As it can be seen from the experimental setup, due to the elevated reflectivity of the Al alloy, the specimen portion to be treated was sprayed with a black paint for high temperature to increase the quantity of the absorbed radiation. A wire thermocouple was welded in the middle of the specimen surface not irradiated by the laser beam to monitor the temperature during the LHT.

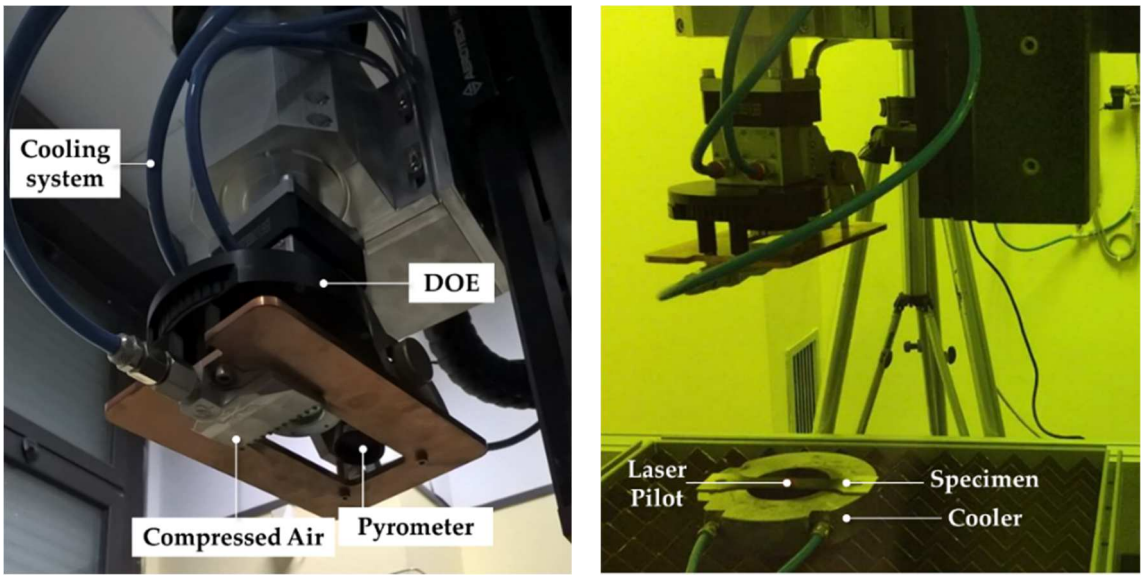

a) b)

Figure 32 LHT tests on AA6082-T6 tensile specimens: a) detailed view of the laser heating head, b) experimental setup

According to what reported in literature, an interaction time in the order of seconds can results effective in dissolving the existing precipitates in an age-hardenable Al alloys [95], thus bringing the material to a more formable condition (as in the case of the SHT): a 5 seconds LHT setting the laser power equal to 750 W was carried out and the temperature monitored via the acquisition of the welded wire thermocouple.

Once cooled down at room temperature, the dog-bone specimens were immediately subjected to the uniaxial tensile tests so that no ageing phenomena could be triggered by a prolonged exposure at room temperature. The adoption of the DIC system gave the big advantage of monitoring the strain evolution at any point of interest: in such a way, coupling the local strain information with the load data from the Instron machine, it became possible to extract several local flow curves from different locations within the same uniaxial tensile test.

2.4.2 Process design by FE numerical simulation

As previously introduced, the HDF approach splits the manufacturing process into two sub-steps: the process design by FE simulation was then carried out both on the preliminary local heating and on the subsequent deep drawing process (in particular, in this latter case, an automatic procedure managed by a genetic algorithm was also created). The experimental setup shown in Figure 32b was then numerically reproduced to preliminary tune the thermal model: the dog-bone specimen was modelled as a 3D deformable body and meshed with 1 mm linear hexahedral elements (type DC3D8), while the thermal properties of the alloy were taken from literature [96]. The heat exchange between the specimen and the surrounding environment as well as between the specimen and the cooler was assumed as convective, setting two different values of the heat transfer coefficient. The tuning of the model was necessary to evaluate the effective heat transfer coefficient as well as the exact portion of the irradiated energy that was absorbed by the material during the treatment.
The optimized thermal boundary conditions coming from the preliminary tuning of the laser heating simulation were then used to numerically predict the temperature distribution during the laser heating of the circular specimens to be subsequently drawn at room temperature: in particular, the value of the feed rate (FR), i.e. the displacement velocity of the laser treatment head, was optimized to effectively solution the flange portion of the blank according to the results of the material characterization at room temperature after the laser heat treatment. In such a way, the lower yield point of the flange portion was expected to improve the material drawing and facilitate the die cavity filling thus improving the achievable LDR, whose final value had to be compared with those belonging to the material in the preliminarily investigated conditions (i.e. T6 and SHT).
The subsequent step regarded the numerical simulation of the deep drawing process when adopting the LHT blanks. In order to create a light enough FE model, the laboratory scale equipment (Figure 36a and discussed in the section 2.4.5) was reproduced according to a 2D axisymmetric approach, as shown in Figure 33a: all the tools (blankholder, die and punch) were modelled as analytical rigid bodies (no meshing was needed) while the blank was modelled as a deformable shell body and meshed with 0.5 mm SAX1 element (2 nodes linear axisymmetric shell element available in the Abaqus library). The blank was modelled as already subjected to the LHT process: thanks to the adoption of a field variable, material properties in the SHT

conditions were applied in the blank peripheral region while the central region was modelled in the T6 state. A linear transition region, whose extent was set equal to 10 mm according to results of the material characterization, was modelled in between implementing the local flow curves coming from the uniaxial tensile test of the LHTed specimen. The experimental FLCs in the T6 and SHT conditions were implemented within the FE model to activate a damage criterion; for the sake of clarity, the modelling of the material distribution coming from the LHT process adopting a field variable is depicted with a 3D representation (one quarter of the whole blank) in Figure 33b.

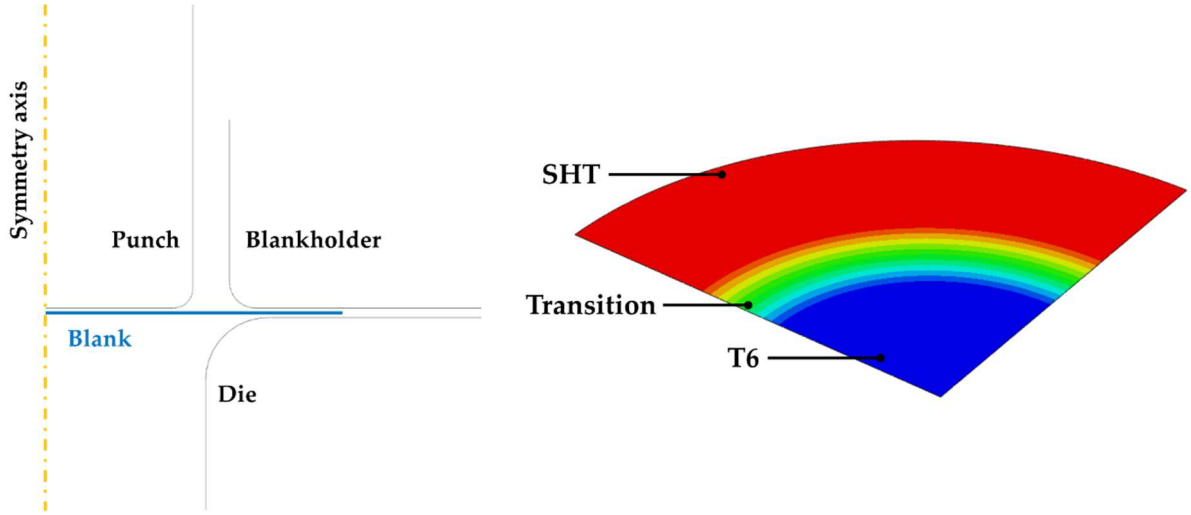

Figure 33 FE model of the deep drawing process: a) 2D axisymmetric approach, b) distribution of material properties over the LHT blank

Material plastic behaviour was modelled according the isotropic Von Mises yield formulation. The contact between the blank and the punch was modelled according to a penalty formulation, setting the coefficient of friction between the blank and the punch equal to 0.2 [43,97,98], while for the other contact pairs (blank/die and blank/blankholder) the coefficient of friction was calculated via an inverse analysis approach, minimizing the error between the experimental punch load-stroke curve coming from an experimental deep drawing test (blank diameter equal to 92 mm, material in T6 condition with a pressure applied by the blankholder equal to 1.5% of the material yield stress) and the correspondent numerical simulations.

2.4.3 Process optimization

Once defined the most influencing process parameters, numerical simulations were aimed at evaluating the extent of the blank portion to be solutioned in order to maximize the LDR at room temperature: such a problem was formulated in the same way as an optimization problem based on the satisfaction of a proper objective function [99,100]. In particular, the described 2D axisymmetric model, being the computational cost of a single run in the order of minutes, was considered particularly

suitable to be coupled with the integration platform modeFRONTIER within an automatic procedure capable of solving the optimization problem managing a large quantity of numerical runs. To create such a procedure, it was necessary to: (i) define the inputs that univocally determine a design and their ranges of variation and (ii) define the goals (objective function) – i.e. define the output variable – of the process that determine the effectiveness of the design. In the case of the deep drawing process optimization, among the available evolutionary algorithm, the multi-objective genetic algorithm MOGA-II was selected for the optimization search, since relying on a smart multi-search elitism able to preserve few excellent solutions without causing premature convergence to local optima [101,102]: the working principle of the MOGA-II is outlined in Figure 34.

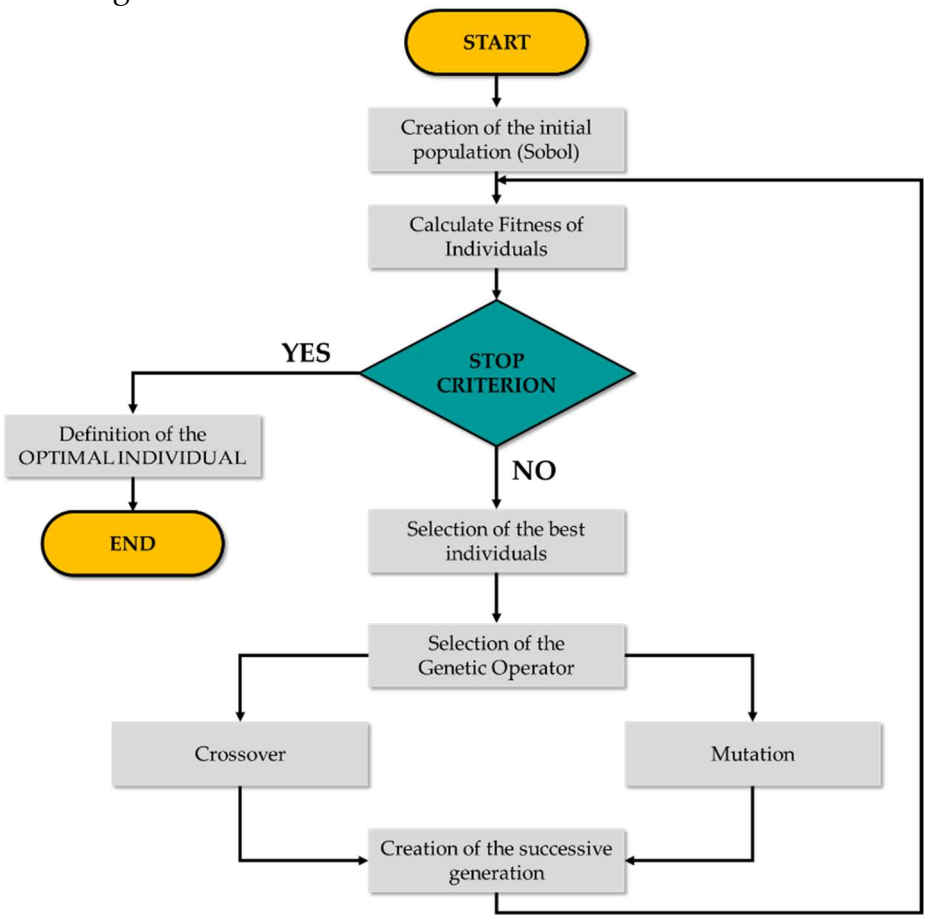

Figure 34 Flowchart of the genetic algorithm adopted to manage the optimization procedure

2.4.4 Laser Heat Treatment

To improve the material drawability, the flange region – i.e. the blank portion that will sustain the highest level of plastic strain – had to be characterized by a low yielding point and a high formability: to properly design the LHT of the circular specimen, the thermal FE model was initially validated on an experimental trial test. A layer of black painting for high temperature was sprayed on the flange portion of an AA6082-T6 sample (diameter equal to 102 mm) as shown in Figure 35a. The circular blank was

then placed between a cylindrical cooler (necessary to avoid the heating of the central region) and a cylindrical holder to keep it in position during the heating (see Figure 35b). The temperature was monitored by means of two wire thermocouples (acquisition frequency set to 5 Hz), welded on the surface not irradiated by the beam and located at the centre of the specimen and at a radial position equal to 46 mm (labelled as TC1 and TC2 in Figure 35a, respectively). The LHT was performed setting a constant laser power of 750 W, feed rate (FR) equal to 10 mm/s with the laser spot centre initially located at a radial position of 46 mm (as depicted in Figure 35a, only a portion of the spot irradiated the flange region). Laser tests were also assisted by the FLIR x6540sc thermal image camera.

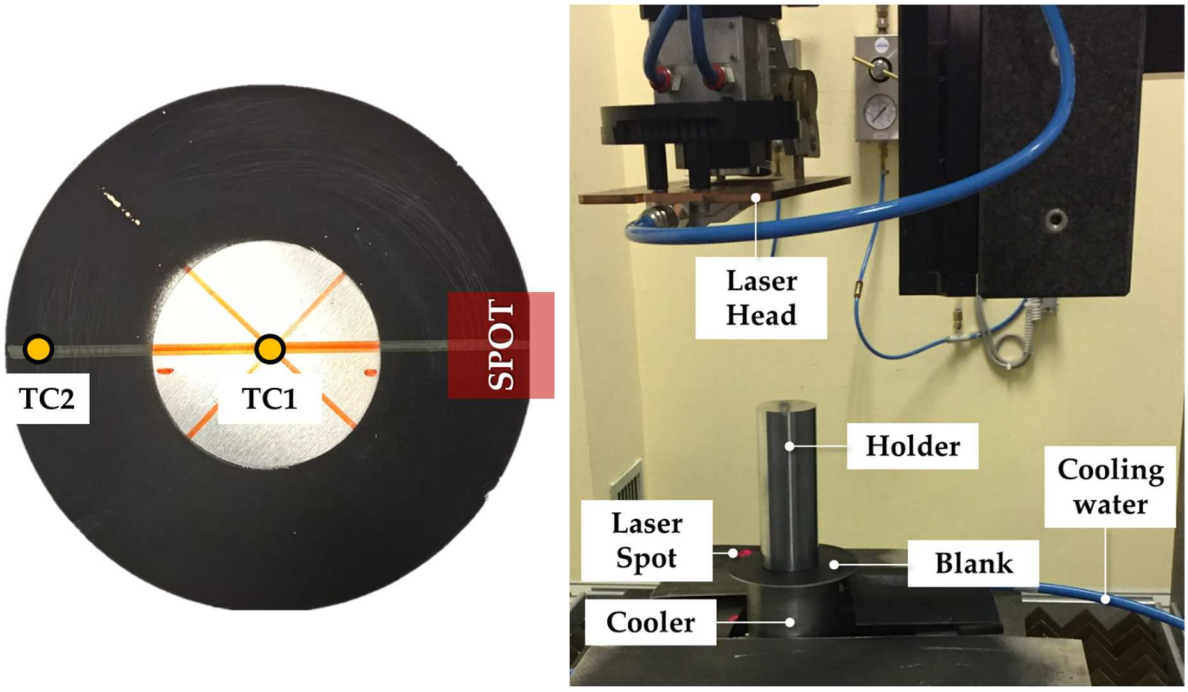

a) b)

Figure 35 Local laser treatment: a) blank preparation, b) experimental setup

2.4.5 Experimental deep drawing tests

As previously anticipated, it was expected that, thanks to a proper distribution of the material properties after the LHT, a higher LDR could be achieved. The increase in the material formability had to be comparted with the reference values of the AA6082 in both the investigated conditions (T6 and SHT). Experimental deep drawing tests were carried out adopting a specifically designed laboratory scale equipment, directly mounted on the Instron machine used for the material characterization (Figure 36a).

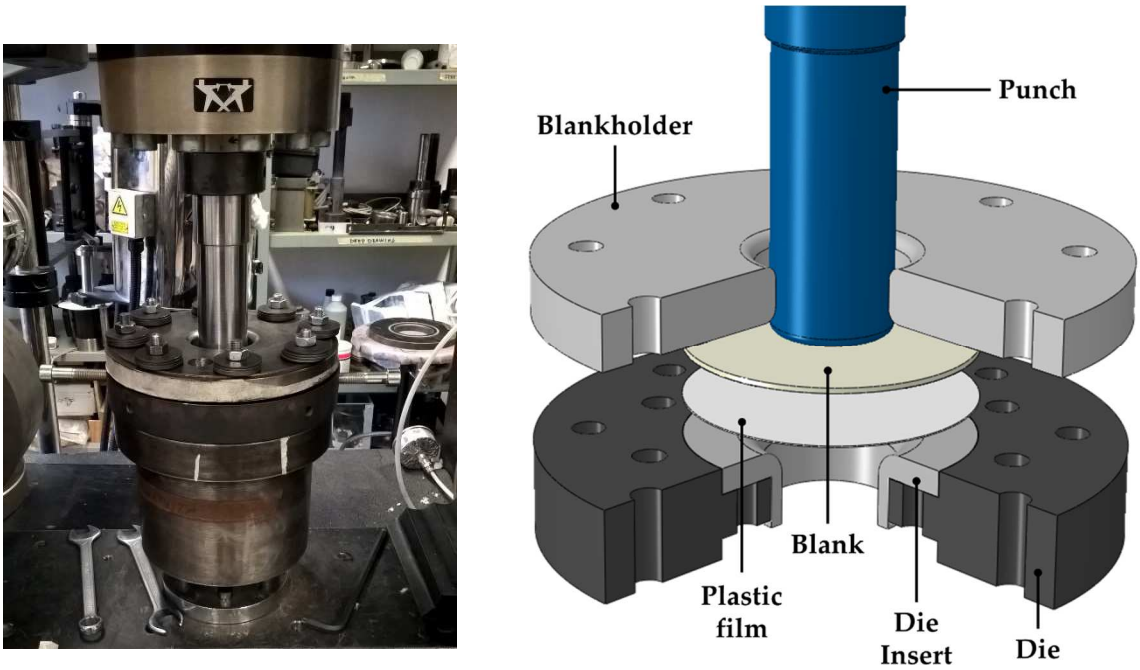

a) b)

Figure 36 Deep drawing equipment: a) experimental setup, b) 3D representation of the components

The main components of the equipment are more clearly reported in the 3D representation of Figure 36b: during the deep drawing tests, the punch (diameter of 46 mm with a fillet radius of 3 mm) forced the blank to be deformed inside the cavity of the die, composed of a bigger disc and a modular insert (diameter equal to 50 mm, entry radius equal to 8 mm) while the blank holder applied a pressure (BHp, Blank Holder pressure) equal to a certain percentage of the material yield stress (usually between 1% and 2%). All the tests were carried out setting a punch speed equal to 6 mm/min and interposing a plastic film (polyethylene, 20 μm thin) between the blank and the insert upper surface to improve the material drawing (reduction of the friction coefficient); in addition, the blank portion in contact with the blankholder was sprayed with a Teflon-based lubricant to reduce the friction at the interface.

2.5 "Heat Before Forming" approach: stamping of a window panel

The HDF approach was then applied on a more challenging component belonging to the category of the window panels as the one discussed in the chapter 2. As pointed out several times in the previous sections, the numerical approach for the process design was once again an unavoidable step preceded by a prior knowledge of the material. Process optimization was adopted also in this case, relying on a different methodology based on the creation of accurate metamodels.

2.5.1 The case study

As previously anticipated, one of the tasks of the project was the identification of several case studies covering a wide portion of the whole industrial production. Among the defined case studies, the most challenging one belongs to the group of the window panels (as the one discussed in the chapter 2): the panel under investigation – a 3D representation of the component is reported in Figure 37a – has a plan size of 1000 mm x 1500 mm with a 76 mm deep non-centred opening (plan size 500 mm x 980 mm) and currently equips the Movia C30 metropolitan train (the red arrows in Figure 37b indicate its position inside the car wagon).

a) b)

Figure 37 Industrial case study: a) 3D representation of the window panel, b) position of the panel within the Movia C30 car wagon

The application of the HBF technology to such a complex component was believed to be an enough challenging test to evaluate the effectiveness of the investigated approach. It has to be underlined that, despite most of the literature available about the local modification of the material properties is focussed on its application to the age-hardenable Al alloys [42,46,50,103], the principle of the HBF approach can be equally applied also to a strain hardenable Al alloys: in this specific case, the starting point was represented by a blank characterized by an initial pre-strain condition and the local heating is intended to anneal the high density of dislocations and increase the formability of the treated region. The only big difference between the two Al alloys categories is that in the case of the strain hardenable Al alloys, the initial cold working cannot be restored with a subsequent heat treatment (as it can be done to restore the T6 condition starting from an SHT state). On the other hand, it was believed that investigating the HBF on a strain hardenable Al alloys could be a more suitable solution for the preliminary investigations due to its stability after the heat treatment. (differently from the AA6082, prone to triggering ageing phenomena if kept at room temperature).

2.5.2 The Prototype Manufacturing Unit

The process design, and in particular, the definition of the most suitable heating strategy to properly modifying the material properties leading to the successful manufacturing of the case study in Figure 37a, was carried out according to the facility available in the productive plant of the O.Me.R. company, i.e. the Prototype Manufacturing Unit. As previously mentioned in the introduction of the present dissertation, the core topic of a joint research project was the final implementation of the HBF process within the company manufacturing procedures: in the framework of this project, one of the most challenging task (currently accomplished) was the design and construction of a Prototype Manufacturing Unit (PMU), based on the combination of all the equipment necessary to carry out the HBF approach. The PMU, as shown in Figure 38, is based on the synergic combination of a Heat Treatment sub-unit and a Stamping sub-unit.

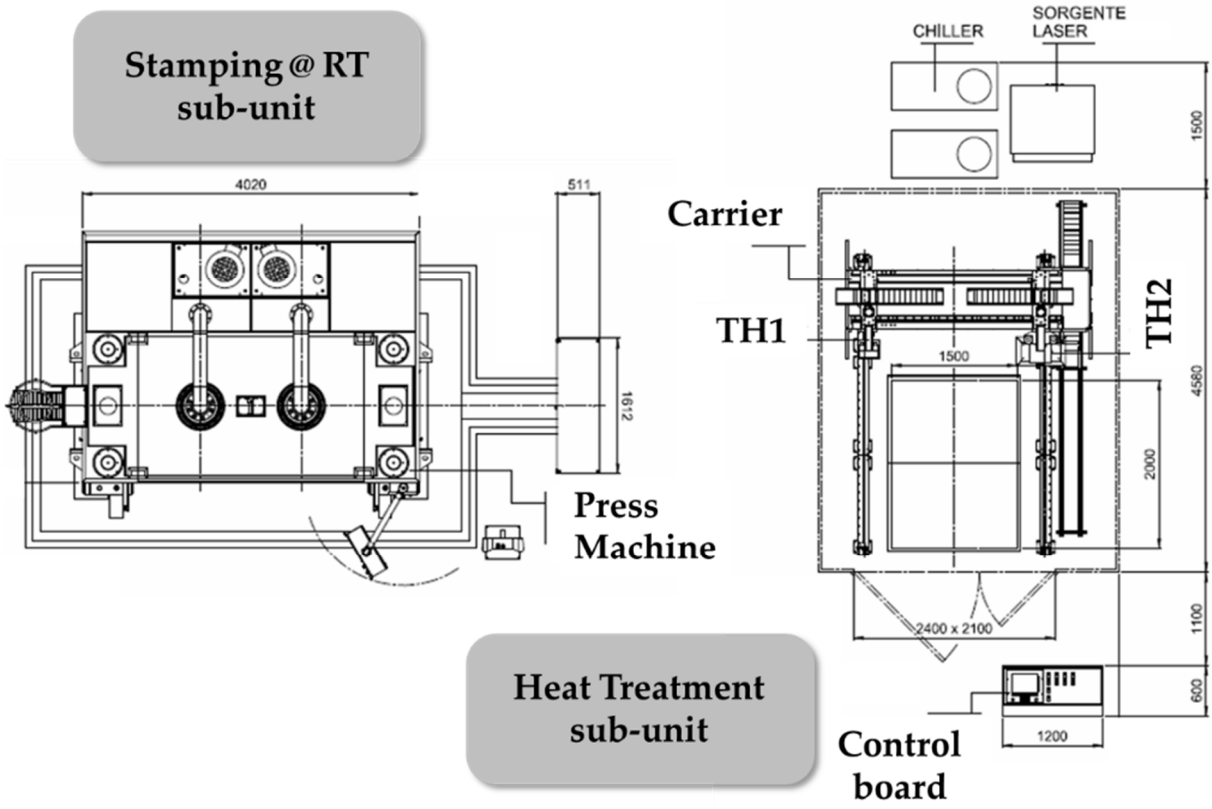

Figure 38 Overview of the two sub-units composing the PMU

The Stamping sub-unit is composed of a G2 two uprights drawing press machine supplied by the Gigant Industries s.r.l. [104] and its main technical specifications are listed in Table 5.

Table 5 Technical specification of the press machine

Technical Specification	Value
Moving table displacement	800 mm
Applied load (min. value)	600 kN
Applied load (max. value)	6000 kN
Speed in working conditions (min. value)	10 mm/s
Maximum speed	300 mm/s
Tables dimension (upper and lower)	1700x2000 mm^2
Load applied by the blankholder (min. value)	200 kN
Load applied by the blankholder (max. value)	2000 kN
Blankholder stroke	200 mm

The most innovative part of the PMU mainly lies in the Heat Treatment sub-unit, whose role is to provide the necessary heating technology to carry out the local treatment in accordance to the component to be manufactured.

Figure 39 Heat Treatment sub-unit: a) workbench and heating device carrier, b) detail of the TH1 and c) detail of the TH2

As shown in Figure 39a, inside the protection cabin, the workbench is composed of a steel frame on which a thick ceramic plate (plan size 1500 mm x 2000 mm) is positioned to improve the contact condition during the heating. The two heating devices are mounted on the same side of a U-shaped carrier (to facilitate the cabling): the displacement of the two treatment heads is thus coupled along the x axis, while the movements along the other two directions are completely uncoupled and thus be controlled according to the specific treatment to be carried out. As previously mentioned, one of the main properties of the Heat Treatment sub-unit has to be its

flexibility, i.e. the capability of the system to provide heating alternatives according to the extent of the region to be treated as well as in accordance with the production volume of a specific component [42]. For this reason, the carrier moves the two Treatment Heads (TH): (i) a 1 kW diode laser (indicated as TH1 in Figure 38, detailed view in Figure 39b) with a top-hat energy distribution over a 10 mm square spot, whose power is modulated (via PID logic control) to ensure a certain level of the heating temperature according to the acquisition of a pyrometer; (ii) a 200 mm x 300 mm rectangular brass conductive plate (indicated as TH2 in Figure 38, detailed view in Figure 39c) equipped with 8 rod cartridges (total electric power equal to 3.2 kW) surrounded by a cooler frame to avoid excessive heat dispersion in order to limit as possible of the transition zone between the treated and the untreated material (temperature monitoring is ensured by two thermocouples acquiring the temperature of both the conductive plate and the blank). As shown in Figure 38, in the proximity of the Heat Treatment sub-unit protection cabin, the control board can be accessed by the operator to set and, subsequently, monitor the heating operations. In particular, the design of the heat treatment, regardless of the heating solution to be adopted, has to be (at the current state of the project activities) designed offline adopting the "Libellula" dedicated software [105] and subsequently transferred on the computer controlling the board panel.

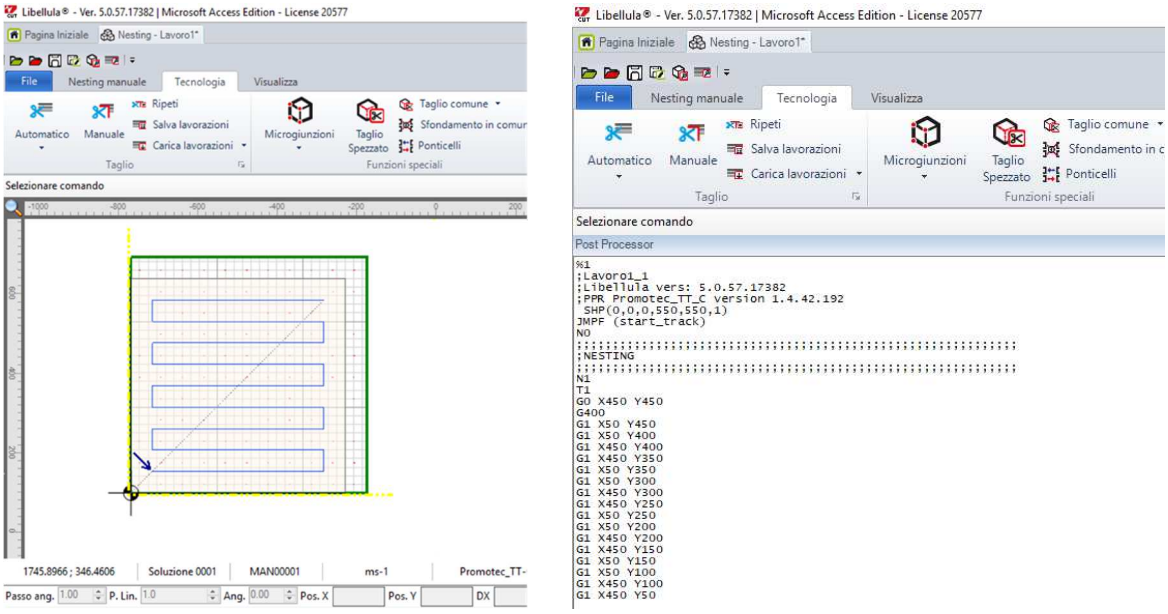

a) b)

Figure 40 Libellula working environment: a) design of the heating track, b) correspondent part program

In the case of the design of a laser heating, the first step regards the design of the laser track within the CAD environment of the software: once completed this first step, the track is transferred in a second environment where it is positioned with respect to the initial blank dimension (Figure 40a shows the positioning of a serpentine shaped track on an initial square blank). Once completed this second step, the laser track is transformed in a so-called "mask" and loaded within the last environment where it is translated in CNC language to obtain the part program of the designed track (Figure

40b). The part program is finally saved on a text file and loaded within the control board via a USB port (one of the final task of the research project is the creation of a protocol-based communication between the software and the control board computer to avoid the intermediate step of manually loading external text file). On the other hand, in the case of the heating by means of the conductive plate, the procedure is quite similar: instead of graphically draw the lines composing the laser track, the coordinates of the geometrical centre of the conductive plate are then specified to compose the heating cycle. Once the part program is loaded, the operator can access to the dedicated panel where the main process parameters can be set according to the specific treatment to be carried out. In the case of the local heating by laser (TH1), once loaded the part program, the laser track is visualized in the lower left corner of the panel (as it can be seen in Figure 41a) highlighted by a yellow polyline on a black background; immediately above it, the current position of the axes is also indicated (x, y and z refer to the TH1, while u and v to the TH2).

a) b)

Figure 41 Local heating by TH1: a) control panel, b) execution of the designed laser track

On the right side of the control panel, the main process parameter can be set: the working temperature, the interaction time with the laser and the laser spot dimension (in particular, the last two parameters are necessary to calculate and adjust continuously the feed rate during the heating). In addition, threshold values in terms of temperature and interaction time are also specified. Figure 41b shows the execution of the designed laser track on the portion of an Al blank previously covered with a layer of graphite spray to increase the radiation absorption. In the case of the other type of heating (TH2), the operator can have access to the second dedicated control panel (see Figure 42a).

a) b)

Figure 42 Local heating by TH2: a) control panel, b) heating of the designed zone

The designed heat treatment is replicated in the lower left corner of the panel showing the consecutive position taken by the conductive plate to complete the designed treatment. On the right side of the panel, in addition to a simplified scheme indicating the dimension of the conductive plate, the working temperature of the conductive plate, the temperature the blank has to reach and the total duration of the heat treatment can be set. Figure 42b shows a moment of the heating by the conductive plate. As it has been shown, the choice to equip the Heat Treatment sub-unit with two different heating technologies was mainly based on improving its flexibility: the adoption of the conductive plate was intended in the case of wider area to be treated, whereas the laser treatment was considered to be suitable to modify the properties over a smaller area or along a complex path that could not else be reproduced. In addition, the two solutions were not intended as alternative but also as integrating each other: in fact, the laser flexibility can be exploited in the preliminary design steps of the heat treatment for a new component or in the case the previous strategy has to be optimized. In such a way, once defined the ultimate extent of the region to be treated, a conductive plate of the defined geometry can then be manufactured and adopted for the components production.

2.5.3 Material characterization

As previously anticipated, the attention was focussed on the same alloy discussed in chapter 2 (warm forming of the window panel), but in this case characterized by an initial pre-strain condition (AA5754-H32). The preliminary knowledge of the material was completed by the characterization tests of the alloy under investigation in the annealed state (H111) at room temperature already discussed in the previous chapters. All the characterization tests were carried out using the same equipment described in the previous sections.

2.5.4 Process design by FE numerical simulation

The adoption of the numerical simulation has been extensively proved to be an effective way to achieve a proper design of the manufacturing processes. In the case here discussed and as done previously, the opening of the window panel was initially modelled as centred with respect to the initial blank shape so that the geometrical symmetry could be exploited and only one quarter modelled (see Figure 43a), thus noticeably reducing the computational time. The approach adopted for the FE model construction resembled the one adopted to design the stamping of the window panel in warm conditions (see section 2.3.3): all the tools were modelled as 3D shell discrete rigid entities (R3D3 and R3D4 elements with an average size equal to 10 mm) while the blank (initial thickness equal to 2 mm) as a deformable shell body (S4R and S3R elements, approximately 20000 nodes with an average element size of 4 mm).

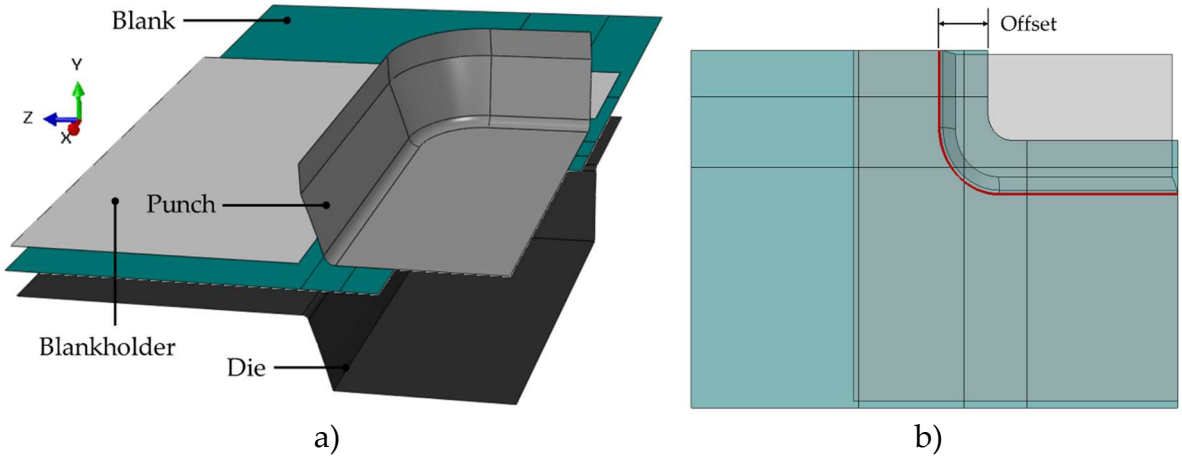

Figure 43 FE model: a) overview of the assembled entities, b) definition of the initial blank geometry

Preliminary numerical simulations were run considering the blank fully in the purchasing conditions (AA5754-H32, implementing the experimentally determined material data). The initial blank shape was at first conceived offsetting the edge of the die entry radius (highlighted in red in Figure 43b) of a quantity equal to the final depth of the window opening (76 mm). Punch stroke profile was modelled as a linear ramp, while the BHF was kept constant for the whole forming step. Also for this set of simulations, the punch started its stroke once the BHF reached its target value.
According to the results of the preliminary numerical runs, the heat treatment was designed to locally modify the material properties in the blank portions where the rupture was predicted [106]. The effect of the heat treatment in terms of material properties distribution was again modelled adopting a field variable capable of associating the material properties (flow curve and FLC) in the annealed conditions with the correspondent geometrical partition on the blank. The blank was then modelled as already subjected to the heat treatment, optimizing the distribution of the post-treatment material properties according to the two heating solutions equipping the PMU described in section 2.5.2.

2.5.5 Process optimization

Once evaluated the blank critical regions from the preliminary FE simulations, the strategy of the laser heating to properly modify the material properties was optimized according to an ordered pattern of square portions, defined as "matrix of spots". Since each stamping run was much more computationally intensive than those discussed in the section 2.4.2, the optimization procedure, integrating the platform modeFRONTIER with the FE model, was completed via the Response Surface Methodology (RSM), i.e. creating at first an accurate metamodel (the Response Surface) and subsequently running a "virtual" optimization (working principle is depicted in Figure 44). The starting point was again based on the identification of an initial population, here indicated as DoE (Design of Experiment) population, in which each individual corresponded to a single numerical run. Once completed the first round of simulations, numerical results were arranged according to properly defined output variables and subsequently fitted via accurate Response Surfaces. The created metamodels were then used as the base for the subsequent "virtual optimization".

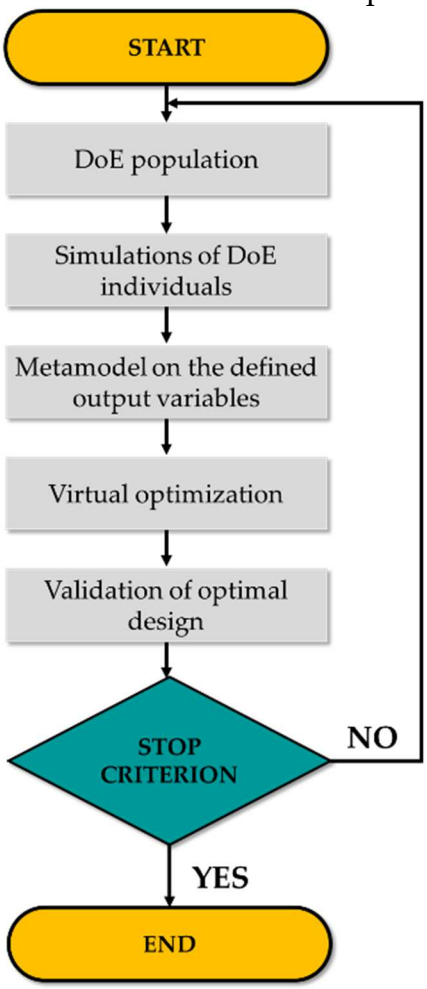

Figure 44 Workflow of the virtual optimization based on the creation of a metamodel

The integration platform modeFRONTIER allows to select among different interpolating algorithms named Radial Basis Functions (RBF) [107,108], particularly suitable to interpolate multivariate scattered data (i.e. data not necessarily sampled on

a regular grid, and for this reason RBF is defined as a meshless method). Being the RBF interpolant, they pass exactly through the training points (i.e. the designs): for this reason, the design set is usually subdivided in: (i) the training sub-set, composed of around 90% of the design table, on which the Response Surface (RS) is actually trained and (ii) the validation set, composed of the remaining 10% of the design table, that is used to validate the accurateness of the RS. In general terms, given a training set of n points sampled from a function $f(\mathrm{x}) : \mathbb{R}^d \rightarrow \mathbb{R}$ as shown in Equation 6.

$$f(\mathrm{x}_i) = f_i, \qquad i = 1,2, \dots, n \tag{6}$$

An RBF interpolant function has the form expressed in Equation 7.

$$s(\mathrm{x}) = \sum_{j=1}^{n} c_j \phi\left(\|x - x_j\|/\delta\right) \tag{7}$$

Where $\|.\|$ is the Euclidean norm in the d-dimensional space, δ a fixed scaling parameter and ϕ is the radial function (or kernel); the RBF interpolant *s(x)* is the linear combination of identical spherical symmetric functions, each centred at the n different training points sites. The integration platform provides 5 different kernel algorithms, whose formulation is reported in Table 6.

Table 6 Available Radial Basis Functions

Name	Abbr.	Formulation	d space
Gaussians	G	$\phi(r) = \exp(-r^2)$	
Duchon's Polyharmonic Splines	PS	$\phi(r) = r^3$	d odd
		$\phi(r) = r^2 \log(r)$	d even
Hardy's MultiQuadrics	MQ	$\phi(r) = (1 + r^2)^{1/2}$	
Inverse MultiQuadrics	IMQ	$\phi(r) = (1 + r^2)^{-1/2}$	
Wendland's Compactly Supported	W2	$\phi(r) = (1 - r)^3 + (3r + 1)$	$d = 1$
		$\phi(r) = (1 - r)^4 + (4r + 1)$	$d = 2,3$
		$\phi(r) = (1 - r)^5 + (5r + 1)$	$d = 4,5$

The RSM based optimization, had not only the big advantage of relying on a limited number of individuals composing the initial DoE population for the construction of an accurate metamodel, but also the optimization procedure – being virtual – needed only few seconds to be completed.

2.6 FE prediction of the post-treatment material properties distribution

In the previous section, all the stamping simulations were carried out modelling the blank as already subjected to the heat treatment thanks to the adoption of a field variable connecting the material properties in different conditions with the correspondent blank portion. On the other hand, as already highlighted in the introduction chapter, the optimization of the preliminary heating step has a strong influence on the outcome of the stamping step. It became then necessary to provide an accurate tool able to, once gathered sufficient information to predict the modification of the material properties according to a specific combination of time and temperature, i.e. according to a specific thermal history. The activities here described started from specifically designed experimental tests based on the physically simulation of the annealing treatment on AA5754 samples, initially in the pre-strained conditions (H32). The dependence material properties with the physically simulated heat treatment was formulated by fitting post-treatment hardness measurements by analytical sigmoidal functions. The created functions were implemented in python script able to analyse the results of a FE simulation, predicting the final property distribution according to the single nodal thermal history.

2.6.1 Physical simulation of the annealing process

The successful implementation of a methodology for a proper prediction of the material distribution after a local heat treatment mainly depended on the prior knowledge of the material properties and how its initial condition could be altered by different combination of the heating temperature and holding time. Once again, the huge potentialities of the physical simulation played a fundamental role to accomplish this first step starting from AA5754 striped specimens (120mm x 30mm, initial thickness 2 mm) initially in the pre-strained (H32) conditions. The Gleeble 3180 system was adopted to simulate an annealing heat treatment composed of: (i) a rapid increase of temperature (heating rate around 1000°C/s), a soaking time of variable duration (from 1 second to 500 seconds) and a rapid cooling with forced air. Once cooled down to room temperature, specimens were subjected to hardness measurements, whose values were then expressed in terms of a variable able to properly describe the effectiveness of the annealing process, indicated as "Degree of Annealing" (DoA), and expressed by Equation 8.

$$DoA=\frac{HV_{H32}-HV_{meas}}{HV_{H32}-HV_{H111}} \quad (8)$$

Equation 8 relates the measured hardness to the limit conditions, represented by initial pre-strain state (HV_{H32}) and the fully annealed one (HV_{H111}): consequently, a more effective annealing could be represented by a DoA tending to 1, whereas a less

effective heating was characterized by a low DoA value. Hardness measurements, for the same value of the soaking time, were fitted by means of the sigmoidal analytical function expressed by Equation 9:

$$DoA=\frac{Offset}{1+\exp[\lambda(T_0-T)]} \quad (9)$$

Where *Offset* represents the maximum value of the sigmoid, λ the steepness of the curve and T_0 approximately the abscissa of the sigmoid midpoint.

2.6.2 The benchmark case study

The prediction of the material properties after the heat treatment, as previously explained, was mainly based on the analysis of each nodal temperature history and the subsequent calculation of the correspondent DoA. The laser heating of a dog-bone specimen was indicated as a benchmark case study: experimental heating on a pre-strained (AA5754-H32) specimen was carried out setting the laser beam power at 500 W for a total duration of 5.5 s (adopting the equipment described in section 2.4.1) and was assisted by the FLIR x6540sc thermal imaging camera to get an accurate distribution of the temperature throughout the whole test. Once cooled down at room temperature, the specimen was subjected to hardness measurements along its longitudinal axis. The experimental conditions were replicated within the Abaqus CAE environment and a pure thermal FE model was created: material thermal properties were taken from literature [109]. The model was then tuned in terms of heat transfer coefficient between the specimen and the surrounding environment and the exact percentage of the laser power absorbed by the material minimizing the difference between the numerical and experimental temperature evolution of a point on the specimen located in correspondence to the geometrical centre of the laser spot. As previously discussed, the minimization of an error function belongs to the group of problems that can be treated as optimization problems [110–112], for which an accurate solution is provided by the synergic combination between the FE model and the integration platform modeFRONTIER within an automatic procedure managed by a multi-objective genetic algorithm.

2.6.3 Calculation of the final distribution of material properties

The accurateness of the FE predictions was considered a key aspect to correctly calculate the distribution of properties after the heat treatment. Once properly tuned the FE model, a python script was run to numerically predict the DoA distribution on the benchmark case study. In particular, the script:

1. Extracted the nodal temperature-time curves to calculate the maximum temperature value;

2. Discretized the area below the temperature-time curve with rectangles whose width (Δt in Figure 45) was equal to the time interval set in the numerical simulation for the field output writing on the odb results file; each rectangle contributed to the total area calculation by a quantity equal to the product between its height – T_{avg}, calculated as the average value of the temperature at the beginning (T_{bi}) and at the end (T_{ei}) of the time interval (shown in the detail of Figure 45) – and its width.
3. Calculated the equivalent time dividing the calculated integral (point 2) by the nodal maximum temperature (point 1).
4. Calculated the correspondent DoA, since known its analytical formulation.

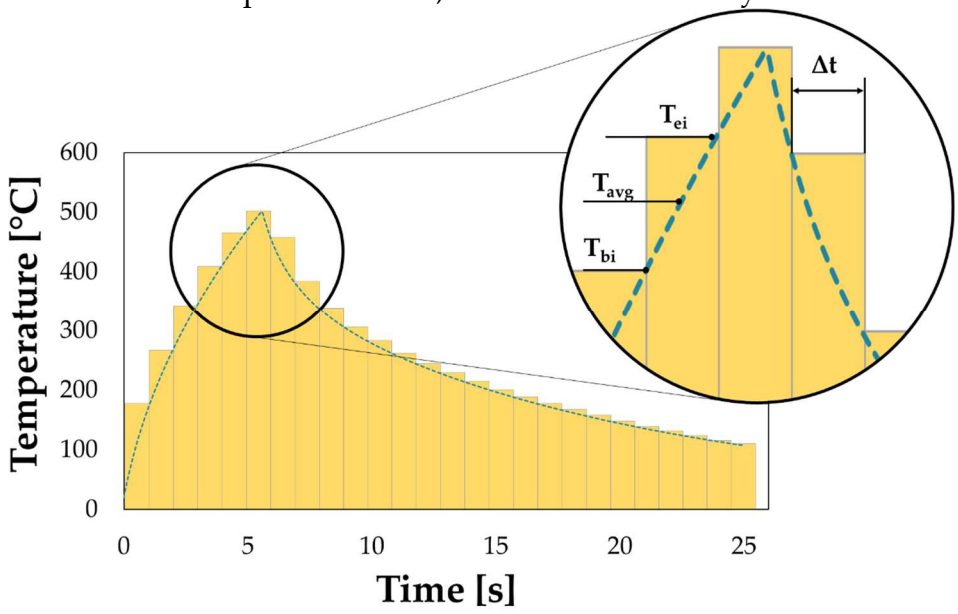

Figure 45 Discretization of the area below the curve

The logic workflow of the created script is graphically reported in Figure 46.

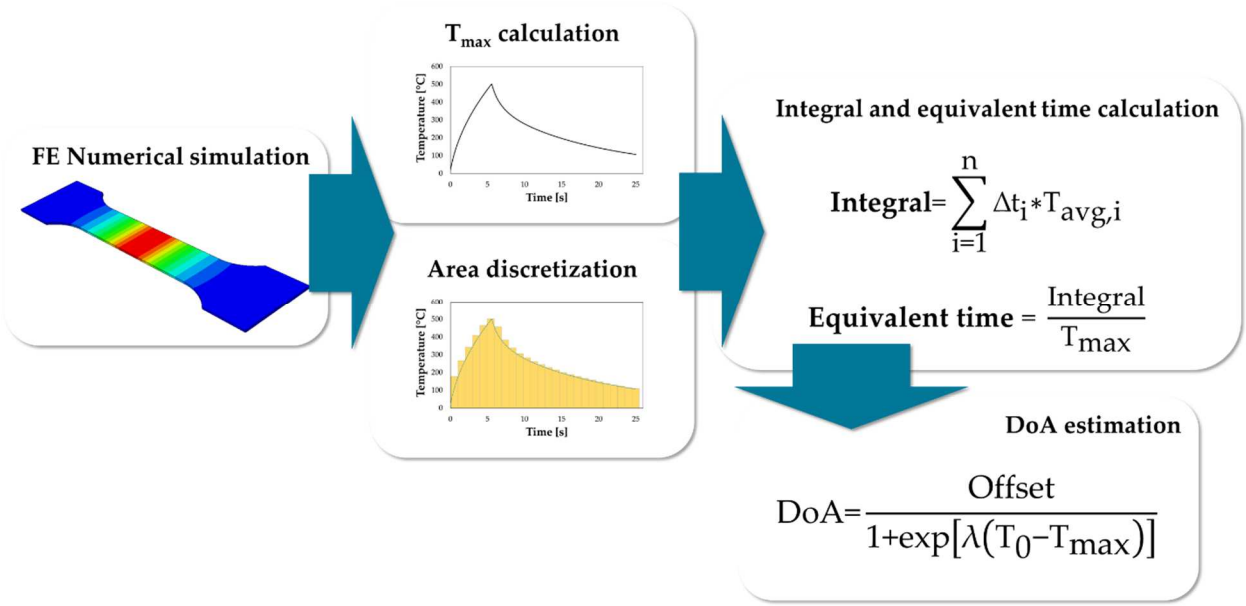

Figure 46 Workflow of the python script

3. The “Heating During Forming” approach

The present chapter reports the main results regarding the "Heat During Forming " approach: in particular, results of the material characterization showed the strong influence of the applied strain rate both on the material resistance and on its formability. Results of the material characterization were useful to properly design the heating strategy once defined the blank deformation zone that was subjected to the highest plastic strain when the stamping was modelled at room temperature and the blank fully in the annealed state. The uncoupled thermo-mechanical approach, discussed in detail in the section 2.3.3, provided the optimal value of the forming process parameters to obtain a perfectly sound component

3.1 Material behaviour in warm conditions

Tensile data coming from the experimental tests were fitted with the hardening model proposed by Hollomon ($\bar{\sigma}=K\bar{\varepsilon}^n$) that relates the equivalent stress ($\bar{\sigma}$) to the equivalent strain ($\bar{\varepsilon}$) by means of two constants – the strength factor K and the strain sensitivity index n – depending on the material. In accordance with the theory and the available data in literature [16], the material behaviour in warm conditions was highly influenced by the test temperature and the applied strain rate: as Figure 47a shows, the flow curve was characterized by higher level of stress when the applied strain rate increased and the material was characterized by a more pronounced hardening behaviour. On the other hand, at a fixed value of the applied strain rate (see Figure 47b), increasing the temperature led to a less resistant material with a more pronounced softening behaviour (the slope of the flow curve decreased when increasing the test temperature).

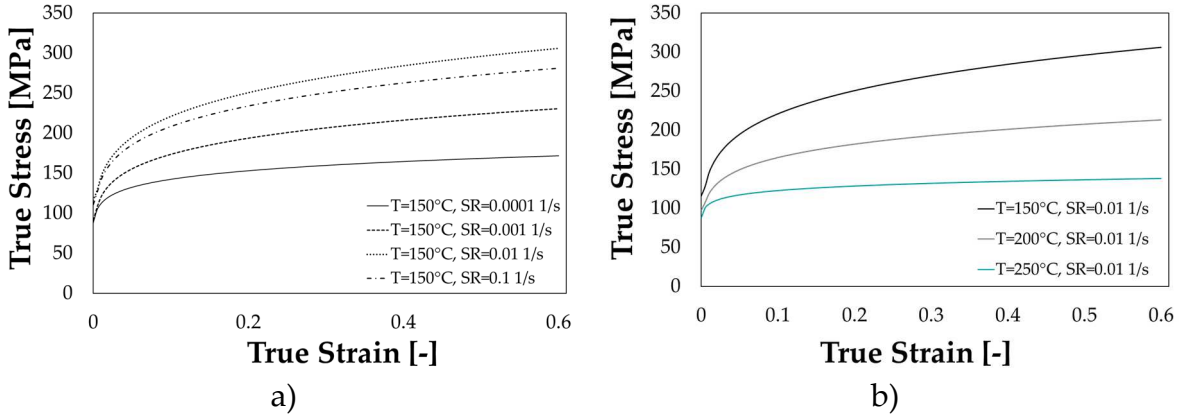

Figure 47 Results of the material characterization: a) effect of the strain rate (T=200°C), b) effect of the temperature (SR=0.01 s-1)

Figure 48a gives a general description of the influence of temperature and applied strain rate on the material yield point (calculated as the tensile stress at the 0.2% level of plastic strain). As mentioned, tensile tests at the strain rate level equal to 0.0001 s^{-1} were useful to obtain information about the elastic behaviour: as expected, and clearly shown in Figure 48b, the calculated value of the Young's modulus (as the slope of the

stress-strain curve within elastic field) exhibited an almost perfectly linear decreasing trend with the test temperature.

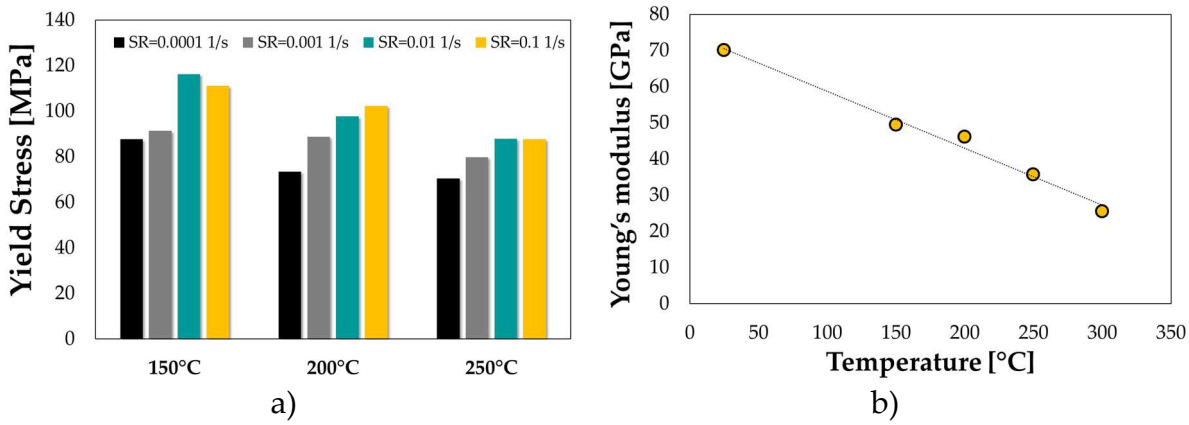

Figure 48 Results of the material characterization: a) yield stress as a function of temperature and strain rate, b) Young's modulus as a function of the test temperature

As regarding the formability in warm conditions, limit strains were calculated using the inverse parabola methodology as reported by the ISO 12004 standard [113]: both the draw (negative minor strain) and the stretch side (positive minor strain) were fitted by a first order linear function.

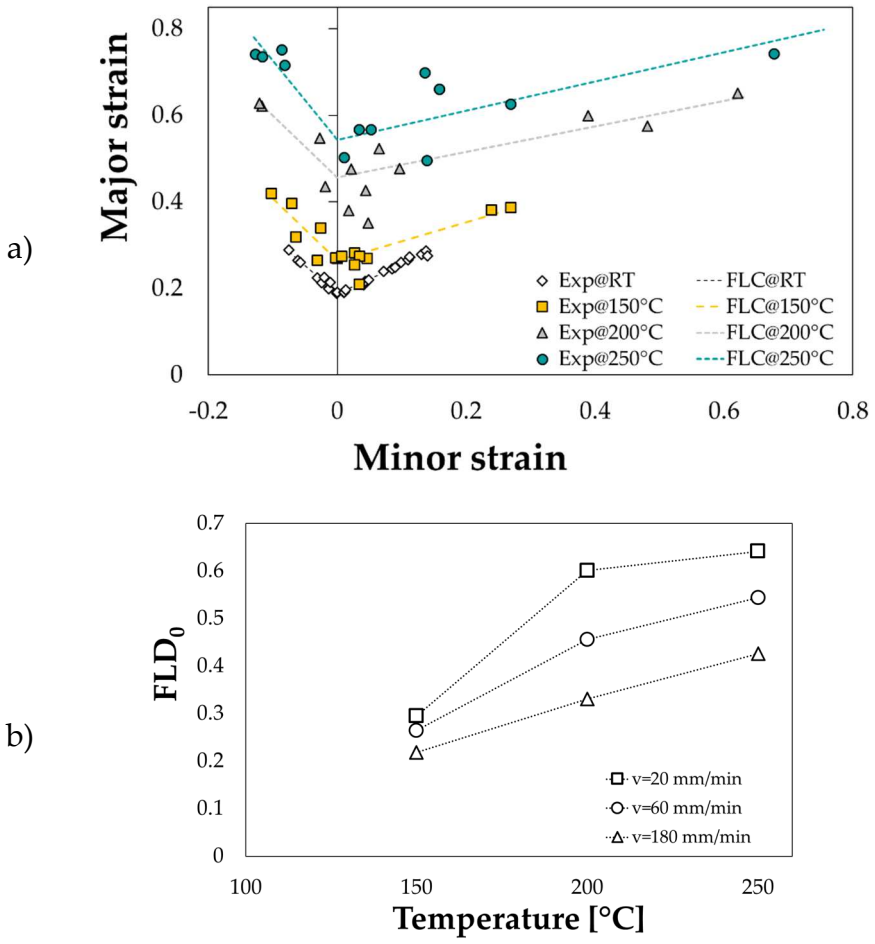

Figure 49 Results of the Nakazima tests: a) FLC as a function of temperature, b) effect of the induced strain rate on the FLD0

Figure 49a shows the remarkable effect the temperature had on the material formability especially when passing from 150 °C up to 200 °C: FLCs were obtained setting the crosshead speed equal to 60 mm/min that corresponded to an average strain rate equal to 0.01 s^{-1}. To evaluate the effect of the induced strain rate on the material formability, other two levels of the crosshead speed were investigated, namely 20 mm/min and 180 mm/min, on the W100 specimens: the parameter FLD_0 – the major strain in the plane strain condition – was remarkably influenced by the forming speed as clearly shown in Figure 49b, where an increase in the induced strain rate was accompanied by a reduction in the material formability, much more evident with the increasing test temperature. Figure 50a, in addition, reports the evolution of the equivalent strain rate of the point where the rupture occurred, demonstrating that the investigated crosshead speed levels induced an average value of the equivalent strain rates comparable to those investigated during the tensile tests. The material formability database was then completed accounting for the strain rate effect: FLCs at the other two investigated crosshead speeds were analytically calculated multiplying the limit strains of the reference curves (i.e. those obtained from the tests at 60 mm/min) by a quantity equal to the ratio between the reference FLD_0 (at 60 mm/min) and its value at the other investigated two crosshead speed values: as an example, FLCs as function of the strain rate at the temperature equal to 200°C are reported in Figure 50b.

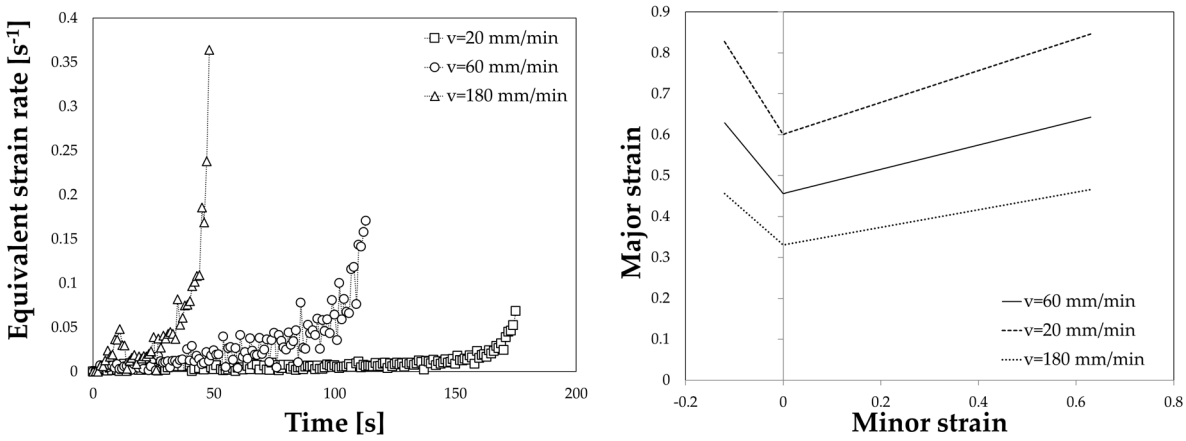

Figure 50 Additional formability tests: a) equivalent strain rate at different crosshead speed, b) effect of the strain rate on the FLC at 200°C

Material data coming from the formability tests were implemented in the FE numerical model (discussed in the section 2.3) to activate an FLC-based damage criterion extremely useful to predict the onset of necking during the stamping simulations.

3.2 Results from the preliminary FE simulations

Preliminary FE simulations of the stamping at room temperature (the blank was modelled fully in the annealed state) were aimed at (i) evaluating the most critic regions (where the highest level of plastic strains was reached) and (ii) defining the initial blank geometry to improve the material draw during the stamping. The implementation of the experimentally determined FLC activated a damage criterion, particularly useful to detect the onset of necking (and possible rupture) in the stamping simulations. The damage criterion activates an output variable, the FLDCRT, defined as the ratio between the nodal major strain (point A in Figure 51a)and the correspondent major strain on the FLC (point B in Figure 51a) for the same value of the minor strain. The model predicts a possible rupture when the FLDCRT variable overcomes the threshold value equal to 1. As a practical rule, a tolerance of about 10% on the threshold value is accepted to account for the Forming Limit Band (a region covering the entire dispersion of the forming limit curves mainly related to the variability and scattering of the material data) [114].

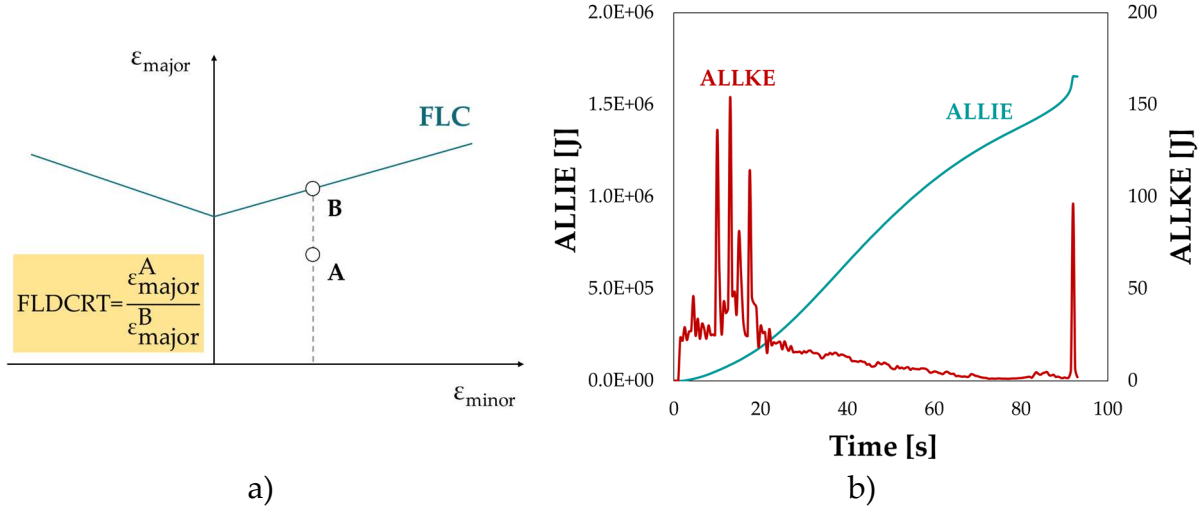

Figure 51 a) graphical description of the FLDCRT variable, b) System internal energy (ALLIE) vs. kinetic energy (ALLKE)

Before analysing the results of the preliminary simulation in terms of strain distribution, it was checked that the kinetic energy of the system (labelled as ALLKE in Figure 51b) resulted negligible with respect to its internal energy (labelled as ALLIE in Figure 51b): in such a way, it was verified that the speeding up due to the mass scaling approach did not alter significantly the numerical results (no inertia effect were predominant and the problem could be still considered quasi static). Results of the preliminary simulation confirmed that the stamping at room temperature was too critic: the highest levels of plastic strain were reached in the corner region of the window opening (see the distribution map of the major principal component of the strain tensor, indicated as *PE Max in Plane* in Figure 52a) where the occurrence of rupture was predicted (the region highlighted in grey in Figure 52b were characterized by a value of FLDCRT close to 1.2).

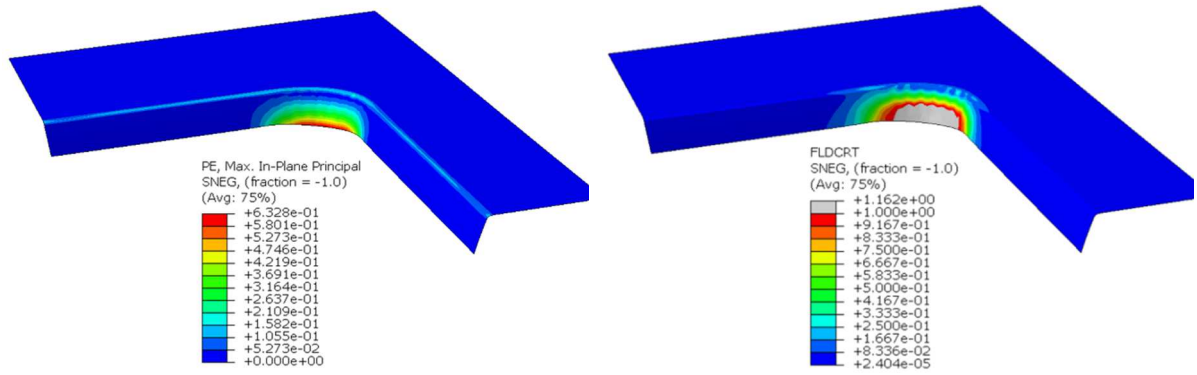

a) b)

Figure 52 Results of the preliminary simulation: distribution map of the a) PE Max in plane and b) FLDCRT variables

3.3 Simulation of the stamping in warm conditions

The uncoupled approach, extensively discussed in section 2.3.3, was based on the initial solution of the thermal problem, in terms of determining the heating strategy – number of active heating elements on the both tools – to obtain an optimal temperature distribution on the blank. The identification of the heating configuration is here briefly recalled and it was based on a code reporting the number of active heaters on the die side followed by the letter "D" and the number of active heaters on the punch side followed by the letter "P". The bar chart in Figure 53 suggests that, even when considering the maximum number of heating elements on both tools (3D4P condition), the highest temperature reached on the punch side was sensibly lower than 650°C. It should also be pointed out that, on the die side, the maximum reached temperature was completely independent from the number of active cartridges on the punch side (and vice versa).

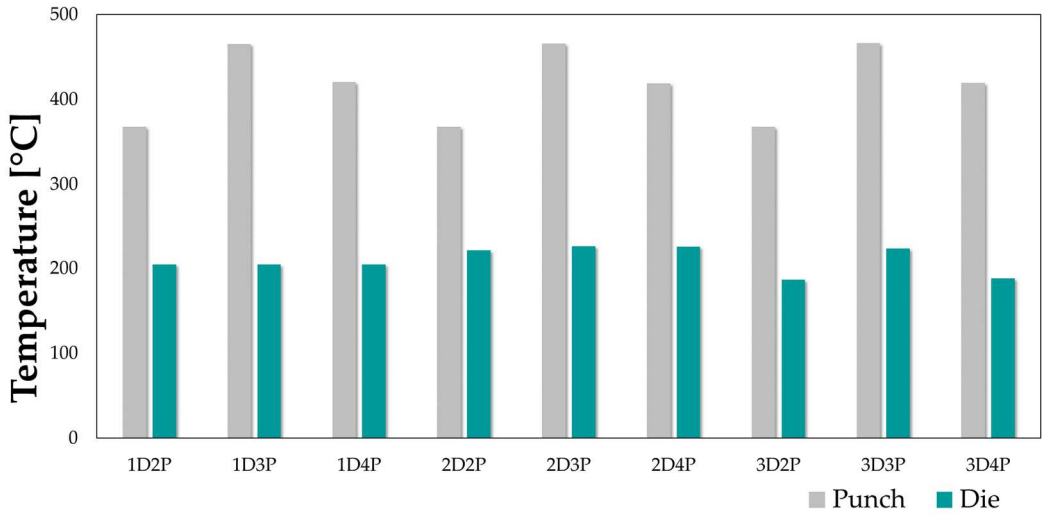

Figure 53 Maximum temperature reached on the die and on the punch

On the other hand, the time needed to reach the target temperature was sensibly affected by the number of active elements. In fact, when two heating elements were activated on the punch side (2D2P curve in Figure 54a) the temperature reached at the end of the heating step was even lower than the target and, once in contact with the blank, tended to decrease during the subsequent 600 s. When increasing the number of active elements to 3 and 4 (2D3P and 2D4P), the target temperature was reached after 1800 s and 1000 s respectively without any decrease during the subsequent blank heating.

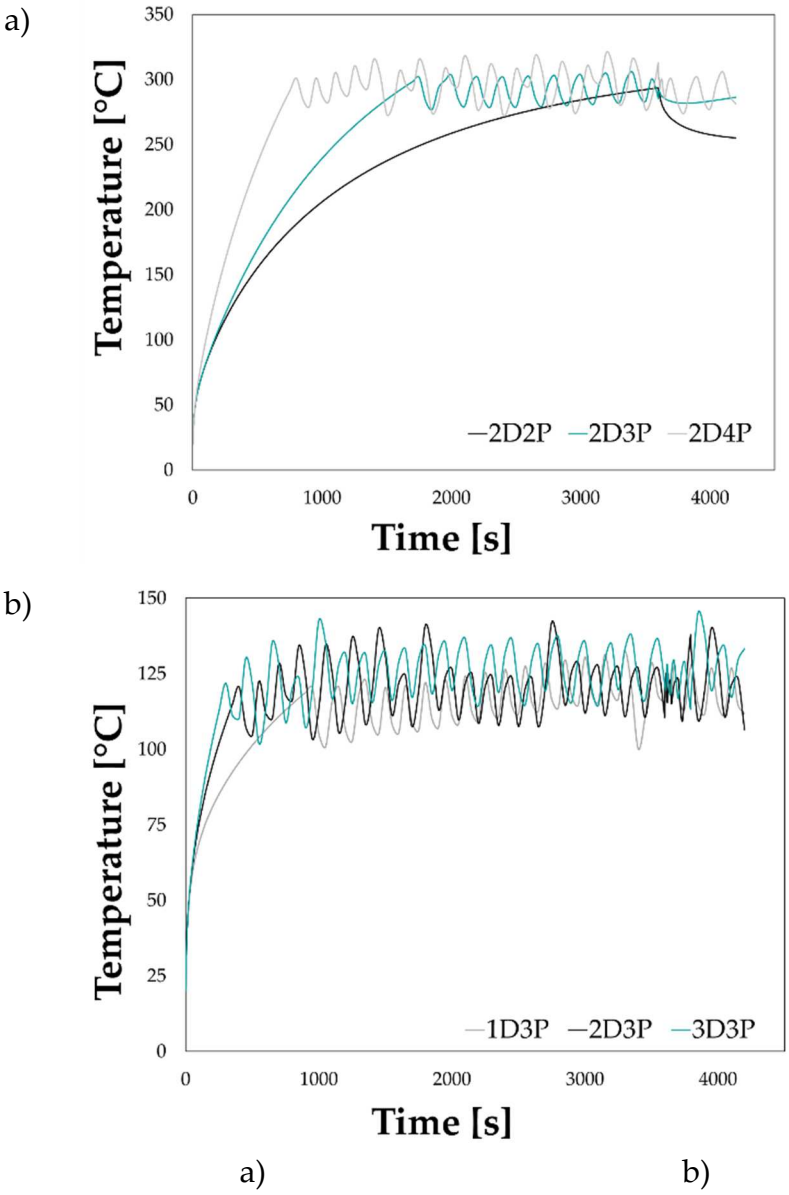

Figure 54 Numerical temperature evolution from the sensor: a) punch side, b) die side

On the die side, as depicted in Figure 54b, one active cartridge resulted to be sufficient to get the prescribed test temperature, whereas increasing the number of active elements had only an influence on the time needed to reach 120°C which resulted more evident when passing from 1 to 2 active heaters (2D3P and 3D3P curve were quite close in terms of time needed to reach the working temperature). The most

important aspect to be investigated regarded the definition of the heating strategy to optimize the final temperature distribution on the blank.

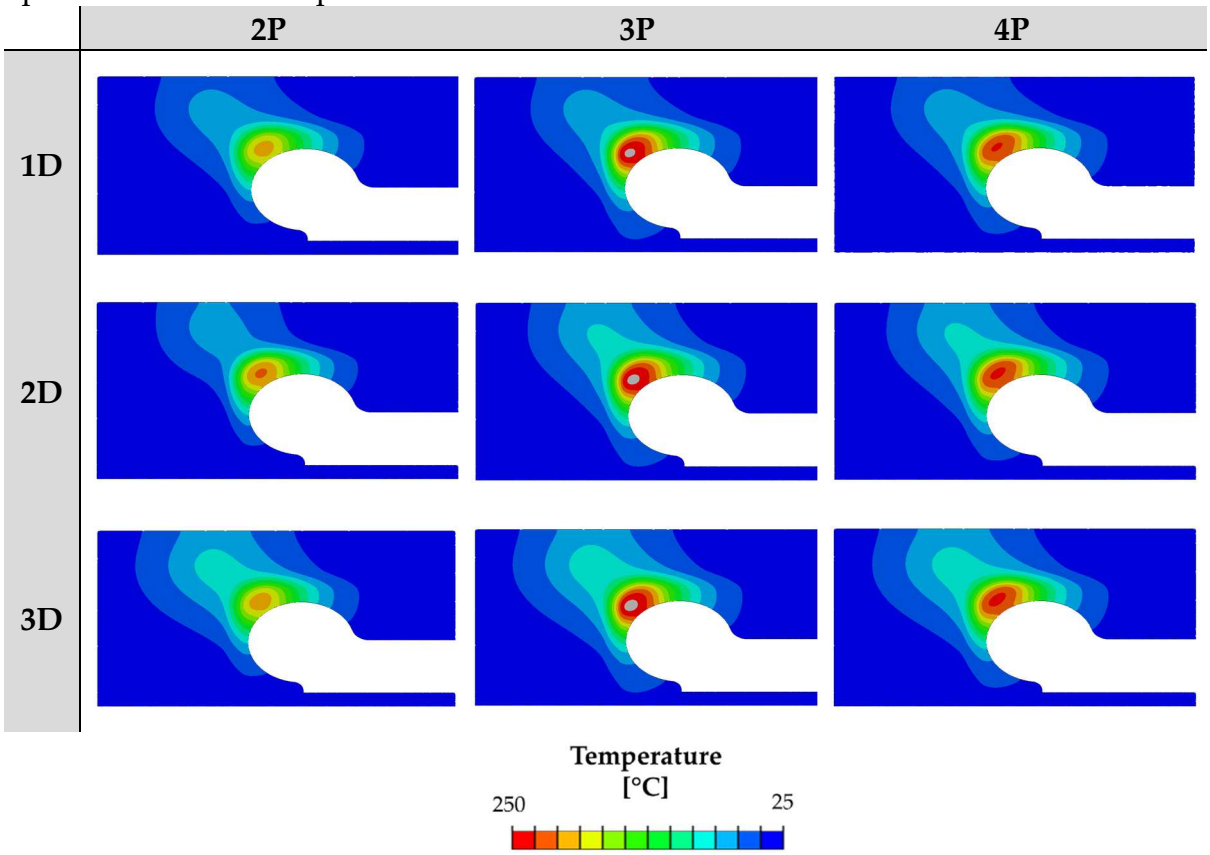

Figure 55 Blank temperature distribution at the end of the heating simulation for the investigated heating strategies

Contour plots in Figure 55 suggest that the heating configuration on the die side had a negligible influence on the final temperature distribution; on the other hand, a favourable distribution was obtained when considering 3 active elements on the punch side: the critic blank portion reached a temperature slightly higher than 250°C at which the material exhibited the highest formability (as demonstrated by the FLCs in Figure 49a). According to the final temperature distribution over the blank and the time needed to achieve the working temperature on both sides, the 2D3P heating scheme was chosen as the optimal heating strategy. The same operative condition was then replicated on the NG#2 blank geometry and a similar final temperature distribution was obtained (see Figure 56).

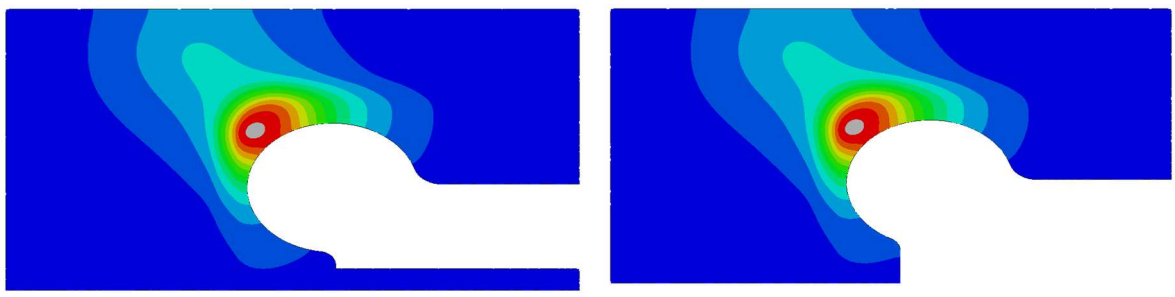

a) b)

Figure 56 2D3P heating strategy: final temperature distribution on a) NG#1 and b) NG#2

The determined temperature distribution was then transferred in the subsequent forming simulation as an initial predefined field; the BHF and the boundary conditions were not changed and set as previously discussed in the preliminary simulations. The mass scaling approach was again applied, keeping the stable time increment set at 10^{-4}. The aim of this second set of numerical simulation was the definition of the process parameters to obtain a sound component. It is widely known that, in warm conditions, the strain rate has a remarkable influence on the material behaviour: for this reason, the stamping was simulated considering three different forming speed velocity, namely 20 mm/min, 60 mm/min and 180 mm/min (resembling the levels investigated during the formability tests), and for each condition the correspondent FLC was implemented.

ID	Punch speed [mm/min]	Cycle time [s]	FLDCRT distribution
2D3P-FS20	20	277	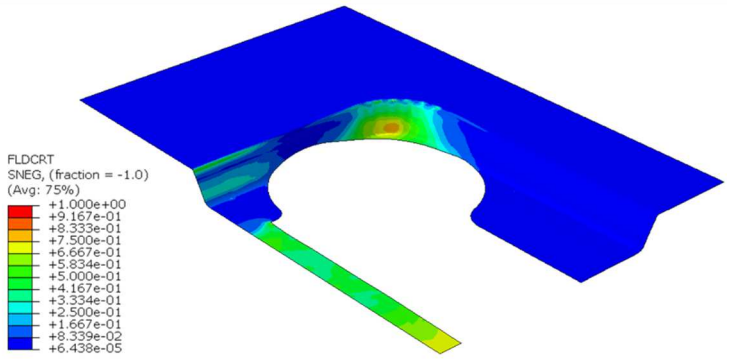
2D3P-FS60	60	91	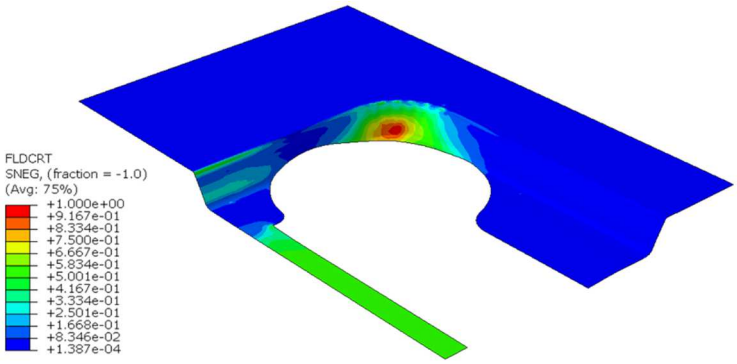
2D3P-FS180	180	31	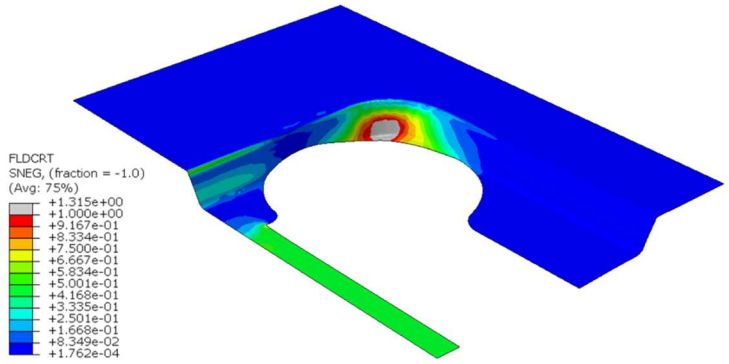

Figure 57 Forming simulation in warm conditions: final FLDCRT variable distribution

Numerical results are reported in Figure 57 in terms of strain severity distribution (FLDCRT output variable); each of the simulated conditions are univocally identified by a code reporting the heating strategy and the forming speed (FS, along with the simulated total time). It is quite clear to denote the remarkable effect of the strain rate on the component stamping: when setting the forming speed at 180 mm/min (ID 2D3P-FS180 in Figure 57c), the process resulted to be still critic and the rupture was predicted in the blank corner region (highlighted in grey and characterized by a FLDCRT value higher than 1.3). On the other hand, when decreasing the forming speed down to 60 mm/min, the strain distribution on the corner region resulted to be less critic and the stamping of a sound component was predicted. A further decrease of the punch speed, as expected, led again to a successful stamping – the corner region was characterized by an even lower value of the FLDCRT – but the cycle time dramatically increased (almost three time higher). As done for the thermal simulations, the influence of the initial blank geometry was also assessed: the comparison of the FLDCRT distribution (Figure 58, a and b) demonstrate that the presence of the central stripe had a negligible effect on the strain distribution of the final component and a sound component could be manufactured starting from the NG#2 initial geometry.

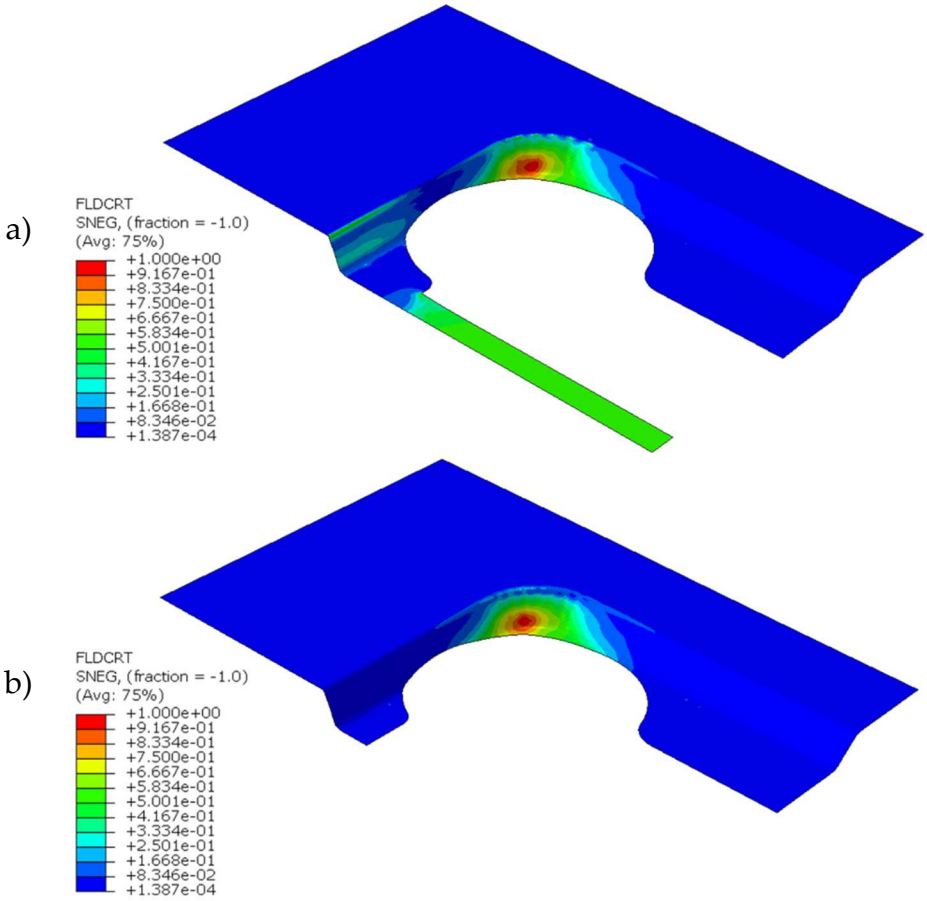

Figure 58 FLDCRT variable distribution: initial blank geometry a) NG#1 and b) NG#2

The design of the warm stamping then suggested that the optimal heating strategy had to be based on 3 active heaters on the punch side and 2 on the die side, while the stamping operations had to be carried out at 60 mm/min.

3.4 Validation of the numerical results via experimental stamping trials

Before the positioning between the tools, both the surfaces of the blank were sprayed with a graphite paste to reduce the friction and to improve the material drawing during the forming step. During the experimental trials, at the end of the blank heating step, the tools were slightly opened and the temperature distribution over the blank acquired by a thermal camera. Experimental temperature acquisition was compared with the numerical results along the path indicated in Figure 59, showing a high level of correspondence thus validating the accurateness of the thermal simulations.

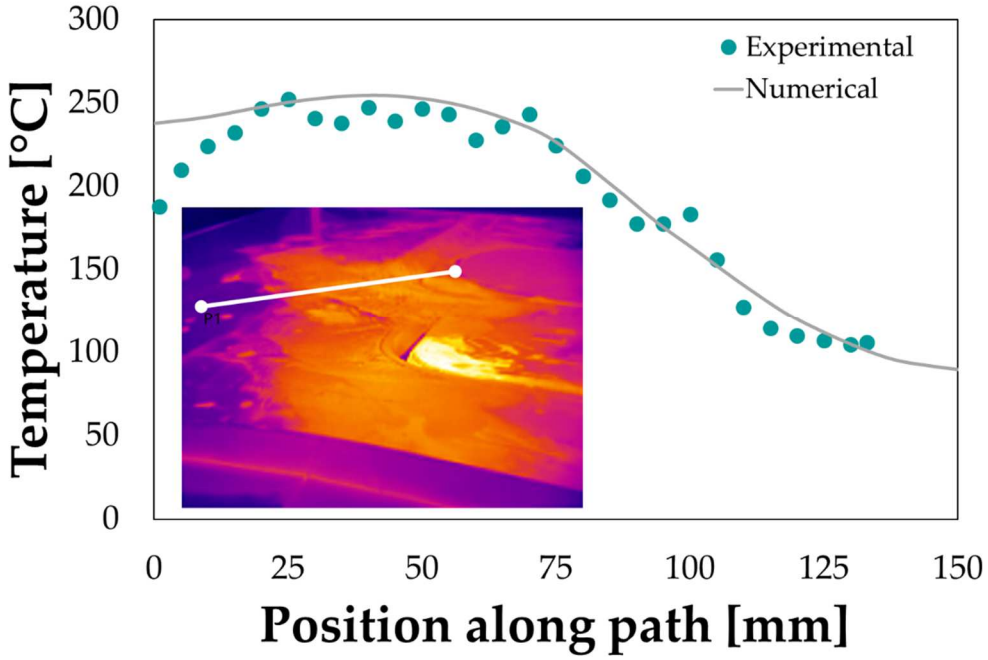

Figure 59 Validation of the thermal runs: experimental vs. numerical temperature distribution along the path

Stamping trials were then carried out according to the numerical simulation discussed in section 3.3: in particular, two stamping speed were taken into account, namely 60 mm/min and 180 mm/min.

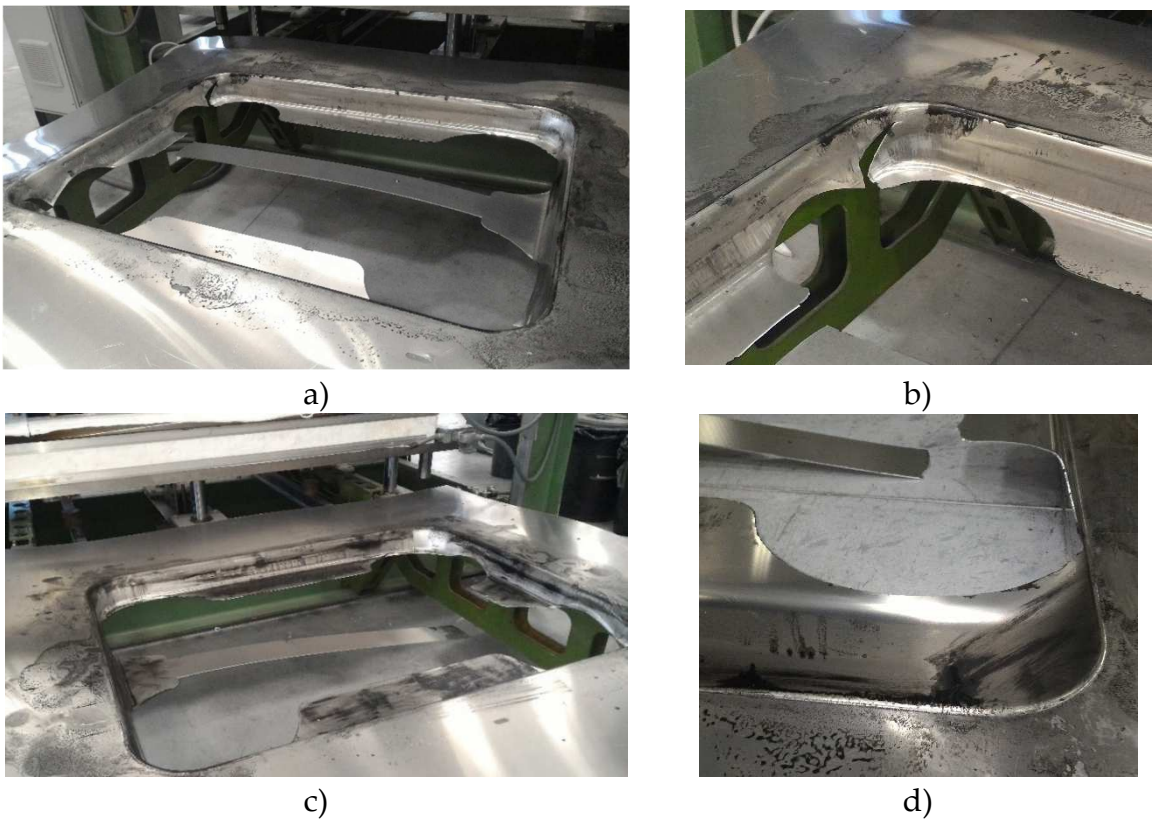

a) b)

c) d)

Figure 60 Stamping trials: a) ruptured panel (v=180 mm/min) and b) detailed view of the rupture; c) sound panel at v=60 mm/min and d) detailed view of the corner region

Results in Figure 60 (a and b) demonstrate that, despite the increased formability due to the warm conditions, the process resulted to be still too critic when the speed was set at the highest level and the blank rupture occurred in the corner region as predicted by the numerical simulation (see FLDCRT distribution map in Figure 57, 2D3P-FS180 condition). On the other hand, when decreasing the forming speed (60 mm/min), no rupture occurred in the corner region, as predicted by the numerical results, and a perfectly sound component was manufactured. To further confirm the accurateness of the FE prediction, stamping trials were also carried out starting from the NG#2 blank geometry: results shown in Figure 61 demonstrate once again that the intermediate level of the forming speed was the optimal one to obtain a sound component.

a) b)

Figure 61 Stamping trials on the NG#2 blank geometry: a) sound panel at v=60 mm/min and b) detailed view of the corner region

3.5 Implementation of the manufacturing process

As described in the previous section, numerical results were obtained under the assumption of the window opening located at the centre of the initial blank panel, which made possible the modelling of only one quarter of the system taking advantage of the geometrical symmetry. As the 3D representation in Figure 15a shows, being the window opening not perfectly symmetric, the whole system (blank and tools) was modelled to further validate the approach. As done for the previous activities, the thermal problem was solved reproducing the whole press machine (as shown in Figure 62a) and implementing the optimal heating strategy (2D3P). Forming simulations were subsequently run modelling the whole blank (Figure 62b)with the imported final temperature distribution as an initial predefined field (the initial blank geometry is reported in Figure 62c). The same load and constraints setting of the previous analyses were maintained for the simulation here described as well as the mass scaling approach to speed up the numerical simulation.

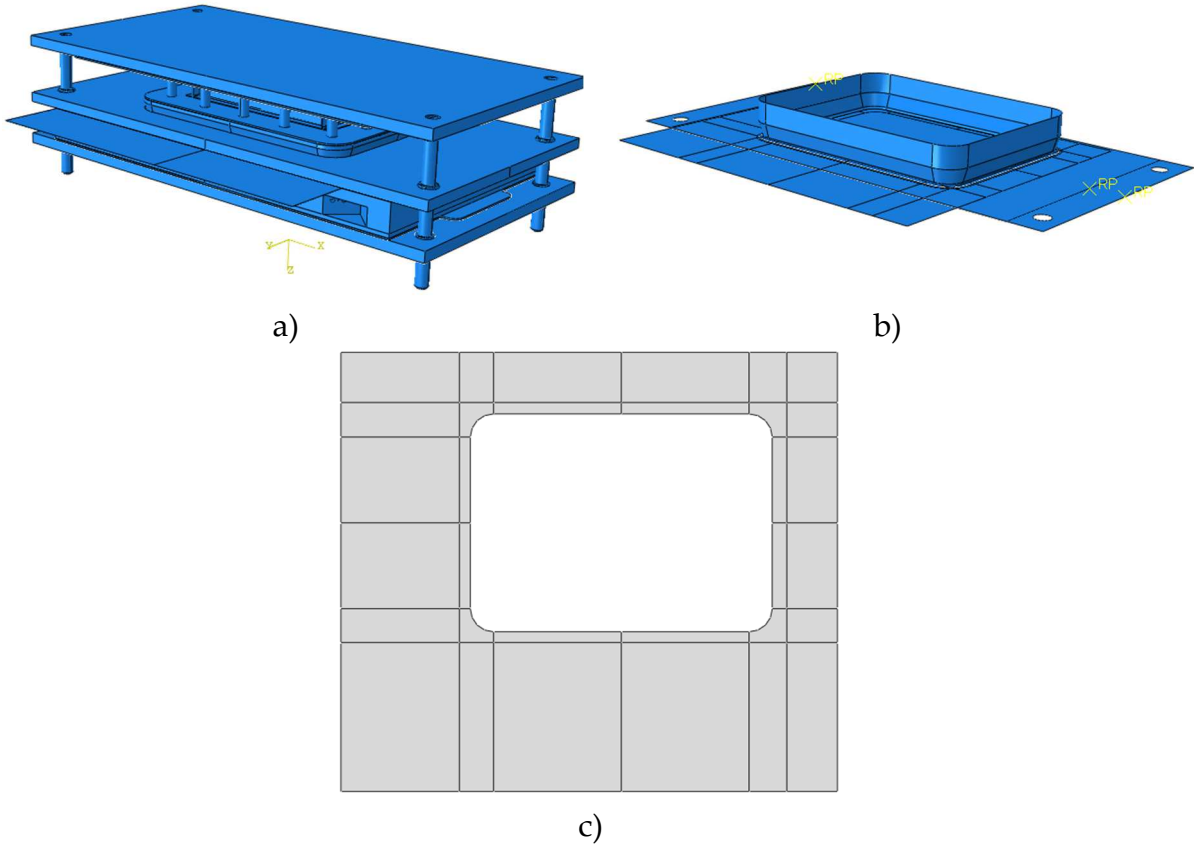

Figure 62 Final process design: a) 3D model for the solution thermal problem, b) 3D model for the forming step, c) optimized blank geometry

Numerical results shown in Figure 63 (a and b) were in accordance with what discussed in the 3.3 section: the corner regions were characterized by the most severe strain condition but, thanks to the improved formability due to the warm conditions,

the FLDCRT value was lower than 1 and the feasibility of stamping of a sound component was then confirmed.

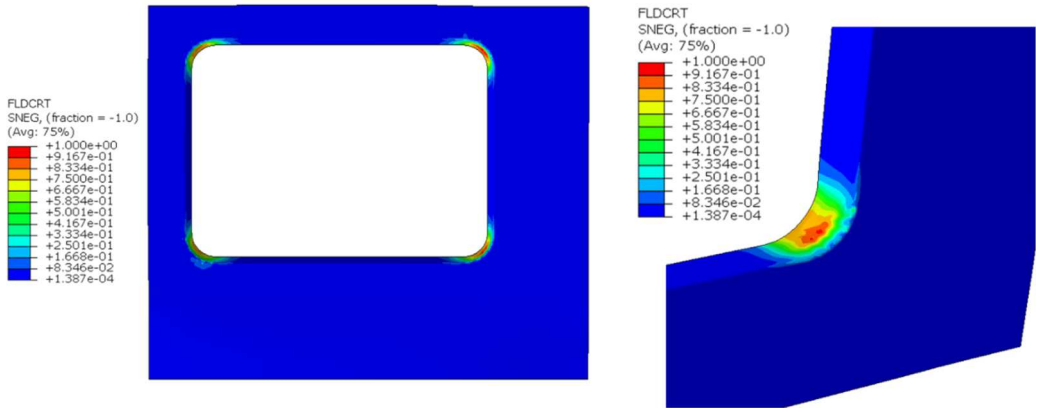

a) b)

Figure 63 Numerical stamping of the whole panel: a) FLDCRT distribution, b) detail of the corner region

As the final step, stamping trials were carried out for validation purposes adopting the blank geometry depicted in Figure 62c: a perfectly sound component was then obtained and its final appearance, after the powder coating, is reported in Figure 64a along with a detailed view of the corner regions (b and c).

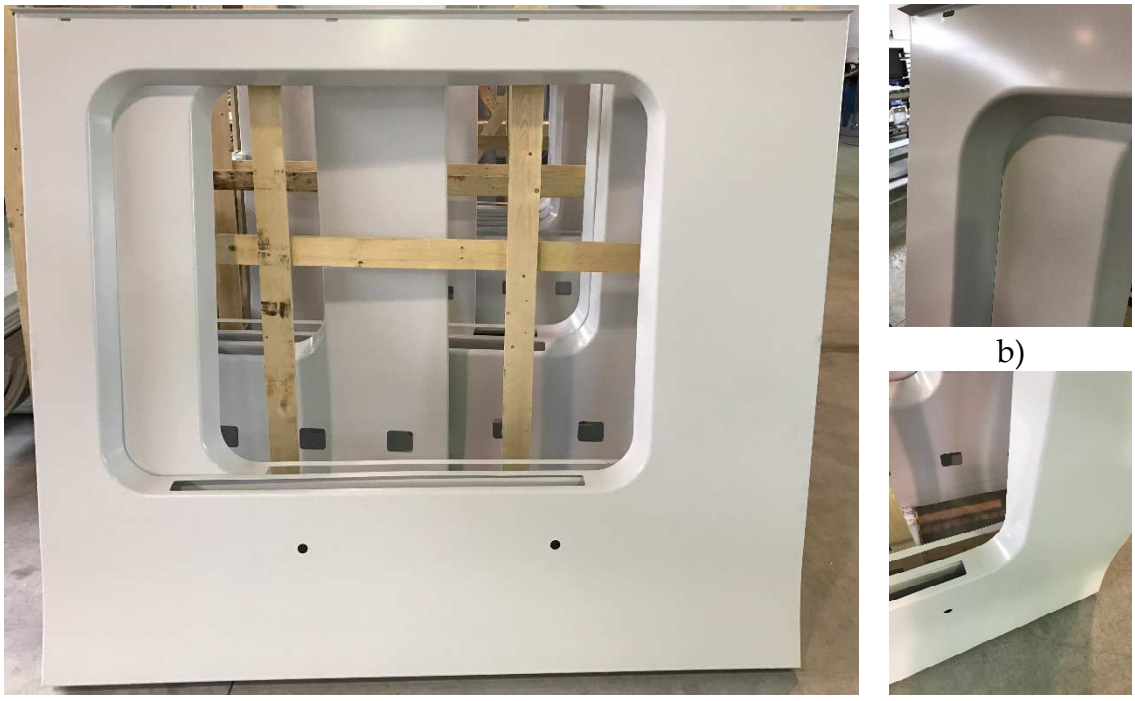

a) b) c)

Figure 64 Window panel: a) after the powder coating, b) and c) details of the angular regions

3.6 Improving the window panel final quality

The HDF approach has demonstrated its effectiveness making possible the stamping of a complex large-scale component in one step processing. The continuous research

to improve not only the process itself but also the final quality of the formed component moved the spotlight on another key aspect: the panel, during its exercise life, may come in contact with millions of passengers and may be damaged by uncontrolled movements or hit and scratched by luggage. For this reason, increasing its dent resistance was considered a good solution to improve the overall quality of the panel. Literature reports that the dent resistance is mainly related with the material yield point [83,84]: in the case of the investigated case study, it implied the design of the process starting from a blank with an initial pre-strain condition (AA5754-H32), which made the limited formability even more pronounced [115]. The results obtained from the stamping trials of the AA5754-H111 panel provided the starting point for the second investigation: tools temperature and forming speed were set for the preliminary stamping of the same prototype geometry this time adopting a blank in pre-strained state (AA5754-H32). As previously done, the blank was sprayed on both sides with graphite and the same heating time (600 s) was considered before starting the stamping operation; the NG#1 geometry (described in Figure 23a) was initially used for the experimental trials.

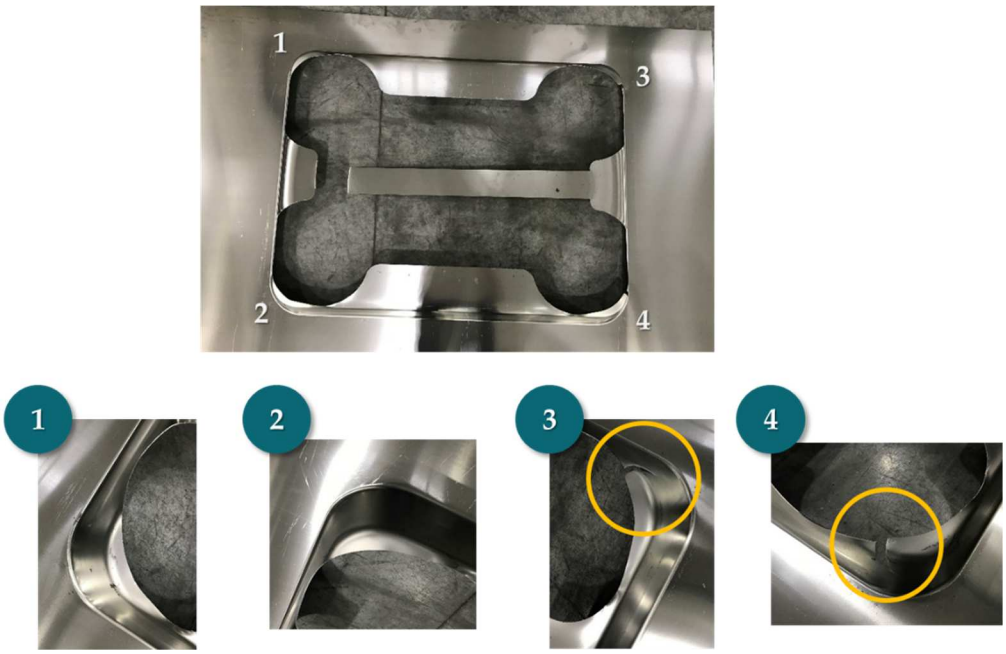

Figure 65 Preliminary experimental trials adopting a blank initially purchased in wrought conditions (AA5754-H32)

Results in Figure 65 suggested that, despite the optimized set of process parameters, the stamping resulted too critic and the rupture occurred in two of the four corner regions (indicated by the yellow circles). It was then concluded that the increased formability gained thanks to the warm conditions was not sufficient and the initial cold working of the material had a bigger influence on the outcome of the stamping. For this reason, the re-design of the forming process started from the preliminary material characterization. Dog-bone specimen extracted from the blank purchased in wrought conditions were subjected to uniaxial tensile tests at different temperature

and strain rates; in the case of the AA5754-H32, the temperature level of 300°C was also investigated.

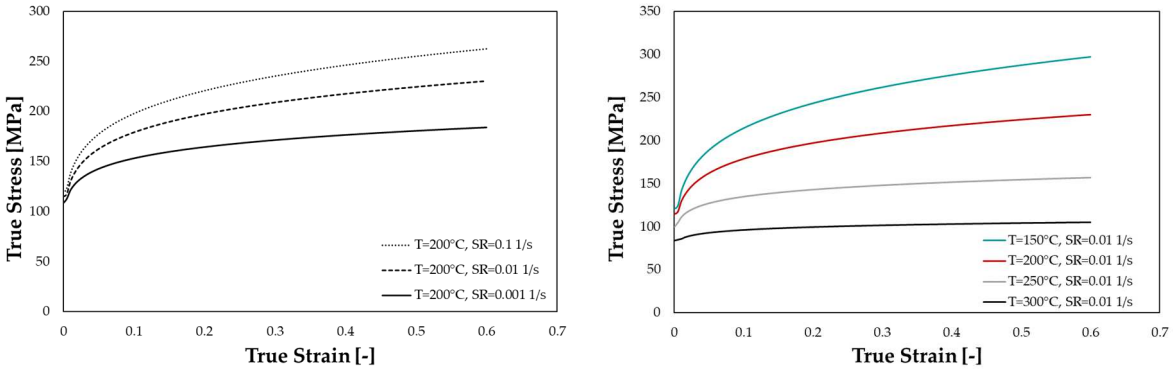

Figure 66 Tensile tests on AA5754-H32 specimens: effect of the strain rate (T=200°C), b) effect of the temperature (SR=0.01 1/s)

Results in Figure 66 show similar results to those reported in Figure 47 in terms of strain rate (a) and temperature (b) effect on the material behaviour. Evolution of the Young's modulus was considered not to be influenced by the initial cold working of the material. The formability limits, in accordance with the previous analyses, were assessed by means of Nakazima test at different temperature levels, setting the punch speed at 60 mm/min. Resulting FLCs in Figure 67 are compared with the forming limits of the same alloy in the annealing state (H111) showing how the formability of the material was remarkably influenced by the initial pre-strain even in warm conditions.

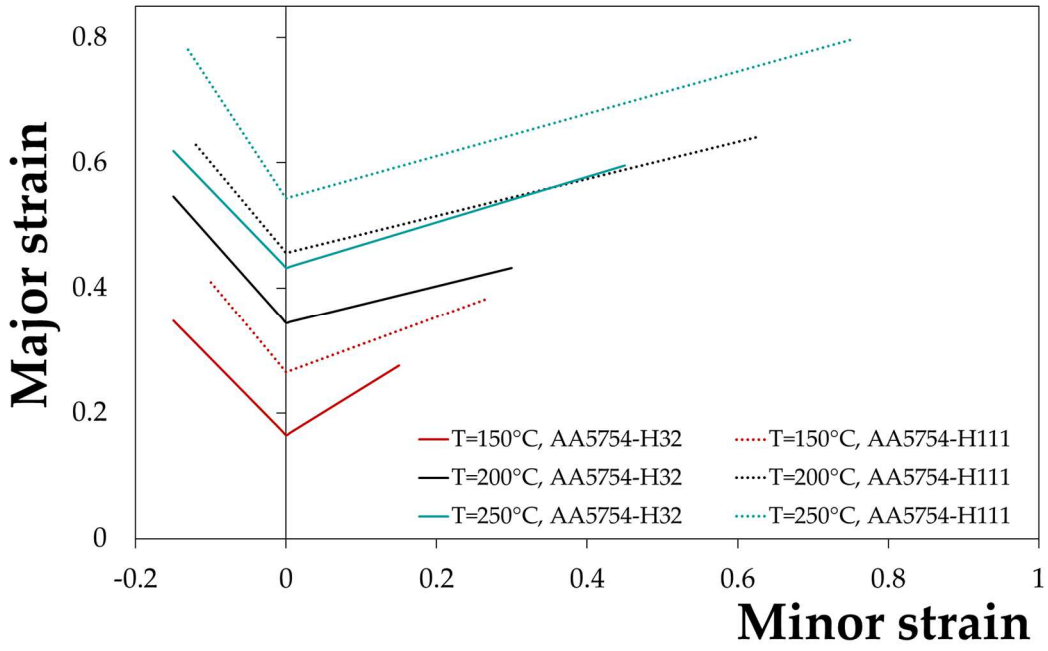

Figure 67 Comparison between forming limits of the AA5754 H32 (continuous line) and AA5754 H111 (dotted line)

The strain rate effect was accounted shifting the reference FLC at the investigated temperature levels by the same factor previously calculated (see section 3.1). If focussing the attention on the FLCs plotted in Figure 67, the formability of the alloy in wrought condition at 250°C (green bold line) was comparable to the one at 200°C but in the annealed state (black dotted line). It was then concluded that a further gain in the material formability was necessary, which could be achieved not only by re-optimizing the temperature distribution over the blank but also the re-defining the operative window of the stamping operation (for example, the forming speed). The same FE model discussed in section 2.3.3 was used simulating at first the blank heating at the end of which the final temperature distribution over the blank could be analysed. As done for the previous thermal simulations, the 2D3P configuration (2 active cartridges on the die side and 3 on the punch side) was modelled. Once again the UAMP user subroutine was used to model the feedback control, setting a higher target temperature both on the punch (370°C) and the one on the die side (170°C, since the maximum admitted temperature of the gas springs was a strict constraint not to be violated). The blank initial geometry labelled as NG#2 (introduced in Figure 23b) was considered for both the thermal run and the subsequent stamping simulations.

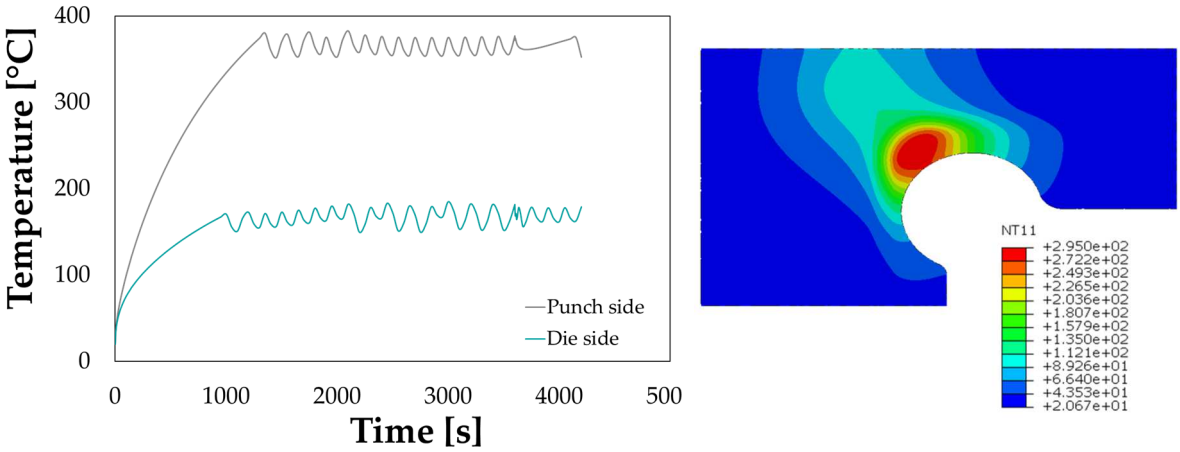

a) b)

Figure 68 Results of the heating simulation: a) final temperature distribution, b) time evolution of the tools temperature

Numerical results shown in Figure 68a confirmed that, with the 2D3P configuration, target temperature on both sides was effectively reached without increasing too much the time needed for the tools heating. The final temperature distribution at the end of the blank heating (Figure 68b) was then imported in the forming simulation as a predefined field; boundary conditions and load applied by the blankholder were kept exactly as the other simulations discussed in section 2.3.3, whereas the effect of the punch speed was investigated over two different levels, namely 60 mm/min (i.e. the optimal value for the stamping of the blank in the annealed state) and 20 mm/min.

ID	Punch speed [mm/min]	Cycle time [s]	FLDCRT distribution
2D3P-PS60	60	91	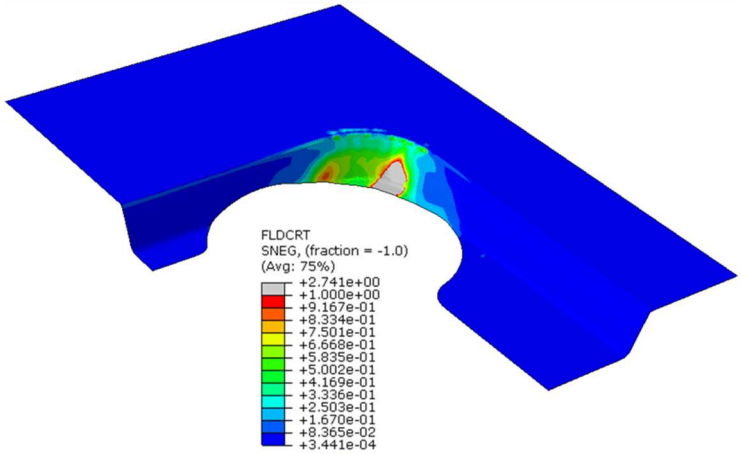
2D3P-PS20	20	277	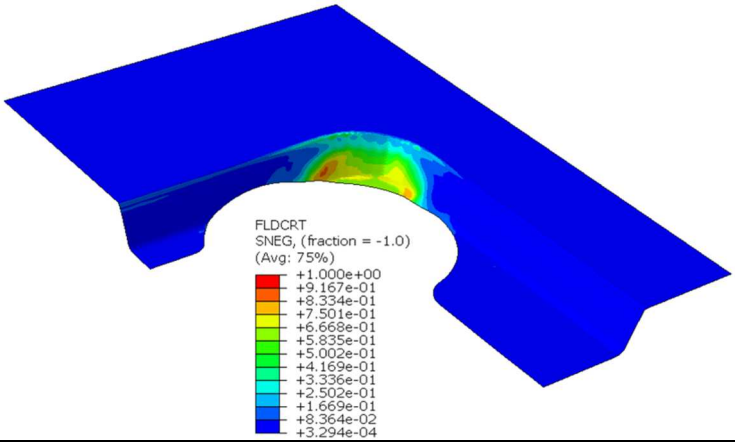

Figure 69 Forming simulation in warm conditions: final FLDCRT variable distribution

Distribution maps of the FLDCRT variable demonstrated that the beneficial effect in terms of material formability gained by the material thanks to the increase, on average, of the temperature were almost completely nullified if a too high punch speed was set: the occurrence of rupture in the critic region of the opening corner is highlighted by the presence of a wide grey area characterized by an FLDCRT value higher than 1 (Figure 69). Only the combination of the increased temperature in the blank deformation zone and a lower strain rate applied to the material (i.e. reducing the punch speed down to 20 mm/min) represented the working window for the manufacturing of a sound component. Experimental stamping trials were carried out to validate the prediction from the numerical model: as done in the previous activities discussed in the section 3.4, the numerical temperature distribution over the blank was compared with the acquisition of a thermal camera used to catch the temperature distribution of the blank at the end of the heating. The comparison along the path highlighted in the thermal picture (Figure 70) confirmed the accurateness of the

numerical model, being the simulated temperature distribution almost perfectly overlapped with the experimental acquisition.

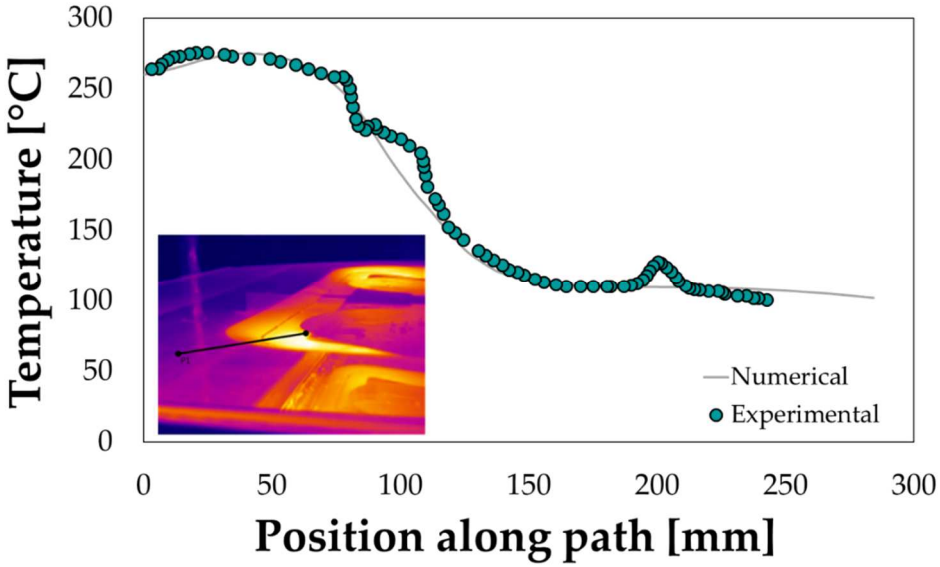

Figure 70 Validation of the thermal runs: experimental vs. numerical temperature distribution along the path

The simulated punch speed levels were then validated once completed the blank heating step. Experimental stamping (Figure 71a) confirmed that, despite the increased temperature on the blank deformation zone, rupture occurred in the corner regions (details are reported in Figure 71b and Figure 71c) when the punch speed was set at 60 mm/min.

a)

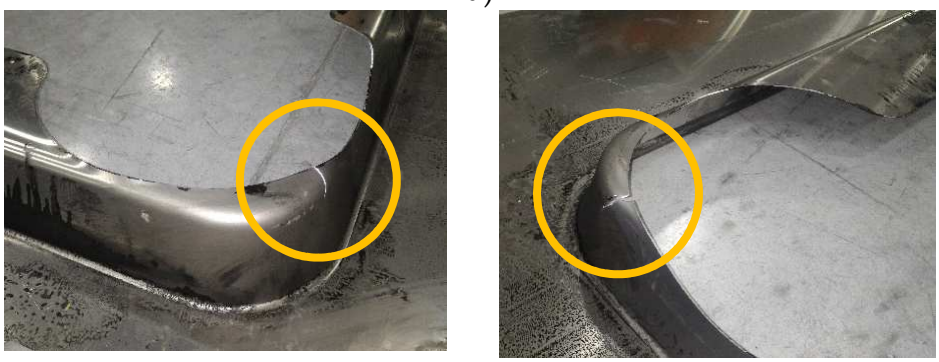

b) c)

Figure 71 Stamping trials: a) ruptured panel (v=60 mm/min), b) and c) detailed view of the occurrence of rupture in the corner regions

When decreasing the punch speed down to 20 mm/min, as predicted by the numerical simulations, the stamping of a sound component was finally achieved.

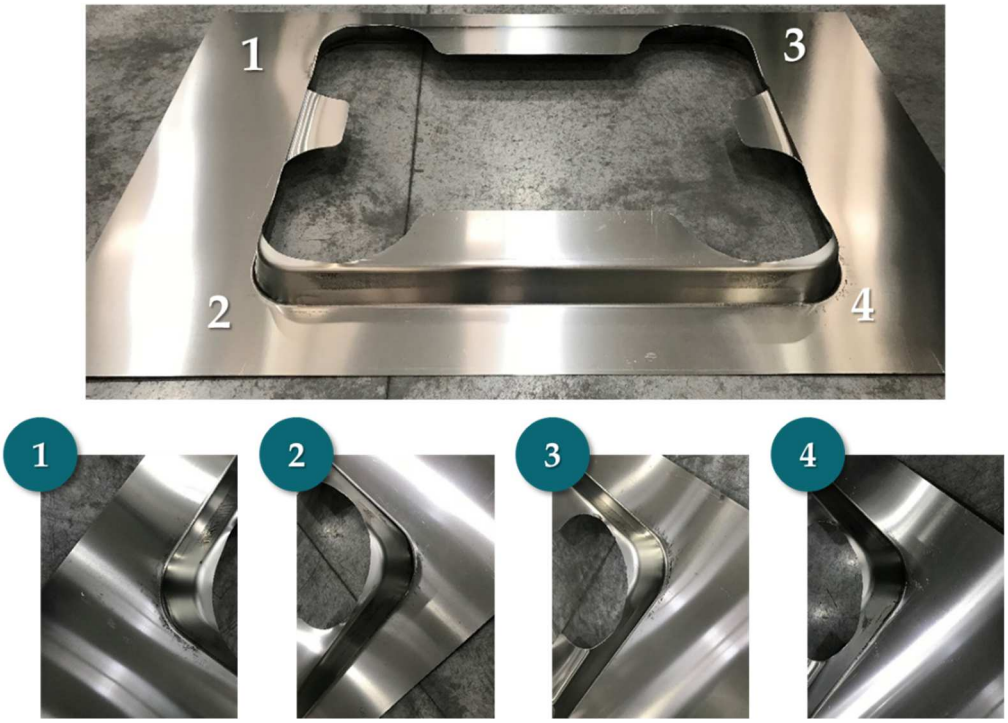

Figure 72 Stamping trial: sound component manufactured setting the punch speed at 20 mm/min

The formed panel, reported in Figure 72 along with the details of the corner regions where no rupture occurred, confirmed once again that only a combination of a proper distribution of temperature and a lower punch speed could create the optimal condition for a successful manufacturing of the final component, thus completely validating the accurateness of the FE process design.

3.7 Effect of the material initial conditions on the blank distortions

As introduced in the section 2.3.5, the final geometry of two window panels, respectively manufactured from (i) a blank in the annealed state (AA5754-H111) and (ii) in the pre-strain condition (AA5754-H32), was acquired by means of the HandyScan 3D laser scanner and the obtained point clouds were imported within the Geomagic working environment. The panels were positioned so that three of the four corner regions remained in contact with the ground, thus emphasizing the distortion on the remaining fourth one.

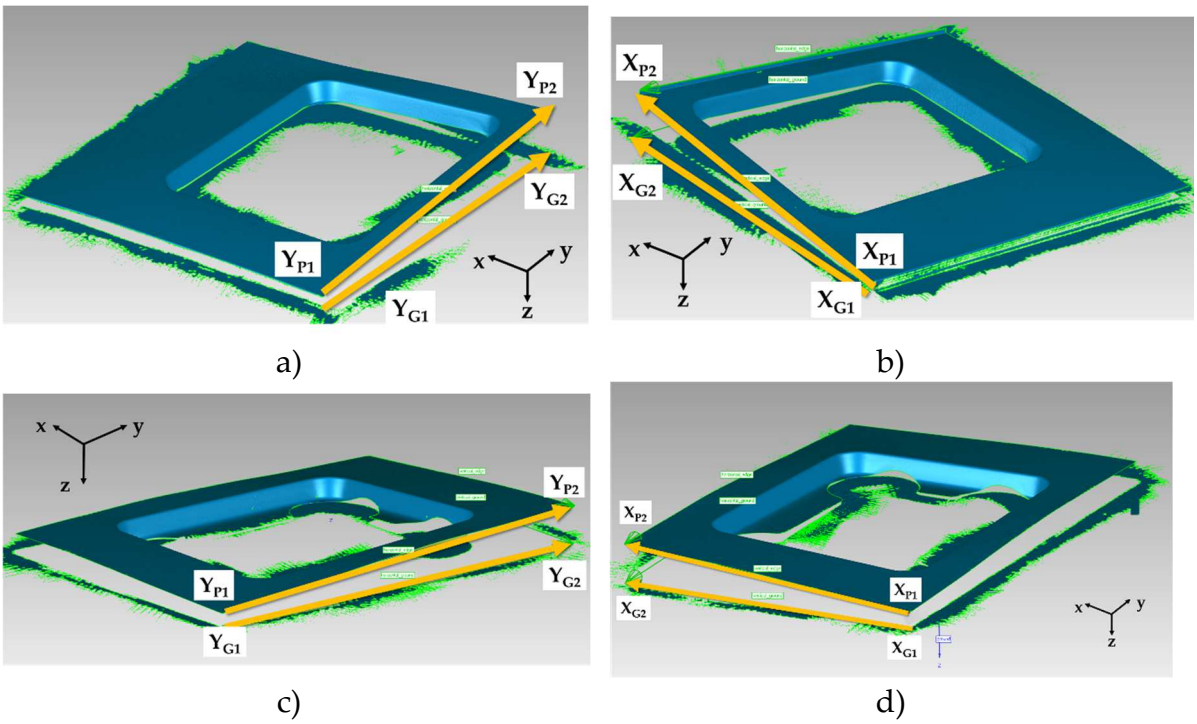

Figure 73 3D laser scanning : acquisition of the deformed edge a) on the yz plane and b) on the xz plane of the AA5754-H111 panel; acquisition of the deformed edge c) on the yz plane and d) on the xz plane of the AA5754-H32 panel

Once imported in the Geomagic environment, an origin point located on the ground was initially defined. The panel distortion were calculated focussing the attention on the deformation of two main orthogonal edges. As shown in Figure 73a, a vector lying on the ground plane was created connecting the two points labelled as Y_{G1} and Y_{G2} (where the subscript G refers to "ground") whereas the two vertices of the blank deformed edge were connected by a second vector (between Y_{P1} and Y_{P2}, with the subscript P standing for "panel"). The measure of the distortion of the panel in the yz principal plane was expressed in terms of the angle between the two created vectors (α_{yz}). The same approach was repeated, as shown in Figure 73b, to evaluate the distortion of the orthogonal edge lying on the xz plane by means of the calculation of the α_{xz} angle. The same approach was adopted also to evaluate the distortion of the second panel. If looking at the bar chart in Figure 74, the angular measurements as an indicator of the panel distortion shows that a better correspondence with the designed geometry could be obtained increasing the initial yield point of the material. It has to be underlined that the advantage in terms of better precision of the final geometry – i.e. the panel is characterized by better fitting coupling during the train car assembly – has to be balanced with the increase in the cycle time, due at first to the increase in the tools target temperature and then to the reduction of the punch speed.

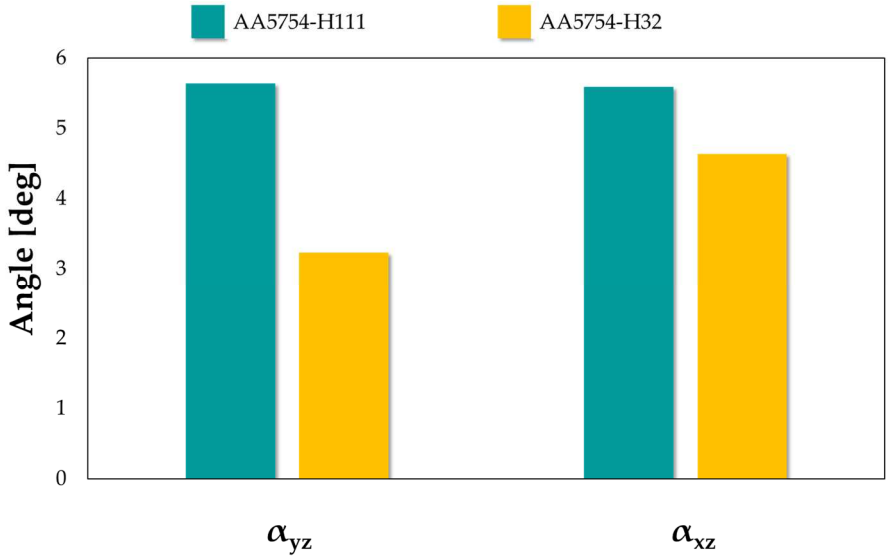

Figure 74 Effect of the initial blank conditions on the panel distortion

4. The “Heating Before Forming” approach

4.1 The "Heating Before Forming" on the deep drawing process

The present chapter resumes the main results regarding the HBF approach applied at the conventional deep drawing process for the manufacturing of a simple geometry like a cylindrical cup.

4.1.1 AA6082 behaviour at room temperature

As previously explained, the tuning of the SHT was accomplished by the physical simulation capable of providing several information from a single experiment. Tests were carried out setting the temperature at the TC2 location equal to 540°C for a holding time equal to 2100 seconds; at the end of the heating, specimens were cooled down with forced air and maintained at room temperature. Evolution of the natural ageing was monitored by means of Vickers hardness measurements (three replications per each test), at regular time intervals, along the longitudinal symmetry axis of the specimen (Qness micro hardness tester Q10 A+, setting a load of 200 g and a dwell time of 15 s). Measured values were then plotted as a function of the heating temperature, calculated in each point of the specimen longitudinal axis being known the analytical formulation of the parabolic distribution.

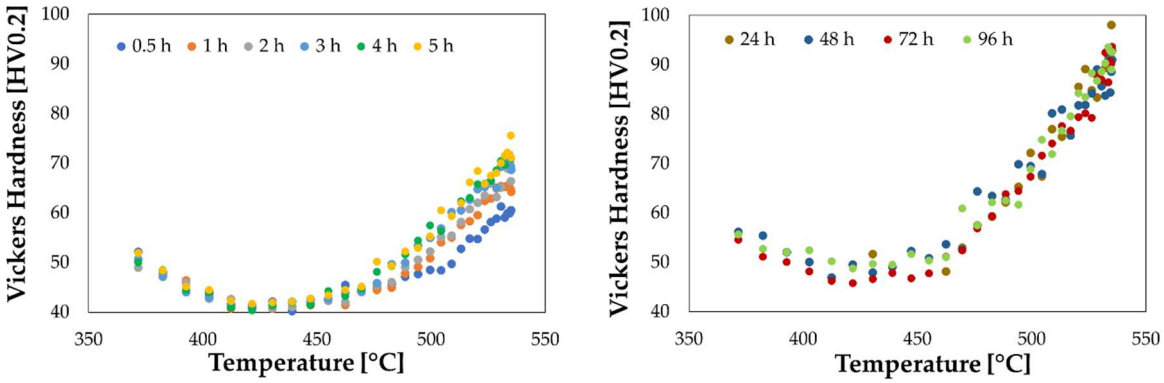

Figure 75 Evolution of the natural ageing phenomena: a) from 30 mins to 5 hours; b) from 1 to 4 days

As shown in Figure 75a, a not negligible increase in the material hardness was found in the region near the TC2 thermocouple (heating temperature of 540°C): the measured values after 0.5 hours resulted to be in accordance with the results proposed by Cuniberti et al. [116], who reported an average material hardness approximately equal to 55 HV in the full SHT condition. As a further confirmation, the physically simulated cycle time at the TC2 position (540°C for 2100 s) was comparable with data reported in literature [116,117]. It was also concluded, as it can be seen from the hardness distribution in Figure 75b, that after 24 hours the natural ageing phenomena saturated almost completely (in the TC2 region, the final hardness was almost twice higher than the one after 0.5 hours of natural ageing). Characterization of the material behaviour was then accomplished by tensile tests investigating: (i) the T6 purchasing

conditions and (ii) the more formable SHT after subjecting the samples to the tuned heat treatment (2100 s at 540°C).

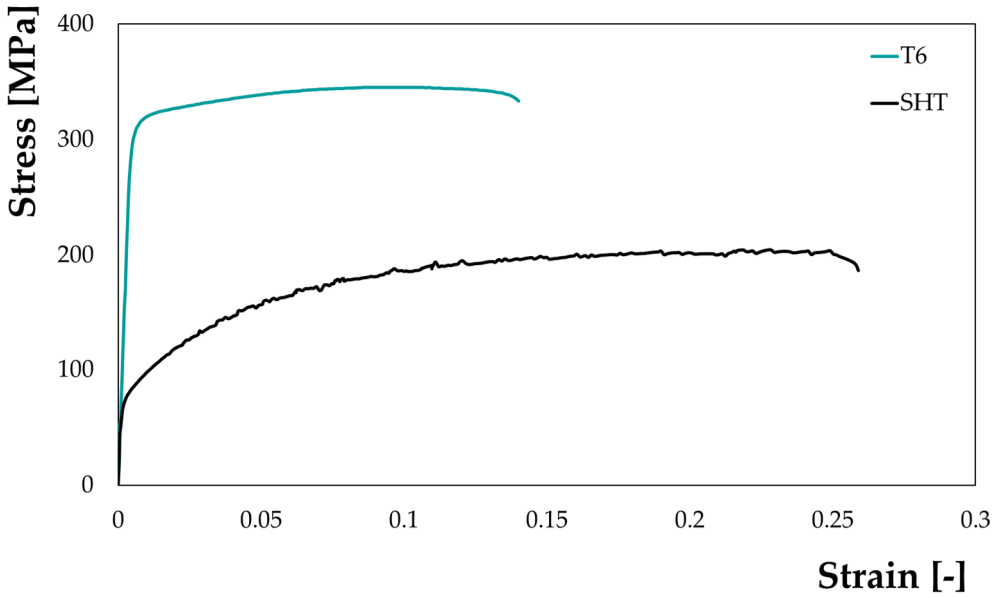

Figure 76 Stress strain curves at room temperature from the uniaxial tensile tests

Results from the tensile tests are reported in terms of stress-strain curves in Figure 76: the SHTed specimen (black bold curve) exhibited a sensibly higher elongation at failure but lower resistance (characterized by a yield point around 70 MPa). The purchasing T6 condition, on the other hand, showed a higher mechanical resistance (yield point higher than 300 MPa) with a very limited elongation at failure (less than 0.15). Material behaviour in the SHT condition was characterized by a serrated flow: literature reports that, immediately after quenching, solute atoms are randomly distributed in solid solution in the Al matrix and interact with dislocations via a Cottrell cloud mechanism [118] assisted by a high vacancy concentration, leading to the observed serrated behaviour in Figure 76. With the proceeding of the natural aging, the solute atoms and vacancies form clusters, reducing the solute quantity in solid solution, thus explaining why the serrations disappeared in the T6 state. As regarding the strain behaviour from formability tests, Figure 77 clearly confirms how the peak hardening conditions remarkably limited the material formability if compared to the material behaviour in the SHT condition (all the tested Nakazima specimens were at first subjected to the heat treatment in furnace and then water quenched to obtain the SSSS condition at room temperature).

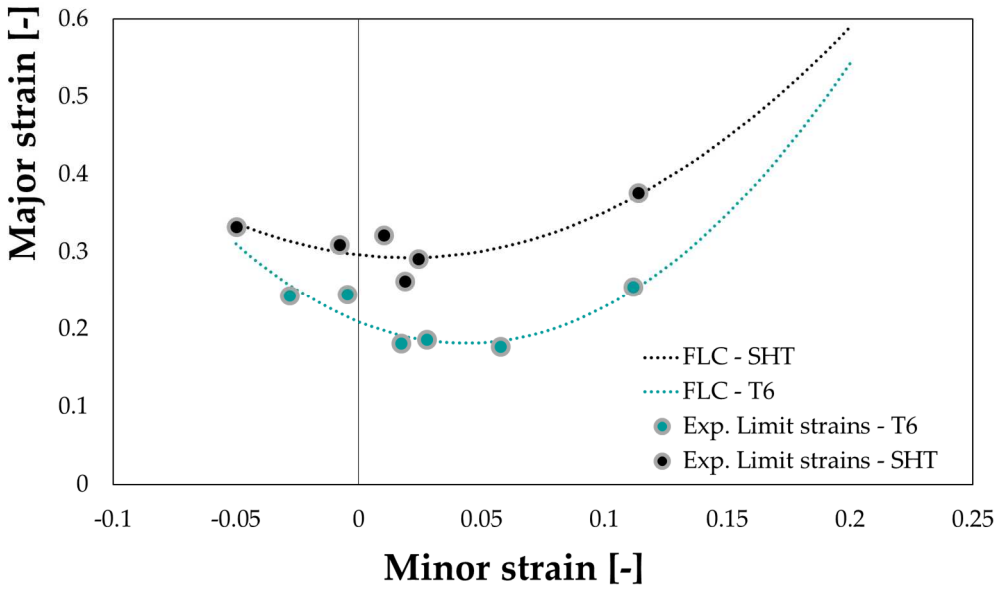

Figure 77 AA6082 Forming Limit curves

As anticipated in section 2.4.1, the characterization step was completed with the uniaxial tensile tests of the specimen after being laser heated. Being the specimen ends continuously in contact with the cooler, a parabolic distribution of temperature evolved during the heating and, for this reason, each point of the specimen experienced a different thermal history. The uniaxial tensile test was carried out setting a crosshead speed of 0.1 mm/s and an acquisition frequency of the DIC cameras equal to 1 Hz. In the post-processing step, the local strain evolution was monitored in several points of interest, located: (i) in correspondence of the spot geometrical centre (labelled as *Centre* in Figure 78a), (ii) at one quarter of the spot dimension (labelled as Quarter in Figure 78a), (iii) at the end of the laser heated portion (labelled as *Spot* in Figure 78a), (iv) at four points located in the transition region immediately after the treated region with a step of 1.6 mm (labelled as *T1, T2, T3, T4* in Figure 78b) along the longitudinal axis of the specimen and (v) far from the treated region where the material was supposed to have maintained its initial conditions (labelled as *MB* in Figure 78b).

a)

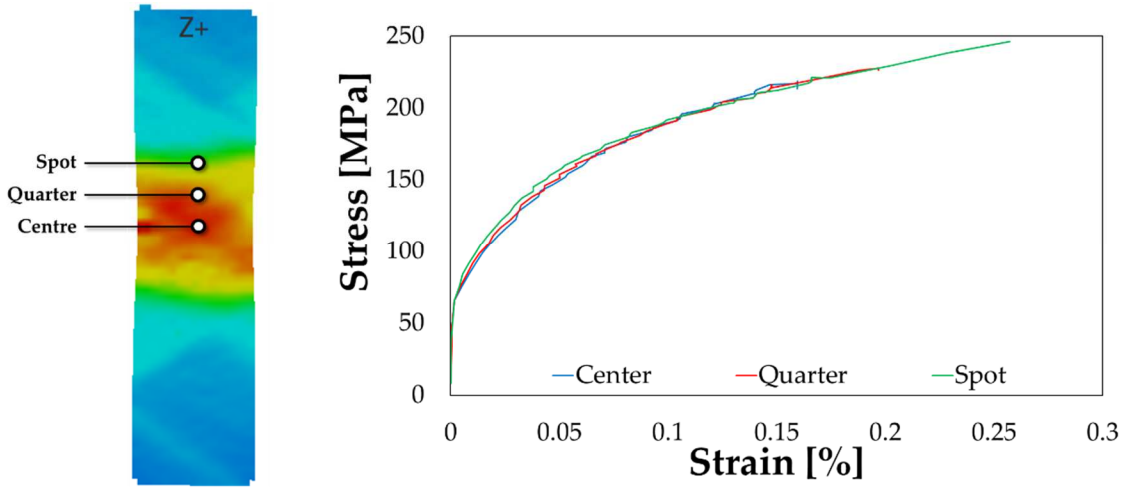

b)

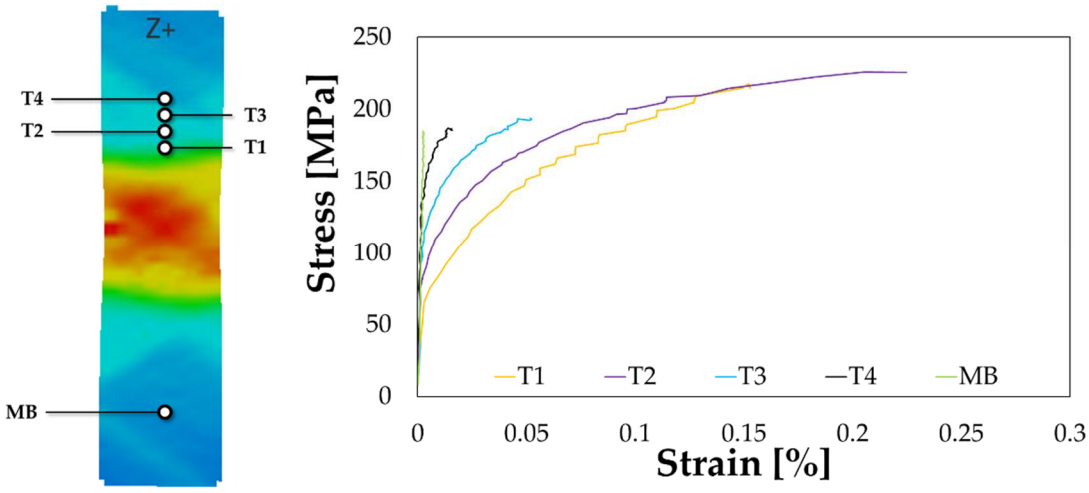

Figure 78 Uniaxial tensile test on the LHT specimen: flow curves from a) the irradiated portion and b) from the transition region and base material

For the sake of clarity, the calculated flow curves have been grouped in two different plots: Figure 78a demonstrates that the whole portion irradiated by the laser beam was uniformly solutioned, being the curves perfectly overlapped. On the other hand, moving through the transition region from the treated portion to the base material, the solutioning was less effective and, as shown in Figure 78b, the material behaviour was characterized by progressively higher resistance; if focussing the attention on the curve at the MB location (light green curve in Figure 78b), no yielding point could be distinctly identified suggesting that the material remained in the elastic region. Results in Figure 79 were further supported when plotting the yield stress of the monitored points as a function of their position along the specimen longitudinal axis.

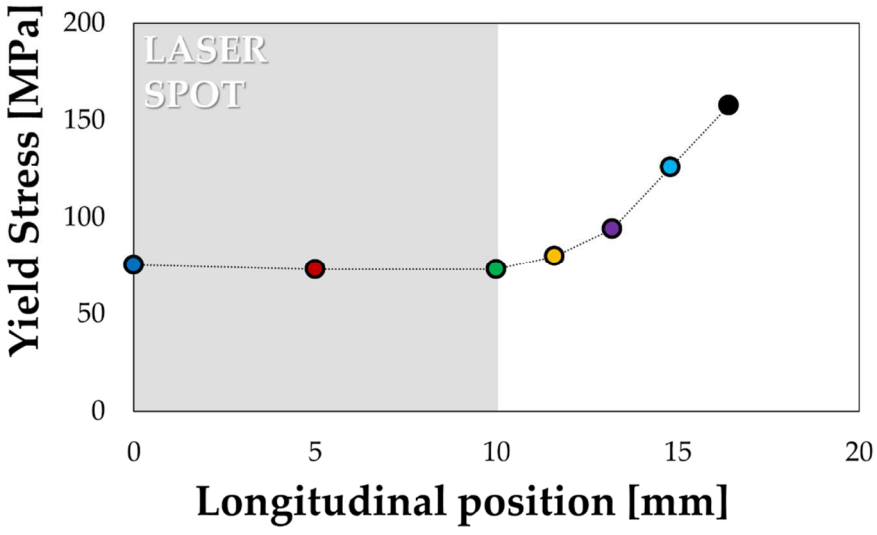

Figure 79 Distribution of the material yield stress along the specimen longitudinal axis

Yield stresses calculated within the treated region (grey box in Figure 79 refers to half spot, being the position 0 coincident with the spot geometrical centre) showed a good accordance (70 MPa) with the results of the uniaxial tensile test on the full SHTed specimen (Figure 76), while the transition region interested approximately 7 mm. The

experimentally determined FLCs (Figure 77) and local flow stress curves (Figure 78, a and b) were implemented within the FE model necessary to complete the subsequent step of the process design.

4.1.2 Solution Heat Treatment via local laser heating

As anticipated in section 2.4.1, the laser heating of the dog-bone specimen, besides being carried out for the characterization purposes, was useful to properly define the thermal boundary conditions – i.e. the heat transfer coefficients and the coefficient of absorbed radiation – of the FE model. The results of the inverse analysis (Figure 80), in terms temperature curve comparison, demonstrates the good correspondence between the numerical and the experimental analysis. In addition, if recalling the results in Figure 78a, the laser heating was effective in solutioning the material in the radiated portion of the specimen.

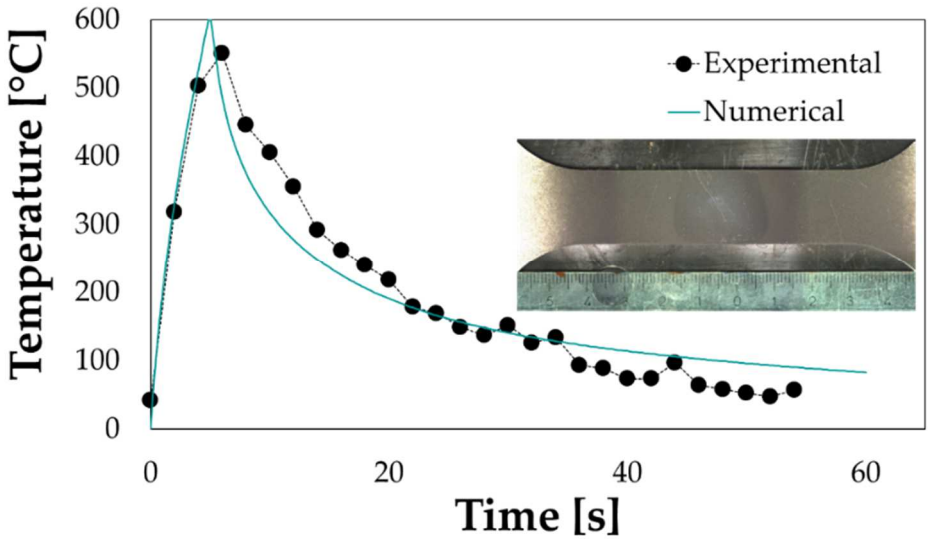

Figure 80 Tuning of the FE thermal model (the detailed view of the treated specimen is also reported)

The optimized boundary conditions were then transferred on the FE model to design the laser heating of the flange portion of the circular specimens to be subsequently drawn at room temperature. The laser heating of a 102 mm diameter specimen was again simulated, setting the FR parameter at 4 mm/s since that value could ensure a time interaction between the material and the laser radiation – the dwell time, calculated by the ratio between the spot dimension and the feed rate – comparable to the one investigated during the laser heating of the tensile specimen. The movement of the laser spot along a circular path was implemented by means of a DFLUX user subroutine written in Fortran language.

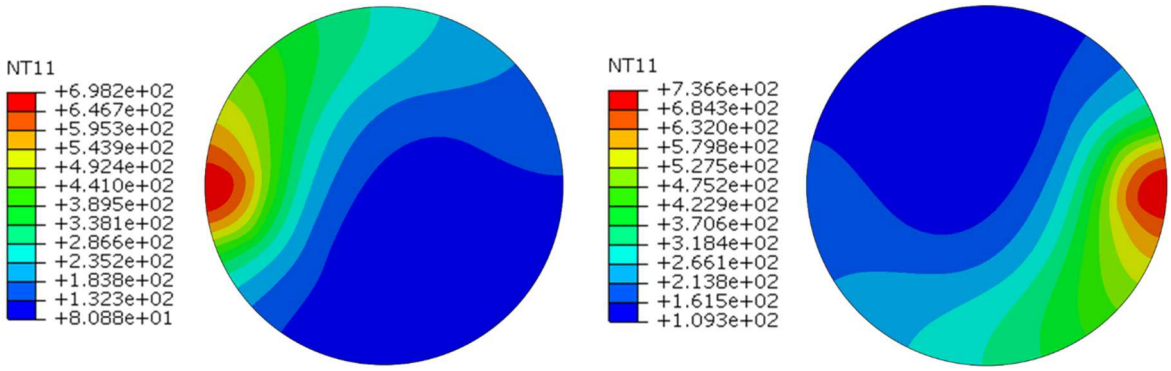

a) b)

Figure 81 LHT numerical simulation (FR=4 mm/s): temperature distribution after a) half and b) at the end of the heating

Numerical results suggested that, since the heat could be dissipated only along the inward direction, the heating conditions resulted more critical than in the case of the dog-bone specimen: in fact, after completing half of the circular path (Figure 81a), the temperature already overcame the alloy melting temperature; as expected, the temperature reached at the end of the heating (Figure 81b) was even higher, suggesting that the simulated FR value had to be increased. For this reason, the same laser heating was simulated again, increasing the FR value up to 10 mm/s; the same operative conditions were experimentally replicated for validation purposes. A good correspondence between the numerical temperature evolution and the acquisition from the two thermocouples (TC1 and TC2, as described in the section 2.4.4) was obtained as shown by Figure 82a and Figure 82b.

a)

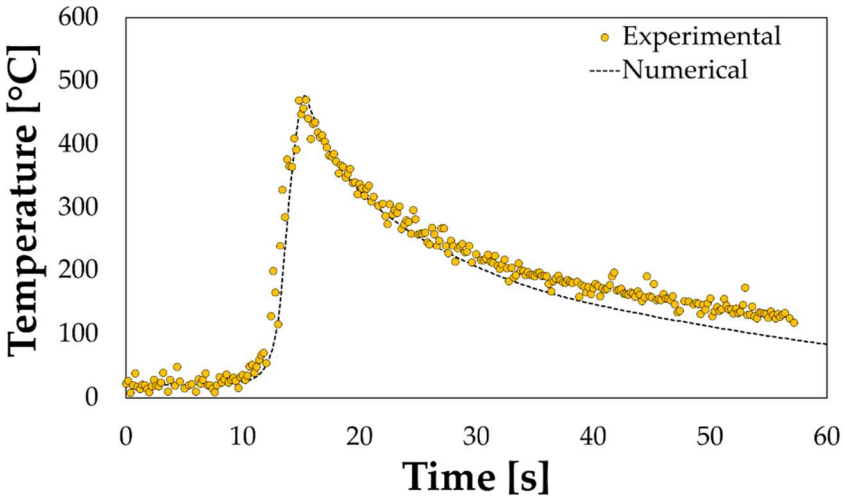

b)

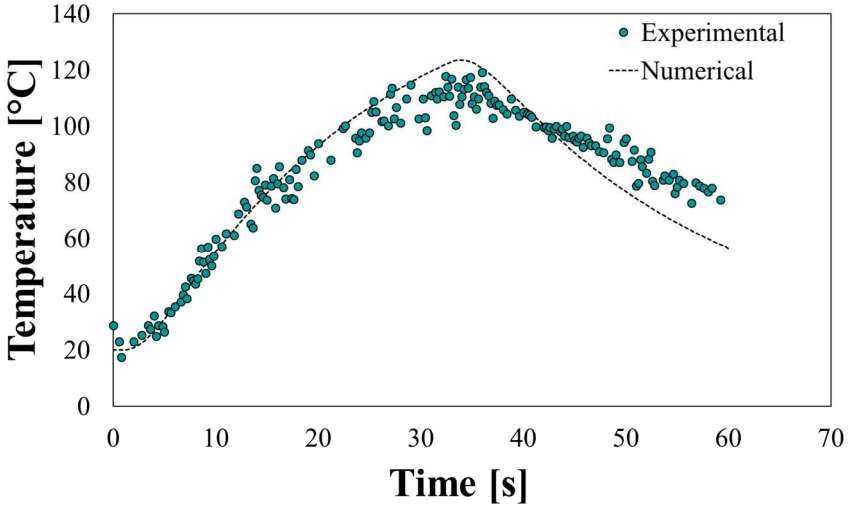

Figure 82. LHT of the circular blank: numerical vs. experimental comparison at the a) TC1 and b) TC2 locations

In addition, the temperature distribution over the blank was monitored with a FLIR x6540sc thermal imaging camera; after the cooling down to room temperature, the specimen was immediately subjected to a series of hardness measurement along a radial path (indicated as *Line 1* in the thermal picture detailed in Figure 83a) to evaluate the effectiveness of the laser treatment.

a)

b)

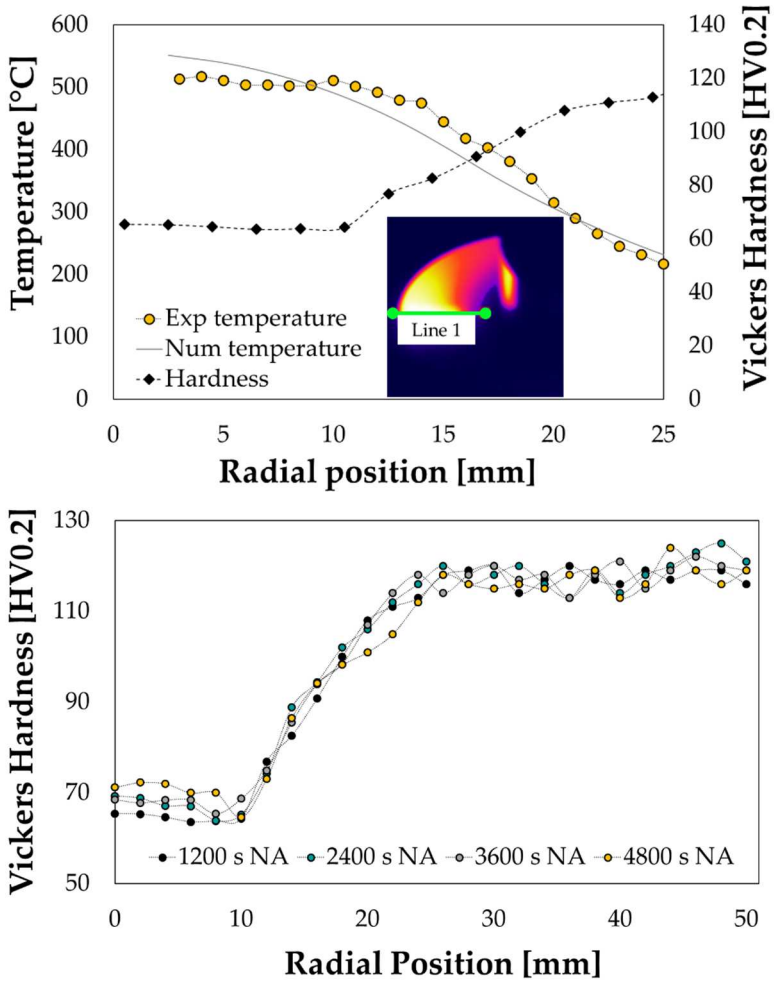

Figure 83 LHT on circular specimen: a) hardness measurement and b) progress of the natural ageing

The camera acquisition suggested that (i) the temperature across the portion irradiated by the laser beam (the *0* radial position was approximately on the blank outer diameter) was quite uniform and close to 500°C, in good accordance with the numerical results shown in Figure 80, and (ii) the laser heating was effective being the hardness values in the treated region comparable to the data reported in literature [116] and sensibly lower than those measured closer to the blank centre (kept in the T6 condition thanks to the continuous contact with the cooler). Moreover, as shown in Figure 83b, the gradual increase of the hardness within the first 10 mm (up to more than 70 HV after an exposure of 4800 s at room temperature) was an undeniable evidence of the natural ageing (NA) occurrence. According to the obtained results, all the local laser heating for the deep treatments were carried out setting a constant laser beam equal to 750 W and the FR parameter at 10 mm/s.

4.1.3 Preliminary deep drawing tests at room temperature

Preliminary deep drawing tests were carried out to evaluate the limits in terms of formability of the two investigated material conditions, i.e. the T6 and the SHT. All the carried-out tests were monitored in terms of punch load-stroke curves, useful to evaluate the influence of the main process parameter on the outcome of the drawing.

a)

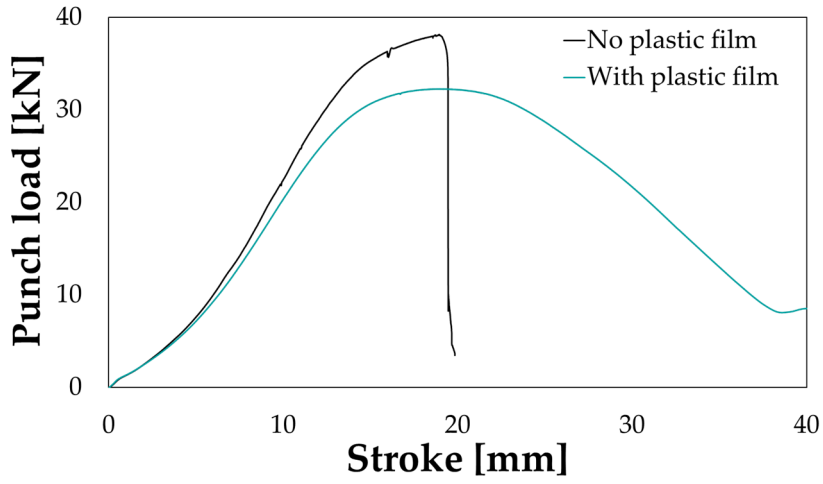

b)

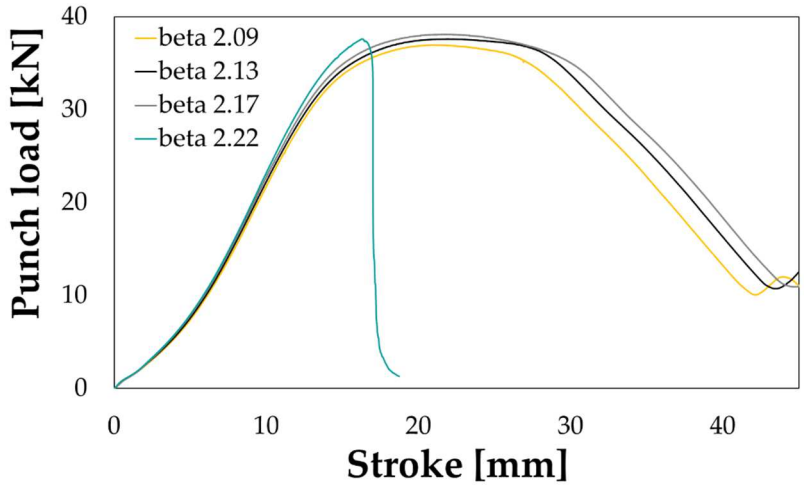

c)

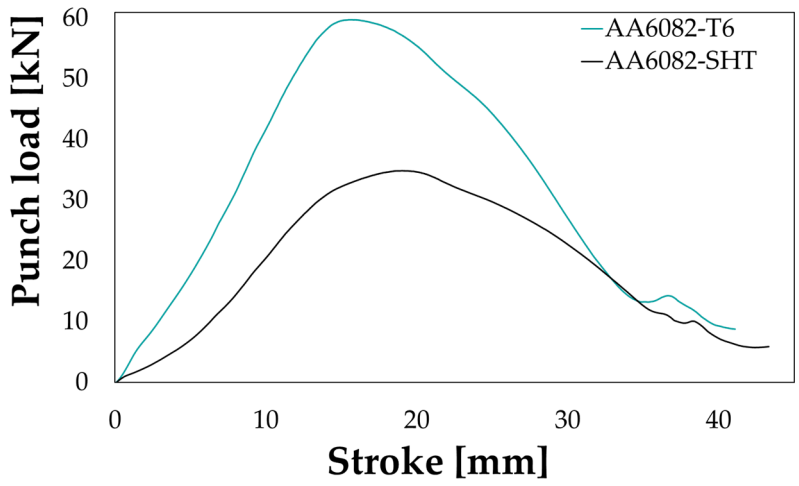

Figure 84 Punch load-stroke curve: effect of a) the friction coefficient (D = 92 mm, BHp = 1.5%, SHT condition), b) the initial blank diameter (SHT condition, BHp = 1%) and c) the initial material condition (D = 88 mm, BHp = 1.5%).

The interposition of the plastic film (green curve), as shown in Figure 84a, was effective in reducing the friction forces generated during the sliding, making possible the correct drawing of a 92 mm diameter blank in the SHT condition (BHp equal to 1.5% of the material yield stress): in fact, in the case of the "bare" contact between the blank and the die and although surfaces in contact were previously lubricated, not only the load applied by the punch during the drawing (black curve) increased more rapidly but also the rupture occurred as indicated the sharp drop of the load approximately after 20 mm stroke. The effect of the initial blank diameter was in accordance with the theory and is reported in Figure 84b: when setting the same friction condition (interposition of the plastic film) and the same BHp level (1% of the material yield stress), the peak value of the load curve increased with the β parameter, defined as the ratio between the initial blank diameter and the punch diameter; when increasing too much the initial diameter, the strain condition became too critical and the rupture occurred (green curve labelled as *"beta 2.22"*). As expected, the initial material conditions had a big influence on the drawing of a 88 mm diameter blank (see comparison in Figure 84c): if setting the same friction conditions (plastic film in both tests) and applying the same BHp (1.5% of the yield stress), the peak load needed to successfully draw the material in the T6 conditions was almost twofold higher than the one needed to draw the material in the SHT conditions. Results of the preliminary deep drawing tests were arranged in β – BHp plots and are reported in Figure 87: green dots refer to sound drawn component, while red crosses to the ruptured cups.

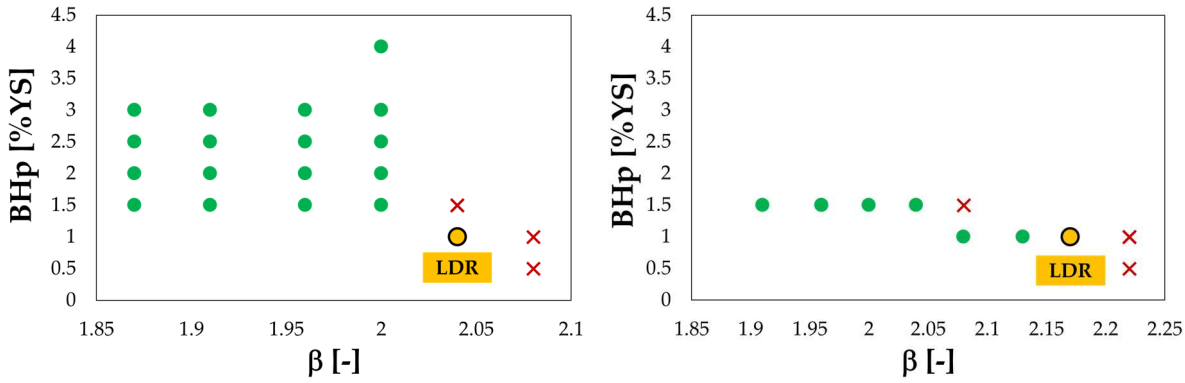

Figure 85 AA6082 experimental deep drawing tests: a) T6 and b) SHT condition

In the case of the T6 condition, it can be noted that, for β values lower than 2, the applied BHp had a negligible influence on the process outcome: the achieved LDR was slightly higher than 2 in accordance with data reported in literature [13,119]. On the other hand, the achieved LDR increased in the SHT conditions (around 2.2) thanks to the improved material formability.

4.1.4 Results from the process optimization

To improve the model accurateness, as mentioned in the section 2.4.2, the friction coefficient for the contact pair blank/tools (die and blankholder) was calculated via an inverse analysis approach, minimizing the error between the experimental punch load-stroke curve coming from an experimental deep drawing test; the best agreement between the numerical and experimental data was reached for a value of the friction coefficient equal to 0.11 (dotted black curve in Figure 86).

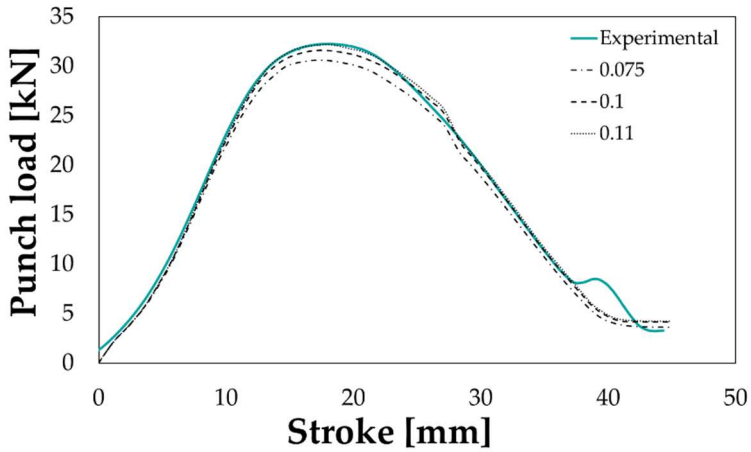

Figure 86 Calibration of the friction coefficient via inverse analysis

The resulting workflow coming from the proper definition of both the input and the output variables of the problem is shown in Figure 87: the created optimization tool was built up combining the *Process Flow*, containing all the possible sequences of actions and conditions necessary for the optimization to proceed (integrating third-party software and logic nodes), and the *Data Flow*, managing what type of data

should be transferred from one step to the other (by means of variable, buffer and file nodes).

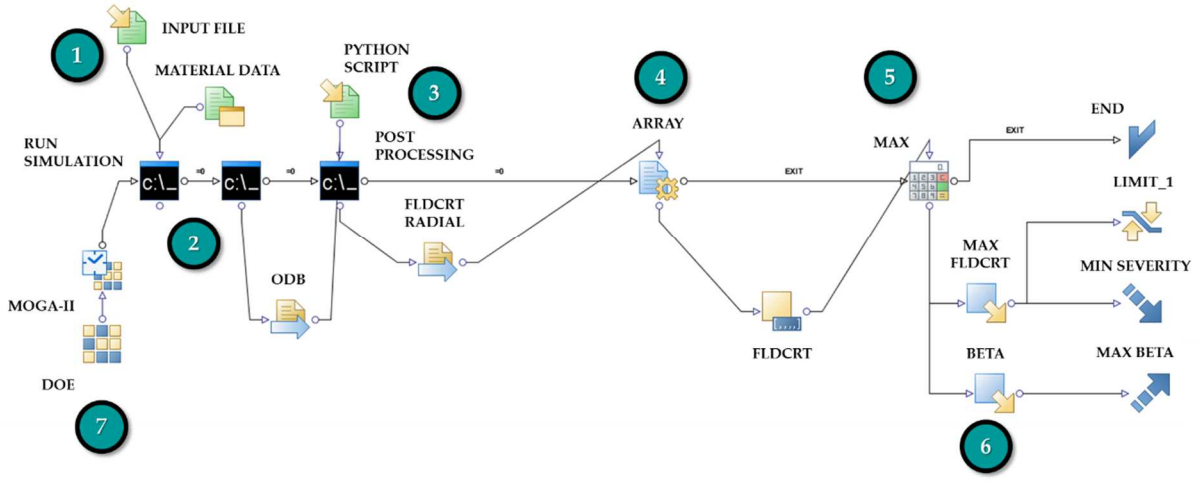

Figure 87 modeFRONTIER design environment for the optimization procedure

The initial blank radius, and the extent of the blank portion in the purchasing (T6) conditions, indicated in Table 7 as R and L_{T6} respectively, were defined as the input variables of the problem along with their variation ranges.

Table 7 Definition of the input variables and their variation ranges

Input Variable	Lower Bound (LB)	Upper Bound (UB)
L_{T6} [%]	5	65
R [mm]	45	60
BHp	Constant and equal to 1.5% of the material yield stress	

Workflow nodes containing the information about the input parameters are not depicted in Figure 87 for the sake of clarity; it should be underlined that, since known the mesh dimension (0.5 mm), the initial and the final node of the blank portion to be modelled in the T6 condition could be determined for each value of the L_{T6} parameter contained in its variation range. Accordingly, the initial and final node of the transition region was determined as well as the last portion of the blank modelled in the SHT condition whose last node was a function of the initial blank radius.

Once defined the value of the inputs at the beginning of each numerical run, the created input file (zone #1 of the workflow) together with the material data file (containing flow curves and FLCs as a function of the field variable) were connected with three different DOS nodes in series (zone #2 of the workflow), whose role was to run the simulation, move the results file (using a transfer node file labelled as *ODB* in Figure 87) in a separate folder and prepare it for the post processing step via a python script file (zone #3 of the workflow).

Results extracted from every single run in terms of distribution of the FLDCRT output variable (the formulation of the variable has been previously described in Figure 51a, section 2.3.1) along the radial direction were written on a text file and transferred to the Output Template node (*ARRAY* node in the zone #4 of the workflow) by means of

a transfer file (*FLDCRT RADIAL*): the FLDCRT values were stored as components of an array and sent to the Calculator node (*MAX*) by means of a buffer node (*FLDCRT*). The calculator node (zone #5 of the workflow) contained the definitions of the two output variables, i.e. the maximum value among the components of the FLDCRT array and the β value. As it can be seen in the zone #6 of the workflow, each of the defined output variables was connected to an objective function so that the optimization procedure globally aimed at maximizing the β value (objective node *MAX BETA*), while minimizing the occurrence of rupture (objective node *MIN SEVERITY*); on this second output variable, a constrain node (labelled as *LIMIT_1*) was added to better drive the optimization toward more feasible results.
Zone #7 of the workflow in Figure 87 contains the two nodes (DOE and Scheduler) where the main settings of the optimization algorithm could be defined: in particular, the initial population was created by means of the node labelled as *DOE* adopting the Sobol algorithm, a deterministic sequence characterized by a sensible reduction of the clustering effect and able to fill the design space in a uniform way (in fact it is included in the category of the "space filler" algorithms). Among the available Scheduler algorithms, the multi-objective genetic algorithm MOGA-II was selected for the optimization search: the algorithm attempted a total number of evaluations equal to the number of individuals of the DOE table (the initial population) multiplied by the number of generations (in this specific case, the stop criterion in Figure 34 was based on the generation and analysis of the whole number of individuals) [101,102].For the specific optimization procedure here discussed, the total number of evaluations was equal to 400 being the initial population based on 20 individuals and the number of successive generations was set equal to 20. Results of the optimization procedure were then analysed in terms of history charts, useful to monitor the evolution of the defined input variables as the optimization proceeded: feasible designs are indicated by a green circle while unfeasible designs – i.e. those violating the constraint applied on the *MAX FLDCRT* output variable – by red triangles.

a)

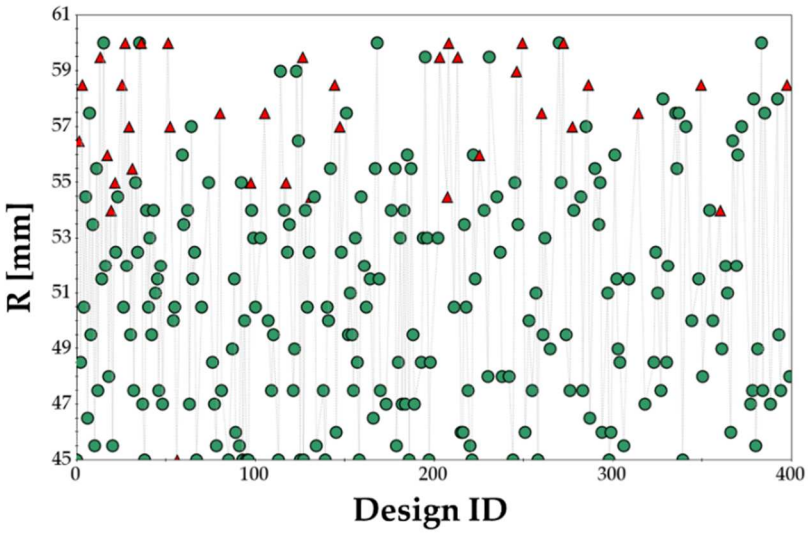

b)

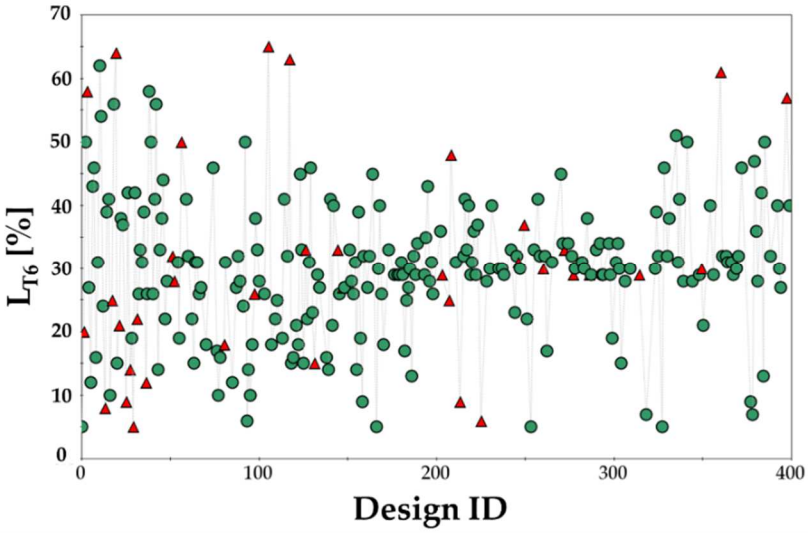

Figure 88 Results of the optimization procedure: history chart of the input parameter a) R and b) L_{T6}

According to the chart in Figure 88a, the optimization predicted a maximum initial diameter that could be drawn without the occurrence of rupture equal to the upper bound of the R variable (60 mm): an LDR value of 2.61 was then predicted, being such a value remarkably higher (more than 20%) than the limits experimentally achieved in both the material conditions.

It is worthy of notice that, as shown by the history chart in Figure 88b, most of the created feasible designs was characterized by a value of the L_{T6} parameter ranging from 30% to 40%. Such a consideration was even more evident if filtering the optimization results arranged in a the parallel coordinate chart, where each design is represented by a broken line connecting the input variable (or more than one) to the defined outputs, as shown in Figure 89: if an LDR value higher than 2.17 (the limit reached in the SHT conditions, see section 4.1.4) had to be achieved and the strain severity had to be kept below the tearing condition (thus below the FLC), the portion to be preserved from the heat treatment had to cover at least 35% of the whole blank.

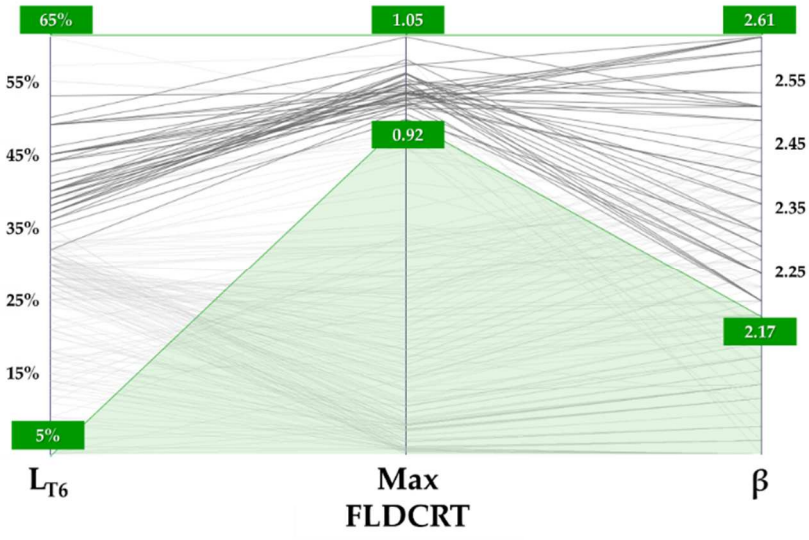

Figure 89 Optimization results: parallel coordinate chart

4.1.5 Validation of the numerical optimization

The deep drawing tests for validation purposes were carried out immediately after having subjected the circular blanks to the LHT to prevent any natural ageing to be triggered by a prolonged exposition at room temperature. The LHT, for all the investigated blank diameters (initially in the T6 condition), was carried out setting: the spot centre initially located at a radial position equal to 46 mm, and (ii) the FR value equal to 10 mm/s. Each local heating was replicated twice, so that the first sample could be used to evaluate the effectiveness of the treatment by hardness measuring while the second one could be subsequently deep drawn. The local treatment operations started from an initial blank diameter equal to 102 mm (the maximum drawn dimension in the SHT condition) and, according to the scheme in Figure 90 (left image), a portion of the spot irradiated the blank surface; if considering the assumption that the whole power was absorbed by the blank (coefficient of absorption equal to 1), the material was irradiated by a theoretical specific power of approximately 2.4 W/mm^2.

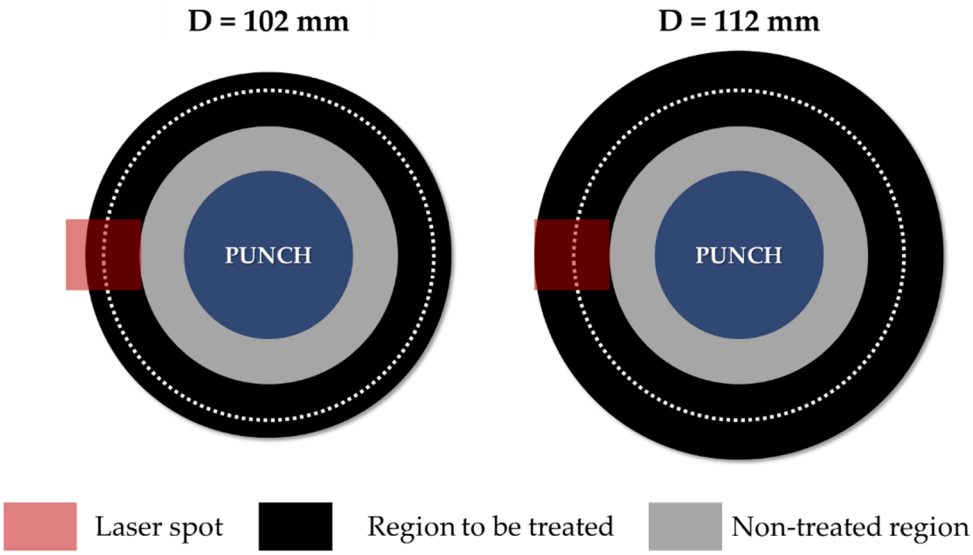

Figure 90 LHT tests: portion of the spot irradiating the surface with the increasing blank diameter

When increasing the blank diameter, a progressively greater portion of the spot irradiated the peripheral region up to the diameter equal to 112 mm (right image in Figure 90): the laser power was then increased accordingly to keep the specific irradiating power constant with the increasing blank diameter. All the laser heating campaign was assisted by the thermal camera and the temperature distribution was acquired along a radial path.

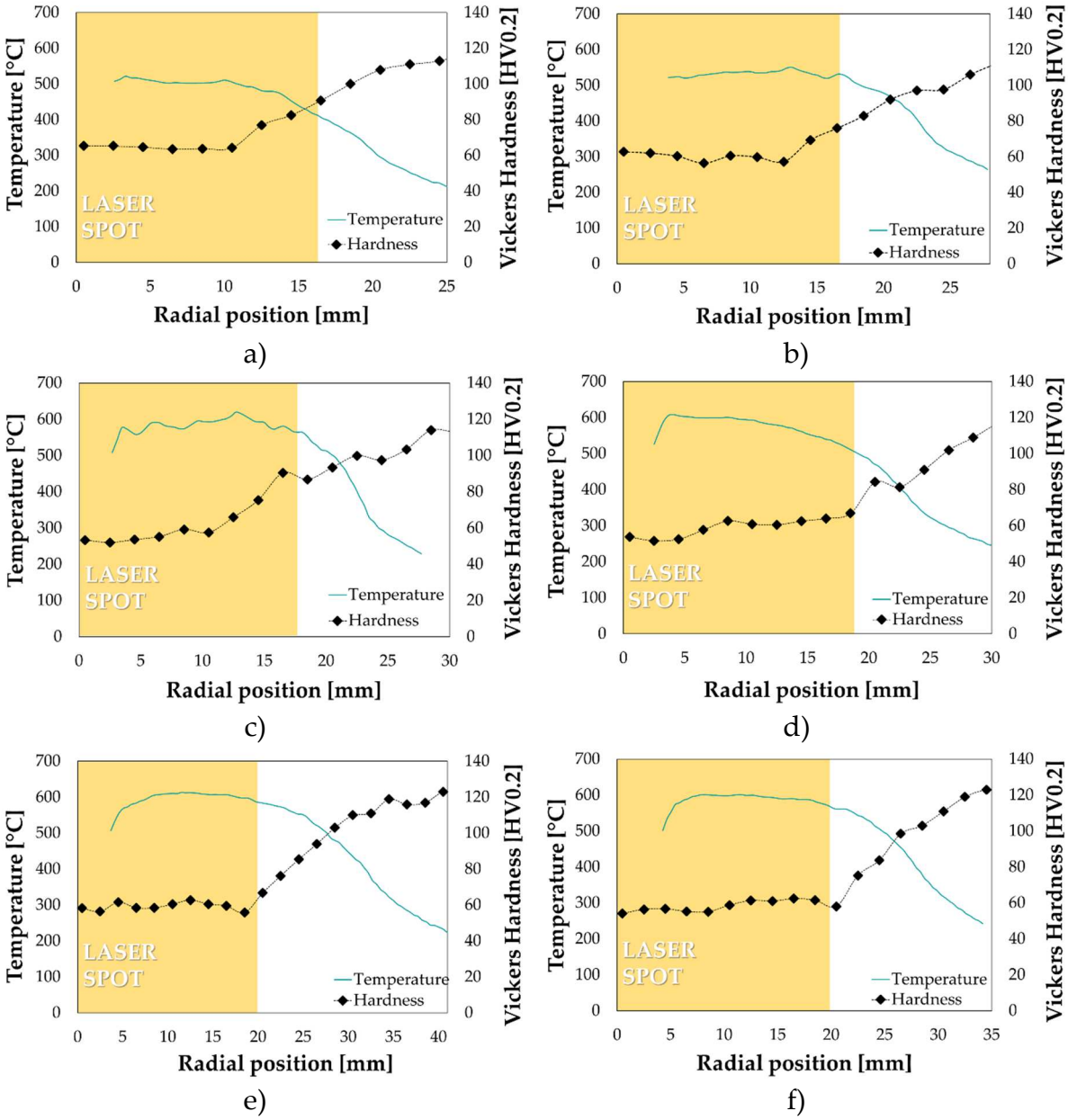

Figure 91 Temperature distribution and hardness measurement after LHT: a) D=102 mm, b) D=104 mm, c) D=106 mm, d) D=108 mm, e) D=112 mm, f) D=114 mm.

Plots in Figure 91 (from a to f with the increasing blank diameter) confirm that the increase of the laser power with the blank diameter led to an almost uniform temperature distribution (higher than 500°C) in the blank region irradiated by the spot (highlighted by the yellow box); in addition, the drop of the hardness was an indisputable evidence of the material effective solution. Subsequent deep drawing tests at room temperature were carried out setting the punch speed equal to 6 mm/min and adopting a value of the BHp equal to 1.5% of the material yield stress (in accordance with the FE simulations). The increasing blank diameter, as already shown in Figure 84b, had an appreciable influence on the shape of the punch load curve as well as on the its peak value (see Figure 92).

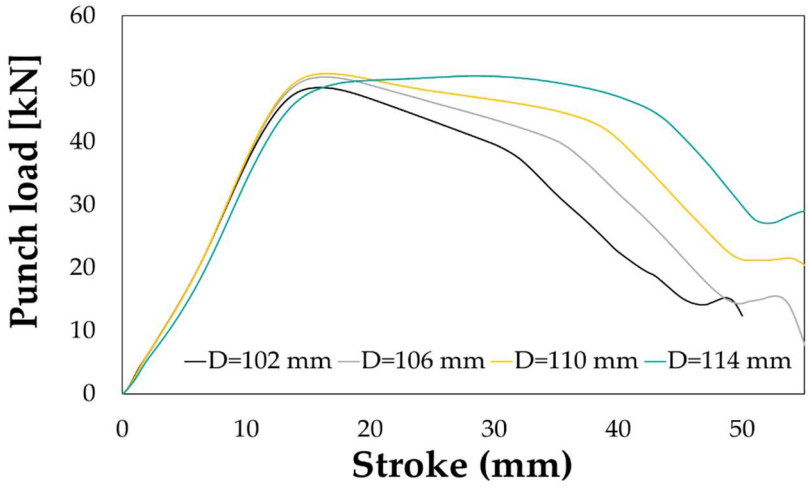

Figure 92 Deep drawing on LHT specimen: effect of the blank diameter

At the end of the deep drawing test with the LHT blanks, an LDR equal to 2.48 – correspondent to a maximum blank diameter equal to 114 mm – was achieved: the increase of the material drawability was the most evident confirmation of the advantages of the local heat treatment in enhancing the formability of the alloy at room temperature. The achieved LDR resulted not only higher than the limit reached in the T6 condition (+22%) – which was quite reasonable because of the limited formability due to the peak hardening condition – but, thanks to the optimal material distribution, even the limit achieved in the more formable SHT condition (+14%) was overcome (Figure 93).

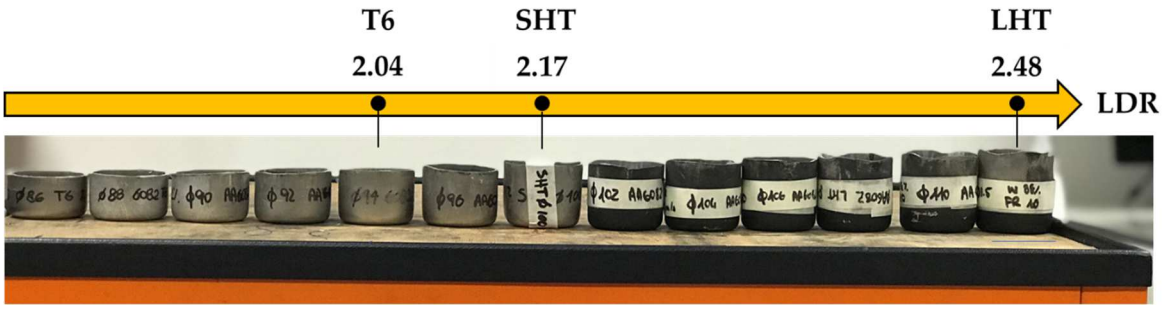

Figure 93 Improvement in the achieved LDR thanks to the local laser treatment

If briefly recalling the results of the optimization round, the numerically estimated LDR was slightly higher than the one experimentally achieved (with a numerical overestimation of the LDR of around 5%): the discrepancy may be attributed both to the neglection of the anisotropy in the formulation of the material yield criterion (the isotropic Von Mises model was adopted for the numerical simulation) but also to the assumption that the material formability within the 10 mm of transition zone between the T6 and the SHT varied linearly. On the other hand, it should be underlined that the difference in the LDR can be considered acceptable and the optimization round quite accurate to predict the enhancement in the material formability with an optimized distribution of properties. As a further confirmation of the accurateness of the optimization procedure, if comparing the experimental results with one of the

feasible design with an initial diameter equal to 114 mm (the maximum one experimentally drawn), it was found that the successful drawing (no occurrence of rupture) was numerically predicted if the blank region in the T6 condition covered 46% of the whole blank: if considering the 10 mm wide transition region, the fully solutioned part had to cover a radial extent slightly higher than 20 mm, exactly equal to the one experimentally measured (see the hardness profile in Figure 91f).

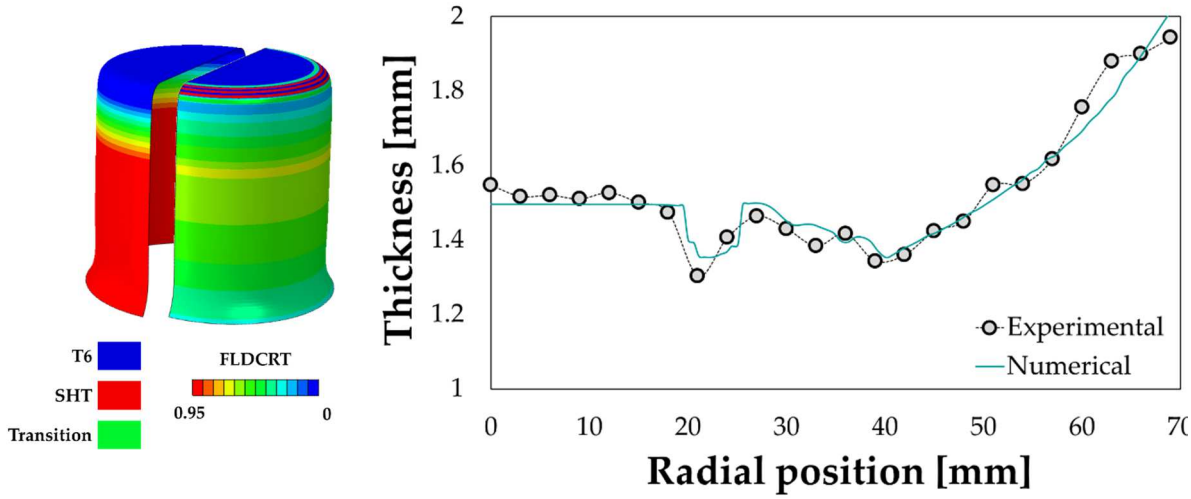

a) b)

Figure 94 Validation of the optimization prediction: a) numerical distribution of material properties and strain severity (FLDCRT), b) numerical vs. experimental thickness distribution

As expected (see the distribution map in Figure 94a), a successful drawing was predicted if maintaining the T6 condition on the blank portion in contact with the punch radius, whereas bringing the whole flange, where the highest plastic strain are reached during the deformation, in the SHT condition. It is worthy of notice that the most severe strain condition, as expected in a conventional cup deep drawing, occurred close to the punch radius – where the FLDCRT parameter resulted close to threshold value – but, thanks to the improved material drawing, rupture could be avoided. Despite the small discrepancy in terms of LDR, the properly tuned FE model (especially in terms of friction coefficient) was able to correctly predict the experimental thickness distribution of the drawn component with the maximum initial blank diameter (114 mm), as shown in Figure 94b.

4.2 The "Heating Before Forming" applied to the stamping of the industrial component

The remarkable results obtained locally modifying the material properties for the deep drawing process paved the way to the HBF application to a more challenging component, belonging to the window panel category as the one discussed in chapter 2. After a preliminary characterization of the AA5754 both in the annealed and in pre-strain conditions, the optimization of the heating strategy was accomplished by an

alternative approach based on the adoption of an accurate metamodel as the base for a subsequent virtual optimization.

4.2.1 AA5754 behaviour at room temperature

Results from material characterization are here presented in terms of flow curves (Figure 95a) and FLC (Figure 95b) of the two investigated material conditions. The effect of the initial cold working not only reflected in an increase of its properties, as expected, but in further limit the material formability, already low at room temperature in the annealed state.

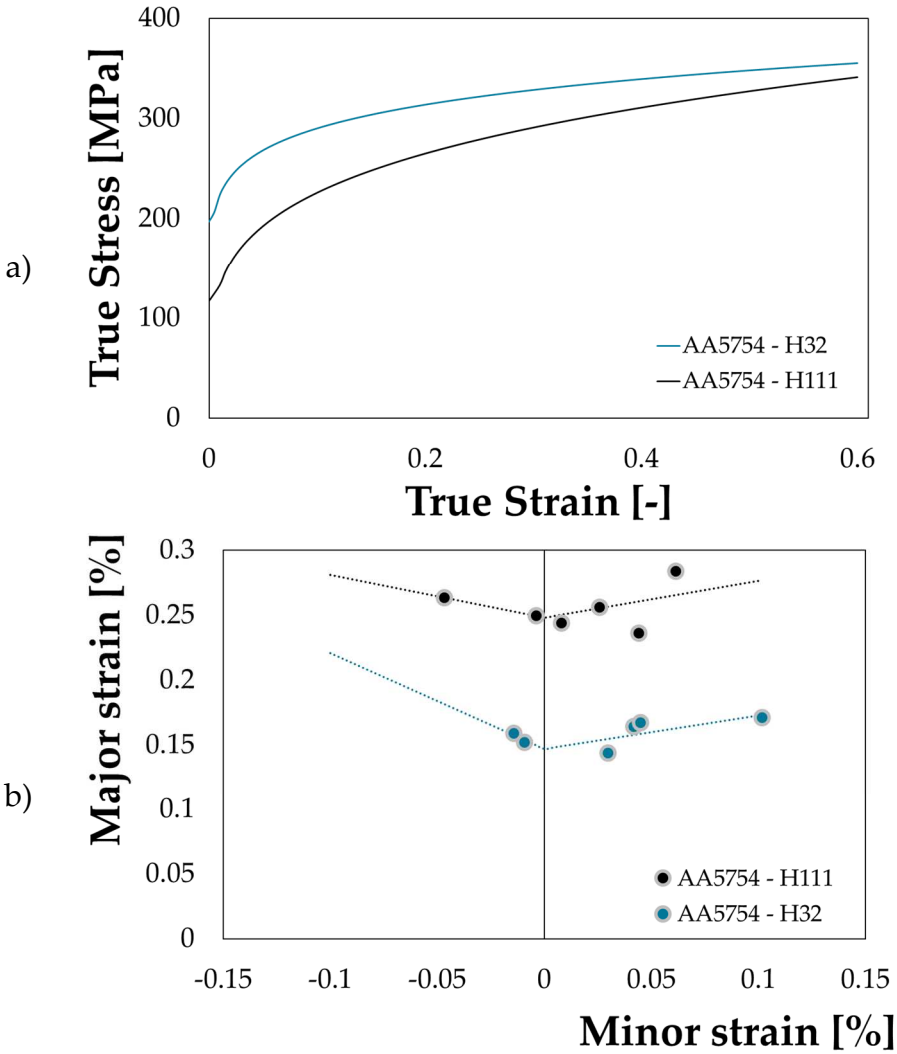

Figure 95 AA5754 characterization at room temperature: a) flow curves and b) FLCs

4.2.2 Results from the preliminary FE simulations

The main purpose of the preliminary FE numerical simulations was to (i) identify the blank critic regions where the local heating had to be applied and the most critical

regions and (ii) investigate the effect of the initial blank geometry on the strain distribution and rupture localization. According to the setting of the FE model relative to the warm forming (section 2.3.3), the simulated time period was initially set at 91 seconds (considering a forming speed of 60 mm/min). Previous numerical runs demonstrated that exploiting the geometrical symmetry of the system in combination with a mass scaling approach was an effective solution to speed up the numerical simulation. In the specific case of the HDF approach, the forming operation has to be carried out at room temperature, at which the effect of the strain rate can be considered negligible: for this reason, the simulated time period was scaled of a factor equal to 9 passing from the initial value of 91 seconds to the reduced one equal to 11 seconds (of which 1 second for the BHF to reach its working value and the other 10 seconds to complete the linear ramp punch stroke). It was then demonstrated that the scaling of the time period did not significantly alter the numerical results since the rupture was predicted for the same punch stroke; as a further confirmation, as shown in Figure 96, the two FLDCRT distributions along the white dotted path resulted almost perfectly overlapped. The time scaling approach had a remarkable influence on the computational cost reducing the time needed to a numerical run to complete from almost 9 (simulated time period equal to 91) down to 1.5 hours (time period equal to 11). Subsequent numerical investigations were then run simulating the scaled time period.

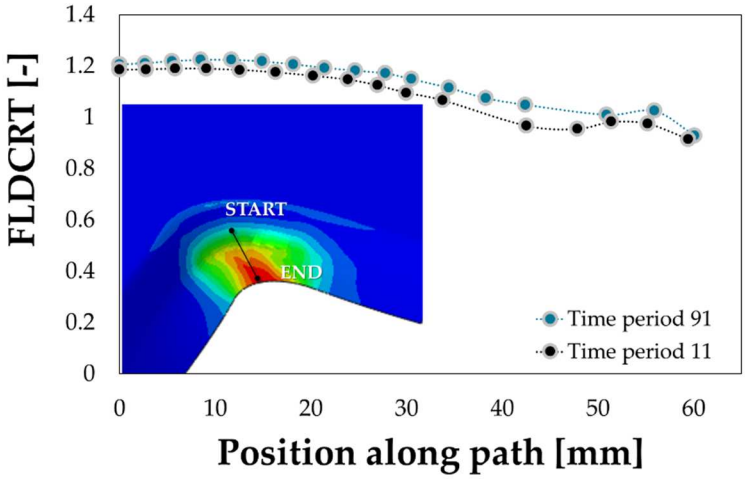

Figure 96 Effect of the time scaling approach on the results of numerical simulation

Beside the preliminary run oriented to the computational time reduction, additional numerical simulations were run to evaluate the effect of the main process parameter on the outcome of the stamping simulation: results were analysed in terms of maximum punch stroke before the occurrence of rupture and blank drawing in points of interest (see Figure 97a).

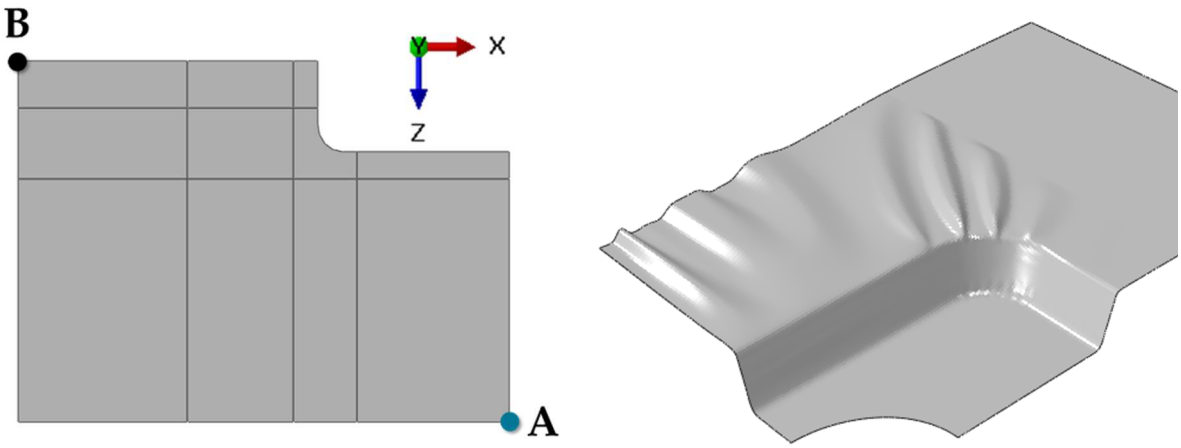

a) b)

Figure 97 Results of the preliminary runs: a) nodes of interest for the blank drawing monitoring, b) excessive wrinkling due to a too low BHF value

When setting the coefficient of friction equal to 0.1, it was found out that when reducing the load applied by the blankholder (BHF) from an initial value of 100 kN to 30 kN, both the maximum punch stroke (from 63 mm to 76.5 mm) and the blank drawing on point A along the z axis (from 39 mm to 55 mm) increased. Nevertheless, a too low value of the BHF (see Figure 97b) led to an excessive wrinkling, thus completely nullifying the improvement in the reached drawing depth. For this reason, all the subsequent numerical simulations were run setting the coefficient of friction equal to 0.1 (it is a commonly used value in literature) and a BHF value of 70 kN (no appreciable difference in the maximum punch stroke and in the blank drawing was found if comparing with the results at BHF equal to 100 kN). As previously anticipated, the main aim of the preliminary runs was the evaluation of the blank critic regions where the local heat treatment had to be applied. The influence of the initial blank shape was then investigated, considering several increasing values of the Offset parameter: as previously done for the preliminary runs, numerical results were analysed in terms of maximum drawing depth at rupture and blank drawing (the scheme of Figure 97a is here recalled).

a)

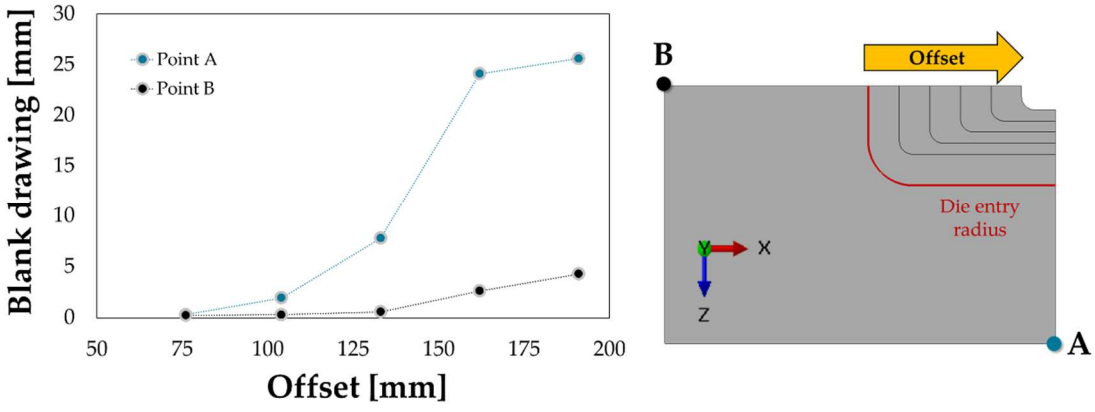

b)

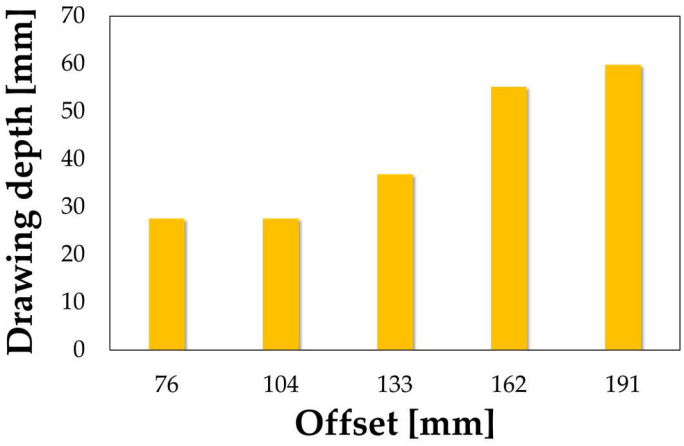

Figure 98 Effect of the initial geometry: a) blank drawing, b) drawing depth at rupture

Blank drawing was monitored in two different nodes of interest, i.e. node A along the z axis and node B along the x axis: as clearly show in Figure 98a, when increasing the Offset parameter, the blank drawing increased accordingly especially on the A node (the drawing along the z axis was sensibly lower for each of the simulated Offset value mainly due to the excess in the material in that region). The increase in the blank drawing, mainly related to the increased portion of the blank in contact with the punch bottom surface, was beneficial in terms of drawing depth: as the bar chart in Figure 98b clearly reports, the punch stroke at which the blank rupture was predicted increased in accordance with the Offset value, reaching the maximum value at almost 60 mm that anyway was still lower than the target punch stroke equal to 90 mm. An alternative initial blank shape was then investigated this time considering a central hole and evaluating the effect of its radius on the outcome of the stamping simulation; also for this second set of numerical runs, the blank was modelled again in the wrought conditions (AA5754-H32). Four different values of the central hole radius were investigated, from 100 mm to 200 mm, and all of them were characterized by a value of the blank drawing along the z axis (Figure 99a) remarkably higher than the one registered with the highest investigated value of the Offset parameter.

a)

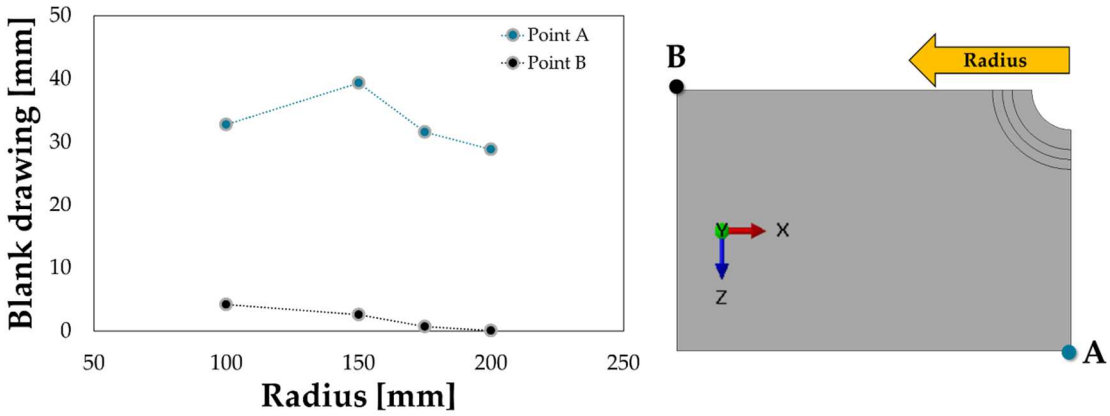

b)

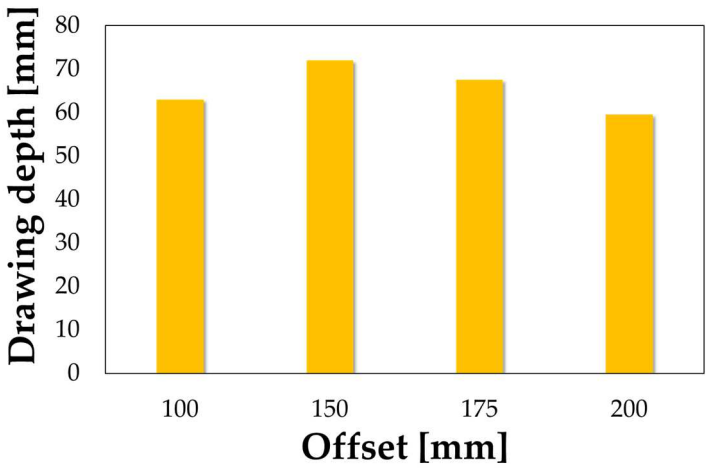

Figure 99 Influence of the central hole radius: a) blank drawing, b) drawing depth at rupture

The increased drawing, whose maximum value was registered with an initial radius of 150 mm, was strictly connected to the maximum drawing depth as already demonstrated in the first set of preliminary simulations; the bar chart of Figure 99b shows that with the optimal value of the central hole radius, the drawing depth at rupture slightly increased up to a maximum value of slightly higher than 70 mm (but still too low). If looking at the FLDCRT distribution in Figure 100, despite an optimized blank geometry and a remarkable increase in the maximum punch stroke before rupture, the stamping at room temperature resulted to be still too critic and, once again, the occurrence of rupture was predicted both near the die entry radius and on the bottom part of the corner region (blank portions highlighted in grey).

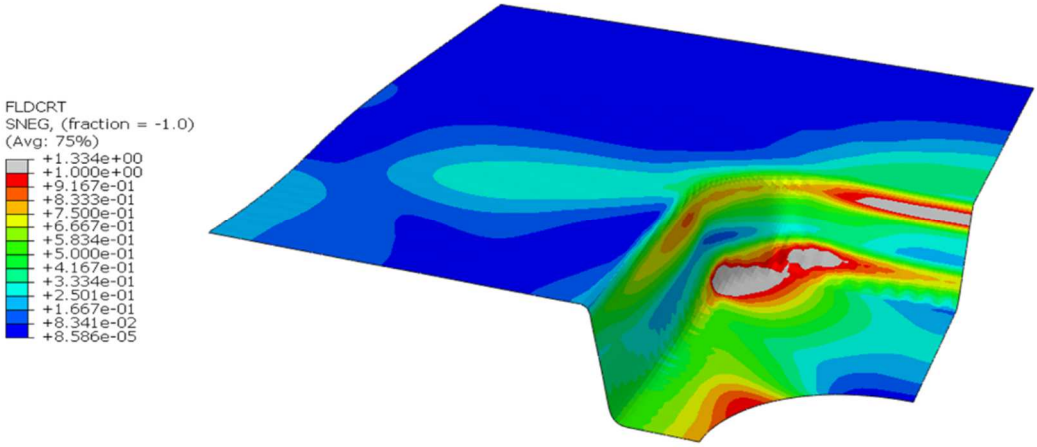

Figure 100 Blank with a 150 mm central hole: FLDCRT distribution at the end of the stamping

The highlighted regions were then considered the target where the local heat treatment had to improve the material formability by completely annealing the initial pre-strained material condition. In accordance with the heating technologies equipping the Heat Treatment sub-unit, the process was numerically designed modelling the heating carried out by both the available heating solutions.

4.2.3 Tailoring the material properties by conductive heating

According to the results of the preliminary numerical runs, the heat treatment was designed to locally modify the material properties in the blank portions where the rupture was predicted [106]. The projection of the final FLDCRT distribution over the undeformed blank (Figure 101a) was useful to properly design the heat treatment: in fact, taking into account the dimension of the conductive plate equipping the TH2 (plan size 200 mm x 300 mm), the treatment was designed based on a sequence of two consecutive heating (H1 and H2) as shown by the scheme in Figure 101b. In such a way, both the treated portions (highlighted in blue) could be annealed and characterized by an improved formability to avoid the occurrence of rupture.

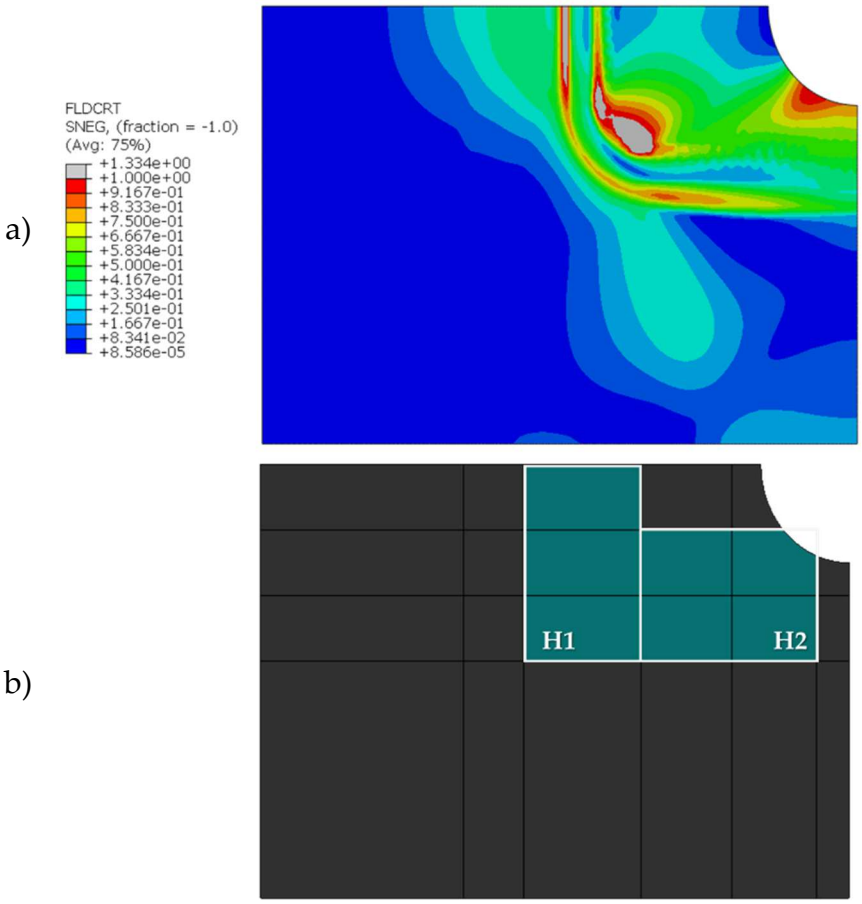

Figure 101 Design of the local heat treatment: a) FLDCRT distribution projected on the undeformed blank, b) sequence of conductive heating

The effectiveness of the designed heat treatment was numerically investigated: as done in the case of the deep drawing process optimization (see section 2.4.2), the stamping simulation was run considering the blank as already subjected to the heat treatment. A field variable was adopted to correctly associate the material properties (flow curve and FLC) in the annealed state (AA5754-H111) to the blank portion subjected to the heat treatment, whereas the remaining part was modelled in wrought condition (AA5754-H32). In particular, two different material distribution were investigated, modelling (i) a sharp change from the blank in wrought condition and the treated area in the annealed state (Figure 102a) or (ii) considering a transition

region (whose extent was equal to 10 mm according to previous investigations) between the two (highlighted in green in Figure 102b)

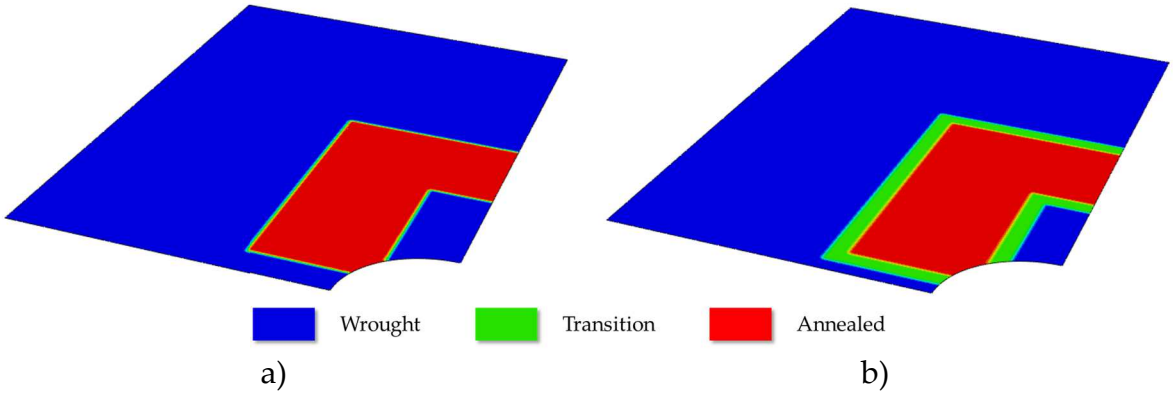

Figure 102 Distribution of the material properties after the heat treatment: a) step change between the wrought and the annealed region, b) modelling the transition region

Stamping simulations were run adopting the same settings (load applied by the blankholder, scaled time period, friction coefficient) of the preliminary runs: results were analysed in terms of FLDCRT variable distribution.

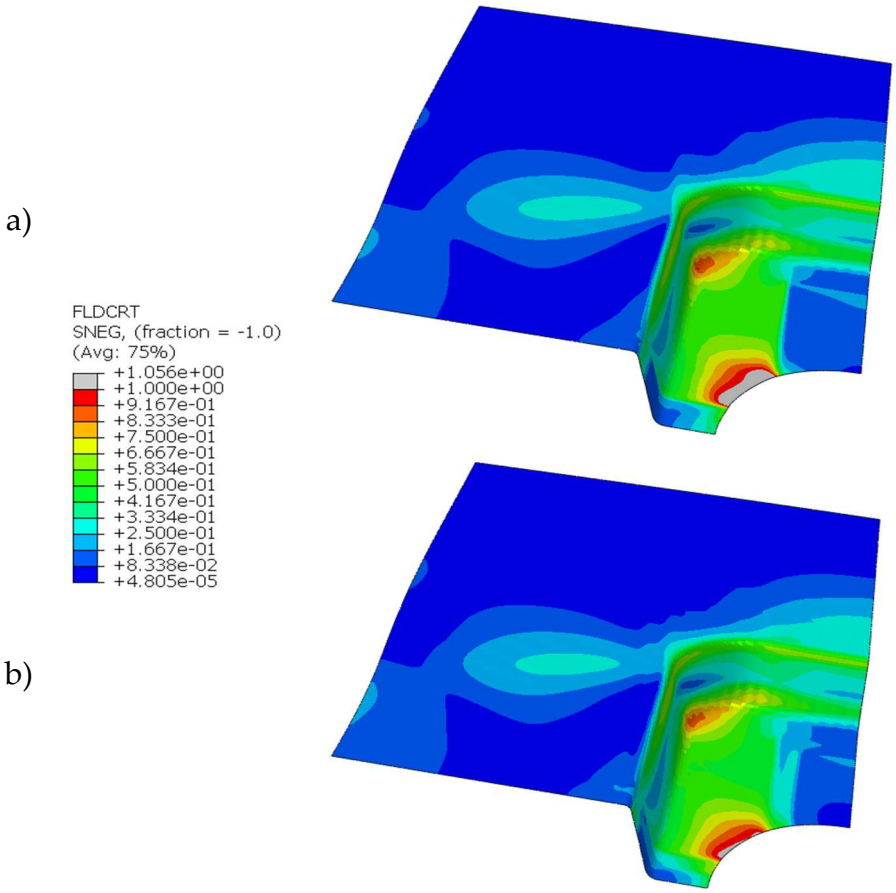

Figure 103 Final FLDCRT distribution: a) sharp change in the material properties, b) modelling the transition region

Results in Figure 103 (a and b) were considered remarkable since confirming the effectiveness of the proposed approach: even in the case of a simpler – and eventually

less accurate – distribution of the material properties based on the sharp transition from the treated to the non-treated blank regions, the local improvement of the material formability in the critic regions revealed to be effective since a sound component could be manufactured. The FLDCRT distribution maps, in both the investigated cases, suggested that thanks to a proper modification of the material properties combined with an optimized initial blank geometry, the critic region moved to the proximity of the circular hole whereas the corner region, where the blank rupture was predicted in the preliminary runs (see Figure 100), was characterized by a value of the FLDCRT lower than 1.

4.2.4 Tailoring the material properties by local laser heating

As already discussed, the Heat Treatment sub-unit is also equipped with a 1 kW diode laser (TH1) able to carry out more complex heating strategy than what is possible with the conductive plate. In this case, again the main aim was to define the best heating strategy to overcome the limit of the material at room temperature but adopting a different approach: thanks to the higher laser flexibility, the heating strategy was designed to be based on a ordered pattern of squared portion arranged in a form of a matrix. For this reason, the approach was then identified as "matrix of spots".

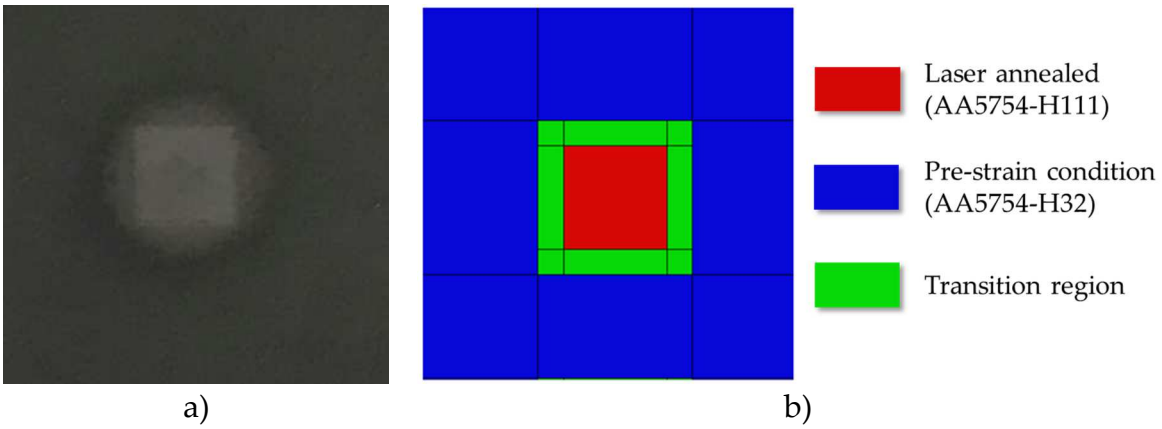

Figure 104 Distribution of the material properties after the laser heating of a single spot: a) experimental laser heating trial, b) FE model

As shown in Figure 104a, experimental laser heating on a AA5754 sample initially in wrought conditions (H32) left a square mark (a 20 mm square spot was used) on the treated area as visible as the surrounding annular region where the material reached an intermediate condition (hardness tests were carried out on the sample once cooled down to room temperature) [120]. The blank was then modelled as already subjected to the heat treatment according to the scheme in Figure 104b: for each of the modelled "square spot", the adoption of a field variable (as already specified in the previous paragraph) ensured the exact association of the material properties in the annealed state and the correspondent geometrical partition on the blank; the extent of the transition region (highlighted in green in Figure 104b) was modelled equal to 5 mm

[120]. The methodology to optimize the extent as well the pattern of the matrix, as already introduced in the section 2.5.5, was based on a double round procedure.

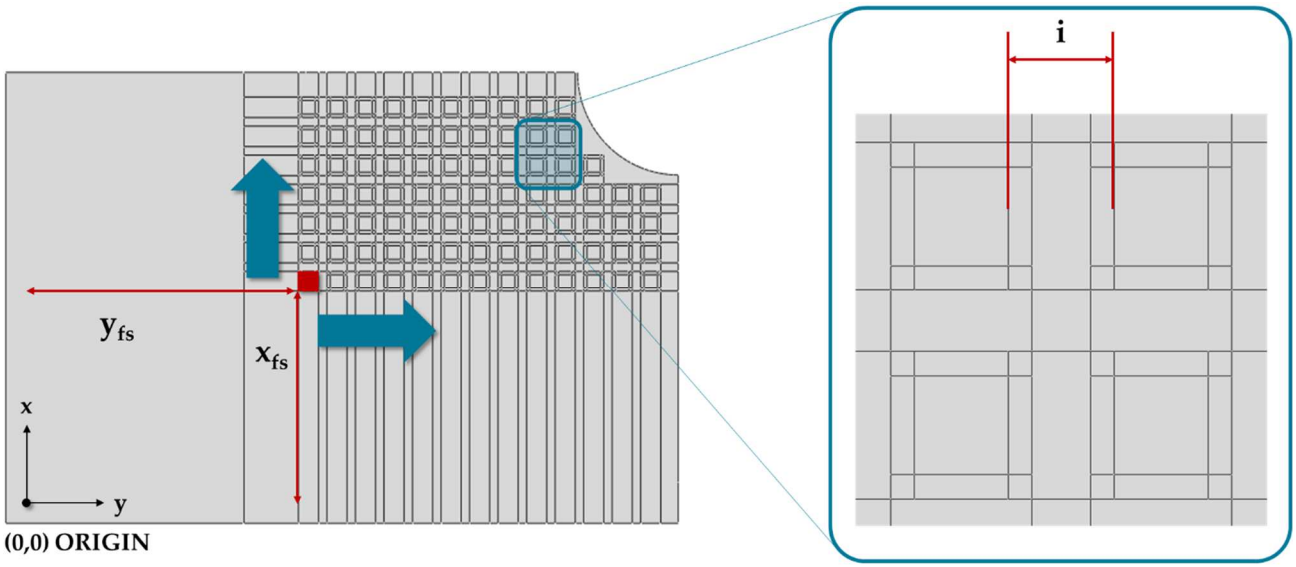

Figure 105 First optimization round: definition of the input variables

For the first optimization round, the coordinates (x_{fs} and y_{fs}) of the first vertex of the first spot (indicated by a red square in Figure 105) and the distance between two consecutive spots (labelled as *i* in the detailed view on the right) were defined as input variables. Once univocally defined the first spot and the distance between two consecutive spots, all the consecutive ones were positioned in order to fill the blank portion in the direction of the increasing *x* and *y* axes (as indicated by the arrow). The variation ranges of the input variable are reported in Table 8.

Table 8 Input variables: definition of the variation ranges

Input Variable	Lower Bound	Upper Bound
x_{fs}	0	572
y_{fs}	0	762
i	15	30

The initial DoE population was created according to a Central Composite Design (CCD) scheme, particularly suitable to build up a second order (quadratic) model without the need to use a 3 level Full Factorial DoE and with a sensible reduction in the number of necessary designs. The CCD contains an embedded factorial design with centre points, augmented with a group of axial points usually indicated as "star points". The created CCD was composed of 15 designs placed at each vertex of the cube (2^n points, where n is the number of factors), at the centre of each cube face (2n) and at the centre of the cube (1). Results from each of the designed numerical runs were analysed in terms of proper output variables: (i) the drawing depth at rupture (indicated in the following as h_r), (ii) the maximum value of the FLDCRT at the end of

the forming step and (iii) the percentage of treated area (A_t) with respect to the whole blank surface.

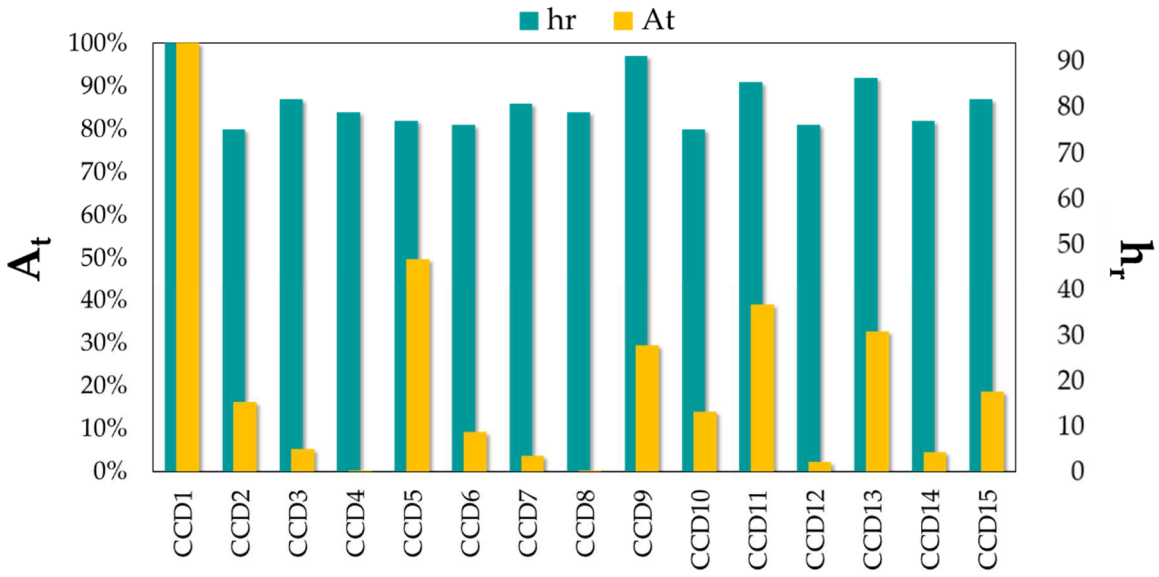

Figure 106 Numerical results of the designs composing the initial DoE

The bar chart in Figure 106 suggests that only for the design labelled as CCD1 – characterized by the initial spot coordinates coincident with the origin and the parameter *i* set at its lower bound – it was possible to complete the punch stroke without the occurrence of rupture: anyway, the heating configuration of the CCD1 covered almost the whole blank surface (as suggested by the value of the A_t parameter) thus approximating the stamping of the component starting from a blank fully in the annealed state which is quite far from the intent of the local modification of the material properties.

Moreover, the CCD9, where the achieved value of h_r was the second highest, was again characterized by the lowest distance between consecutive spots, as a further confirmation that the *i* parameter had a big influence on the feasibility of the stamping.

Data from the designs belonging to the CCD, both in terms of input and output variables, were arranged in a spreadsheet and imported directly within the modeFRONTIER environment: thanks to a wizard procedure, once indicated the columns containing the input data and those the output data, the workflow was automatically build up.

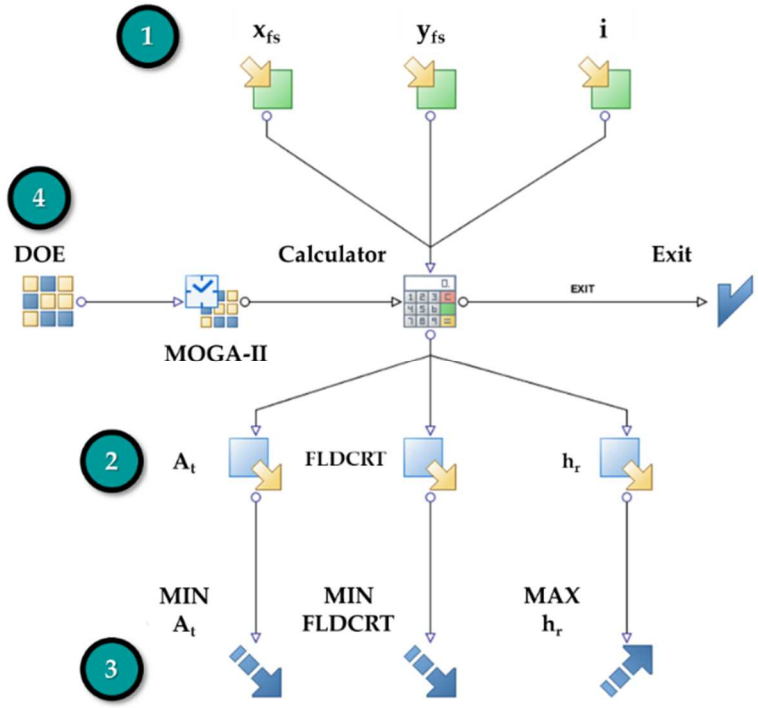

Figure 107 modeFRONTIER workflow for the first optimization round

In the created workflow (Figure 107), the input variables (zone #1) are connected to the calculator node that, in turns, is connected to the output variables (zone #2). Once chosen the algorithm and created the RS, a good way to check the accurateness of the fitting procedure was to look at the Mean Leave-One-Out Error (MLOOE): it was calculated excluding, in turn, each point belonging to the training set and its predicted value was compared to the known one (the smaller this value on average, the better the surface trained on the whole dataset).

As a rule of thumb, the fitting of the training set was considered accurate when the MLOOE resulted lower than 0.2. In addition to the MLOOE, the scaling parameter had a big influence on the shape of the radial function: a too low scaling parameter may lead to several narrow peaks centred at the training points and a bad fitting in the remaining part of the design space, while a too high scaling parameter may end up in a too "smooth" surface not even able to properly fit the design data (for this reason, the scaling parameter is automatically managed according to the specific RBF algorithm, with the exception of the PS for which the scaling parameter is always equal to 1).

Once created the two sub-set from the whole design table, RS were created adopting the 5 available RBF algorithm for each of the defined output variables. In the following, only the procedure to choose the best algorithm for the FLDCRT output variable is discussed in detailed: similar criteria were adopted for the algorithm choice on the other two output variables. Results of the RS construction on the FLDCRT variable were at first analysed in terms of MLOOE values.

Table 9 RBF fitting performance on the FLDCRT output variable

RBF	Abbr.	MLOOE
Hardy's MultiQuadrics	MQ	0.252
Inverse MultiQuadrics	IMQ	0.223
Gaussians	G	0.227
Duchon's Polyharmonic Splines	PS	0.779
Wendland's Compactly Supported	CS	0.416

As shown in Table 9, none of the available algorithm provided a satisfactory fitting of the training set (MLOOE always higher than 0.2): such a situation did not compromise the choice of a suitable algorithm, but it just moved the attention on another criterion. The Function Plot was a powerful tool to evaluate the accurateness of the RS, since plotting all the created surfaces simultaneously on multiple 2D graphs (Figure 108).

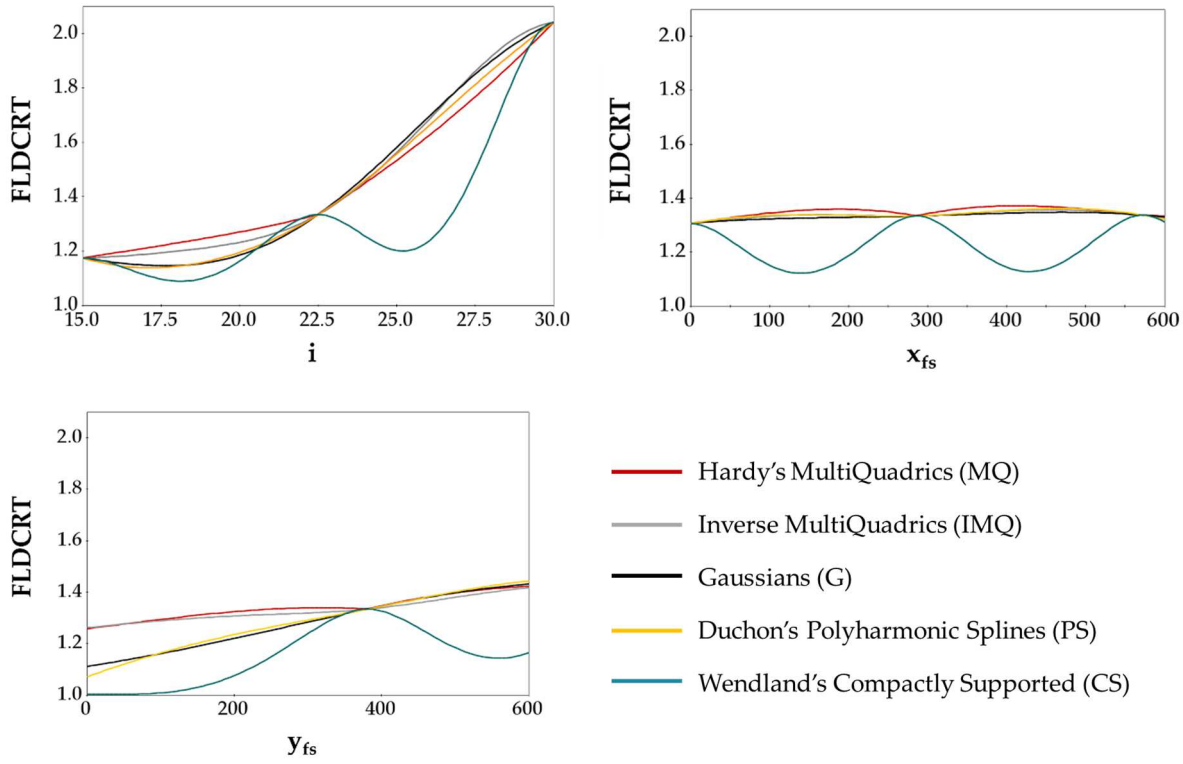

Figure 108 Function plot on the FLDCRT output variable

It became clear that the shape of the RS created with the CS algorithm (dark green curves in the Function Plot) was quite different from the other; in addition, the PS surface was also discarded since showing the highest value of the MLOOE (almost three times higher than the value of the remaining three algorithms). The Distance Plot, i.e. the plot showing the distance between the known value of the designs belonging to the validation set and those predicted by the RS, was used to finally choose the most accurate RBF.

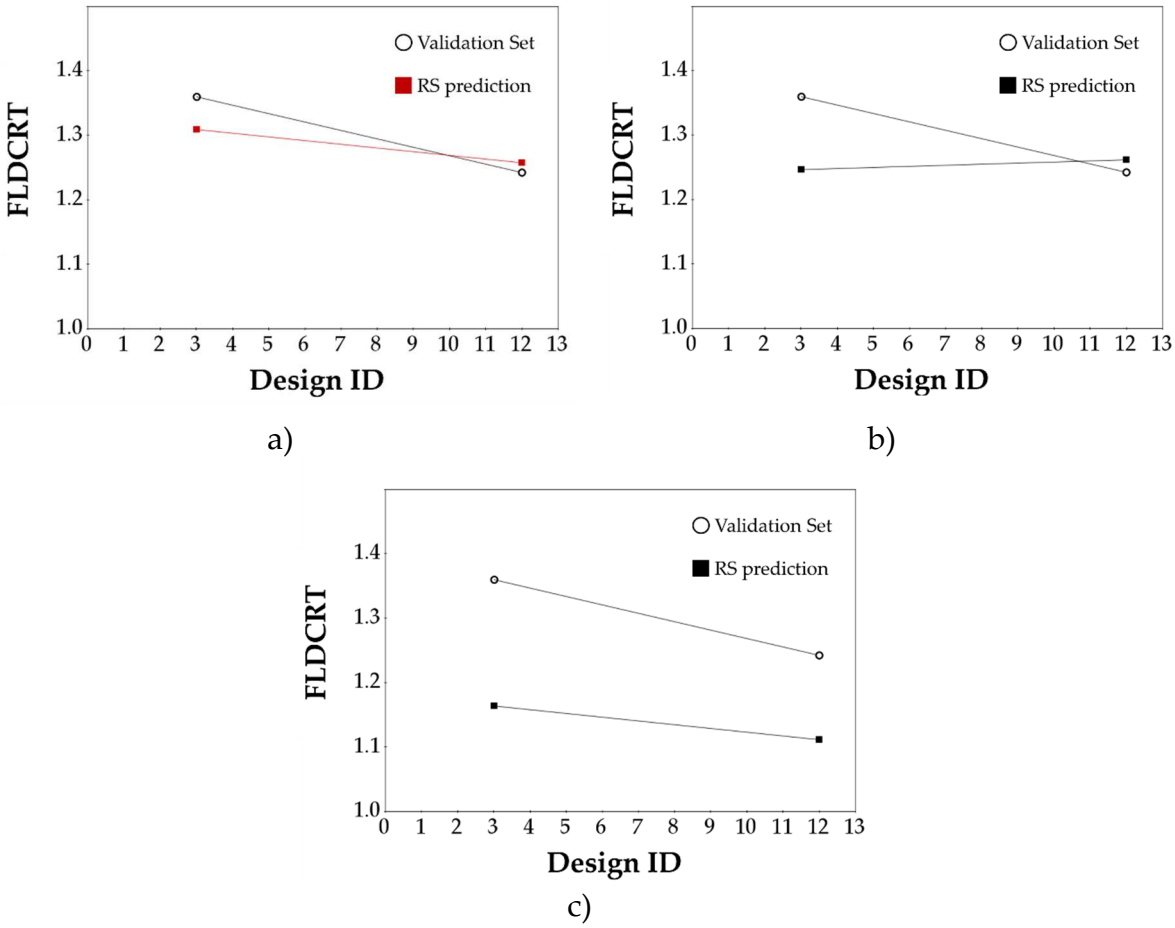

Figure 109 Distance plots on the validation set: a) Hardy's MultiQuadrics (MQ), b) Inverse MultiQuadrics (IMQ), c) Gaussians (G)

It is quite evident that the Hardy's MultiQuadrics (MQ) algorithm (Figure 109a) was characterized by the best prediction of the designs belonging to the validations set and, for this reason, it was chosen as the best algorithm for generating the RS on the FLDCRT output variable (the 3D visualization is reported in Figure 110a). The procedure above described was repeated for the construction of the metamodels on the other two output variables: in particular the Inverse MultiQuadrics (IMQ, shown in Figure 110b) was chosen for the h_r variable, while the Hardy's MultiQuadrics (MQ) showed the best fitting on the A_t data (see Figure 110c). The 3D explore of the created RS confirmed that when increasing the extent of the treated area (low values of the coordinates of the first spot), the possibility to manufacture a sound component increased accordingly, i.e. higher value of the drawing depth with a lower level of the strain severity in the critic regions.

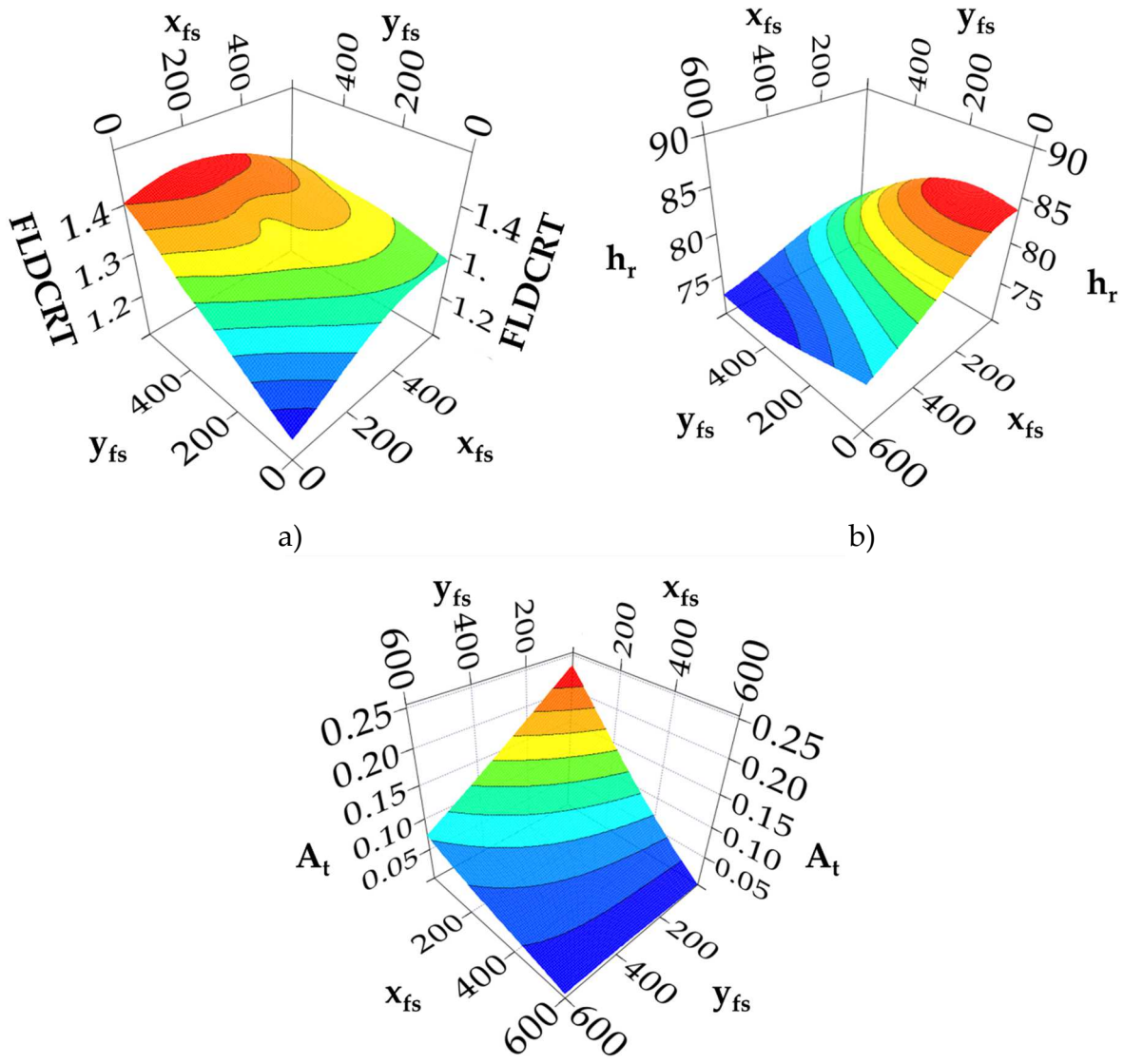

Figure 110 RS on the output variables: a) FLDCRT (MQ), b) h_r (IMQ), c) A_t (MQ)

If briefly recalling what already discussed, one objective function was defined for each of the output variable (zone #3 in the workflow of Figure 107): the optimization was then driven to obtain "optimal" design characterized by an increased drawing depth (maximization of the h_r variable), reduced occurrence of rupture (minimization of the FLDCRT variable) and a reduced extent of the blank annealed portion (minimization of the A_t variable). Within the Scheduler node (zone #3 in the workflow of Figure 107), the MOGA-II was chosen as optimization algorithm considering 100 successive generations and setting the created RS as the base for the optimization to proceed. Due to the huge number of created virtual designs (1500 in total), a viable way to correctly analyse the optimization results was to isolate the Pareto designs, i.e. those optimal designs that could not be further improved in terms of one optimization objective without deteriorating the performance of some of the other objectives. The isolated Pareto designs, plotted on a 4D bubble chart (Figure 111), confirmed the preliminary indications coming from the RS: higher value of the drawing depth avoiding the

occurrence of rupture (FLDCRT close to the threshold value, considering the Forming Limit Band) could be reached only increasing the extent of the annealed portion (blue bubbles with small diameter).

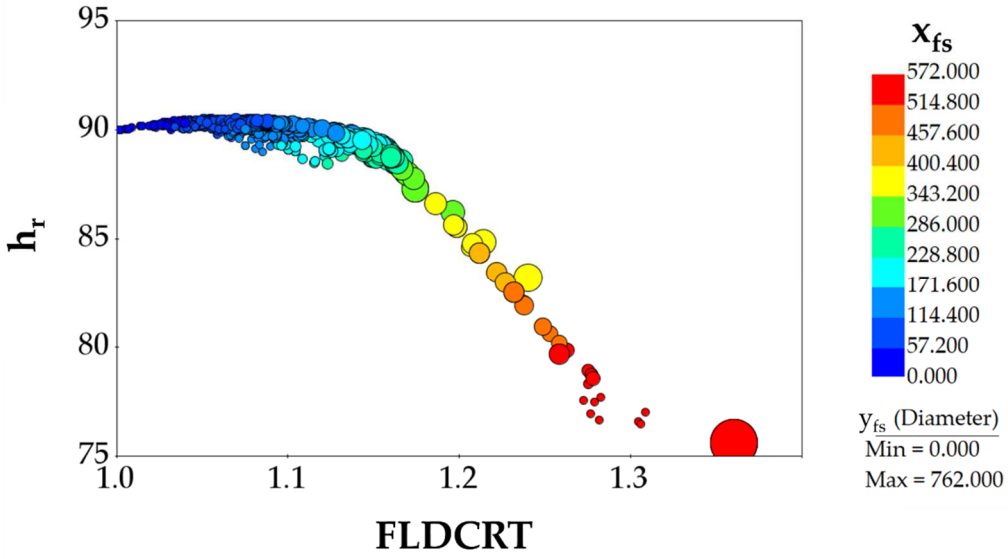

Figure 111 4D bubble chart on Pareto designs: influence of the extent of the annealed portion

Another important aspect was highlighted by plotting again the Pareto designs, but as a function of the *i* parameter as shown in Figure 112: to increase the possibility of manufacturing a sound component – maximization of the drawing depth limiting the strain severity – the distance between consecutive spots had to be kept at its lowest value (15 mm).

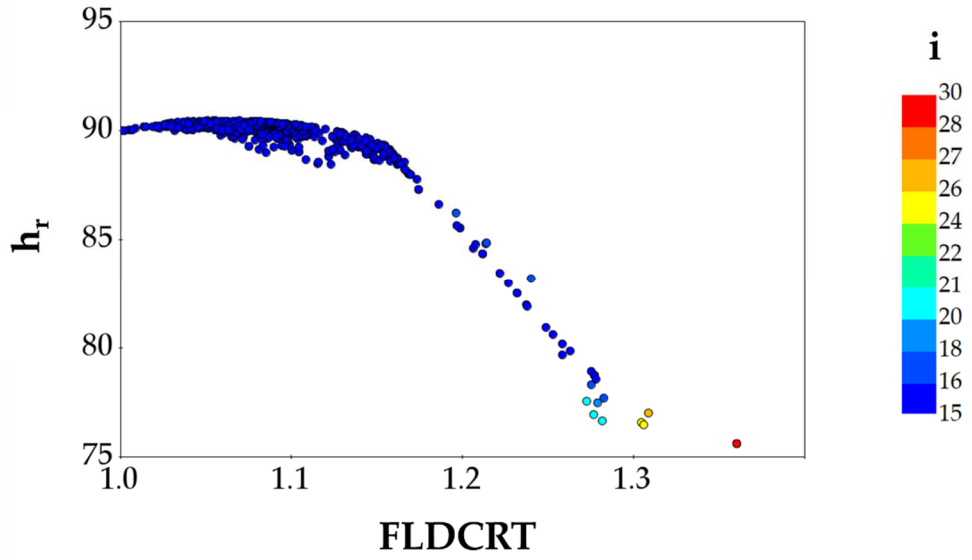

Figure 112 Bubble chart on Pareto designs: influence of the i parameter

It has to be underlined that all the Pareto designs were characterized by a value of the h_r parameter never higher than 90 mm, which was considered a remarkable evidence of the well-posedness of the optimization problem as no constraint was specified on

that output variable. The accurateness of the optimization results was further checked running additional simulation to validate the predicted value of some of the designs belonging to the Pareto front: designs to be validated were chosen after analysing the correlation matrix, extremely useful to evaluate the linear association between two variables by means of a correlation factor ranging from +1 (variables perfectly positively correlated) to -1 (variables perfectly negatively correlated).

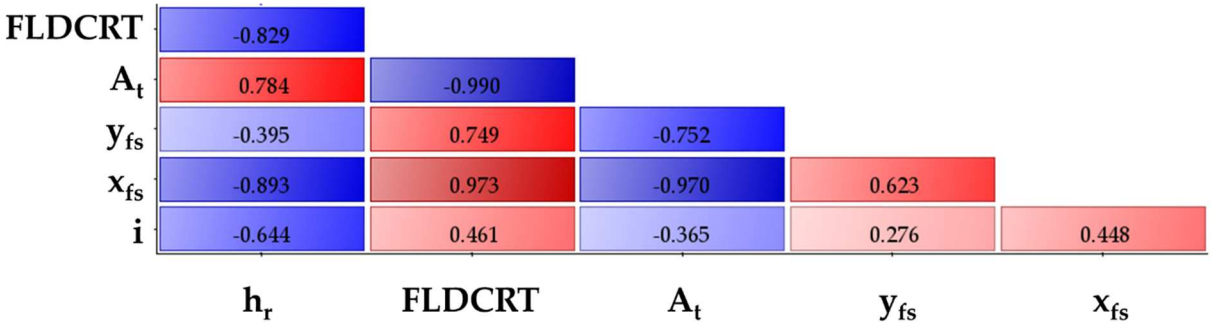

Figure 113 First optimization round: correlation matrix on Pareto designs

Correlation coefficients in Figure 113 demonstrated the strong influence the x coordinate of the first spot had on the output variables: for this reason, two Pareto designs characterized by the same x_{fs} value were picked for validation purposed (input and predicted output values are listed in Table 10).

Table 10 Pareto designs for validation purposes

ID design	i	x_{fs}	y_{fs}	FLDCRT	h_r	A_t
69	15	273	332	1.17	88.2	0.11
214	15	273	232	1.16	88.5	0.13

Results of the validation runs were then put in comparison with the prediction of the genetic algorithm showing a high level of correspondence: both the virtual designs overestimated the strain severity (less than 4%) while underestimating the maximum drawing depth (less than 2%).

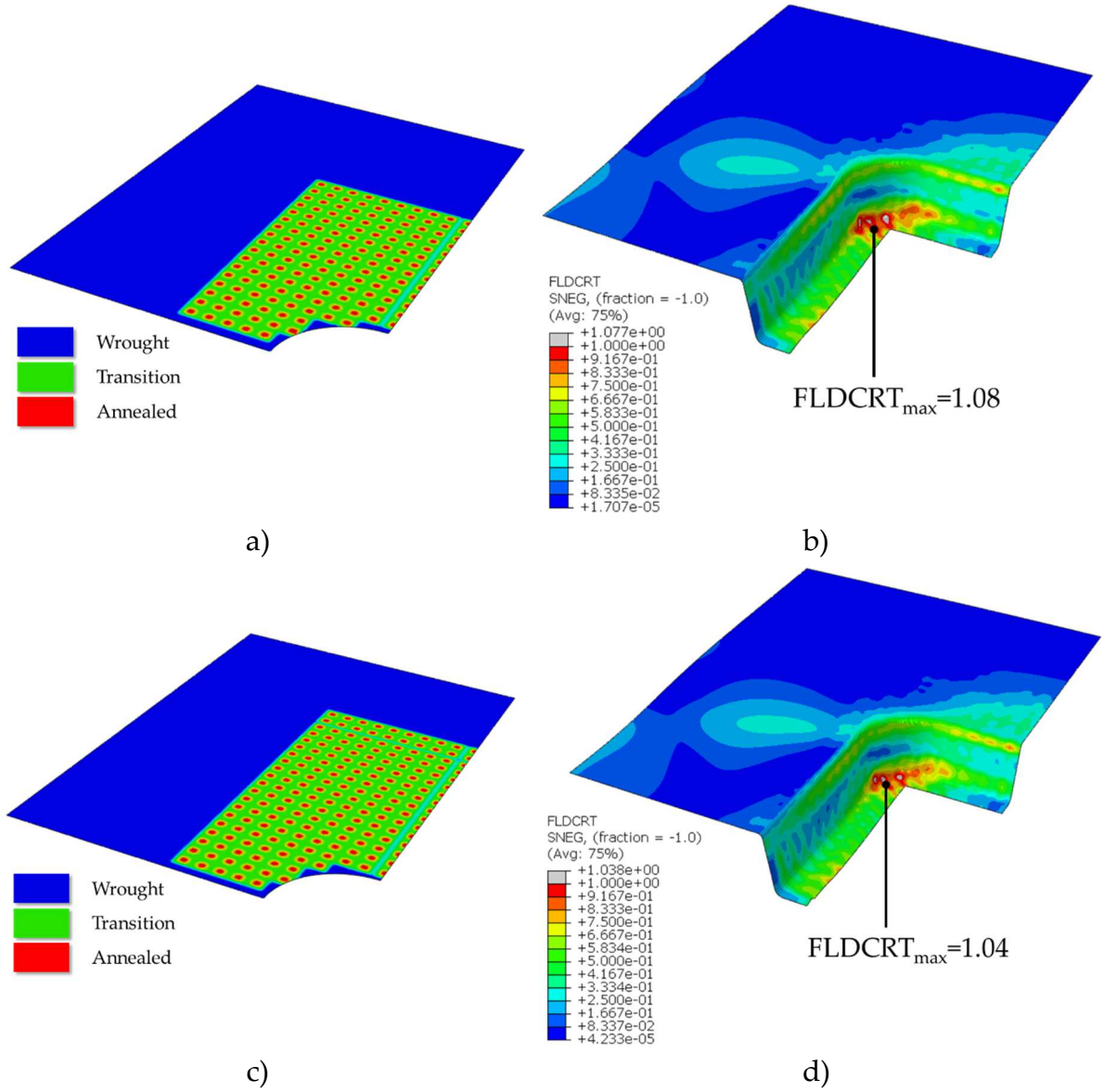

Figure 114 Simulation runs for validation purposes: a) material properties and b) FLDCRT distributions on Design #69; c) material properties and d) FLDCRT distributions on Design #214

When comparing the resulting distribution of the material properties (Figure 114a vs. Figure 114c), it is clear to denote that the increased extent of the annealed portion is strictly related to the different value of the y_{fs} parameter. Nevertheless, the difference in the maximum FLDCRT values was less than 3% and, in both cases, the correct manufacturing of a sound component was then predicted. For this reason, the Design #69 was considered the optimal one since predicting a correct stamping of the component but with a reduction in the annealed area approximately equal to 15%.
Despite the presented results suggested a viable way to effectively stamp the designed component, the question about the necessity to anneal even the blank region in contact with the flat bottom surface of the punch remained still open: for this reason, a second optimization run was designed with the precise aim of evaluating an alternative optimal configuration characterized by an even more reduced treated area. A second workflow was then created: the origin in Figure 105 was moved in correspondence of

vertex of the first spot vertex in the case of the optimal heating configuration of Design #69 (i.e. the best design from the first optimization round) while the distance between consecutive spots was kept constant at 15 mm (it was not included in the list of the input variables, as suggested by the bubble chart in Figure 112). Moreover, the number of rows (N_r, highlighted in yellow) and columns (N_c, highlighted in dark green) of spots were included as additional input variables; Figure 115 refers to one of the DOE designs characterized by a heating strategy based on four columns and three rows of spots.

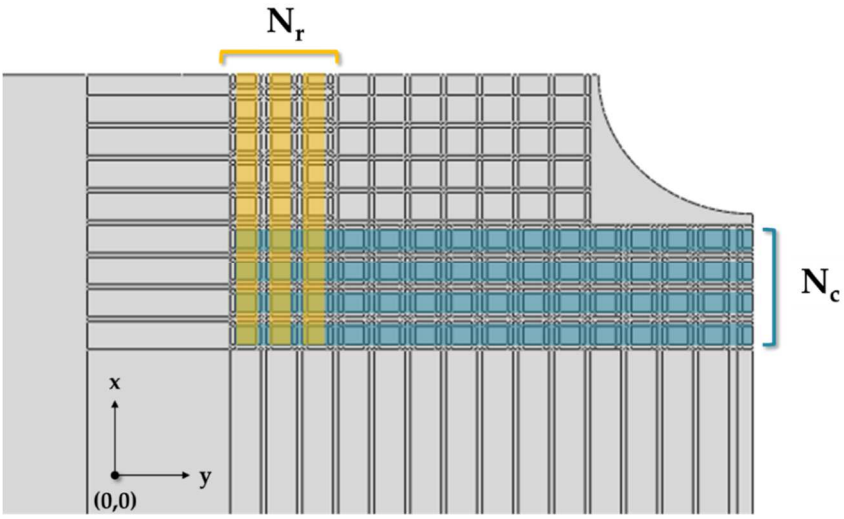

Figure 115 Graphical description of the input variables for the second optimization round

The created workflow (Figure 116) is quite similar to the one proposed in Figure 107, except for the presence of two constraints on the input variable N_c and N_r: in fact, the number of rows (and columns) could range from 1 to a maximum value that was a function of the x_{fs} and y_{fs} value (i.e. according to the position of the first spot).

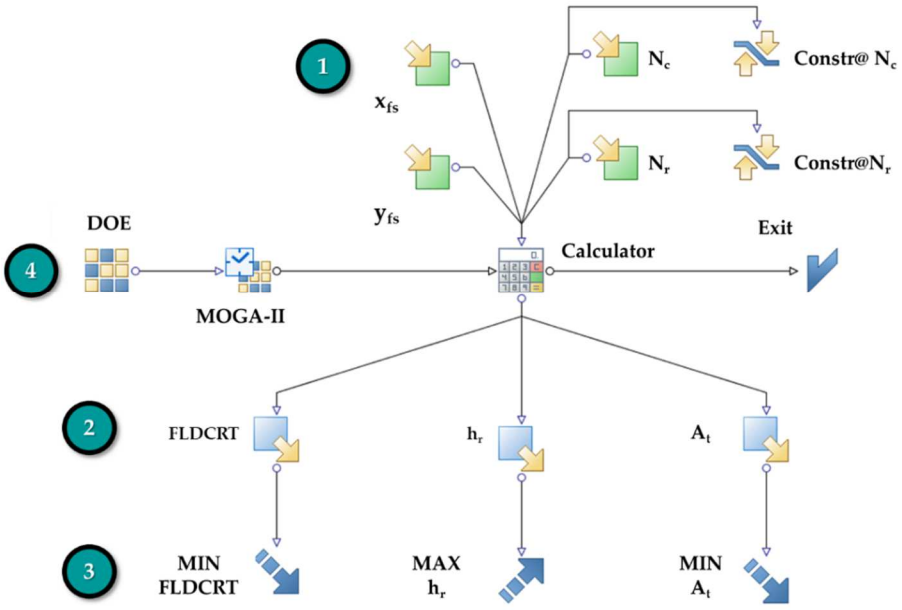

Figure 116 modeFRONTIER workflow for the second optimization round

A DoE set of designs was created, this time adopting the Sobol algorithm able to fill the design space in a uniform way avoiding clustering phenomena [121]. As done for the previous optimization round, results from the DOE designs were analysed in terms of the same output variables (visible in the zone #2 of the workflow in Figure 116); output values were then fitted by interpolating RBF, choosing the best algorithm according to the criteria described in the previous section. For this second optimization round, RS created with the Hardy's MultiQuadrics (MQ) provided the best fitting for all the output variables: a 3D representation of the created RS is reported in Figure 117.

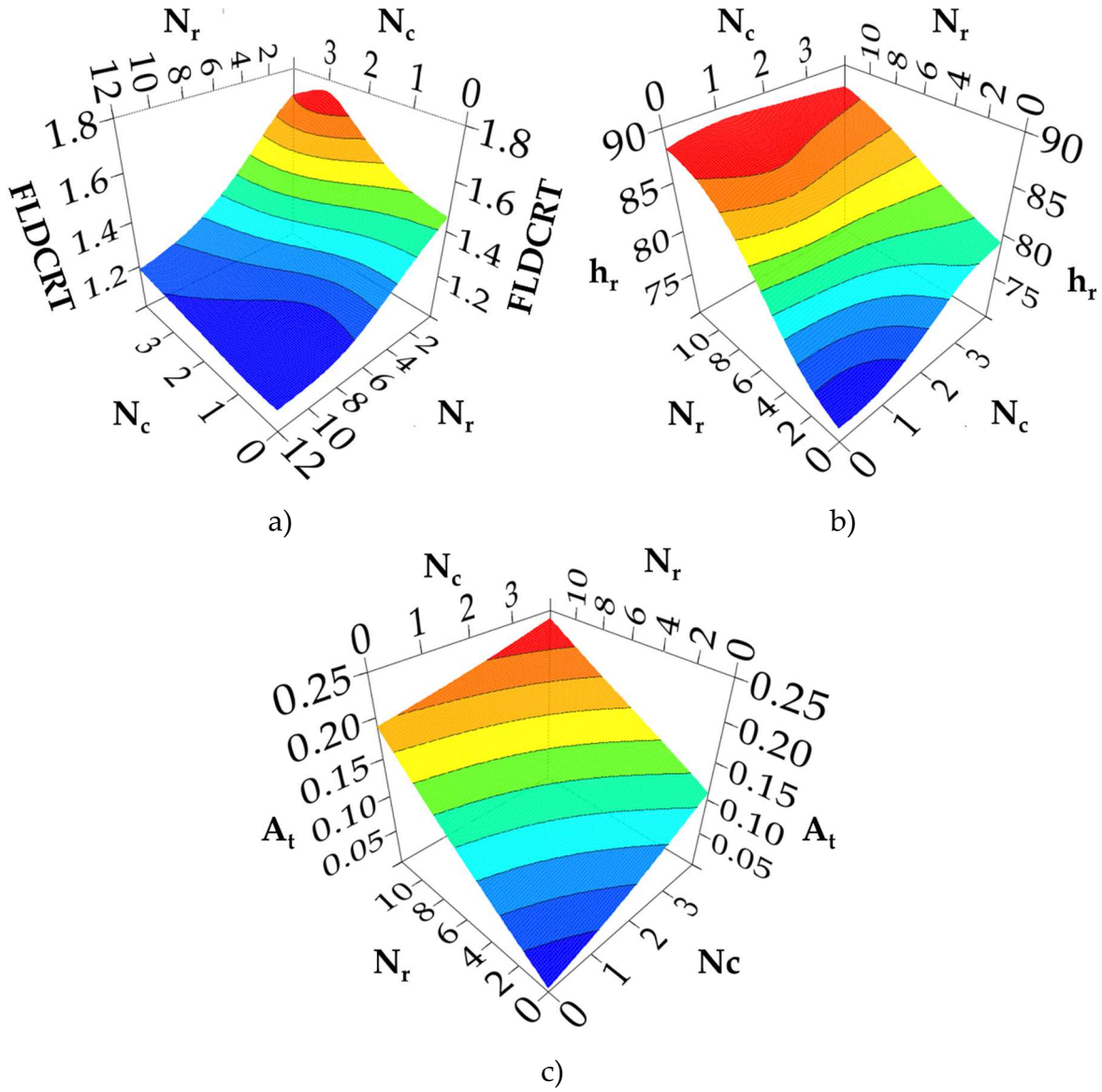

Figure 117 RS on the output variables: a) FLDCRT (MQ), b) hr (MQ), c) At (MQ)

Subsequent optimization was then run adopting the same setting, i.e. the MOGA-II as optimization evolutionary algorithm setting the same number of successive generations (100); as done for the first round, no constraint was applied on the output variable.

Optimization results were analysed through the Parallel Coordinate Chart shown in Figure 118: variables (both input and output) were represented by equally spaced parallel vertical axes, whereas each design (both belonging to the DOE and those virtually created by the genetic algorithm) were represented by a polyline connecting vertices on the axes.

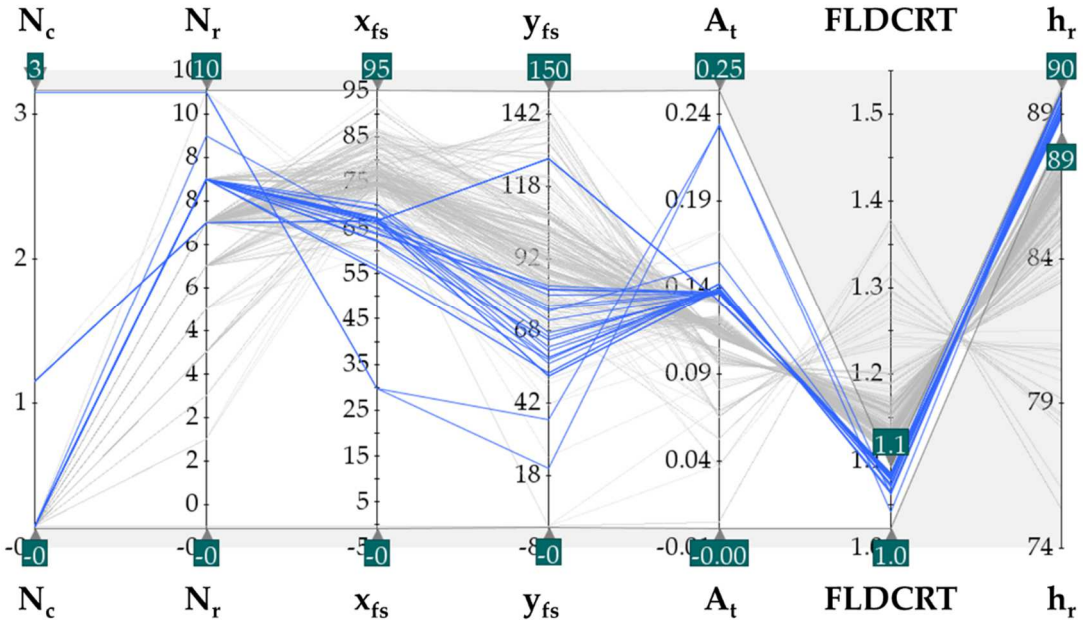

Figure 118 Results of the second round of optimization: parallel coordinate chart

Variation range of the vertical axes were filtered to isolate only the designs characterized by the highest value of the drawing depth at rupture (h_r) and a maximum value of FLDCRT between 1 and 1.1: the polylines suggested that a sound component could be manufactured by reducing the number of spot columns while considering a number of spot rows at least equal to 7.

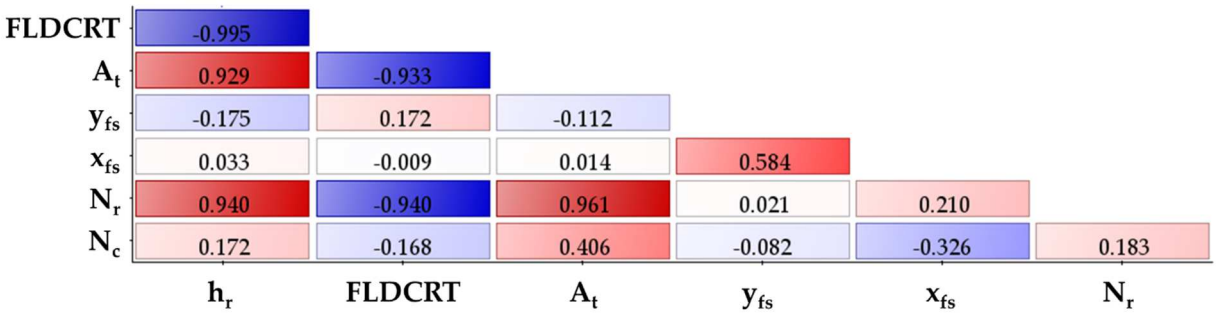

Figure 119 Second optimization round: correlation matrix on Pareto designs

The analysis of the correlation factors between the variables confirmed the indications coming from the Parallel Coordinate Chart (see Figure 119): the maximum strain severity as well as the drawing depth at rupture were much more affected by the number of spot rows (N_r) than the number of spot columns (N_c).
Also for the second optimization round, some of the designs belonging to the Pareto front were selected for the validation purposes: the input variables and the predicted

output values of the picked designs are listed in Table 11. Design #108 was considered since predicting the highest drawing depth, while the other two designs were chosen since characterized by comparable coordinates of the first spot, no spots columns and only one spots row of difference between the two.

Table 11 Pareto designs for validation purposes

ID design	Nc	Nr	x_{fs}	y_{fs}	FLDCRT	h_r	A_t
108	1	8	68.7	94.2	1.06	90	0.15
768	0	7	66.3	85.4	1.09	87	0.12
1217	0	8	46.5	104.7	1.07	88	0.14

Validation runs were analysed again in terms of the FLDCRT variable: the optimization algorithm once again slightly overestimated the maximum strain severity (see contours maps shown in Figure 120b, Figure 120d and Figure 120f). Moreover, it is worthy of notice that all the validated design reached the final punch stroke, thus were all characterized by a value of the drawing depth equal to 90 mm: the chosen heating configuration, in addition, were able to sensibly reduce the strain severity in the critic regions, since the FLDCRT distribution maps suggested the absence of possible blank rupture.
Results from the validation runs indicated the Design #768 as the optimal one since predicting the stamping of a sound component (the grey areas located far from the final panel geometry) with a sensible reduction of the treated area (no spot columns and one spot row less than the Design #1217). Finally, the two best designs coming from the two optimization rounds were compared, in particular in terms of blank drawing in two nodes of interest as done previously in the section 4.2.2 and graphically explained in Figure 99b.

Table 12 Best designs coming from the two rounds of optimization

Design ID	FLDCRT	Point A draw [mm]	Point B draw [mm]
#69 (1st round)	1.077	47.7	0.535
#768 (2nd round)	1.043	50.84	1.35

If comparing data reported in Table 12, the optimal heating configuration coming from the second optimization round was considered even more effective than the one coming from the first round: not only the percentage of the annealed area was sensibly reduced, but also the increased blank drawing (especially along the z axis on point A) pushed the strain severity to be localized far from the corner region and out of the window panel final geometry.

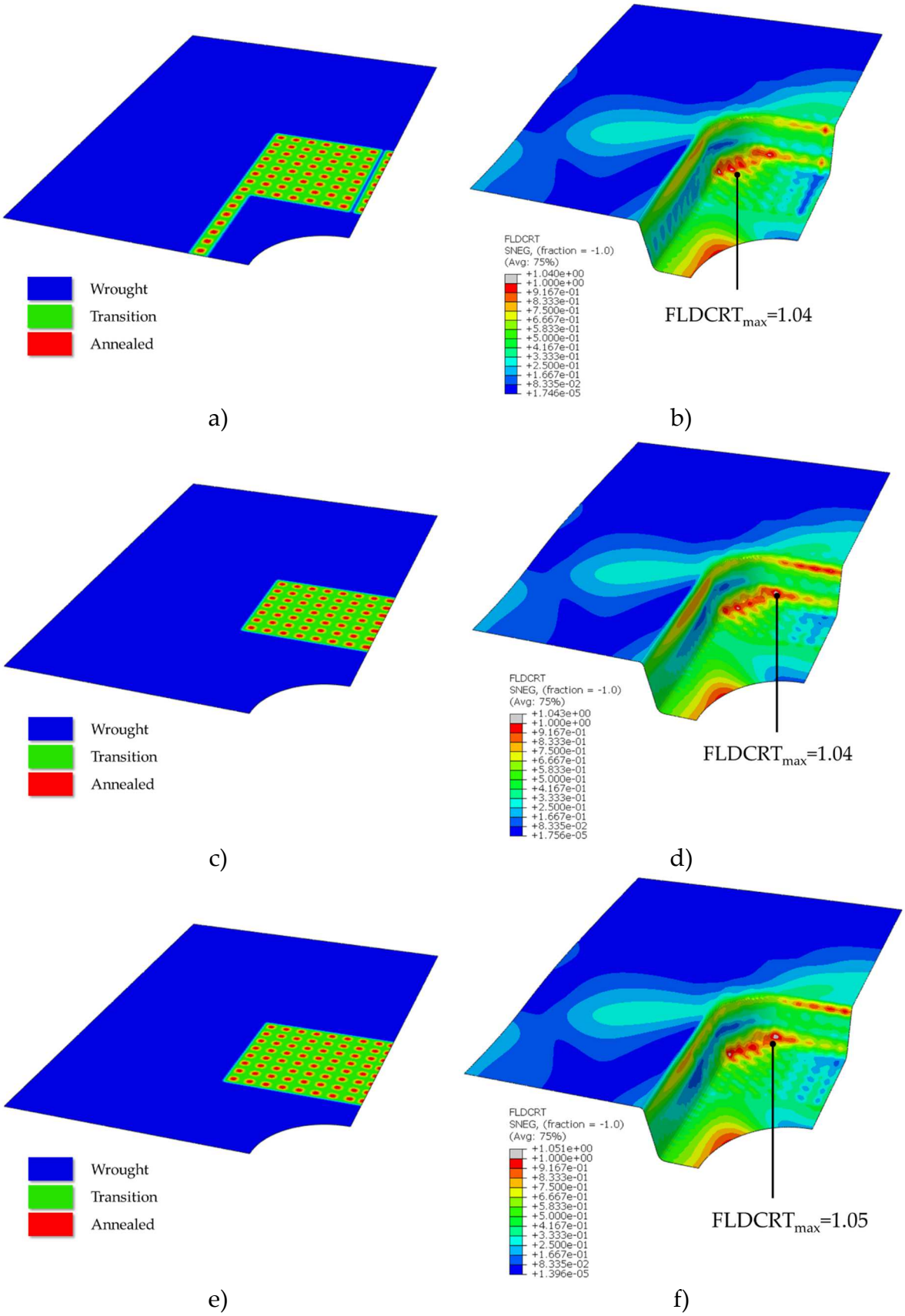

Figure 120 Simulation runs for validation purposes: a) material properties and b) FLDCRT distributions on Design #108; c) material properties and d) FLDCRT distributions on Design #768; e) material properties and f) FLDCRT distributions on Design #1217

4.3 Numerical prediction of the material properties after the heat treatment

The combination of the FE-based process design with the innovative optimization procedure provided an undeniable evidence of the advantages of HBF approach. On the other hand, as extensively discussed in section 4.1 and 4.2, the effect of the material distribution on the outcome of the stamping process was investigated modelling the blank as already subjected to the heat treatment. It is worthy of notice that the development and optimization of a numerical tool able to provide an accurate numerical prediction of the material properties after a specific heat treatment is of fundamental importance on the way to the definitive implementation of the HBF approach within an industrial environment (that is one of the main tasks of the For.Tra.In. research project).

4.3.1 Material properties from the annealing simulated tests

As introduced in the section 2.6.1, the annealing treatment was physically simulated at different temperature and soaking time levels, whose effect on the material properties was directly estimated by subjecting the striped sample, once cooled down to room temperature, to hardness measurements. As an example,
Figure 121 shows the results of the hardness measurements on the specimen heated at different temperatures (ranging from 300°C to 550°C) and considering a soaking time of 1 second: it is clearly denotable how the hardness tended to drop more pronouncedly as the heating temperature increased, reaching its lowest value at 550°C; the same plot reports the evolution of the Degree of Annealing (DoA, analytically expressed by Equation 8) variable, able to quantify in a relatively simply form the effect of the heat treatment was effective in fully annealing the material or not.

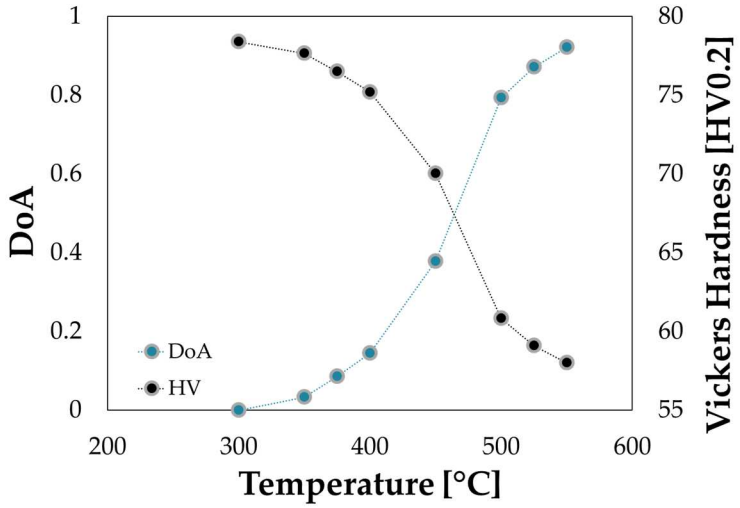

Figure 121 Hardness from physical simulation of the heat treatment, soaking time 1 seconds

The curves plotted in
Figure 121 could induce to the misleading consideration that the measured hardness was the results of holding the material at a certain temperature for the value of the imposed soaking time.

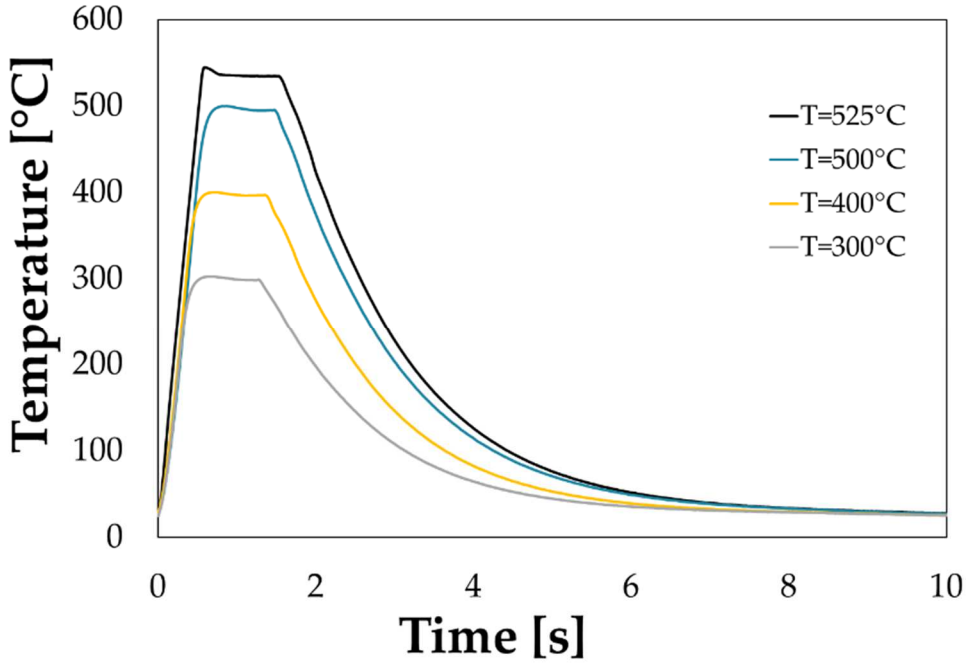

Figure 122 Temperature evolution with time

If focussing the attention on the area below the temperature evolution with time (curves are shown at 4 of the 8 investigated levels of temperature for the sake of clarity), it can be seen that the portion below the cooling part can be considered comparable (or eventually bigger) to the one relative to the soaking time. A more detailed analysis was then carried out on each of the acquired temperature curves: a Matlab code was written to read the experimental data from a spreadsheet and calculate the single contributions of the sub-areas relative to the heating, the soaking and the cooling steps.
The staked bar charts in Figure 123 (from a to f) clearly show that the contribution of the cooling phase to the overall value of the area below the curve got decreasing as the soaking time increased. In order to get rid of any misinterpretation, the total area below each curve was divided by the maximum temperature (in this case the maximum temperature corresponded to the test temperature) to calculate the equivalent time: in such a way, the final hardness value – and, consequently, the DoA achieved at the end of the heating – could be related to a quantity describing the time the material was subjected to the maximum heating temperature. The equivalent time was a fundamental importance since is one of the variable that the post-processing python script adopts to evaluate the nodal DoA.

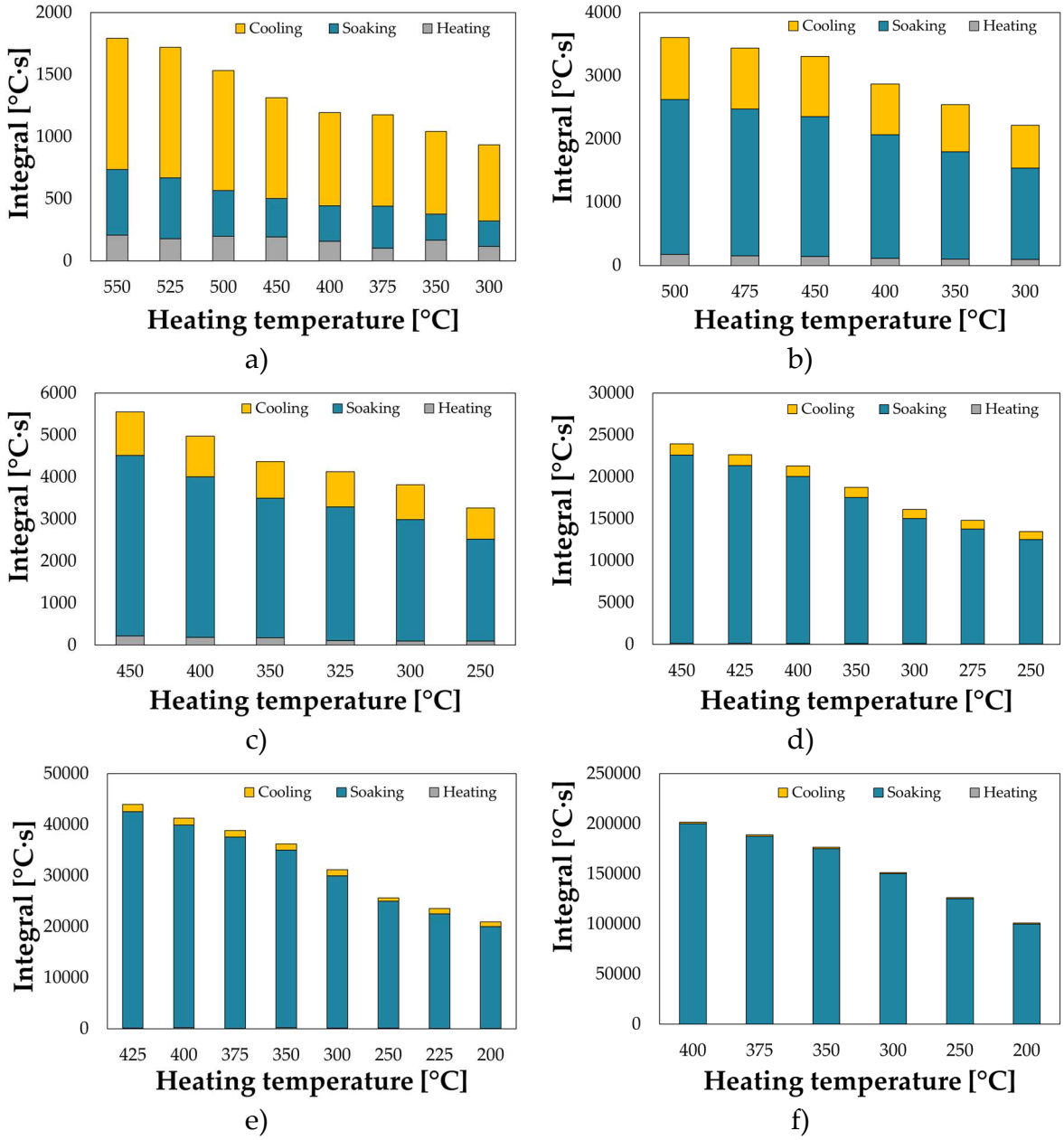

Figure 123 Stacked integral contribution: a) 1 second soaking, b) 5 seconds soaking, c) 10 seconds soaking, d) 50 seconds soaking, e) 100 seconds soaking, f) 500 seconds soaking

The hardness curves, once expressed in terms of equivalent time, were then fitted by means of a sigmoid function, whose analytical formulation is briefly recalled from Equation 9 (the meaning of the function constants have been already explained in the section 2.6.1).

$$DoA=\frac{Offset}{1+\exp[\lambda(T_0-T)]} \tag{9}$$

Experimental hardness points, grouped by the same equivalent heating time, were fitted by the mentioned analytical formulation with a good level of accordance as shown in Figure 124 (a and b, grouped in two separate plots for a better understanding): since the Offset parameter represents the amplitude of the sigmoidal

function (or alternatively the maximum value it could assume), it was set at the fixed value equal to 1, whereas the other two parameters (λ and T_0) were obtained minimizing the error between the analytical and the experimental hardness value.

a)

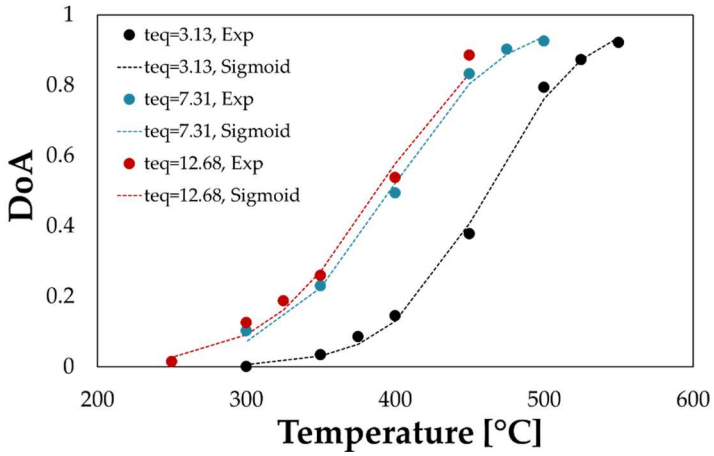

b)

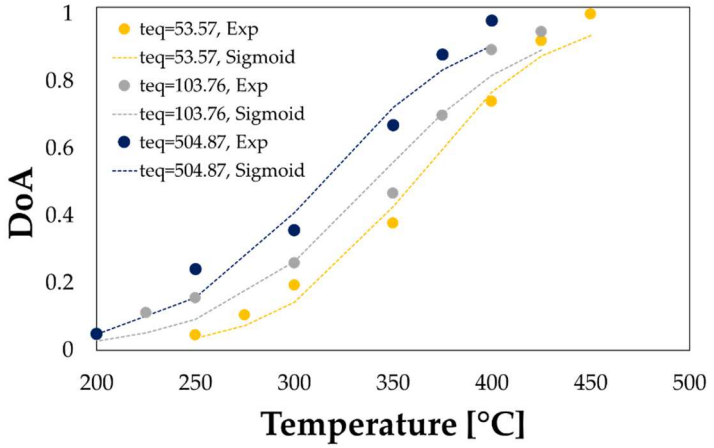

Figure 124 Fitting experimental hardness measurements by an analytical sigmoid function: soaking time a) from 3.13 to 12.68 and b) from 53.57 to 504.87

Plots suggested that comparable value of hardness, i.e. of DoA, could be achieved a lower temperature only by increasing remarkably the soaking time (for higher treatment duration, the soaking time was almost equal to the equivalent time). Sigmoid constants were then expressed as a function of time by means of logarithmic formulations, as shown in Figure 125 (a and b).

a)

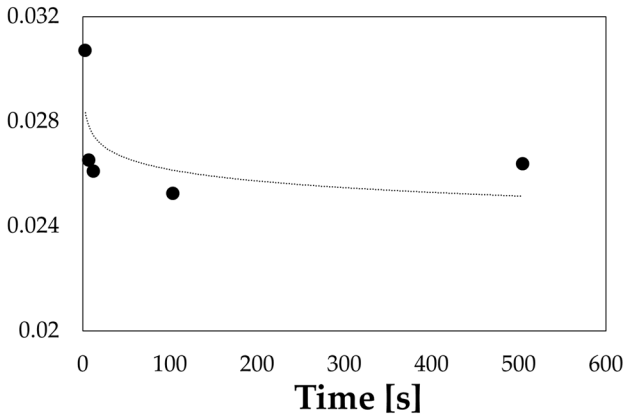

b)

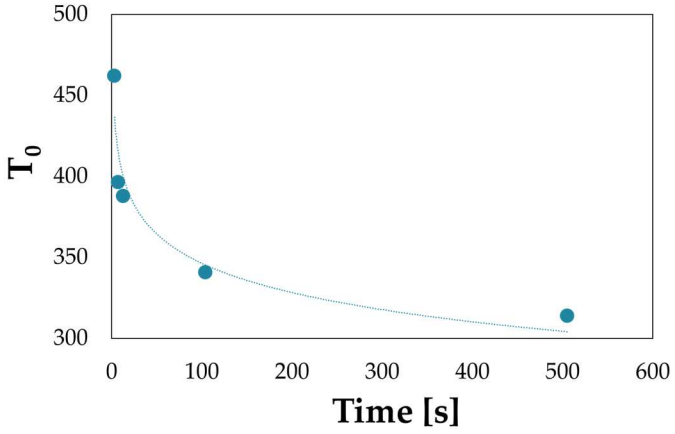

Figure 125 Sigmoid constants as a function of temperature: a) λ and b) T0

4.3.2 FE results of the benchmark model

The inverse analysis with the aim of improving the accurateness of the FE model started with the definition of the variation ranges of the two input variables, the heat transfer coefficient (HTC) and the coefficient of absorption (η), are listed in Table 13.

Table 13 Definition of the variation ranges for the input variables

Input Variable	Lower Bound	Upper Bound
HTC [W/mm²K]	0	100
η	0	1

An initial population of 50 individuals – each individual corresponded to a single numerical run – was created adopting the Sobol algorithm and 20 successive generations were considered (the MOGA-II was again adopted as optimization evolutionary algorithm). Results from the optimization were analysed in terms of input variable evolution by means of the history charts.

a)

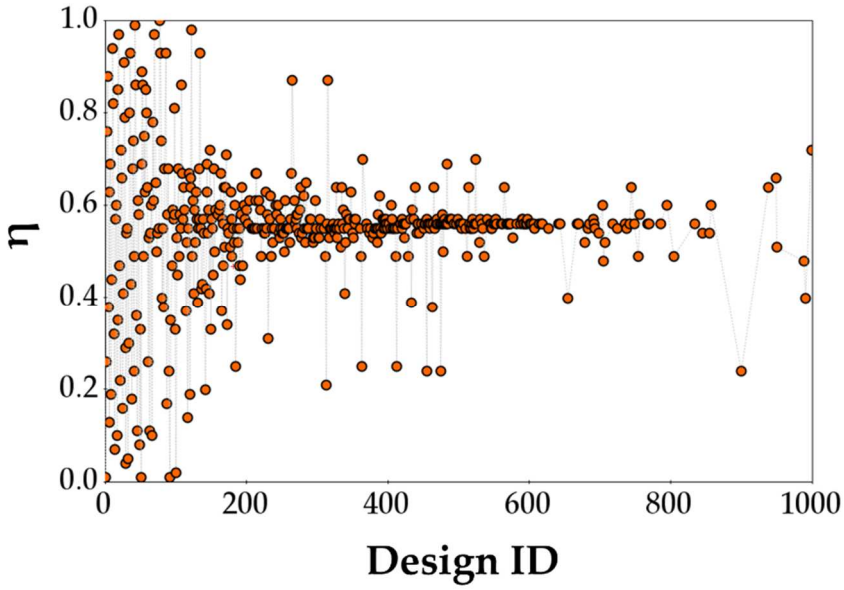

b)

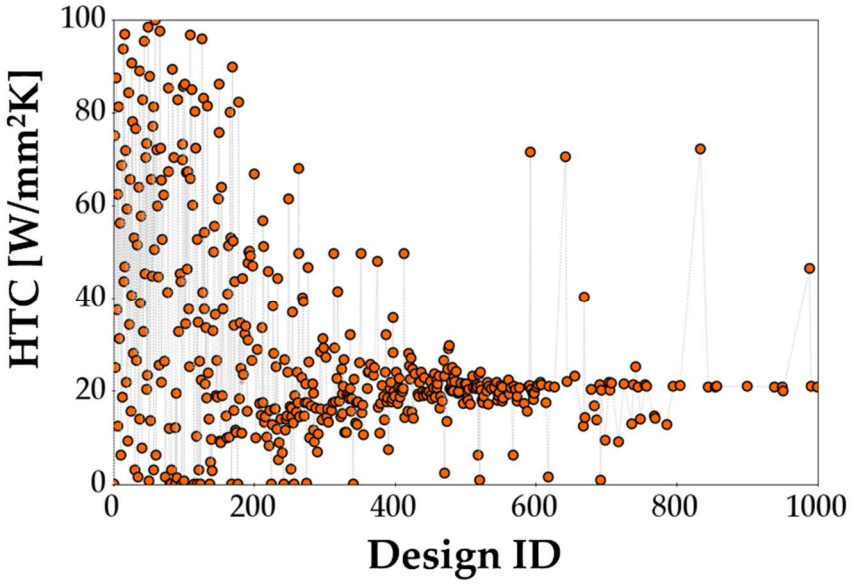

Figure 126 Results of the optimization procedure: history charts of a) η and b) HTC

Evolution of the input variables demonstrated that the genetic algorithm converged toward a stable condition, characterized by a value of the coefficient of absorption around 0.55 (Figure 126a) whereas the HTC parameter settled around a value of 20 W/mm²K (Figure 126b). The accurateness of the genetic algorithm could then be proved comparing the numerical temperature evolution of the monitored node relative to the best individual – i.e. the one able to minimize the error function – and the experimental acquisition from the thermal camera in the same point (highlighted in yellow in Figure 129).

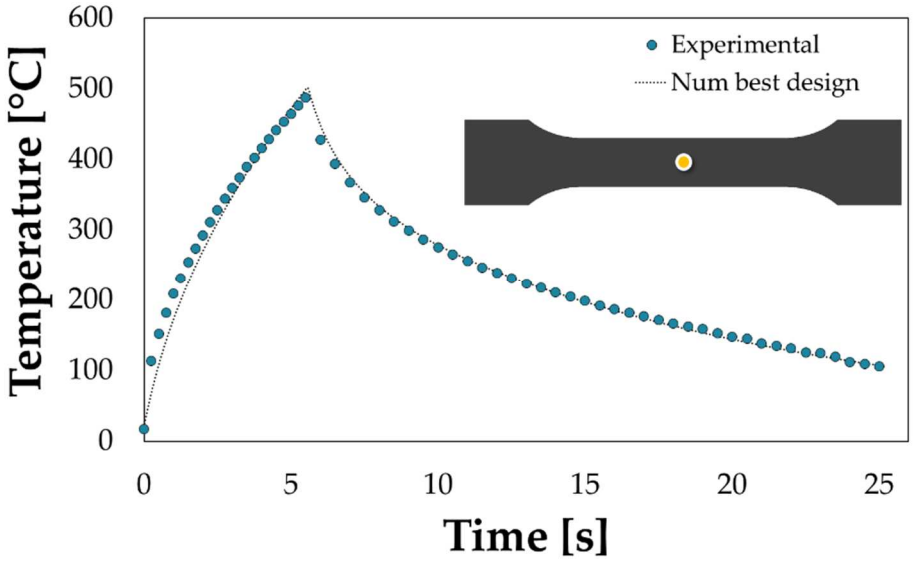

Figure 127 Best design of the optimization procedure

Numerical results from the best design were also analysed in terms of temperature distribution along a longitudinal symmetry path during both the heating and the cooling.

a)

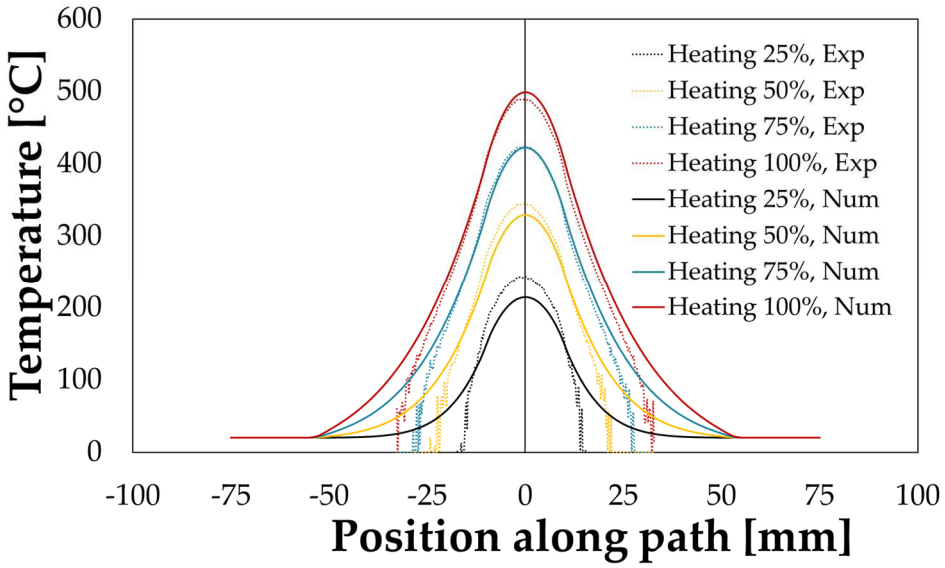

b)

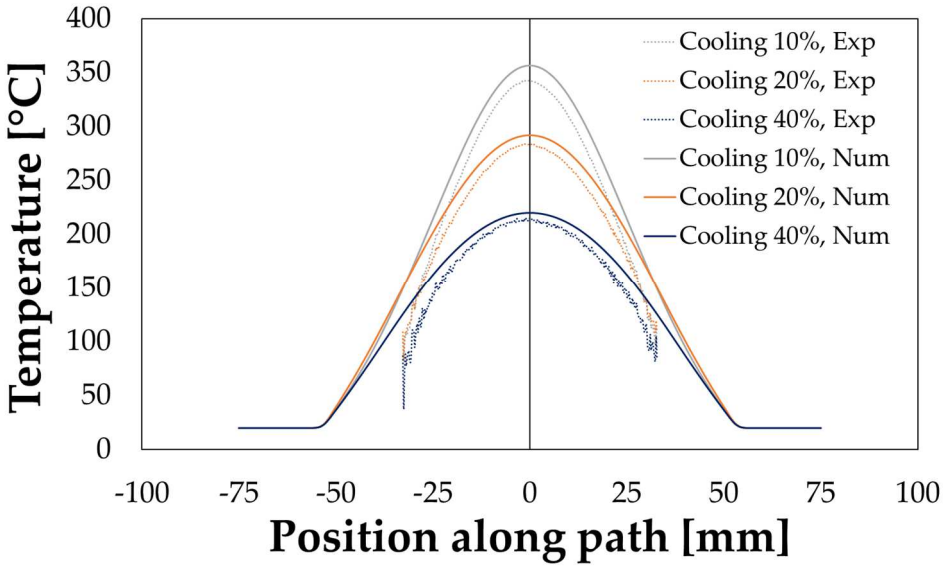

Figure 128 Temperature distributions along the longitudinal symmetry path during a) the heating phase and b) the cooling down to room temperature

The tuned model was then able to successfully predict the distribution of temperature during the laser heating as the good correspondence between numerical and experimental data clearly shows in Figure 128a; on the other hand, the model slightly overestimated the temperature distribution during the cooling down to room temperature, even though the error was always lower than 5%.

4.3.3 Numerical vs Experimental DoA distribution

The laser treated specimen was, once cooled down at room temperature, was subjected to hardness measurements along its longitudinal axis.

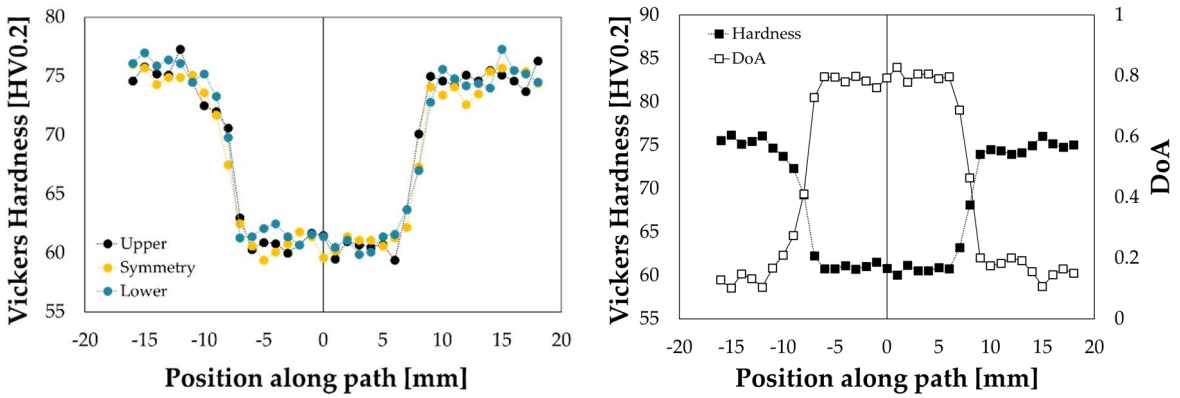

Figure 129 Laser heated dog bone specimen: a) hardness measurement along three parallel paths, b) average hardness and DoA distribution

Hardness distributions in Figure 129a refers to three parallel lines of investigation, i.e. the one along the longitudinal symmetry and the other two from opposite sides of the first one with an offset of 5 mm (labelled as Upper and Lower): the portion irradiated by the laser beam shows an evident drop in the hardness as an evidence of the occurred annealing (not complete according to the results obtained during the physical simulation tests) with a good overlapping as an evidence of the uniformity in the heating of the irradiated specimen portion. The average hardness distribution was then calculated and plotted on the same graph (Figure 129b) together with the correspondent distribution of the experimental DoA variable. The python script, whose working principle was discussed in 2.6.3, was run on the results of the best design coming from the inverse analysis and the numerical DoA distribution was compared with the experimental measurement: the comparison, shown in Figure 130, shows the capability of the created methodology in satisfactorily catch the experimental data with a slight overestimation of the post-treatment material properties in the transition regions.

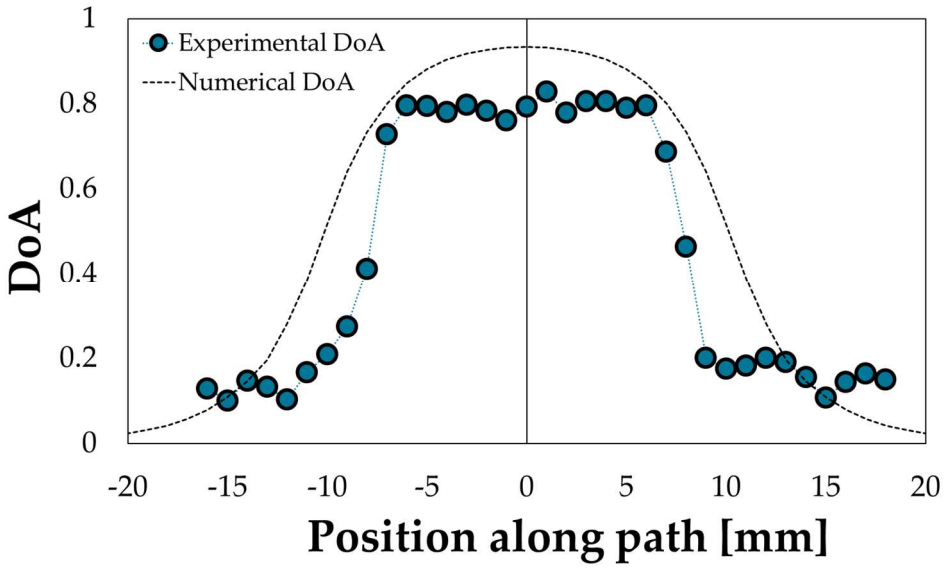

Figure 130 Numerical vs. experimental DoA distribution along the longitudinal path

It should be underlined that the numerical prediction of the DoA distribution is mainly dependent from the width of the single rectangular area approximating the nodal temperature curve (see Figure 45): to evaluate the sensibility of the DoA calculation to this parameter, the numerical best design coming from the inverse analysis was run again several time changing the frequency at which the solver wrote the field variable on the odb results file.

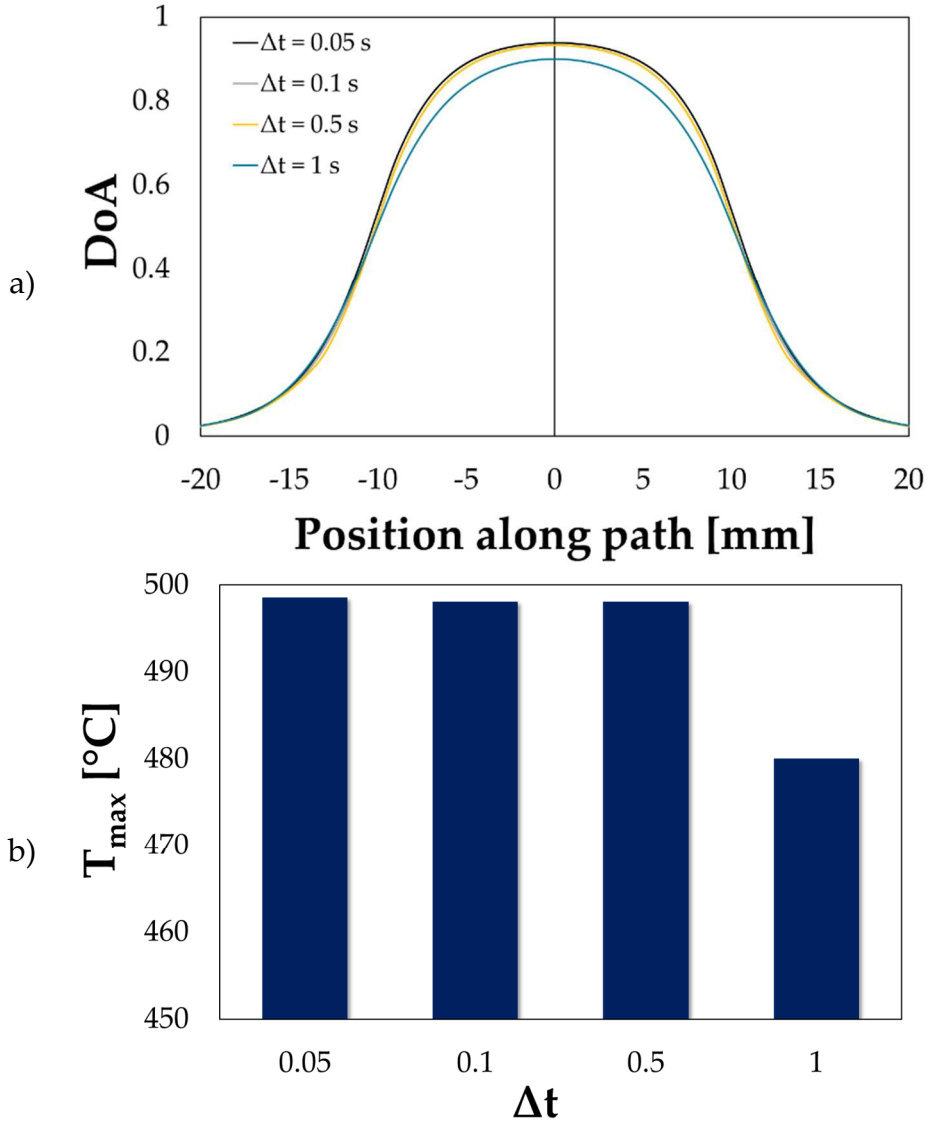

Figure 131 Effect of the field variable writing frequency: a) DoA distribution, b) maximum temperature of the node located at the geometrical spot centre

As shown in Figure 131a, not appreciable difference could be caught when increasing the time frequency from 0.05 up to 0.5 seconds (one order of magnitude), which was not the case when it was further increased to 1 second. The discrepancy can be explained looking, as an example, to the maximum temperature calculated by the script for the same node (i.e. the one located at the geometrical spot centre): the coarser discretization of the area below the curve due to the increase of the calculation time step up to 1 second led to the identification of a maximum temperature lower than the

one calculated by the script with a smaller time step. At the same time, it is worthy of notice to underline that when decreasing the calculation time step, the total time needed to complete the DoA computation increased remarkably. As a final consideration, it can be stated that the proposed procedure can be considered a valuable way to satisfactorily predict the material properties, whose computational costs has to be still optimized according to the dimension of the numerical model (simulated time period and/or total number of the nodes).

Conclusions

The demand for continuously lighter structures for mass transportation mean has been driving the design criteria of the last years: the vehicle lightweighting achieved by a massive adoption of Al alloys must be matched with the big obstacle of its poor formability at room temperature.

The state-of-the-art in terms of overcoming such a limitation suggests two main approaches: the first one based on the increase of the working temperature so that the forming operation are carried out in warm conditions, whereas the second one splits the manufacturing processes imposing a prior local heating to properly modify the material properties and carry out the forming operation at room temperature. Regardless of the specific solution, it has been strongly underlined that the adoption of a FE-based methodology represents an unavoidable step to correctly design the manufacturing process. In addition, it has been also demonstrated that the accurateness of the numerical prediction is strongly dependent, among several other factors, on the availability of accurate material data: for this reason, the characterization methodologies were specifically designed according to the approach to be investigated.

In the case of the first discussed approach, indicated as the "Heading During Forming", the prior knowledge of the alloy behaviour in warm conditions was fundamental to investigate the effect of the temperature and the strain rate on the material behaviour. Differently from the conventional approach based on heating up the whole blank before the stamping operation, the HDF approach was based on the increase of the temperature only in the deformation zones of the blank, still following the principle of locally modifying the material properties. In addition, the uncoupled thermo-mechanical approach (explicit solver to solve the forming step) provided an alternative solution to simulate the process avoiding the fully coupled formulation (implicit solver) whose final convergence might have been hindered by issues related to the contact and material modelling. The preliminary FE simulations combined with the results of the material characterization in warm conditions suggested the target to be achieved in terms of heating temperature in the blank deformation zone.

The optimization of the heating strategy was then followed by a more accurate stamping simulation including a material model temperature and strain rate dependent. Despite the yield formulation was demanded to the isotropic Von Mises formulation, the excellent validation of the numerical results was an undeniable evidence of the well-posedness of the FE-based approach. The same approach was also useful to improve the process performance, showing that the operative window could be easily re-designed by numerical simulations if the initial material conditions had to be changed (to satisfy the requirement of improving the overall quality of the component in terms of dent resistance).

As already been reported by literature, the technological gain of the HDF approach is partially counterbalanced by the complexity of the necessary equipment, which moves the attention on the other investigated methodology. In this case, the approach based on the prior material characterization, followed by the creation of a reliable numerical model and the final experimental validation was kept the same. In fact, it has been demonstrated that, if optimizing the material distribution at the end of the preliminary local heating, a remarkable improvement of the material formability could be achieved: it was clearly demonstrated when the HDF approach was applied to the manufacturing of a simple geometry, as in the case of the cup drawing. A preliminary material characterization, completed by the investigation of the material properties in the post-treatment conditions was fundamental to design, by means of an FE approach, the laser heating that had to be applied in the peripheral region of the circular specimen to be subsequently drawn at room temperature. In addition, the synergic integration of the FE model with the optimization capabilities provided by the integration platform modeFRONTIER boosted up the potentialities of the numerical process design: the exact extent of the region to be solutioned was in fact determined and the improvement in the numerical LDR was experimentally validated with high precision. The effectiveness of the approach was even more deeply confirmed when applied to a more challenging case study as the window panel for railway applications: once again the implementation of the numerical results to create accurate metamodels to be used as the bases for a virtual optimization resulted to be a highly efficient solution to properly design the distribution of the material properties to enhance the formability of the alloy and predict a correct stamping of the component.

Nevertheless, it has to be underlined that the preliminary process design via the HDF approach relied completely on the adoption of a field variable to model the post-treatment material properties distribution, thus always considering the blank as already subjected to the heat treatment. The need to improve the quality and the prediction capability of the numerical model represented the driving force toward a further development, mainly based on the definition of a post-processing procedure able to predict the distribution of the mechanical properties after the local heating. Also in this case, the formulation of the procedure started from a specific characterization methodology based on the physical simulation of the annealing treatment. Results from the preliminary tests were then used to formulate a new variable, the Degree of Annealing (DoA), able to quantify the effect of a specific combination of temperature and holding time to bring the material under investigation (the AA5754) from an initial wrought condition (H32) to the annealed one (H111). It is strongly believed that the adoption of such a procedure is able, thanks to a more precise identification of the post-treatment distribution of properties, to boost up the accurateness of the numerical predictions. The DoA analytical estimation

and its application to a simple case as the laser annealing of a dog-bone specimen has been initially formulated during the visiting period at the Ohio State University and represents only the first step toward a more effective process design, opening the way to the subsequent activities aimed at implementing a more refined material constitutive modelling capable of associating material properties, more advanced yield surface formulations and FLC based damage criteria for each DoA level.

References

[1] J. German, Hybrid vehicles: Trends in technology development and cost reduction, 2015 Int. Counc. Clean Transp. (2015) 1–18.

[2] A. Yildiz, A. Piccininni, F. Bottiglione, G. Carbone, Modeling chain continuously variable transmission for direct implementation in transmission control, Mech. Mach. Theory. 105 (2016) 428–440. https://doi.org/10.1016/j.mechmachtheory.2016.07.015.

[3] C.D. Keeling, S.C. Piper, R.B. Bacastow, M. Wahlen, T.P. Whorf, M. Heimann, H.A. Meijer, Atmospheric CO2 and 13CO2 Exchange with the Terrestrial Biosphere and Oceans from 1978 to 2000: Observations and Carbon Cycle Implications BT - A History of Atmospheric CO2 and Its Effects on Plants, Animals, and Ecosystems, in: I.T. Baldwin, M.M. Caldwell, G. Heldmaier, R.B. Jackson, O.L. Lange, H.A. Mooney, E.-D. Schulze, U. Sommer, J.R. Ehleringer, M. Denise Dearing, T.E. Cerling (Eds.), Springer New York, New York, NY, 2005: pp. 83–113. https://doi.org/10.1007/0-387-27048-5_5.

[4] S.I. of Oceanographic, The Keeling curve, (n.d.). https://scripps.ucsd.edu/programs/keelingcurve/.

[5] I.E. Agency, Railway Handbook 2017, 2017.

[6] International Energy Agency, The Future of Rail. Opportunities for energy and the environment, (2019) 171. www.opsi.gov.uk/click-use/index.htm,.

[7] A. Poznak, D. Freiberg, P. Sanders, Automotive Wrought Aluminium Alloys, Elsevier Ltd., 2018. https://doi.org/10.1016/B978-0-08-102063-0.00010-2.

[8] a. H. Musfirah, a. . Jaharah, Magnesium and Aluminum Alloys in Automotive Industry, J. Appl. Sci. Res. 8 (2012) 4865–4875.

[9] W.J. Joost, Reducing vehicle weight and improving U.S. energy efficiency using integrated computational materials engineering, Jom. 64 (2012) 1032–1038. https://doi.org/10.1007/s11837-012-0424-z.

[10] K. Kumar Dama, V. Suresh Babu, R.N. Rao, State of the Art on Automotive Lightweight Body-in-White Design, Mater. Today Proc. 5 (2018) 20966–20971. https://doi.org/10.1016/j.matpr.2018.6.486.

[11] J. Hirsch, Recent development in aluminium for automotive applications, Trans. Nonferrous Met. Soc. China (English Ed. 24 (2014) 1995–2002. https://doi.org/10.1016/S1003-6326(14)63305-7.

[12] DIN EN 45545-2, Railway applications - Fire protection on railway vehicles - Part 2: Requirements for fire behaviour of materials and components, (2016).

[13] D.V. Wilson, Aluminium versus steel in the family car - the formability factor, J. Mech. Work. Technol. 16 (1988) 257–277.

[14] S. Kalpakjian, S.R. Schmid, Manufacturing processes for engineering materials, Pearson Education, Singapore; London, 2017.

[15] K. Iwanaga, H. Tashiro, H. Okamoto, K. Shimizu, Improvement of formability from room temperature to warm temperature in AZ-31 magnesium alloy, J. Mater. Process. Technol. 155–156 (2004) 1313–1316. https://doi.org/10.1016/j.jmatprotec.2004.04.181.

[16] D. Li, A. Ghosh, Tensile deformation behavior of aluminum alloys at warm forming temperatures, Mater. Sci. Eng. A. 352 (2003) 279–286. https://doi.org/10.1016/S0921-5093(02)00915-2.
[17] F. Ozturk, H. Pekel, H.S. Halkaci, The effect of strain-rate sensitivity on formability of AA 5754-O at cold and warm temperatures, J. Mater. Eng. Perform. 20 (2011) 77–81. https://doi.org/10.1007/s11665-010-9652-y.
[18] S.S. Panicker, S.K. Panda, Formability Analysis of AA5754 Alloy at Warm Condition: Appraisal of Strain Rate Sensitive Index, Mater. Today Proc. 2 (2015) 1996–2004. https://doi.org/10.1016/j.matpr.2015.07.169.
[19] P.A. Tebbe, G.T. Kridli, Warm forming of aluminium alloys: An overview and future directions, Int. J. Mater. Prod. Technol. 21 (2004) 24–40. https://doi.org/10.1504/ijmpt.2004.004737.
[20] R. Neugebauer, T. Altan, M. Geiger, M. Kleiner, A. Sterzing, Sheet metal forming at elevated temperatures, CIRP Ann. - Manuf. Technol. 55 (2006) 793–816. https://doi.org/10.1016/j.cirp.2006.10.008.
[21] S. Toros, F. Ozturk, I. Kacar, Review of warm forming of aluminum-magnesium alloys, J. Mater. Process. Technol. 207 (2008) 1–12. https://doi.org/10.1016/j.jmatprotec.2008.03.057.
[22] L.F. Simões, V. M., Coër, J., Laurent, H., Oliveira, M. C., Alves, J. L., Manach, P. Y., & Menezes, Influence of the yield criteria in the numerical simulation of an AA5745-O cylindrical cup, Congr. Métodos Numéricos En Ing. (2013).
[23] T. den Boogaard, P. Bolt, R.J. Werkhoven, M. Hout, Aluminium sheet forming simulations: influence of the yield surface, J. Mater. Process. Technol. - J MATER Process TECHNOL. (2002).
[24] M. Jain, J. Allin, M.J. Bull, Deep drawing characteristics of automotive aluminum alloys, Mater. Sci. Eng. A. 256 (1998) 69–82. https://doi.org/10.1016/s0921-5093(98)00845-4.
[25] G. Palumbo, L. Tricarico, Numerical and experimental investigations on the Warm Deep Drawing process of circular aluminum alloy specimens, J. Mater. Process. Technol. 184 (2007) 115–123. https://doi.org/10.1016/j.jmatprotec.2006.11.024.
[26] S. Bruschi, T. Altan, D. Banabic, P.F. Bariani, A. Brosius, J. Cao, A. Ghiotti, M. Khraisheh, M. Merklein, A.E. Tekkaya, Testing and modelling of material behaviour and formability in sheet metal forming, CIRP Ann. - Manuf. Technol. 63 (2014) 727–749. https://doi.org/10.1016/j.cirp.2014.05.005.
[27] A.E. Tekkaya, J.M. Allwood, P.F. Bariani, S. Bruschi, J. Cao, S. Gramlich, P. Groche, G. Hirt, T. Ishikawa, C. Löbbe, J. Lueg-Althoff, M. Merklein, W.Z. Misiolek, M. Pietrzyk, R. Shivpuri, J. Yanagimoto, Metal forming beyond shaping: Predicting and setting product properties, CIRP Ann. - Manuf. Technol. 64 (2015) 629–653. https://doi.org/10.1016/j.cirp.2015.05.001.
[28] M. Baral, J. Ha, Y.P. Korkolis, Plasticity and ductile fracture modeling of an Al–Si–Mg die-cast alloy, Int. J. Fract. 216 (2019) 101–121. https://doi.org/10.1007/s10704-019-00345-1.

[29] J. Ha, M. Baral, Y.P. Korkolis, Plastic anisotropy and ductile fracture of bake-hardened AA6013 aluminum sheet, Int. J. Solids Struct. 155 (2018) 123–139. https://doi.org/10.1016/j.ijsolstr.2018.07.015.
[30] H. Tian, B. Brownell, M. Baral, Y.P. Korkolis, Earing in cup-drawing of anisotropic Al-6022-T4 sheets, Int. J. Mater. Form. 10 (2017) 329–343. https://doi.org/10.1007/s12289-016-1282-y.
[31] F. Barlat, D.J. Lege, J.C. Brem, A six-component yield function for anisotropic materials, Int. J. Plast. 7 (1991) 693–712. https://doi.org/10.1016/0749-6419(91)90052-Z.
[32] F. Barlat, J.C. Brem, J.W. Yoon, K. Chung, R.E. Dick, D.J. Lege, F. Pourboghrat, S.H. Choi, E. Chu, Plane stress yield function for aluminum alloy sheets - Part 1: Theory, Int. J. Plast. 19 (2003) 1297–1319. https://doi.org/10.1016/S0749-6419(02)00019-0.
[33] F. Barlat, H. Aretz, J.W. Yoon, M.E. Karabin, J.C. Brem, R.E. Dick, Linear transfomation-based anisotropic yield functions, Int. J. Plast. 21 (2005) 1009–1039. https://doi.org/10.1016/j.ijplas.2004.06.004.
[34] D. Banabic, F. Barlat, O. Cazacu, T. Kuwabara, Advances in anisotropy and formability, Int. J. Mater. Form. 3 (2010) 165–189. https://doi.org/10.1007/s12289-010-0992-9.
[35] D. Banabic, T. Kuwabara, T. Balan, D.S. Comsa, An anisotropic yield criterion for sheet metals, J. Mater. Process. Technol. 157–158 (2004) 462–465. https://doi.org/10.1016/j.jmatprotec.2004.07.106.
[36] N. Abedrabbo, F. Pourboghrat, J. Carsley, Forming of AA5182-O and AA5754-O at elevated temperatures using coupled thermo-mechanical finite element models, Int. J. Plast. 23 (2007) 841–875. https://doi.org/10.1016/j.ijplas.2006.10.005.
[37] S. Novotny, M. Geiger, Process design for hydroforming of lightweight metal sheets at elevated temperatures, J. Mater. Process. Technol. 138 (2003) 594–599. https://doi.org/10.1016/S0924-0136(03)00042-6.
[38] G. Palumbo, A. Piccininni, Numerical-experimental investigations on the manufacturing of an aluminium bipolar plate for proton exchange membrane fuel cells by warm hydroforming, Int. J. Adv. Manuf. Technol. 69 (2013) 731–742. https://doi.org/10.1007/s00170-013-5047-1.
[39] G. Palumbo, A. Piccininni, P. Guglielmi, V. Piglionico, D. Sorgente, Investigation about the oil pressure rate in the warm hydroforming of an Al-Mg alloy component, 1 (n.d.).
[40] S. Mahabunphachai, M. Koç, Investigations on forming of aluminum 5052 and 6061 sheet alloys at warm temperatures, Mater. Des. 31 (2010) 2422–2434. https://doi.org/10.1016/j.matdes.2009.11.053.
[41] H. Gedikli, Ö.N. Cora, M. Koç, Comparative investigations on numerical modeling for warm hydroforming of AA5754-O aluminum sheet alloy, Mater. Des. 32 (2011) 2650–2662. https://doi.org/10.1016/j.matdes.2011.01.025.
[42] M. Geiger, M. Merklein, U. Vogt, Aluminum tailored heat treated blanks, Prod.

Eng. 3 (2009) 401–410. https://doi.org/10.1007/s11740-009-0179-8.
[43] A. Piccininni, G. Di Michele, G. Palumbo, D. Sorgente, L. Tricarico, Improving the hydromechanical deep-drawing process using aluminum tailored heat treated blanks, Acta Metall. Sin. (English Lett. 28 (2015). https://doi.org/10.1007/s40195-015-0347-0.
[44] K. Siefert, M. Merklein, W. Nester, M. Grünbaum, Enhancement of forming limits of aluminum alloys using an intermediate heat treatment, AIP Conf. Proc. 1315 (2010) 359–364. https://doi.org/10.1063/1.3552469.
[45] A.M. Sulzberger, M. Merklein, W. Staufner, D. Wortberg, Methodology to Produce Locally Heat-Treated EN AW-5182 Aluminum Alloy Sheet Metal Parts, Key Eng. Mater. 504–506 (2012) 113–118. https://doi.org/10.4028/www.scientific.net/KEM.504-506.113.
[46] M. Merklein, H. Nguyen, Advanced laser heat treatment with respect for the application for Tailored Heat Treated Blanks, Phys. Procedia. 5 (2010) 233–242. https://doi.org/10.1016/j.phpro.2010.08.049.
[47] H. Fröck, M. Graser, B. Milkereit, M. Reich, M. Lechner, M. Merklein, O. Kessler, Precipitation behaviour and mechanical properties during short-term heat treatment for tailor heat treated profiles (THTP) of aluminium alloy 6060 T4, Mater. Sci. Forum. 877 (2017) 400–406. https://doi.org/10.4028/www.scientific.net/MSF.877.400.
[48] M. Lechner, A. Kuppert, M. Merklein, Comprehensive Material Characterization for an Intermediate Heat Treatment, Key Eng. Mater. 549 (2013) 39–44. https://doi.org/10.4028/www.scientific.net/KEM.549.39.
[49] M. Geiger, M. Merklein, M. Kerausch, Finite element simulation of deep drawing of tailored heat treated blanks, CIRP Ann. - Manuf. Technol. 53 (2004) 223–226. https://doi.org/10.1016/S0007-8506(07)60684-2.
[50] A. Kahrimanidis, M. Lechner, J. Degner, D. Wortberg, M. Merklein, Process design of aluminum tailor heat treated blanks, Materials (Basel). 8 (2015) 8524–8538. https://doi.org/10.3390/ma8125476.
[51] M. Lechner, A. Kuppert, H. Hagenah, Optimization of the heat treatment layout and blank outline of THTB, 557 (2013) 2465–2471. https://doi.org/10.4028/www.scientific.net/KEM.554-557.2465.
[52] J. Christensen, C. Bastien, Numerical Techniques for Structural Assessment of Vehicle Architectures, in: J. Christensen, C.B.T.-N.O. of V.S.S. Bastien (Eds.), Nonlinear Optim. Veh. Saf. Struct., Butterworth-Heinemann, Oxford, 2016: pp. 51–105. https://doi.org/https://doi.org/10.1016/B978-0-12-417297-5.00002-X.
[53] K.H. Yang, Chapter 8 - Modal and Transient Dynamic Analysis, in: K.-H.B.T.-B.F.E.M. as A. to I.B. Yang (Ed.), Academic Press, 2018: pp. 309–382. https://doi.org/https://doi.org/10.1016/B978-0-12-809831-8.00008-8.
[54] Dassault Systems, Abaqus Analysis User's Manual, (2017).
[55] K.-J. Bathe, E.L. Wilson, Numerical methods in finite element analysis, Prentice-Hall, Englewood Cliffs, NJ, 1976. http://cds.cern.ch/record/105356.
[56] Transportation Bombardier, FLEXX Eco Bogies Technical Data, (n.d.).

http://www.bombardier.com/content/dam/Websites/bombardiercom/supporting-documents/BT/Bombardier-Transportation-Bogies-FLEXX-Eco.pdf.
[57] Transportation Bombardier, MITRAC 500 Driven by Reliability, (n.d.). https://www.bombardier.com/content/dam/Websites/bombardiercom/supporting-documents/BT/Bombardier-Transportation-MITRAC-500.pdf.
[58] I. 6892-1, Metallic materials - Tensile testing - Part 1: Method of test at room temperature, 2009.
[59] ISO 6892-2, Metallic materials -- Tensile testing -- Part 2: Method of test at elevated temperature, 2011.
[60] Y. Fujii, T. Shinmiya, Y. Yamasaki, K. Higai, Method for drawing forming limit diagram for press forming, crack prediction method, and method for manufacturing pressed components, EP2839896B1, 2012.
[61] S.P. Keeler, W.A. Backofen, Plastic instability and fracture in sheets stretched over rigid punches, ASM Trans. Q. 56 (1963) 25–48.
[62] S.P. Keeler, Determination of Forming Limits in Automotive Stampings, SAE Tech. Pap. Ser. 1 (2010). https://doi.org/10.4271/650535.
[63] G.M. Goodwin, Application of Strain Analysis to Sheet Metal Forming Problems in the Press Shop, SAE Tech. Pap. Ser. 1 (2010) 380–387. https://doi.org/10.4271/680093.
[64] N.J. Den Uijl, L.J. Carless, 3 - Advanced metal-forming technologies for automotive applications, in: J.B.T.-A.M. in A.E. Rowe (Ed.), Woodhead Publishing, 2012: pp. 28–56. https://doi.org/https://doi.org/10.1533/9780857095466.28.
[65] H.J. Bong, F. Barlat, M.G. Lee, D.C. Ahn, The forming limit diagram of ferritic stainless steel sheets: Experiments and modeling, Int. J. Mech. Sci. 64 (2012) 1–10. https://doi.org/10.1016/j.ijmecsci.2012.08.009.
[66] P. Hora, L. Tong, B. Berisha, Modified maximum force criterion, a model for the theoretical prediction of forming limit curves, Int. J. Mater. Form. 6 (2013) 267–279. https://doi.org/10.1007/s12289-011-1084-1.
[67] K. Nakazima, T. Kikuma, K. Hasuka, Study on the formability of steel sheet, Yamata Tech. Rep. 264 (1968) 8517–8530.
[68] Z. Marciniak, K. Kuczyński, Limit strains in the processes of stretch-forming sheet metal, Int. J. Mech. Sci. 9 (1967) 609–620. https://doi.org/10.1016/0020-7403(67)90066-5.
[69] M.R. Tharrett, T.B. Stoughton, Stretch-Bend Forming Limits of 1008 AK Steel, SAE Tech. Pap. Ser. 1 (2010). https://doi.org/10.4271/2003-01-1157.
[70] R.B. Kelly, S.B. Leen, I.R. Pashby, A.R. Kennedy, The measurement of friction for superplastic forming of Ti-6Al-4V, 448 (2004) 111–116. https://doi.org/10.4028/www.scientific.net/MSF.447-448.111.
[71] J. Min, T.B. Stoughton, J.E. Carsley, J. Lin, Compensation for process-dependent effects in the determination of localized necking limits, Int. J. Mech. Sci. 117 (2016) 115–134. https://doi.org/10.1016/j.ijmecsci.2016.08.008.
[72] T. Abovyan, G.T. Kridli, P.A. Friedman, G. Ayoub, Formability prediction of

aluminum sheet alloys under isothermal forming conditions, J. Manuf. Process. 20 (2014) 406–413. https://doi.org/10.1016/j.jmapro.2014.08.003.
[73] R. Sowerby, E. Chu, J.L. Duncan, Strains in Metalforming, 17 (1982) 95–101.
[74] Z. Tan, L. Melin, C. Magnusson, Application of an image processing technique in strain measurement in sheet metal forming, J. Mater. Process. Tech. 33 (1992) 299–310. https://doi.org/10.1016/0924-0136(92)90215-E.
[75] C.D. Schwindt, M. Stout, L. Iurman, J.W. Signorelli, Forming Limit Curve Determination of a DP-780 Steel Sheet, Procedia Mater. Sci. 8 (2015) 978–985. https://doi.org/10.1016/j.mspro.2015.04.159.
[76] S. Dicecco, M. Di Ciano, C. Butcher, M. Worswick, Limit Strain Characterization in an Aluminum Die-Quenching Process, IOP Conf. Ser. Mater. Sci. Eng. 418 (2018). https://doi.org/10.1088/1757-899X/418/1/012035.
[77] K. Wang, J.E. Carsley, B. He, J. Li, L. Zhang, Measuring forming limit strains with digital image correlation analysis, J. Mater. Process. Technol. 214 (2014) 1120–1130. https://doi.org/10.1016/j.jmatprotec.2014.01.001.
[78] M.A. Sutton, J.J. Orteu, H.W. Schreier, Image Correlation for Shape, Motion and Deformation, Springer, 2009.
[79] H. Hu, J. Liang, Z. Tang, X. Guo, L. Li, Digital speckle based strain measurement system for forming limit diagram prediction, Opt. Lasers Eng. 55 (2014) 12–21. https://doi.org/10.1016/j.optlaseng.2013.10.017.
[80] J. Min, T.B. Stoughton, J.E. Carsley, J. Lin, Comparison of DIC Methods of Determining Forming Limit Strains, Procedia Manuf. 7 (2017) 668–674. https://doi.org/10.1016/j.promfg.2016.12.099.
[81] Watlow, WATLOW FIREROD® Cartridge Heaters, (n.d.) 7–56. https://www.watlow.com/en/products/heaters/cartridge-insertion-heaters/firerod-cartridge-heaters.
[82] S. Spring, Nitrogen gas cylinders, 2015.
[83] G. Ekstrand, N. Asnafi, On testing of the stiffness and the dent resistance of autobody panels, Mater. Des. 19 (1998) 145–156. https://doi.org/Doi: 10.1016/s0261-3069(98)00028-4.
[84] S. Holmberg, P. Thilderkvist, Influence of material properties and stamping conditions on the stiffness and static dent resistance of automotive panels, Mater. Des. 23 (2002) 681–691. https://doi.org/10.1016/S0261-3069(02)00079-1.
[85] Creaform, Creaform - Portable 3D measurement solutions, (n.d.). https://www.creaform3d.com/en/portable-3d-scanner-handyscan-3d.
[86] R.P. Garrett, J. Lin, T.A. Dean, An investigation of the effects of solution heat treatment on mechanical properties for AA 6xxx alloys: Experimentation and modelling, Int. J. Plast. 21 (2005) 1640–1657. https://doi.org/10.1016/j.ijplas.2004.11.002.
[87] K. Zheng, L. Zhu, J. Lin, T.A. Dean, N. Li, An experimental investigation of the drawability of AA6082 sheet under different elevated temperature forming processes, J. Mater. Process. Technol. 273 (2019) 116225. https://doi.org/10.1016/j.jmatprotec.2019.05.006.

[88] S. Dadbakhsh, A. Karimi Taheri, C.W. Smith, Strengthening study on 6082 Al alloy after combination of aging treatment and ECAP process, Mater. Sci. Eng. A. 527 (2010) 4758–4766. https://doi.org/10.1016/j.msea.2010.04.017.
[89] H.W. Höppel, L. May, M. Prell, M. Göken, Influence of grain size and precipitation state on the fatigue lives and deformation mechanisms of CP aluminium and AA6082 in the VHCF-regime, Int. J. Fatigue. 33 (2011) 10–18. https://doi.org/10.1016/j.ijfatigue.2010.04.013.
[90] M. El-Shennawy, K. Abdel-Aziz, A.A. Omar, Metallurgical and mechanical properties of heat treatable aluminum alloy AA6082 welds, Int. J. Appl. Eng. Res. 12 (2017) 2832–2839.
[91] Y. Birol, E. Gokcil, M.A. Guvenc, S. Akdi, Processing of high strength EN AW 6082 forgings without a solution heat treatment, Mater. Sci. Eng. A. 674 (2016) 25–32. https://doi.org/10.1016/j.msea.2016.07.062.
[92] G. Mrowka-Nowotnik, J. Sieniawski, A. Nowotnik, Effect of heat treatment on tensile and fracture toughness properties of 6082 alloy, J. Acheivements Mater. Manuf. Eng. 32 (2009) 162–170.
[93] J. Osten, B. Milkereit, C. Schick, O. Kessler, G. Meyruey, V. Massardier, W. Lefebvre, M. Perez, B. Milkereit, N. Wanderka, C. Schick, O. Kessler, W.S. Miller, L. Zhuang, J. Bottema, A.J. Wittebrood, P. De Smet, A. Haszler, A. Vieregge, Continuous cooling precipitation diagrams of Al-Mg-Si alloys, Mater. Sci. Eng. A. 730 (2018) 2830–2848. https://doi.org/10.1016/j.msea.2012.04.033.
[94] J.L. Murray, A.J. McAlister, The Al-Si (Aluminum-Silicon) system, Bull. Alloy Phase Diagrams. 5 (1984) 74–84. https://doi.org/10.1007/BF02868729.
[95] M. Geiger, M. Merklein, D. Staud, M. Kaupper, An inverse approach to the numerical design of the process sequence of tailored heat treated blanks, Prod. Eng. 2 (2008) 15–20. https://doi.org/10.1007/s11740-007-0072-2.
[96] W. yu MA, B. yu WANG, J. guo LIN, X. feng TANG, Influence of process parameters on properties of AA6082 in hot forming process, Trans. Nonferrous Met. Soc. China (English Ed. 27 (2017) 2454–2463. https://doi.org/10.1016/S1003-6326(17)60272-3.
[97] H.S. Halkaci, M. Turkoz, M. Dilmec, Enhancing formability in hydromechanical deep drawing process adding a shallow drawbead to the blank holder, J. Mater. Process. Technol. 214 (2014) 1638–1646. https://doi.org/10.1016/j.jmatprotec.2014.03.008.
[98] E. Öztürk, M. Türköz, H.S. Halkacı, M. Koç, Determination of optimal loading profiles in hydromechanical deep drawing process using integrated adaptive finite element analysis and fuzzy control approach, Int. J. Adv. Manuf. Technol. 88 (2017) 2443–2459. https://doi.org/10.1007/s00170-016-8912-x.
[99] A. Piccininni, G. Di Michele, G. Palumbo, D. Sorgente, L. Tricarico, Improving the Hydromechanical Deep-Drawing Process Using Aluminum Tailored Heat Treated Blanks, Acta Metall. Sin. (English Lett. 28 (2015) 1482–1489. https://doi.org/10.1007/s40195-015-0347-0.
[100] A. Piccininni, G. Palumbo, A. Lo Franco, D. Sorgente, L. Tricarico, G. Russello,

Multi objective genetic algorithm to optimize the local heat treatment of a hardenable aluminum alloy, AIP Conf. Proc. 1960 (2018) 1–6. https://doi.org/10.1063/1.5034965.
[101] S. Poles, MOGA-II An improved Multi-Objective Genetic Algorithm, ModeFRONTIER User Man. (2003) 16.
[102] S. Poles, E. Rigoni, T. Robič, MOGA-II Performance on Noisy Optimization Problems, Proc. Int. Conf. Bioinspired Optim. Methods Their Appl. (2004) 51–62.
[103] N. Hung, M. Marion, Improved Formability of Aluminum Alloys using Laser Induced Hardening of Tailored Heat Treated Blanks, Phys. Procedia. 39 (2012) 318–326. https://doi.org/10.1016/j.phpro.2012.10.044.
[104] Gigant Industries, (n.d.). https://gigant-industries.com/en/g2-2-uprights-hydraulic-presses-gigant/.
[105] Libellula laser software, (n.d.). https://www.libellula.eu/.
[106] A. Piccininni, G. Palumbo, A. Lo Franco, Numerical simulation of the stamping process of a AA5754 railway vehicle component using a Locally Annealed Blank, in: NUMIFORM 2019 13th Int. Conf. Numer. Methods Ind. Form. Process., 2019: pp. 413–416.
[107] E. Rigoni, Technical Report 2007-001 Radial Basis Functions Response Surfaces, (2007) 18.
[108] E. Rigoni, Technical Report 2007-002 Radial Basis Functions : Large Scale Problems Benchmark, (2007).
[109] O. El Fakir, L. Wang, D. Balint, J.P. Dear, J. Lin, T.A. Dean, Numerical study of the solution heat treatment, forming, and in-die quenching (HFQ) process on AA5754, Int. J. Mach. Tools Manuf. 87 (2014) 39–48. https://doi.org/10.1016/j.ijmachtools.2014.07.008.
[110] A. Piccininni, D. Sorgente, G. Palumbo, Genetic Algorithm based inverse analysis for the superplastic characterization of a Ti-6Al-4V biomedical grade, Finite Elem. Anal. Des. 148 (2018) 27–37.
[111] D. Sorgente, G. Palumbo, A. Piccininni, P. Guglielmi, L. Tricarico, Modelling the superplastic behaviour of the Ti6Al4V-ELI by means of a numerical/experimental approach, Int. J. Adv. Manuf. Technol. 90 (2017) 1–10. https://doi.org/10.1007/s00170-016-9235-7.
[112] T. Bhoskar, O.K. Kulkarni, N.K. Kulkarni, S.L. Patekar, G.M. Kakandikar, V.M. Nandedkar, Genetic Algorithm and its Applications to Mechanical Engineering: A Review, Mater. Today Proc. 2 (2015) 2624–2630. https://doi.org/10.1016/j.matpr.2015.07.219.
[113] 12004-2 ISO, Metallic materials - Sheet and strip - Determination of forming-limit curves - Part 2: Determination of forming-limit curves in the laboratory, 2008.
[114] D. Banabic, M. Vos, Modelling of the forming limit band -a new method to increase the robustness in the simulation of sheet metal forming processes, CIRP Ann. - Manuf. Technol. 56 (2007) 249–252.

https://doi.org/10.1016/j.cirp.2007.05.058.
[115] A. Piccininni, P. Guglielmi, A.L. Franco, G. Palumbo, Stamping an AA5754 Train Window Panel with High Dent Resistance Using Locally Annealed Blanks, J. Phys. Conf. Ser. 896 (2017). https://doi.org/10.1088/1742-6596/896/1/012095.
[116] A. Cuniberti, A. Tolley, M.V.C. Riglos, R. Giovachini, Influence of natural aging on the precipitation hardening of an AlMgSi alloy, Mater. Sci. Eng. A. 527 (2010) 5307–5311. https://doi.org/10.1016/j.msea.2010.05.003.
[117] B. Milkereit, N. Wanderka, C. Schick, O. Kessler, Continuous cooling precipitation diagrams of Al-Mg-Si alloys, Mater. Sci. Eng. A. 550 (2012) 87–96. https://doi.org/10.1016/j.msea.2012.04.033.
[118] J.P. Hirth, J. Lothe, T. Mura, Theory of Dislocations (2nd ed.), J. Appl. Mech. 50 (1983) 476–477. https://doi.org/10.1115/1.3167075.
[119] Y. Wang, Y. Cheng, P. Zhang, G. Luo, P. Li, K. Jiang, Effect of lubrication conditions on the forming limit of deep drawing of 6061 aluminum alloy sheet, Mater. Sci. Forum. 944 MSF (2018) 85–91. https://doi.org/10.4028/www.scientific.net/MSF.944.85.
[120] A. Piccininni, G. Palumbo, A.L. Franco, D. Sorgente, L. Tricarico, G. Russello, Multi objective genetic algorithm to optimize the local heat treatment of a hardenable aluminum alloy, in: AIP Conf. Proc., 2018. https://doi.org/10.1063/1.5034965.
[121] C. Cervellera, M. Gaggero, D. Macciò, Low-discrepancy sampling for approximate dynamic programming with local approximators, Comput. Oper. Res. 43 (2014) 108–115. https://doi.org/10.1016/j.cor.2013.09.006.